Development of techniques for analysis of cosmogenic nuclides, application to exposure histories and controls on production rates

Ana Carracedo Plumed

Submitted in fulfilment of the requirements for the degree of

Doctor of Philosophy

April 2017

School of Geographical and Earth Sciences

College of Science and Engineering

SUERC

University of Glasgow

Abstract

Cosmogenic nuclides produced in terrestrial rocks provide a versatile way of quantifying Earth surface processes. Accurate calculation of the surface age and erosion rates determined from cosmogenic nuclide concentrations requires knowledge of their production rate. Cosmogenic ^{3}He ($^{3}He_{cos}$) and ^{21}Ne ($^{21}Ne_{cos}$) are commonly used nuclides, and in contrast to ^{10}Be and ^{26}Al, they can be used in a wide array of minerals. The production rate of $^{3}He_{cos}$ and $^{21}Ne_{cos}$ depends on mineral chemical composition and in mafic minerals varies with the Mg/Fe ratio. Theoretical models have estimated that the production of $^{3}He_{cos}$ in olivine is ~10% higher than in pyroxene and ~55% higher in the case of $^{21}Ne_{cos}$. The main aims of this work are to test empirically the $^{3}He_{cos}$ and $^{21}Ne_{cos}$ production rate variations with chemical composition of the target mineral, and to apply stable ($^{3}He_{cos}$) and radioactive ($^{10}Be_{cos}$) cosmogenic nuclides in olivine to unravel the exposure history of the Mount Hampton nunatak in West Antarctica.

The *ThermoScientific* Helix SFT multi-collector mass spectrometer at SUERC was set up to perform simultaneous collection of ^{3}He and ^{4}He improving the measurement reproducibility by approximately 3 times compared to peak jumping collection using the MAP 215-50. The He extraction technique using a diode laser was refined achieving ±0.4% (2σ) and ±4.6% (2σ) precision for analysis of ~15 mg of pyroxene and olivine respectively. For samples of greater mass (50-250 mg) achieving complete degassing was challenging, especially in the case of olivine. However, reliable data was obtained when degassing pyroxene with exposure ages for the lava flows from Kula Volcanic Province, Western Turkey, ranging from < 1.8 to 11.2 ka; which is in agreement with previously published data (Heineke et al., 2016). The laser technique was successfully used for extracting He isotopes from detrital gold grains from different localities around Scotland. Unravelling the source of ^{3}He has proved challenging and requires further development. However, the extraction technique has proved reliable and has the potential for analysis of tens to hundreds of grains from the same deposit in relatively sort time generating large data sets required for provenance studies.

The homogeneous composition of mafic minerals from six lherzolite xenoliths from Mount Hampton yields low variation theoretical production rates. $^{3}He_{cos}$ and $^{21}Ne_{cos}$ were measured in olivine, orthopyroxene, clinopyroxene and spinel from each xenolith. The results confirm empirically the compositional control of cosmogenic nuclide

production rates. Therefore, a correction factor to scale for composition is recommended. The high altitude (~3 km) and high latitude (~76˚S) of the Mount Hampton xenoliths has generated some of the highest concentrations measured on terrestrial samples, comparable to those of extra-terrestrial material. Relative production rate variation of cosmogenic isotopes with altitude was found from the analysis of $^{3}He_{cos}/^{10}Be_{cos}$ ratios in accessory minerals from the Himalayas (~27˚N) at elevations of 2.8 to 4.8 km (Gayer et al, 2004; Amidon et al., 2008) suggesting tertiary spallation reactions in rocks with sufficient energy to produce $^{3}He_{cos}$ but not enough energy to produce $^{10}Be_{cos.}$ This was not observed in the Mount Hampton xenoliths with $^{21}Ne_{cos}/^{3}He_{cos}$ ratios varying from 0.25 ± 0.04 in the case of clinopyroxene to 0.40 ± 0.04 in the case of olivine. These are in agreement with previously published ratios from lower altitudes and simply reflect the chemical composition control of the $^{3}He_{cos}$ and $^{21}Ne_{cos}$ production rates.

The combination of stable and radioactive cosmogenic nuclides is an established tool for unravelling complex exposure histories in quartz-bearing surfaces. Here I have measured $^{10}Be_{cos}$ in olivine from six xenoliths from Mount Hampton and combined with the results of $^{3}He_{cos}$ from olivine from the same samples to understand the rate of landscape change above the West Antarctic Ice Sheet (WAIS). Several scenarios of complex exposure history were considered with the data being consistent with two possible scenarios for the Mount Hampton nunatak: (1) intermittent cold-based ice cover during the Plio-Pleistocene glacial cycles with a long-term erosion rate of < 7 m/Ma and (2) being ice-free since the time of formation (11.4 Ma) and experiencing a dramatic increase on erosion rates involving the removal of up to 3 m of material in the last 1.5 Ma at an average erosion rate of ~0.3 m/Ma since eruption. The results from this work demonstrate that dramatic changes in erosion rates over long periods of time can generate cosmogenic nuclide signatures typical of complex exposure without requiring burial and revealed the dynamic nature of the landscape in the high elevation mountaintops above the WAIS.

Contents

List of tables

List of Figures

Appendices

Preface

The analyses and data reported in this thesis have been undertaken by the author with the exception of the ^{10}Be analyses presented in Chapter 6, which have been provided by the SUERC AMS laboratory.

The samples used on Chapter 5 and Chapter 6 were donated by Prof. John Smellie who collaborated with the interpretation of the results presented in Chapter 6. The models used for data interpretation in Chapter 6 have been design in collaboration with Dr. Angel Rodes who has written the Matlab codes.

Acknowledgments

This PhD would not have happened without the help and support of my supervisors Prof. Fin Stuart and Prof. Darren Mark. I am indebted to them for giving me an opportunity and believing in my abilities to complete this work. I am thankful to them for sharing their scientific knowledge and for their good advise all the way through the PhD. It has been a privilege to work with them.

I would like to thank Dr. Cristina Persano without whose generous opportunity I would not have been able to start this journey. I would also like to thank Jim Imlach and Ross Dymock for their invaluable help in the laboratory, their creativity to problem solving and their patience when things go wrong, typically at the end of the day on a Friday! Thanks also to Andrew Tait for his invaluable help with setting up the Helix SFT and for his kindness and patience in explaining the complexities of mass spectrometry. A special thank you goes to Dr. Luigia di Nicola who has trained me in the laboratory and has always been there. I want to thank her also for helping me in understanding the results especially when they are complex and don't tell us what we expected. Thanks to Dr. Angel Rodes for his patience and help in generating models for interpretation of the data and also for always being available to help, thanks for his generosity in sharing not only his incredible mathematical knowledge but also his car.

Thanks to Peter Davidson, Dr. Clive Rice, Dr. John Faithful and Prof. Manuel Moreira for donating samples for analysis. Special thanks to Prof. John Smellie for his generosity in donating the Mount Hampton xenoliths and for sharing his knowledge of west Antarctica, which has been essential for interpreting the data.

Thanks to Dr. Karl Burke for his help setting up the Helix SFT and his patience when things were not looking that hopeful. Thanks to Dr. Halim Mutlu and Dr. Kiymet Deniz for their help with the fieldwork in Turkey. Thanks to Dr. Pete Burnard for sharing his lab at CRPG and his knowledge on noble gas mass spectrometry, I will always remember him with admiration. Thanks to Dr. Dan Barfod for his patience explaining how to use the CO_2 laser. Thanks to Dr Martha Zurakowska, Dr. Ma Yan and Benedikt Ritter for their help in the lab. Thanks to Catriona Lamb and Veselina Yakimova for their enthusiasm and help with element composition analysis Thanks also to Dr. Valerie Olive

for sharing her knowledge of chemistry and ICP mass spectrometry and for her patience explaining chemistry to a geologist.

Thanks to my fellow PhD students (Domokos, Brett, Pete, Sevi, Kieran, Jess, Helen and Kim) for making this an enjoyable journey and for always being happy to listen and help and always keen for a laugh. Last but not least I would like to thank my family and friends for always being supportive through the good and not so good times and special thanks to Ally for always being by my side.

Declaration

I declare that, except where explicit reference is made to the contribution of others, this thesis is the result of my own work and has not been submitted for any other degree at the University of Glasgow or any other institution.

Signed:

Name: Ana Carracedo Plumed

Glossary of commonly used abbreviations

Symbol	*Definition*
$^{3}He_{cos}$	Cosmogenic helium
$^{3}He_{nuc}$	Nucleogenic helium
$^{4}He^{*}$	Radiogenic helium
$^{21}Ne_{cos}$	Cosmogenic neon
$^{10}Be_{cos}$	Cosmogenic beryllium
ol	Olivine
cpx	Clinopyroxene
opx	Orthopyroxene
sp	Spinel
Fo	Forsterite content (100 x Mg/(Mg+Fe)
En	Enstatite content (100 x Mg/(Mg+Fe+Ca)
SFT	Split flight tube
CDD	Compact Discrete Dynode
SEM	Scanning electron microscope
EPMA	Electron probe micro analyser
HESJ	He standard of Japan (Matsuda et al., 2002)
MSWD	Mean square weighted deviation: measure of the scatter of a dataset
RSD	Relative standard deviation
R_A	$^{3}He/^{4}He$ atmospheric ratio, 1.399×10^{-6} (Mamyrin et al., 1970)
SLHL	Sea level high latitude
CTN	Cosmogenic thermal neutrons
GCR	Galactic cosmic rays
SCR	Solar cosmic rays
KVP	Kula volcanic province
WAIS	West Antarctic Ice Sheet
EAIS	East Antarctic Ice Sheet
ECR	Executive Committee Range
MBL	Marie Byrd Land
SUERC	Scottish Universities Environmental Research Centre

1. Introduction

Galactic cosmic radiation consists of high-energy nucleons that originate from sources outside the solar system. These particles have enough energy to generate nuclear disintegrations in the upper atmosphere of Earth generating a complex cascade of nuclear interactions that propagate through the atmosphere (Lal and Peters, 1967). This secondary cosmic radiation consists of three components: electromagnetic (e.g. γ and β radiation), hadronic (e.g. neutrons and protons) and mesonic (e.g. kaons and muons). The intensity of the secondary radiation is attenuated by nuclear interactions with particles in the atmosphere (Lal and Peters, 1967). A component of the primary cosmic nucleons (mostly protons) are of sufficient energy to generate secondary nucleons (mostly neutrons) and mesons (mostly muons) that are capable of reaching the Earth surface. These particles interact with nuclei in the upper few metres of the Earth producing cosmogenic nuclides (Gosse and Philips, 2001).

Cosmogenic nuclides are generated by a variety of nuclear reactions: spallation, thermal neutron capture and muon-induced nuclear disintegrations. The products of these reactions are referred to as *in situ*-produced terrestrial cosmogenic nuclides (Gosse and Philips, 2001). The probability of a particular reaction occurring depends largely on the reaction cross sections (Masarik and Reedy, 1994; Heisinger et al., 2000a, 2000b). At the Earth's surface spallation is the main mechanism of production of cosmogenic nuclides (Lal, 1991; Masarik and Beer, 1999). Spallation reactions involve a high-energy particle (> 10 MeV), typically a neutron, colliding with a target nucleus and breaking it into several lighter particles (cosmogenic nuclei, neutrons and protons) (Templeton, 1953). Spallation reactions favour the production of particles that are of slightly less mass than the target nuclei or much lighter particles (e.g. ^{24}Mg (n,α) ^{21}Ne). Thermal neutron capture reactions involve the absorption of low-energy secondary neutrons (~0.025 eV) by target nuclei (e.g. ^{6}Li (n, α) ^{3}H (β^-) ^{3}He). Muons are short-lived sub-atomic particles of the lepton family (similar to electrons) with lower probability of interacting with nuclei than neutrons, however they are able to penetrate to greater depths (Lal, 1988). In the top few centimetres production from negative muon capture accounts for 1-3 % of the total cosmogenic production (Brown et al., 1995; Heisinger et al., 2002). However, at depths greater than 2-3 m below the surface the muon components dominate the production of cosmogenic nuclides (Lal and Peters, 1967; Braucher et al., 2003).

The primary cosmic-ray flux is deflected by the Earth's magnetic field and attenuated by the reactions with atmospheric particles. The production of cosmogenic nuclides is proportional to the intensity of the secondary cosmic-ray flux, which decreases with atmospheric depth (Gosse and Phillips, 2001). Therefore, the production rate of *in situ* cosmogenic nuclides is dependent on altitude and latitude; rates are lowest at sea level and low latitudes and increasing with latitude and altitude (Lal, 1991). Scaling factors account for the variability on the cosmic-ray flux with altitude and latitude accounting for the influence of the Earth's magnetic field changes, atmospheric pressure anomalies and solar modulation (Brochers et al., 2016 and references therein). The production of cosmogenic nuclides at the Earth's surface is also dependent on the mass of the target element and therefore is controlled by chemical composition (Lal, 1991; Masarik, 2002; Kober et al., 2005). Quantifying the rate of change of the production rate of cosmogenic nuclides improves the accuracy of the calculation of the production rate for a specific surface.

The analysis of cosmogenic nuclides at the Earth's surface is a useful tool for understanding the time and duration of exposure and the rate of erosion of a particular surface. Assuming a constant cosmic-ray flux over time, it is possible to infer the exposure history of a surface by measuring the abundances of *in situ* produced cosmogenic nuclides. Therefore, understanding the production rates of cosmogenic nuclides is imperative to accurately determine the history of an exposed surface. Combining stable (e.g. ^{21}Ne) and radioactive (e.g. ^{10}Be, ^{26}Al) it is possible to unravel complex exposure histories of exposure, burial and erosion (Kober et al., 2007; Strobl et al., 2012; Di Nicola et al., 2012). Burial dating using stable and radionuclides relies on the different type of accumulation of the two nuclides. Stable nuclides accumulate over time at a constant rate as long as they are exposed with no erosion and stop accumulating when they are shielded from cosmic rays (buried). Radionuclides decay during the time of accumulation at a rate that depends on their half-lives and continue decaying when samples are buried. To date this method has been restricted to ^{21}Ne, ^{10}Be and ^{26}Al in quartz. Applying this to surfaces were quartz is not available (e.g. olivine-bearing basalts) will extend the capability of the technique, which constitutes the major contribution of cosmogenic nuclides to Earth science applications (Balco and Shuster, 2009b).

1.1 Research aim and questions

This work focuses on how cosmogenic ^{3}He and ^{21}Ne production rate varies with chemical composition of the target mineral and the use of stable and radioactive cosmogenic nuclides to unravel exposure histories and the development of a technique for accurate measurements of cosmogenic ^{3}He. The main issues addressed in this thesis:

(1) Developing new mass spectrometer and laser extraction system for routine analysis of cosmogenic He
(2) Exploring the capability of the degassing technique for analysis of different materials: old exposed samples, young lava flows and detrital gold grains.
(3) How does the mineral chemical composition control the production rate of cosmogenic ^{3}He and ^{21}Ne in mafic minerals?
(4) Does a particular elemental production model provide a more accurate prediction of such chemical control?
(5) Does cosmogenic ^{3}He in combination with ^{10}Be provide a valid alternative to understand landscape change in surfaces were quartz is not available?
(6) How does the landscape evolve in long-exposed arid environments like Antarctica?

1.2 Research approach

In order to adequately answer all the research questions important technical development was required. This involved the setting up of the ThremoFisher Helix SFT mass spectrometer for precise measurements of He isotopes and the development of a laser technique for He extraction. Several test were performed in different materials in order to understand the potential and limitations of the gas extraction technique involving the analysis young lava flows for which field work was required and the analysis of detrital gold grains in order to test this material for cosmogenic ^{3}He exposure dating studies.

The use of cosmogenic nuclides for exposure dating requires accurate knowledge of their production rate. Quantifying the chemical control of cosmogenic ^{3}He and ^{21}Ne production rates in mafic minerals is essential for accurate interpretation of their concentrations in an exposed surface. Long-exposed lherzolite xenoliths from Mount Hampton, West Antarctica were employed for this purpose as they contain a suite of mafic minerals with different compositions allowing for comparison of their respective

cosmogenic signatures. The results obtained were then compared with two theoretical models (Masarik, 2002; Kober et al., 2005).

Unravelling landscape change is a widely used application of the combination of cosmogenic stable and radioactive nuclides that currently is mostly restricted to quartz-bearing surfaces. To test our ability to extend this technique to olivine-bearing surface were quartz is not available cosmogenic ^{3}He and ^{10}Be in olivine from Mount Hampton were analysed. The results from the two cosmogenic nuclides were combined to understand the rate of landscape change above the West Antarctic Ice Sheet.

Cosmogenic ^{3}He and ^{21}Ne analyses were undertaken in the Noble Gas Laboratory at Scottish Universities Environmental Research Centre (SUERC) and the ^{10}Be analyses were performed at the AMS facility also at SUERC.

1.3 Thesis structure

This thesis is divided into seven chapters that are briefly descried below:

Chapter 2 introduces the background theory of production of cosmogenic nuclides, then concentrates on the cosmogenic noble gas isotopes. The production of cosmogenic He and Ne is discussed in detail followed by a review of the applications. This chapter also describes the ^{10}Be-^{21}Ne systematics and reviews previous work of cosmogenic ^{10}Be in olivine.

Chapter 3 provides a description of the Helix SFT mass spectrometer and the purification line and a thorough characterization of its performance.

Chapter 4 describes the noble gas extraction and purification techniques. Several different laser-degassing methods are compared and a protocol for routine He extraction is determined. Results from CRONUS pyroxene standard are compared with a global inter-calibration (Blard et al., 2015). To explore the capabilities of the degassing technique two case studies are included, covering the development of the laser degassing technique for analysis of young exposed samples using olivine and pyroxene from Holocene lavas from the Kula Volcanic Province (Western Turkey) and comparing with recently published data (Heineke et al., 2016). A second case study involving the analysis of individual gold grains

from alluvial deposits in Scotland assessing the potential of the laser technique for exposure dating detrital gold.

Chapter 5 reports the results of cosmogenic ^{3}He and ^{21}Ne in mafic minerals from Mount Hampton, West Antarctica. The chemical composition of the minerals analysed is reported and theoretical production rates are calculated. This chapter provides a comparison of the empirical data with theoretical estimations using the approaches of Masarik (2002) and Kober et al. (2005) providing a recommendation for quantifying the effect of the chemical composition on production rates.

Chapter 6 combines the cosmogenic ^{3}He results for olivine obtained in the previous chapter with ^{10}Be data from olivine from the same samples. Different models of exposure history are considered in order to unravel the rate of landscape change in the summit of Mount Hampton above the West Antarctic Ice Sheet.

Chapter 7 synthetizes the conclusions from this work and provides suggestions for future research.

2. Cosmogenic nuclides

2.1 In situ cosmogenic nuclides

2.1.1 Introduction

The discovery of naturally occurring radioactive ^{14}C produced by cosmic radiation in the Earth's atmosphere (Libby, 1946) set the start of the search for other cosmic ray produced isotopes in terrestrial and extra-terrestrial samples. The first in-situ produced cosmogenic nuclide to be identified was ^{3}He when Paneth (1952) analysed iron meteorites for ^{4}He U-Th dating finding excess ^{3}He that was attributed to be produced by cosmic rays. In-situ produced ^{36}Cl was the first cosmogenic nuclide to be studied in terrestrial rocks for the purpose of exposure dating (Davis and Schaeffer 1955). The first attempts to determine the production of cosmogenic nuclides were performed during 1960's (Lal and Peters, 1962; Bhandari et al., 1965; Lal and Peters, 1967). The studies concentrated on extra-terrestrial material due to significantly higher production rates than at the Earth's surface. In the late 1970s Srinivasan (1976) analysed cosmogenic ^{126}Xe in barite from a sedimentary unit in southern Africa introducing the potential of cosmogenic noble gasses for exposure dating.

The development of noble gas mass spectrometry and accelerator mass spectrometry since 1980's allowed the measurement of low concentrations of cosmogenic nuclides in terrestrial samples (Hohenberg, 1980; Klein et al., 1982; Elmore and Phillips, 1987; Sano and Wakita, 1988; Sano et al., 1982; Sano et al., 2008). The lowering of detection limits by $\sim 10^{6}$ resulted in an explosion in the measurement of cosmogenic nuclides at the Earth's surface in the late 1980s; ^{3}He (Kurz, 1986; Craig and Poreda, 1986), ^{10}Be and ^{26}Al (Nishiizumi et al., 1986; Klein et al., 1986; Nishiizumi et al., 1987), ^{36}Cl (Phillips et al., 1986) and ^{21}Ne (Marti and Craig, 1987). Since then multiple studies of in-situ produced cosmogenic nuclides have been performed for different Earth science applications.

2.1.2 Commonly used terrestrial cosmogenic nuclides

Cosmogenic nuclides that are rare in surface minerals and soils have resolvable natural interferences and are produced and retained in common minerals can be used for Earth science applications (Dunai, 2010). Cosmogenic nuclides can be stable (^{3}He, ^{21}Ne, ^{22}Ne, ^{36}Ar, ^{38}Ar, Kr and Xe isotopes) and radioactive (^{10}Be, ^{14}C, ^{26}Al, ^{36}Cl, ^{41}Ca and ^{53}Mn) (Table 2.1). Of those, the cosmogenic nuclides that are most commonly used in Earth science applications are ^{3}He, ^{21}Ne, ^{22}Ne, ^{10}Be, ^{26}Al and ^{36}Cl.

Table 2.1. Compilation of the stable and radioactive cosmogenic nuclides and their target elements and minerals.

Nuclide	*Half-life*	*Main target elements*	*Main target minerals*
Stable			
^{3}He		O, Mg, Al, Si, Ca, Fe	Olivine, pyroxene
^{21}Ne		Mg, Al, Si, Ca	Quartz, pyroxene, olivine
^{36}Ar		K, Ca	Feldspar, amphibole, pyroxene
Radioactive			
^{53}Mn	3.7 ± 4 Ma	Fe, Mn	Fe-bearing minerals
^{10}Be	1.39 ± 0.02 Ma	O, Si, Mg	Quartz
^{26}Al	708 ± 17 ka	Si	Quartz
^{36}Cl	301 ± 2 ka	K, Ca, Fe, Ti	Carbonates, feldspar, whole rock
^{41}Ca	104 ± 4 ka	Fe, Ti	Fe-Ti oxides
^{14}C	5.73 ± 0.03 ka	O, Si	Quartz

Radioactive nuclides are in order of decreasing half-life (^{53}Mn: Honda and Imamura, 1971; ^{10}Be: Chmeleff et al., 2010; ^{26}Al: Nishiizumi, 2004; ^{36}Cl: Holden, 1990; ^{41}Ca: Kutschera et al., 1992; ^{14}C: Lederer et al., 1978).

The stable cosmogenic nuclides accumulate at a constant rate when a surface is continuously exposed. Consequently, there is no limit on the exposure age that they can record. When production rate is known, then the concentration of the cosmogenic nuclide in the sample is directly related to its exposure age (Gosse and Philips, 2001). On the other hand, radioactive cosmogenic nuclides decay at a constant rate (λ [s^{-1}]) as they are produced. The half-life ($T_{1/2} = \ln(2)/ \lambda$) of each nuclide governs the decay rate, reaching saturation after a exposure time of 2-3 times their half-lives and they can be considered extinct after 5-6 half-lives (Faure and Mensing, 2005). This limits the maximum exposure time that a radionuclide can be used for (Figure 2.1).

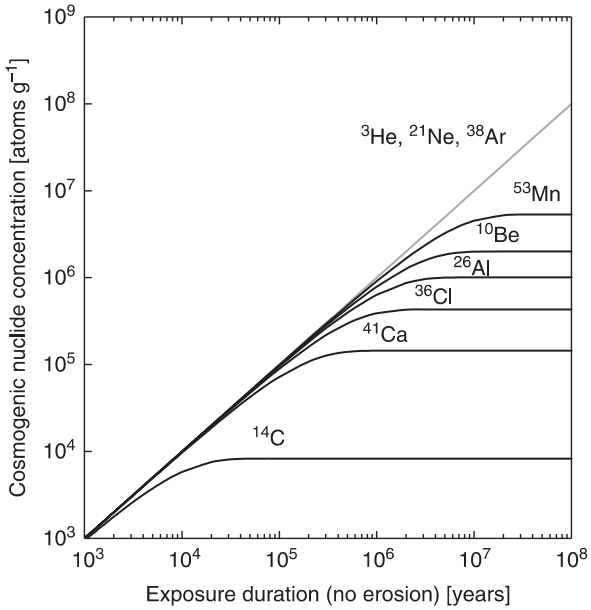

Figure 2.1. Accumulation of cosmogenic nuclides in a non-eroding surface (after Dunai 2010). When there is no erosion, the radioactive nuclides reach saturation directly in relation to their half-lives while the concentration of stable nuclides increase continuously over exposure time.

2.1.3 Mechanisms of production of cosmogenic nuclides at the Earth's surface

Galactic cosmic radiation originates from outside the solar system and consists of high-energy nucleons, mostly protons with enough energy (~1 to ~10^{10} GeV) to produce nuclear disintegrations in the upper atmosphere (above 100 gcm^{-2}). This is the primary cosmic-ray flux and the interactions with nuclei of atoms in the upper atmosphere originate a cascade of secondary nucleons (e.g. protons and neutrons) and mesons (e.g. Kaons and muons) with the same properties as the primary nucleons. As this nuclear cascade progresses through the atmosphere it loses energy to successive collisions (Figure 2.2). Neutrons being electrically neutral do not suffer ionization losses unlike protons (Lal and Peters, 1967) therefore the composition of the hadronic cascade changes from proton-dominated in the upper atmosphere to neutron-dominated at the Earth's surface with a composition of 98 % neutrons at sea level (Masarik and Beer, 1999). The consequent energy loss of the primary cosmic rays due to successive spallation reactions through the nuclear cascade causes the neutron-dominated flux at sea level to have energies ranging from < 1 eV to 100 MeV (Gordon et al., 2004).

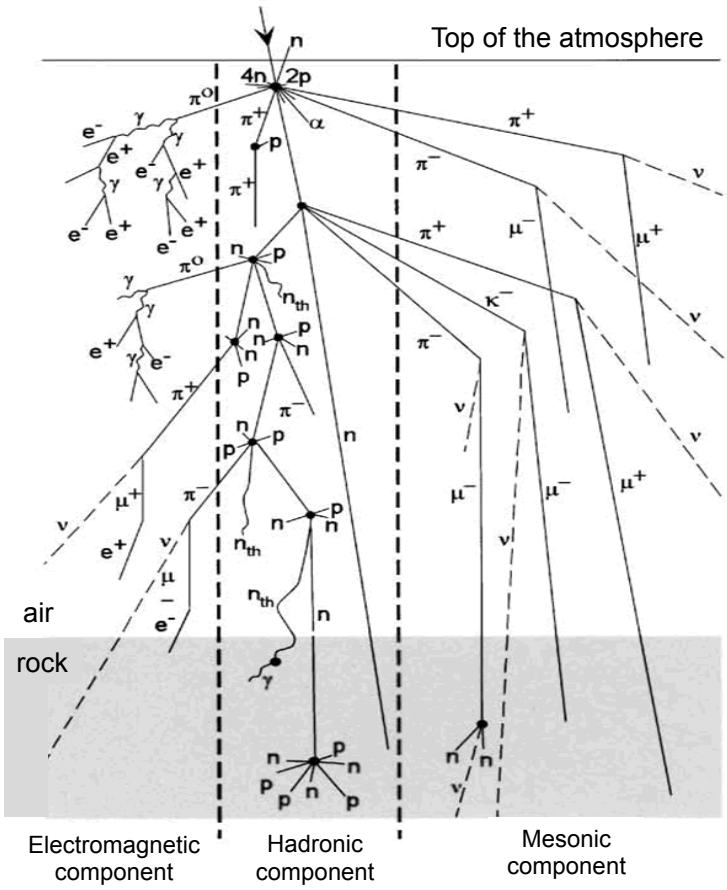

Figure 2.2. Major components of the cosmogenic cascade showing the production of secondary particles in the atmosphere and in rock (modified from Gosse and Phillips, 2001). n: neutron, p: proton, e^+: positron, e^-: electron, κ : kaon, ν : neutrino, π :pion , μ :muon.

Secondary cosmic-ray particles are responsible for the majority of the cosmogenic nuclide production at the Earth's surface due to spallation reactions (Lal, 1991; Masarik and Beer, 1999). Secondary particles are mainly neutrons of different energies (high-energy neutrons: 10 MeV to 10 GeV; fast-neutrons: 0.1 to 10 MeV; slow-neutrons: 100 eV to 100 keV; epithermal neutrons: 0.5 to 100 eV and thermal neutrons: ~ 0.025 eV; Dunai, 2010) and muons.

High-energy and fast neutrons are those responsible for inducing spallation reactions and this is the main mechanism of production of cosmogenic nuclides at the Earth's surface. Spallation is an energy process in which a neutron collides with a target nucleus (e.g. Si) and breaks from it several (3 to 10) lighter particles (e.g. ^{3}He) (Templeton, 1953). The mass distribution of the product of spallation is bimodal favouring product masses that are slightly less than the target mass or much lighter particles (Gosse and Phillips, 2001). As an example, when ^{28}Si is the target of spallation, the most probable nuclides to be produced are those of masses 27 to 25 and 1 to 3. For all the target elements

that produce cosmogenic nuclides those of mass 1 to 3 are always part of the spallation products. This is partly why spallogenic ^{3}He has the greatest production rate.

The high-energy and fast neutron flux decreases almost exponentially with increasing depth below the Earth's surface (Figure 2.3) proportionally to the depth (z, cm), the density of the rock (ρ, g/cm^3) and the attenuation length (Λ, g/cm^2) as follows:

$$N_{(z)} = N_0 \, e^{-z\rho/\Lambda} \qquad [2.1]$$

where $N_{(z)}$ and N_0 are the number of spallation-produced nucleons at depth and at the surface respectively (Dunne et al., 1999). The attenuation length for spallation reactions has been determined by fitting an exponential function to cosmogenic nuclide concentrations in rocks collected at different depths or from continuous rock cores (Kurz, 1986; Brown et al., 1992) the results vary from 150 to 170 g/cm^2 with a value of 160 g/cm^2 commonly adopted (Gosse and Phillips, 2001; Balco et al., 2008). This is the value that has been adopted for the calculations made in this work following the recommendations of Balco et al. (2008). Considering a rock density of 2.6 g/cm^3 and attenuation length of 160 g/cm^2, the production rate due to spallation at 3 m below the earth's surface represents 1% of the production rate at the surface.

Thermal neutron capture reactions also produce cosmogenic nuclides. Thermal neutrons are low-energy secondary particles (~ 0.025 eV) with relatively high probability of being absorbed by some nuclei (Masarik and Reedy, 1995). The production of cosmogenic nuclides due to thermal neutron capture depends on the macroscopic thermal-neutron absorption reaction cross-section (Σ_{th}, cm^2/g), which is proportional to the elemental thermal neutron cross section ($\sigma_{th,k,}$ barns = 10^{-24} cm^2/atom) and the concentration of the target element (N_k, atom/g):

$$\Sigma_{th} = \Sigma \, \sigma_{th,k} \, N_k \qquad [2.2]$$

The high absorption cross-section of nitrogen for thermal neutrons (1.9 barns) causes that the macroscopic absorption cross-section in the atmosphere (0.06 cm^2/g) is about one order of magnitude greater than that in a rock (0.004 to 0.008 cm^2/g). The thermal neutron flux in rocks is approximately one order of magnitude higher than in the atmosphere (Phillips et al., 2001). The thermal neutron flux in rocks is directly derived from high-energy neutrons moderated by interaction with atoms in the rocks. The diffusive

behaviour of the thermal neutrons produces a thermal neutron flux profile that, unlike the spallation profile, increases with depth until ~ 50 g/cm^2 and then decreases with further depth (Figure 2.3).

Some thermal neutron absorption reactions have large cross-sections producing considerable amounts of commonly used cosmogenic nuclides: $^{6}Li(n,\alpha)^{3}H(\beta^{-})^{3}He$; $^{14}N(n,p)^{14}C$; $^{35}Cl(n,\gamma)^{36}Cl$ and $^{39}K(n,\alpha)^{36}Cl$ (Lal, 1987; Phillips et al., 2001; Dunai et al., 2007). Thermal neutron capture can also be originated within the rock by α-particles product of radioactive decay of elements such as uranium and thorium causing (α,n) reactions and can be relevant in the case of stable nuclides such as ^{3}He (Dunai et al., 2007).

Muons are the product of the decay of unstable mesons produced by primary cosmic ray reactions in the upper atmosphere with energies of ~ 4 GeV (Eidelman et al., 2004). Their interaction with matter is weak, mainly via ionization; therefore they penetrate deeper into the surface than neutrons so that muon induced ionization is the main mechanism of cosmogenic nuclide production below the Earth's surface (Lal, 1988). The attenuation length for muon production is about 1500 g/cm^2 (Brown et al., 1995), one order of magnitude greater than that for spallation. Muonic interactions that produce cosmogenic nuclides involve mainly the capture of slow negative muons (μ^-) by charged nuclei (Lal, 1988) and production due to fast muon interactions (Gosse and Phillips, 2001). Negative muon reactions can produce ^{10}Be, ^{26}Al, ^{36}Cl and other nuclides. In the top centimetres of the Earth's surface production rate from negative muon capture accounts for 1-3 % of the total cosmogenic radionuclide production (Brown et al., 1995; Heisinger et al. 2002). In the case of ^{3}He the production rate due to negative muon capture is negligible at least on the first 2.7 m below the Earth's surface (Farley et al., 2006). In the case of ^{21}Ne the production due to negative muon capture has been determined to account for 8 ± 4 % of the total production at sea level high latitude (Balco and Shuster, 2009a) and it is supported by the calculations of Fernandez-Mosquera et al. (2010). The differences in the attenuation lengths for cosmogenic nuclide production mean that at depths greater than ~2 m below the surface the muon components of the secondary cosmic radiation dominate the production of cosmogenic nuclides (Lal and Peters, 1967) (Figure 2.3).

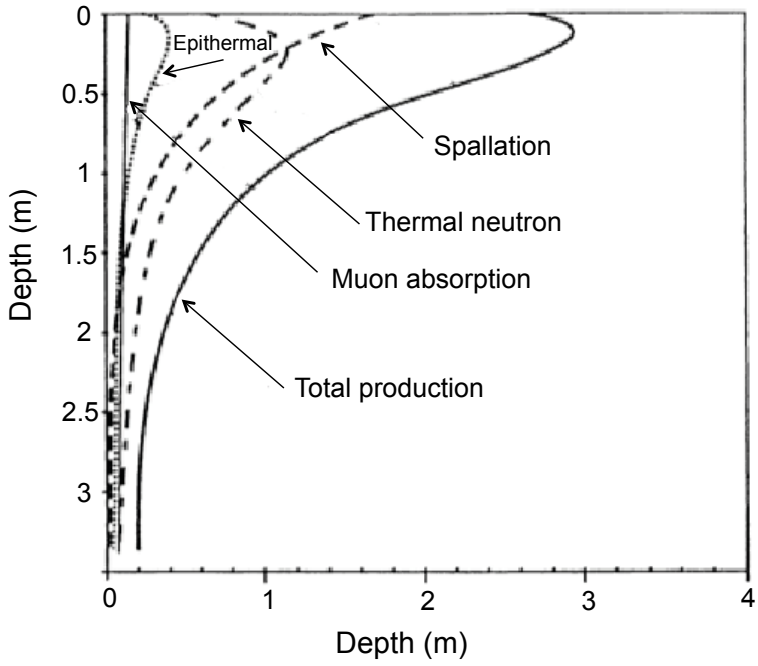

Figure 2.3. Contribution of the different cosmogenic nuclide production reactions with depth, the case of ^{36}Cl (modified from Gosse and Phillips 2001). At the surface spallation is the dominant source of production of cosmogenic nuclides with thermal neutron produced and muon absorption being the dominant mechanisms at depth.

2.1.4 Spatial and temporal variations on the cosmogenic nuclides production rate

The primary cosmic-ray flux is dominantly composed of protons that are deflected as they pass through the Earth's magnetic field. The particles momentum to charge ratio is defined as rigidity (R[GeV]). The cut-off rigidity (R_c) is the minimum rigidity required for a charged particle to penetrate the Earth's magnetic field (Stormer 1935). The cut-off rigidity of galactic cosmic ray protons varies with latitude (Figure 2.4). It is highest at the equator (> 10 GeV) where incoming primary cosmic rays incise the geomagnetic field vertically. Consequently the intensity of secondary cosmic-ray flux is lowest at the equator and highest at high latitudes (> 58˚) where cut-off rigidity is < 2 GeV (Dunai, 2001; Desilets et al., 2006). The production rate of cosmogenic nuclides increases with geomagnetic latitude, reaching a plateau at latitudes above 58˚ as at those latitudes all the particles responsible for producing cosmogenic nuclides are able to reach the Earth's surface (Gosse and Phillips, 2001).

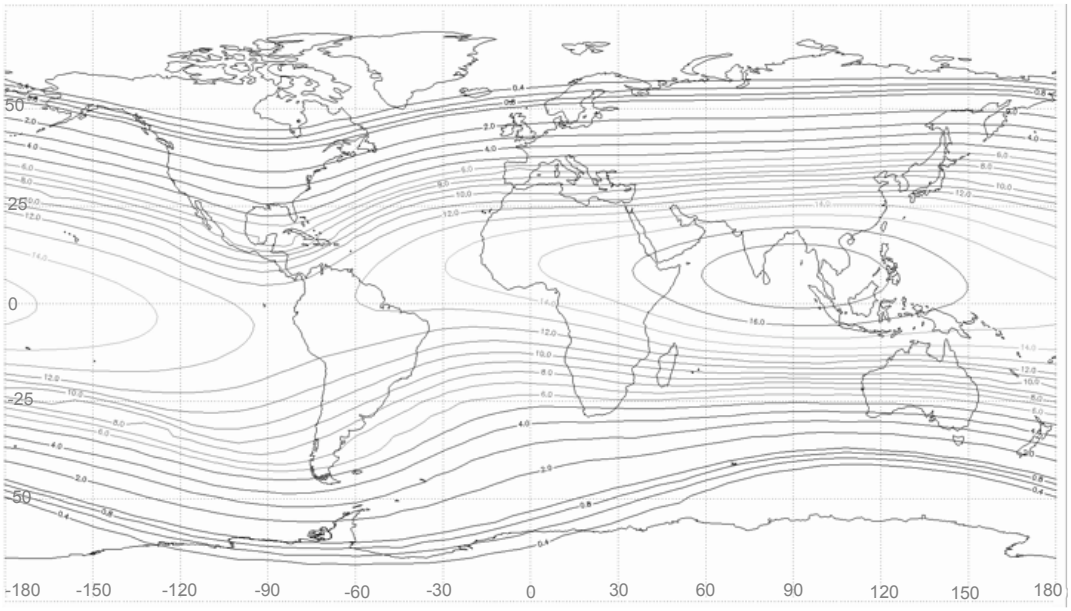

Figure 2.4. Influence of the geomagnetic field on effective vertical cut-off rigidities (modified from Desilets et al., 2006). The contour lines represent the vertical cut-off rigidities (GeV) as measured by Shea and Smart (1983).

The Earth's geomagnetic field is more complex than a simple dipole field model (Gall, 1960) which ads further complexity to the global cosmic-ray flux intensity over the surface of the Earth (Stone, 2000; Gosse and Philips, 2001). The non-dipole components of the Earth's magnetic field cause variations in the inclination with respect to the geomagnetic latitude. The intensity of the secondary cosmic-ray flux is sensitive to changes on the inclination of the geomagnetic field (Rothwell, 1958), which has an effect on the cut-off rigidity. Over long time scales it can be assumed that the dipolar position averages to the geographic poles (geocentric axial dipole GAD) (Merill et al., 1998; Dunai, 2000; Lifton et al., 2008) although this cannot be assumed when studying Holocene or late Pleistocene samples (Dunai, 2000; Lifton et al., 2008) since non-dipole effects may not average to a GAD in that short time frame. Small changes in pole orientation can be responsible of significant variations in the cosmic-ray intensities particularly for mid latitudes (~30˚) affecting the outcome of cosmogenic nuclide interpretations. At mid latitudes a 5˚ error on the geomagnetic pole position could account for 10 to 15 % variation in the spallogenic nucleon intensity at sea level and 4 km of elevation (Lifton et al., 2008). It is therefore recommended to choose an appropriate scaling model that includes the temporal variations of the non-dipole magnetic field (Dunai, 2000; Lifton et al., 2005; Lifton et al., 2008; Lifton et al., 2014) for appropriate interpretation of cosmogenic nuclides signatures in the case of Holocene surfaces.

2.1.5 Available scaling models

The production of cosmogenic nuclides is proportional to the intensity of the secondary cosmic-ray flux. Using cosmogenic nuclides for Earth science applications requires accurate knowledge of the local production rate. Typically production rates are scaled for altitude and latitude and, as a convention, all the production calibration studies are normalized to the production rate at sea level and high latitude (SLHL). Scaling factors account for the variability on the cosmic-ray flux with altitude and latitude accounting for the influence of the Earth's magnetic field dipole and non-dipole changes, atmospheric pressure anomalies and solar modulation.

The available scaling models can be divided based on their neutron reaction counting method. The earliest efforts were made by Lal (1991) based on atmospheric measurements of nuclear disintegrations in photographic emulsions in combination with neutron detectors. This is a time independent scaling factor that assumes constant production rate. It uses nuclear disintegration polynomials with input parameters for latitude and altitude. This scaling model was re-parameterized by Stone (2000) accounting for geographic latitude and atmospheric pressure. Stone (2000) modified the equations of Lal (1991) in terms of atmospheric pressure instead of altitude to account correctly for global pressure variations. In order to add time dependence to the Lal(1991)/Stone(2000) scaling model, Balco et al. (2008) proposed a scaling scheme that introduces a correction for paleomagnetic variation based on data from Nishiizumi et al. (1989).

Scaling models based on experimental data from neutron monitors (Desilets and Zreda, 2003; Desilets et al., 2006; Dunai, 2000; Lifton et al., 2005; Lifton et al., 2008) are time dependent and account for geomagnetic field variations. The scaling scheme of Dunai (2000) incorporates the non-dipole components of the Earth's magnetic field (relevant for low latitudes) and is based on an analytically calculated cut-off rigidity and atmospheric pressure. Desilets and Zreda (2003) proposed improvements on the available scaling methods that considered the differences in energies and attenuation lengths involved in thermal neutron and spallation reactions. This framework was further developed by Desilets et al. (2006) using experimental data from low latitudes (Hawaii and India) to characterize altitude profiles of neutron fluxes. This scaling factor is based on the assumption that cosmic ray intensity varies as a function of cut-off rigidity at a given atmospheric depth. Lifton et al. (2005, 2008) proposed a time dependent model that

incorporates the effects of the dipole and non-dipole magnetic field variations and the solar modulation on the cosmic ray flux. This scaling factor is based on elevation dependence of the production by spallation considering the solar modulation and cut-off rigidity calculated using trajectory tracing. There are discrepancies between the models based on nuclear disintegration and the neutron-monitor based, especially at high elevation and low latitude.

A new scaling framework (LSD) recently published by Lifton et al. (2014) is the first model that does not rely on empirical dataset from particle detectors. It is a time dependent model based on analytical equations of secondary cosmic ray flux obtained from basic cosmic-ray physics. It incorporates the dipole and non-dipole magnetic field variations as well as the solar modulation. The model incorporates a variation to account for nuclide dependence (more significant at low latitude and high altitude) by incorporating cross-sections for the different reactions. This model allows for identification of the biases that generate the discrepancies between the different scaling models. The altitude dependent flux variation with geomagnetic latitude seems to be the main cause of the bias. Being underestimated at high geomagnetic latitudes by Lal (1991)/Stone (2000) and overestimated by the monitor-based scaling models (Desilets et al. 2006, Dunai 2000, Lifton et al. 2008) at low geomagnetic latitude.

For the purpose of this work two different scaling models have been used. In the case of the exposure dating of the lava flows from the Kula Volcanic Province, Turkey (Section 4.4), the scaling model proposed by Lifton et al. (2014) has been used as it incorporates the dipole and non-dipole magnetic field variations and accounts for nuclide dependence relevant especially when dating young exposed surfaces at mid latitudes. In the case of unravelling the exposure history of Mount Hampton (Chapter 6) the scaling scheme proposed by Balco et al. (2008) based on Lal(1991)/Stone(2000) has been used as this is the most commonly used scaling scheme for studies of interpretation of two cosmogenic nuclides incorporating time dependency and global pressure variations.

2.1.6 Effects of chemical composition on the production rate of cosmogenic nuclides: theoretical models

Theoretical modelling of the production rate of the different cosmogenic nuclides on Earth has been the subject of several studies based on the chemical control of the

production of cosmogenic nuclides (Yokoyama et al., 1977; Lal, 1990; Masarik & Reedy, 1995; Masarik & Beer, 1999; Masarik, 2002; Kober at al., 2005). Yokoyama et al. (1977) published the first theoretical estimation of the production rates of radionuclides in terrestrial rocks (granite, basalt and limestone). The calculation of the production rates considered only the production by cosmic ray flux using the same three-step cascade model used for lunar samples (Yokoyama et al., 1973). They also performed experimental measurements of production rates of ^{22}Na and ^{24}Na in aluminium and magnesium targets at different mountain elevations that agree with their theoretical calculations. The precision to which they calculated the production rates is ~20% for ^{7}Be, ^{22}Na, ^{24}Na, ^{26}A1, ^{36}C1, ^{37}At, ^{53}Mn, ^{54}Mn and ^{55}Fe, and ~35% for ^{3}H, ^{10}Be, ^{14}C and ^{39}Ar.

Lal (1991) published theoretical estimates for the production rates of cosmogenic isotopes of He, Ne and Ar in different target elements (O, Mg, Al, Si, Ca and Fe) based on proton excitation functions and reaction cross-section data from Lavielle et al. (1989). The theoretical calculations of Lal (1991) estimated production of ^{3}He in O, Si, Mg, Al and Fe. He proposed the ^{3}He production rate in Mg is ~1.8 times higher than that in Fe. The production of ^{21}Ne was estimated for Mg, Al, Si and Fe with Mg being the main target element (~4.6 higher production than Fe). The uncertainties of these theoretical estimations are considered to be > 25-30 %. Since the theoretical calculations of Lal (1991) are based on interactions with high-energy protons the production rates estimated are lower than experimental measurements (Poreda and Cerling, 1992).

Based on the previous work of Masarik and Reedy (1995), Masarik and Beer (1999) proposed a theoretical estimation of the energy of the neutron flux calculated using Monte Carlo model based on GEANT (Burn et al., 1987) and MCNP (Briesmeister, 1993) code systems to simulate production and transport of the galactic cosmic ray particles in the Earth's atmosphere for energies up to hundreds of GeV. Particle fluxes were calculated as a function of geomagnetic latitude, altitude, geomagnetic field intensity, solar modulation and chemical composition. Masarik and Beer (1999) calculated the production rate (P) of a specific nuclide (j) at depth (D) in the Earth's surface following equation 2.3:

$$P_{\mathrm{j}}(\mathrm{D}) = \sum_i \mathrm{N_i} \sum_k \int_0^{\infty} \sigma_{\mathrm{ijk}}(E_{\mathrm{k}}) \times J_{\mathrm{k}}(E_{\mathrm{k}}, D) dE_{\mathrm{k}} \qquad [2.3]$$

where, N_i is the number of atoms for target element i per kg material in the sample, $\sigma_{ijk}(E_k)$ is the cross section for the production of nuclide j from the target element i by

particles of type k with energy E_k, and $J_k(E_k,D)$ is the total flux of particles of type k with energy E_k at location D inside the atmosphere. The particle fluxes Jk(Ek,D) are calculated using the GEANT and MCNP codes and the cross sections $\sigma_{ijk}(E_k)$ are those evaluated from many measurements (Alsmiller and Barish, 1981; Wilson and Costner, 1975).

Their production rate calculations were based on an elemental composition of the atmosphere in wt % of 75.5 % N, 23.2 % O, 1.3 % Ar; and an average composition of the Earth's surface of 0.2% H, 47.3% O, 2.5% Na, 4.0% Mg, 6.0% Al, 29.0% Si, 5.0% Ca and 6.0% Fe. Uncertainties in the production rate calculations correspond to uncertainties in the excitation functions and are considered to be within 30-50%. In 2002 Masarik (2002) revisited the calculation of the production rate of cosmogenic nuclides for the major element calculated from new particle fluxes and updated excitation functions. Production rates by neutrons only at SLHL for the main target elements for ^{3}He, ^{10}Be, ^{14}C, ^{21}Ne, ^{26}Al and ^{36}Cl were reported (table 2.2).

Kober et al. (2005) proposed new theoretical estimations based on the particle fluxes proposed by Masarik and Beer (1999) and the nuclide specific reaction cross-sections from irradiation experiments of Leya et al. (2000). They modelled the production rate of ^{3}He, ^{10}Be and ^{21}Ne for their target elements (O, Mg, Al, Fe and Ni for ^{3}He; O, N, Mg, Al, Ca, Fe and Ni for ^{10}Be and Na, Mg, Al, Ca, Fe and Ni for ^{21}Ne) using production rate ratios relative to Si. Their model based the element specific production of ^{21}Ne on the experimentally determined ^{21}Ne production in Si from Niedermann et al. (1994) and Niedermann (2000). The production of ^{3}He and ^{10}Be were based on the ^{3}He and ^{10}Be production in Si extrapolated from calculated ^{3}He/^{21}Ne and ^{10}Be/^{21}Ne production ratios. Results for elemental production rates calculated by Kober et al. (2005) are summarized in Table 2.2.

Table 2.2. Element specific production rates (atoms/g/yr) for cosmogenic ^{3}He, ^{10}Be and ^{21}Ne reported by Masarik (2002) and Kober et al. (2005) for their main target elements.

		Production rates from different target elements (atoms/g/yr)							
Nuclide	*Theoretical model*	*O*	*Na*	*Mg*	*Al*	*Si*	*Ca*	*Fe*	*Ni*
^{3}He	Masarik (2002)	128.7	-	110.8	102	106	57.7	38.5	-
	Kober et al. (2005)	191	-	182	160	129	-	95	91
^{10}Be	Masarik (2002)	9.82	-	1.74	1.03	0.89	-	0.35	-
	Kober et al. (2005)	6.54	24.49	1.93	1.61	3.28	1.12	1.86	1.45
^{21}Ne	Masarik (2002)	-	102	175.1	62.4	41.7	1.8	0.187	-
	Kober et al. (2005)	-	208	189	60	44	17	1	1

The methods of Masarik (2002) and Kober et al. (2005) have been compared by Fenton et al. (2009) on a calibration study of ^{3}He and ^{21}Ne production rates in olivine and pyroxene from the western Grand Canyon, USA. The experimental results conclude that the Masarik (2002) method underestimates the ^{3}He production rates and/or overestimates the ^{21}Ne production rates resulting on overestimation of the $^{21}Ne/^{3}He$ ratios with respect to those obtained experimentally. In the case of Kober et al. (2005) the ^{21}Ne production rates overlap within uncertainty those obtained from the Masarik (2002) method but the production rates of ^{3}He of Kober et al (2005) are anomalously high. In this case the theoretical elemental production rates for ^{3}He were compared to experimental production rate from Fe-Ti oxides analyses, which corroborated their findings. This agreement of the theoretical and experimental data found by Kober et al. (2005) could have been partly due to an overestimation of the ^{3}He due to implanted cosmogenic thermal neutron produced ^{3}He from coexistent minerals such as hornblende and biotite (Dunai et al., 2007). Since the theoretical calculations of Kober et al. (2005) for ^{3}He production rates seem to be highly overestimated, the most commonly adopted method to scale production rates for different chemical compositions is that of Masarik (2002).

In this work I am attempting to understand the relative production of the different commonly used minerals (olivine and pyroxene) for cosmogenic ^{3}He and ^{21}Ne studies (Chapter 5). The relative production rates are then compared with the elemental production rate calculations of Masarik (2002) and Kober et al. (2005) in order to determine which method predicts more accurately the relative production rate of cosmogenic ^{3}He and ^{21}Ne in different mafic minerals.

2.2 Helium

Helium has two stable isotopes ^{3}He and ^{4}He, which can be produced from different sources. In minerals ^{3}He can have three different components: cosmogenic ^{3}He ($^{3}He_{cos}$), nucleogenic ($^{3}He_{nuc}$) and magmatic ($^{3}He_{mag}$). ^{4}He can have two components: radiogenic ($^{4}He^{*}$) and magmatic ($^{4}He_{mag}$) (Figure 2.5). Identifying the different He components is required to identify the cosmogenic component. The different production mechanisms of He are discussed in this section.

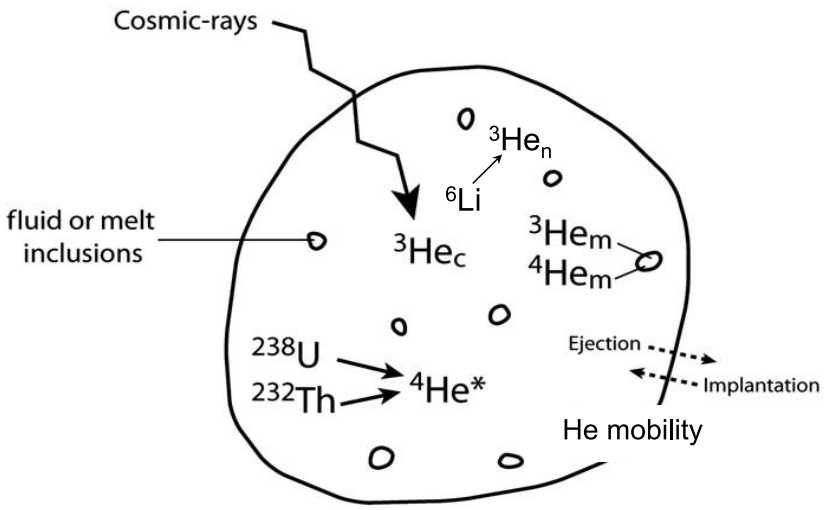

Figure 2.5. Sources of helium in mafic minerals (modified from Blard and Farley 2008). The helium magmatic component ($^{3}He_{m}$ and $^{4}He_{m}$) is trapped in fluid and melt inclusions while radiogenic ($^{4}He^{*}$), nucleogenic ($^{3}He_{n}$) and cosmogenic ($^{3}He_{c}$) store in the mineral lattice.

2.2.1 Cosmogenic He ($^{3}He_{cos}$)

Spallation is the dominant production mechanism of $^{3}He_{cos}$ and its precursor ^{3}H (half life 12.6 years) in minerals at the Earth's surface (Trull et al., 1991). Below the surface, the production due to spallation decreases exponentially (see previous section) with the contribution from fast muons becoming relevant at depths below 900 g/cm^{2} (~ 3 m of rock) (Lal, 1987). At the Earth's surface, $^{3}He_{cos}$ is produced from high-energy neutron collisions with all elements except from H, although the main target elements in mafic minerals are O, Mg, Si, Al and Fe (Lal, 1988). Its low detection limit makes the $^{3}He_{cos}$ dating technique to allow for dating of surfaces of exposure as young as < 1 ka (Kurz et al., 1990). Helium has the smallest Van der Waals radius of all cosmogenic nuclides (1.07 pm, Bandenhoop and Weinhold, 1997), and it can diffuse through structural channels and defects in minerals. Consequently it is not quantitatively retained at surface temperatures by many of the commonest rock-forming minerals like quartz and feldspars over geological time (Trull et al., 1991; Farley, 2007). $^{3}He_{cos}$ is quantitatively retained at surface temperatures by mafic minerals, which have low ionic porosity (e.g. olivine and pyroxene) (Trull et al., 1991; Schäfer et al., 1999; Margerison et al., 2004).

Olivine and pyroxene are the most commonly used target minerals for $^{3}He_{cos}$ studies. $^{3}He_{cos}$ has been successfully measured in other minerals like apatite, titanite, zircon (Farley et al., 2006), magnetite, hematite, ilmenite (Kober et al., 2005) and hornblende (Margerison et al., 2004). These studies offer the feasibility of analysing $^{3}He_{cos}$ in mineral

phases that coexist with other cosmogenic nuclides target minerals such as Be, Al in quartz. The $^{3}He/^{4}He$ ratio of pure cosmogenic helium is ~0.2-0.3 (Wieler, 2002) is 10^{5} times higher than the $^{3}He/^{4}He$ ratio of the atmosphere (R_A=1.39 x 10^{-6}; Mamyrin et al., 1970) and 10^{4} to 10^{7} higher than the ratio in rocks (0.1 to 50 R_A) (Ballentine and Burnard, 2002; Graham, 2002; Stuart et al., 2003). This large difference is key to resolving the contribution of cosmogenic helium from other components.

2.2.2 Nucleogenic He ($^{3}He_{nuc}$)

$^{3}He_{nuc}$ is produced by the reaction of cosmogenic and radiogenic thermalized neutrons with nuclei. The production rate of cosmogenic thermal neutrons (CTN) is proportional to the elemental thermal neutron cross-section and the concentration of the target element (Phillips et al., 2001). In the case of He the thermal neutron absorption reaction $^{6}Li(n,\alpha)^{3}H(\beta^{-})^{3}He$ have large cross-section (942 barn) capable of producing considerable amounts of ^{3}He (Lal, 1987; Andrews and Kay, 1982). A reaction with ^{10}B produces 10^{4} less ^{3}He than with ^{6}Li due to its smaller reaction cross-section (0.05 barn) and it can be neglected (Lal, 1987; Andrews and Kay, 1982). CTN capture produces one ^{3}He and one α-particle. ^{4}He is produced as a result of the α-particle gaining two electrons resulting in a nucleogenic $^{3}He/^{4}He$ ratio of 1 (Dunai et al., 2007).

Radiogenic thermalized neutrons produce $^{3}He_{nuc}$ by (α,n) reactions in light elements in rocks induced by α-particles emitted from nuclides in the U- and Th-decay chain (Martel et al., 1990). These reactions together with spontaneous fission of U^{238} are a source of neutrons in rocks producing ~2 neutrons per gram of rock per ppm of U per year. The neutron production rate from Th is approximately one third of the production from U (Feige et al., 1968).

The production rate of $^{3}He_{nuc}$ for a neutron flux of 1 neutron/cm^{2}/year is 6.13×10^{-6} atoms/g/year/ppm of Li (Lal, 1987). The $^{3}He_{nuc}$ production rate will vary proportionally with the intensity of the neutron flux and the amount of Li in a rock. The radiogenic thermal neutron flux is controlled by U-and Th-decays (Lal, 1987). The absorption mean free path for neutrons range from ~ 50 cm in granite and basalt to ~ 76 cm in ultramafic rocks, consequently the radiogenic neutron flux is homogeneous (Lal, 1987). The intensity of the radiogenic neutron flux is ~ 2,800 neutrons/cm^{2}/year in granite and as low as 1.4 neutrons/cm^{2}/year in ultramafic rocks (Lal, 1987). At sea level and high latitude (SLHL),

the CTN flux ranges from 50,000 neutrons/cm^2/year in basalts to 140,000 neutrons/cm^2/year in carbonates (Phillips et al., 2001). The intensity of the CTN flux varies with latitude and altitude, reaching minimum value of 28,000 at sea level at the equator (Lal, 1991; Dunai, 2000). At the Earth's surface the $^3He_{nuc}$ production is dominated by CTN flux with the radiogenic neutron flux becoming important only at depths below 2000 g/cm^2 (~ 7m of granite rock) (Lal, 1987).

The concentration of Li in an exposed sample determines the concentration of $^3He_{nuc}$. A typical crustal rock contains ~ 35 ppm of Li (Teng et al., 2004). The production of $^3He_{nuc}$ in such a rock from radiogenic thermal neutrons is ~ 0.7 atoms/g/year and ~13 atoms/g/year from CTN. The CTN production represents 13 to 19 % of the ^{3}He atoms produced by spallation if homogeneous Li concentration in a rock is assumed (Farley et al., 2006). The production of $^3He_{nuc}$ can be considered negligible in Li-poor minerals such as olivine and pyroxene (where $^3He_{cos}$ is mostly analysed) with Li concentrations typically below 2 ppm (Ryan and Kyle, 2004). In minerals with moderate Li concentrations (> 5 ppm) the $^3He_{nuc}$ production can be significant accounting for 15 to 70% of the total cosmogenic production in silicate minerals with high amounts of Li (50-200 ppm) like hornblende and biotite (Dunai et al. 2007).

In the $^6Li(n,\alpha)^3H$ reaction the ^{3}H nucleus is ejected with a kinetic energy of 2.7 MeV equivalent to a stopping rage of ~ 30 μm in common minerals (Ziegler, 2004; Farley et al., 2006). Dunai et al. (2007) estimated that Li-free spheres of 30 to 200 μm would accumulate 74 to 11 atoms/g/year of ^{3}He (SLHL) if embedded in biotite with 290 ppm Li. Their calculations were based on the equation proposed by Farley et al. (2006):

$$P_a = P_i\,[1-0.75x(S/R)+0.625x(S/R)^3]+P_h\,[0.75x(S/R)-0.625x(S/R)^3] \qquad [2.4]$$

where, P_a is the apparent production rate (atoms/g/year), P_i and P_h are the in-situ production rates in the mineral of interest and its host, S is the stopping range (μm) and R is the radius of the mineral of interest (μm). This observation together with those made by Farley et al. (2006) suggests that when analysing lithium-free mineral phases embedded on neighbouring minerals or hosting rock with higher Li contents, avoiding smaller fractions (< 250 μm) can help to control the effect of implanted ^{3}He, which could result in an overestimation of the $^3He_{cos}$ concentration in the sample and ultimately overestimating the exposure age.

2.2.3 Magmatic helium ($^3He_{mag}$ and $^4He_{mag}$)

Magmatic helium is trapped in fluid- and melt-inclusions during mineral formation. Fluid and melt inclusions are trapped in minerals during crystallization from melts. Helium can be released from fluid and melt-inclusions by in vacuo crushing (Hilton et al., 1993; Scarsi, 2000; Stuart et al., 2003; Moreira and Madureira, 2005; Blard et al., 2006; Blard et al., 2008). Prolonged and/or intense crushing of the minerals can release helium from the matrix of the finest grains (< 140 μm) (Hilton et al., 1993; Scarsi, 2000; Blard et al., 2006) and by thermal diffusion (Blard et al., 2008). Mild crushing of bigger grains is required to avoid this problem (Scarsi, 2000; Stuart et al., 2003; Blard et al., 2008).

The melt-derived He isotopes provide information on the time-integrated (U+Th)/He history of the mantle source (Kurz and Jenkins, 1982; Craig and Poreda, 1985; Stuart et al., 2003). The magmatic He is a tracer of the primordial mantle flux from the Earth's interior with $^3He/^4He$ ratios 5-50 times higher than the atmospheric $^3He/^4He$ ratio (R_A, 1.39 x 10^{-6}, Mamyrin et al., 1970). In contrast $^3He/^4He$ ratios 10 to 100 times lower than air are typical of continental crust signature as radiogenic ^4He from U- and Th-decay (Aldrich and Nier, 1948) causes the $^3He/^4He$ ratio to decrease below that of air (Ballentine and Burnard, 2002; Stuart et al., 2003).

The magmatic $^3He/^4He$ ratios released from the crushing experiments is used for isolating the cosmogenic component in the cases where there is no contribution from radiogenic ^4He (Craig and Poreda, 1986; Kurz, 1986) (see section 2.2.5). When radiogenic ^4He is present in a sample, for example in geologically old basalts (> 100 ka), this needs to be quantified by determination of the U and Th concentrations in the mineral and the hosting rock (Dunai and Wijbrans, 2000; Blard and Farley, 2008). Alternatively, in the case of geologically old rocks, avoiding the mineral phases with trapped helium, for example analysing microphenocrysts in lava, can reduce the three-component problem to a two component (Williams et al., 2005). In this case the radiogenic $^3He/^4He$ ratio needs to be characterized by analysing material shielded from cosmic rays (Margerison et al., 2005).

2.2.4 Radiogenic ^{4}He (^{4}He)*

^{4}He* is produced in a rock by in-situ radioactive decay of U^{238}, U^{235}, Th^{232} and in some phases like monazite by Sm^{147}. The ^{4}He* present in a mineral embedded in a rock depends on its U, Th and Sm content and also on the U, Th and Sm content of the hosting rock and the mineral grain size as the long stopping distance of α-particles may cause the presence of implanted ^{4}He* (Blard and Farley, 2008). The concentration of U and Th in olivine and pyroxene phenocrysts is so low that the production of ^{4}He* can be considered negligible especially in young rocks (< 100 ka) although it has been demonstrated that implanted ^{4}He* from surrounding U-rich phases can be significant (Dunai and Wijbrans, 2000; Blard and Farley, 2008). In mafic phenocrysts such as olivine and pyroxene, the ejection distance of α-particles is approximately 20 μm (Zielger, 1977) producing an exchange of ^{4}He* between minerals. For instance, basalts tend to be enriched in U and Th relative to olivine and pyroxene phenocrysts and may result in the implantation of ^{4}He*. Therefore, calculating the ^{4}He* production rate in a mineral has to account for ejection and implantation of ^{4}He* to and from the hosting rock. Blard and Farley (2008) proposed an equation that includes both mechanisms:

$$P_4 = I_4 [1 - 1.5 \text{ x } (S/D) + 0.5 \text{ x } (S/D)^3] + M_4 [1.5 \text{ x } (S/D) - 0.5 \text{ x } (S/D)^3] \quad [2.5]$$

where, I_4 and M_4 are the ^{4}He* production rate (atoms/g/year) within the mineral of interest and the hosting rock respectively, S is the stopping distance of the α-nuclei (μm) and D is the diameter of the crystal (μm). Assuming secular equilibrium, I_4 and M_4 can be calculated (Wolf et al., 1988):

$$I_4 \text{ (or } M_4) = 8 \text{ x } [^{238}U] \text{ x } \lambda_{238} + 7 \text{ x } [^{235}U] \text{ x } \lambda_{235} + 6 \text{ x } [^{232}Th] \text{ x } \lambda_{232} \quad [2.6]$$

where, $[^{238}U]$, $[^{235}U]$, $[^{232}Th]$ are the correspondent isotope concentrations for the mineral (in the case of I_4) and the hosting rock (in the case of M_4) and λ_{238}, λ_{235}, λ_{232} their respective decay constants.

If the ^{4}He* present in a mineral is not appropriately estimated and it is attributed to the magmatic component it will result in an overestimation of the $^3He_{mag}$ and consequent underestimation of the $^3He_{cos}$ concentration (Dunai and Wijbrans, 2000; Blard and Farley, 2008). Correction for U and Th concentration of the mineral and the surrounding rock is

then necessary for a correct interpretation of the He concentrations (Dunai and Wijbrans, 2000; Blard and Farley, 2008).

2.2.5 $^3He_{cos}$ calculation

$^3He_{cos}$ is retained in the mineral lattice and the helium magmatic component (^3He and ^4He) is trapped in fluid- and melt-inclusions. Isolating the cosmogenic component is imperative for cosmogenic exposure dating applications. In mafic minerals, such as olivine and pyroxene, vacuum crushing has been a widely adopted method of releasing the magmatic He trapped in the fluid- and melt- inclusions (see section 2.2.3). To calculate the cosmogenic component present in the mineral matrix, the remaining powder from the crushing experiment is melted in vacuo. If negligible contribution of radiogenic He is assumed, the concentration of $^3He_{cos}$ can be calculated by subtraction of the magmatic component released by crushing $(^3He/^4He)_{crush}$ from the helium released from the melt $(^3He/^4He)_{melt}$ following equation 2.7 (Craig and Poreda, 1986; Kurz, 1986):

$$^3He_{cos} = [(^3He/^4He)_{melt} - (^3He/^4He)_{crush}] \times {}^4He_{melt} \quad [2.7]$$

In cases where $^4He^*$ is present in the mineral lattice, this protocol leads to an overestimation of the magmatic ^3He content and therefore underestimation the $^3He_{cos}$ concentration (Blard et al., 2005). The total $^4He^*$ has to be calculated considering both the production from U and Th within the phenocrysts and implanted from the surrounding groundmass (see section 2.2.4). Blard et al. (2005) proposed the following equations to calculate the $^4He^*$ concentration and include it in the calculation of $^3He_{cos}$:

$$^4He^* = (I_4 + P_4) \times t \quad [2.8]$$

$$^3He_{cos} = {}^3He_{melt} - [(^4He_{melt} - {}^4He^*) \times (^3He/^4He)_{crush}] \quad [2.9]$$

where I_4 and P_4 are the implantation and production rate of $^4He^*$ in atoms/g/year and t is the rock age in years. This method requires an independently calculated age of the host rock, which is not available in all cases. When the age of the rock is unknown an alternative method is needed. The analysis of a shielded sample will provide information of the inherited helium and allow for the $^4He^*$ to be discriminated (Blard et al., 2005):

$$^4He^* = {}^4He_{melt} - [(^3He_{melt} \times (^4He/^3He)_{crush}] \quad [2.10]$$

The nucleogenic He component can be significant when analysing Li-rich mineral phases or small crystals within a Li-rich groundmass. In this case knowledge of the major and trace element composition of the host rock is required in order to apply the appropriate production of $^3He_{nuc}$ (Farley et al. 2006). Correction for $^3He_{nuc}$ is not as straightforward as the $^4He^*$ correction since the production of $^3He_{nuc}$ not only depends on the Li concentration but also on the duration over which the helium is retained, which is related to the (U-Th)/He age (Farley 2002). In many cases the $^3He_{nuc}$ can be effectively determined by analysing a shielded sample (Margerison et al., 2005; Amidon and Farley, 2011).

2.2.6 Ejection distance and implantation of $^3He_{cos}$

The ejection distances of nuclei are a function of charge, and the composition and density of the material they have to traverse. Given the same kinetic energy, low-charge nuclei will travel further than those with higher charge (Zielger et al., 2008). Spallation reactions that produce cosmogenic ^3He and its precursor ^3H do not have strict upper energy limits, having a wide range of energies (from tens to hundreds of MeV). ^3He and ^3H average kinetic energies are approximately 10-20 MeV and 5-10 MeV respectively (Powell et al., 1959). Considering the density of olivine, these energies correspond to average ejection distances of 54-170 μm and 70-220 μm for ^3He and ^3H respectively (Ziegler et al., 2008) (Figure 2.6). When the size of the mineral grains used for exposure dating are similar to the ejection distances, a considerable proportion of the $^3He_{cos}$ found in a mineral may have been produced outside that mineral and a similar proportion of $^3He_{cos}$ produced in the mineral may have been implanted into the hosting rock. Accounting for implantation and ejection requires accurate knowledge of the $^3H/^3He$ ratio from spallation production. Currently there is no consensus on this ratio with estimates ranging between 1 (Masarik, 2002) and ~ 0.5 (Kober et al., 2005). In any case, the apparent mineral production rate is proportional to the grain size, which becomes more relevant as the difference of production rates of the mineral of interest and the hosting rock increase. Two examples of large production rate variations are the production rate in zircons in granites (Farley et al., 2006) and that in iron oxides in felsic rocks (Dunai et al., 2007).

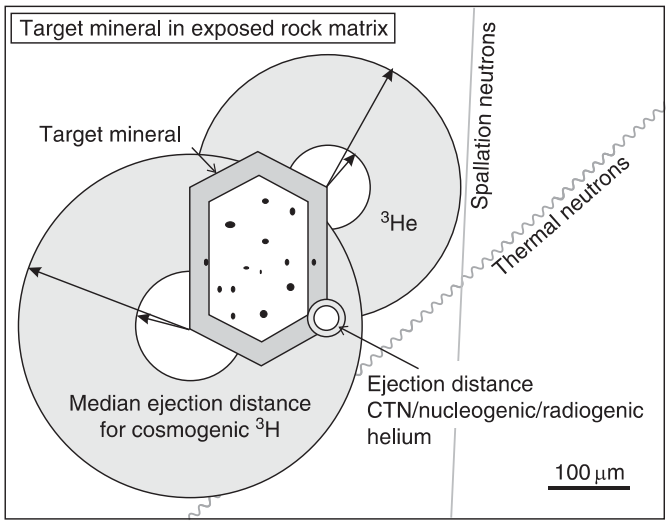

Figure 2.6. Ejection distances from nuclear reactions in an exposed mineral sample (after Dunai 2010). Ejection distances for cosmogenic ^{3}H and ^{3}He vary from 54 to 220 μ m. Thermal neutron produced, nucleogenic and radiogenic helium have ejection distances of 20 to 30 μ m, with helium mobility of those components happening mostly in the grain rim.

2.2.7 $^3He_{cos}$ production rate

The use of $^3He_{cos}$ for Earth science applications requires the knowledge of the production rate of ^{3}He at the latitude and altitude of the studied surface. To calculate $^3He_{cos}$ production rate an independent dating of a well-preserved surface is needed. Most of the cosmogenic He calibration studies use the eruption/exposure age of a well-preserved lava flow. Knowing the age (t, years) of a well preserved surface and measuring the concentration of $^3He_{cos}$ (atoms/g) in the sample allows the calculation of the local $^3He_{cos}$ production rate (P^3He_{cos}, atoms/g/year) integrated over the time since eruption (Kurz et al., 1990).

The majority of the production rate studies use mafic minerals (Kurz et al., 1990; Poreda and Cerling, 1992; Cerling and Craig, 1994; Licciardi et al., 1999; Dunai and Wijbrans, 2000; Ackert et al., 2003; Blard et al. 2006, Licciardi et al. 2006, Goehring et al., 2010; Foeken et al. 2012, Blard et al., 2013; Fenton et al., 2013; Fenton and Niedermann, 2014; Delunel et al., 2016). Fewer calibration studies have been performed in other ^{3}He retentive minerals like apatite, zircon, titanite, kyanite, garnet (Farley et al., 2006; Gayer et al., 2008; Amidon et al., 2009), Fe-Ti oxides (Bryce & Farley, 2002; Kober et al., 2005; Shuster et al., 2012) and hornblende (Amidon et al., 2012).

Absolute production rates of $^{3}He_{cos}$ in mafic minerals have been empirically calculated at different latitudes and altitudes (Figure 2.7). Goehring et al. (2010) compiled the published in-situ cosmogenic $^{3}He_{cos}$ production rates measured at different latitudes and altitudes and scaled to SLHL using different scaling models (Lal 1991/Stone, 2000; Dunai, 2001; Lifton et al., 2005 and Desilets et al. 2006). Goehring et al. (2010) proposed a global average of 121 ± 11 and 113 ± 18 atoms/g/year at SLHL for olivine and pyroxene respectively when the scaling model of Lal (1991)/Stone (2000) is applied. The uncertainties on these empirically calculated production rates make the global average production rates indistinguishable between mineral phases therefore mineral compositions were not included in the recommended global average being $^{3}He_{cos}$ production rate at SLHL 120 ± 9.4 atoms/g/year for olivine and pyroxene. Since the work of Goehring et al. (2010), five more calibration studies have been performed, three in the northern hemisphere (Foeken et al., 2012; Fenton et al., 2013 and Fenton and Niedermann, 2014) and two in the southern hemisphere (Blard et al., 2013 and Delunel et al., 2016).

The most recently published $^{3}He_{cos}$ production rate calibration study (Delunel et al., 2016) compiles the published $^{3}He_{cos}$ rate calibration studies performed to date and recalculates the global average using the work of Cerling and Craig (1994), Licciardi et al. (1999, 2006), Dunai and Wijbrans (2000), Ackert et al. (2003), Blard et al. (2006, 2013), Goehring et al. (2010), Amidon and Farley (2011), Foeken et al. (2012), Fenton et al. (2013), Fenton and Niedermann (2014) and Delunel et al. (2016). Based on the observations of Goehring et al. (2010), Delunel et al (2016) do not distinguish between olivine and pyroxene for their global average $^{3}He_{cos}$ production rate calculation giving a new calculated value of 120 ± 16 atoms/g/year in agreement with the previous one.

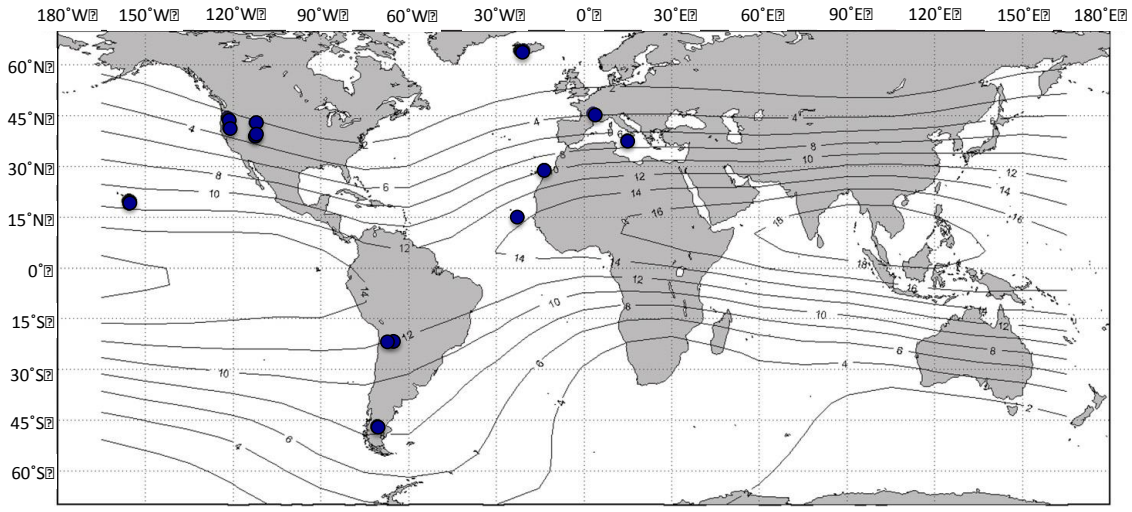

Figure 2.7. Map showing the locations of the $^{3}He_{cos}$ calibration sites (modified from Goehring et al., 2010). The contour lines show the AD 1950 cut-off rigidity (Lifton et al., 2005).

2.2.7.1 Theoretical models of $^3He_{cos}$ production rate in mafic minerals

The production rate of $^3He_{cos}$ decreases as the atomic mass of the target element increases (Masarik & Beer, 1999). Two main theoretical models have been proposed for the elemental control on $^3He_{cos}$ production rates in minerals (Masarik, 2002; Kober et al., 2005). Discrepancies between the two models are significant in the particular case of ^3He due to different assumption made on the production of ^3He and its precursor ^3H. Masarik (2002) considered the production of nuclides only by neutrons assuming $^3He/^3H$ production ratio of 1. Kober et al. (2005) based on the different reaction cross-sections of the proton and neutron induced production of ^3He and ^3H, they considered the relative $^3He/^3H$ production ratios higher than 1 using the element specific values of Leya et al. (2000): 1.73[O], 3.0[Fe], 2.22[Mg], 2.28[Al], 2.16[Si] and 3.0[Ni]. As a result, the elemental specific $^3He_{cos}$ production rates proposed by Kober et al. (2005) are 1.48, 1.64, 1.57, 1.22 and 2.44 times higher than Masarik (2002) for O, Mg, Al, Si and Fe respectively. The $^3He_{cos}$ production rate in a mineral can be calculated as the sum of the element production rate multiplied by its weight fraction for the major elements present in the mineral. Since the elemental production rates are different for each model, the mineral production rate using Masarik (2002) (Equation 2.11) and Kober et al. (2005) (Equation 2.12) can be calculated as follows:

$$^3He_{cos}=128.7[O]+110.8[Mg]+102[Al]+106[Si]+57.5[Ca]+38.5[Fe] \quad [2.11]$$

$$^3He_{cos}=191[O]+182[Mg]+160[Al]+129[Si]+95[Fe]+91[Ni] \quad [2.12]$$

$^3He_{cos}$ is mainly analysed in mafic minerals, with olivine and pyroxene being the minerals most widely used. Olivine in ultrabasic rocks typically has a range of forsterite content (Fo, Mg/(Mg+Fe)) of Fo_{96}-Fo_{85}, with higher forsterite content olivine crystallizing earlier. In gabbroic rocks olivine phenocrysts have lower forsterite contents Fo_{80}-Fo_{50} (e.g. Deer et al. 1992). Both models show a difference in the $^3He_{cos}$ production rate in commonly observed olivine compositions (Fo_{70}-Fo_{95}). Masarik (2002) model predicts 11% difference in the production rate of $^3He_{cos}$ and Kober et al. (2005) model predict a difference of 7% (Figure 2.8).

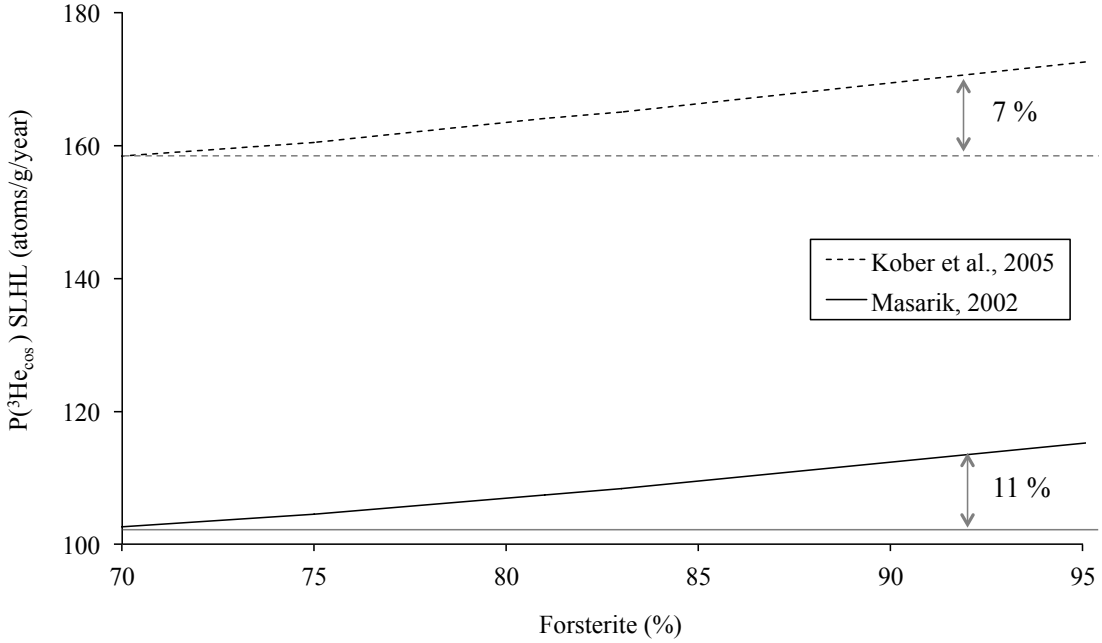

Figure 2.8. Theoretical $^{3}He_{cos}$ production rate at SLHL in basaltic olivine based on forsterite % (Mg/(Mg+Fe)) calculated using Masarik (2002) and Kober et al. (2005) theoretical models.

The enstatite content (En, Mg/(Mg+Fe+Ca)) in commonly analysed pyroxene range from 30 to 55. The production rate of $^{3}He_{cos}$ calculated using Masarik (2002) model predicts 6 % difference between En_{30} and En_{55} and the model of Kober et al. (2005) predicts a 5 % difference (Figure 2.9).

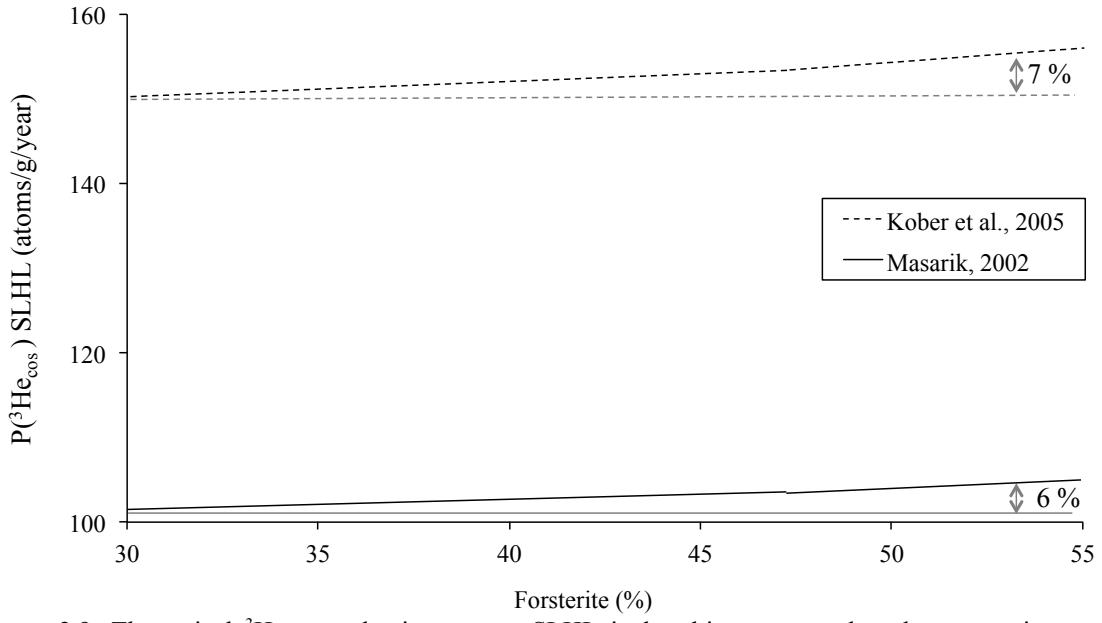

Figure 2.9. Theoretical $^{3}He_{cos}$ production rate at SLHL in basaltic pyroxene based on enstatite content (Mg/(Mg+Fe+Ca)) calculated using Masarik (2002) and Kober et al. (2005) theoretical models.

Theory predicts variation on the production of $^{3}He_{cos}$ with mineral composition. Taking the average of the typical olivine and pyroxene compositions the production rate of $^{3}He_{cos}$ in olivine appears to be 6% (Masarik 2002) and 7% (Kober et al. 2005) higher than

that for pyroxene. The production rates calculated using Kober et al. (2005) are ~ 1.5 times greater than those calculated using Masarik (2002).

2.2.7.2 Comparison of the theoretical calculations with $^3He_{cos}$ production rate calibration studies in mafic minerals

Data from previously published $^3He_{cos}$ production rate calibrations are summarized in Figure 2.10. The production rates are scaled to SLHL using Lal(1991)/Stone(2000) scaling factor. The reported production rates are compared against the magnesium content of the target mineral analysed. The forsterite content of the olivine minerals used in this compilation range from Fo_{71} (Ackert et al. 2003) to Fo_{89} (Licciardi et al. 2006) yielding production rates of 130 ± 7 and 132 ± 4 respectively, showing difference in the production rate between such range of Mg content. Theoretical models predict 6% (Masarik, 2002) and 4% (Kober et al., 2005) difference between the two end members. The uncertainties of the measurements are 5% and 3% for Fo_{71} and Fo_{89} respectively making the predicted differences unresolvable.

Comparing the $^3He_{cos}$ production rates in olivine and pyroxene from the same calibration study, Ackert et al. (2003) calculated a $^3He_{cos}$ production rate for olivine of 130 ± 7 atoms/g/year and for pyroxene 125 ± 15 atoms/g/year. In this case although the average values reveal a 4 % difference in production rate between the two minerals, the uncertainties on the average values make this difference indistinguishable. Foeken et al. (2012) reported values of production rate for olivine and pyroxene of 101 ± 8 and 94 ± 3 atoms/g/year respectively. This represent a difference of 7 %, which is in agreement with theoretical calculations of Masarik (2002) although the uncertainties on the average make the production rates indistinguishable. The data from Fenton et al. (2013, 2014) show no clear correlation between the production rate and Mg content as previous studies, arguing that the reason of the differences in the production rate with Mg content could be related to an underestimation of the nucleogenic component. Comparing the average production rate from all the pyroxene studies (118 ± 24 atoms/g/year) to that from all the olivine studies (120 ± 14 atoms/g/year) they are indistinguishable. The $^3He_{cos}$ production rate variation with Mg content expected from theoretical calculations cannot be appreciated with the current data. The uncertainties associated with the analytical procedures and those related to the scaling factors applied in order to be able to compare all the data, can leave the compositional control of production rate unresolvable. However, when scaling is not

necessary (i.e. coexisting olivine and pyroxene) and uncertainties of the measurements are reduced, scaling production rates for composition using theoretical elemental production rates can be a valid approach.

Comparing the theoretical values for $^{3}He_{cos}$ production rate for olivine and pyroxene calculated using Masarik (2002) and Kober et al. (2005) it seems that the model of Masarik (2002) gives a more accurate value of the production rate in olivine whist the model of Kober et al. (2005) seems to yield production rate values that are closer to the empirical results in the case of pyroxene. In addition to this, the high uncertainties don't allow for distinguishing the production rate of ^{3}He in different mafic minerals. It is therefore still no clear which of the models is most appropriate for composition scaling although to date the elemental production rates of Masarik (2002) are the most commonly used for compositional scaling.

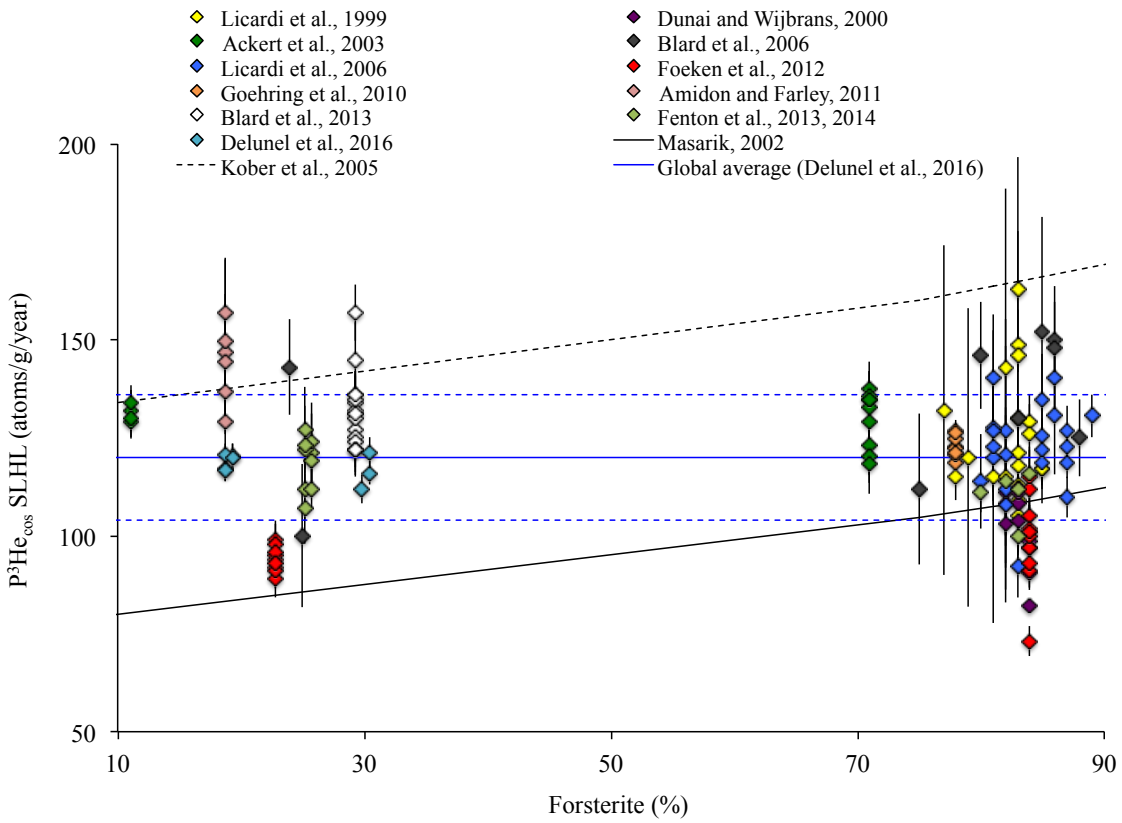

Figure 2.10. $^{3}He_{cos}$ production rate from previously published calibration studies. The production rates are scaled for SLHL using Lal(1991)/Stone(2000) scaling factor. The black line represents the theoretical production rate of Masarik (2002) and the dotted line that of Kober et al. (2005). The blue lines represent the global average and the standard deviation. Uncertainties are reported as 1 σ . Values of forsterite content around 22-25% are those of pyroxene plotted as a normalized forsterite content (Poreda and Cerling, 1992).

2.2.8 $^{3}He_{cos}$ applications

Cosmogenic ^{3}He concentration in combination with scaled $^{3}He_{cos}$ production rate is used for many Earth's science applications. The majority of $^{3}He_{cos}$ studies used volcanic olivine and pyroxene although some studies have proven the efficiency of the application of $^{3}He_{cos}$ technique in other mineral like hematite, apatite and zircon (Shuster et al. 2012, Amidon and Farley 2011). The technique relies on two main characteristics of the ^{3}He: (1) its low detection limit, allowing for dating of young basalts (Cerling and Craig, 1994; Licciardi et al, 1999; Fenton and Niedermann, 2014; Heineke et al., 2016) that cannot be dated accurately with other techniques, and (2) its accumulation and retention in minerals over geological time, allowing for dating of very old surfaces (Margerison et al., 2004; Evenstar et al., 2009) that cannot be dated with radionuclides.

2.3 Neon

Neon has three stable isotopes ^{20}Ne, ^{21}Ne and ^{22}Ne with similar rates of production by spallation reaction (Niedermann, 2002). ^{20}Ne is the most abundant isotope of the three in the atmosphere with $^{21}Ne/^{20}Ne$ and $^{22}Ne/^{20}Ne$ ratios of 0.00296 and 0.102 respectively (Eberthardt et al., 1965). Cosmogenic ^{21}Ne ($^{21}Ne_{cos}$) is generally used in exposure age and erosion rate studies due to its lowest natural abundance. The concentration of neon in the atmosphere is 18.2 ppm (Eberhardt et al., 1965; Porcelli et al., 2002) therefore all exposed samples contain atmospheric and cosmogenic neon. Cosmogenic neon has a relatively low detection limit permitting the analysis of small sample sizes (~100 mg). Its Van der Waals radius is 14% larger than helium (Badenhoop and Weinhold, 1997), consequently neon is quantitatively retained over geological time in all helium retentive minerals (see section 2.2) and in quartz and sanidine (Kober et al., 2005) although it is not quantitatively retained in other feldspars like plagioclase (Bruno et al., 1997; Schäfer et al., 1999). Quartz, olivine and pyroxene are the target minerals used in the majority of cosmogenic neon studies, quartz being the most commonly used (Niedermann, 2002).

2.3.1 Cosmogenic Ne ($^{21}Ne_{cos}$)

The three stable isotopes of neon (^{20}Ne, ^{21}Ne and ^{22}Ne) present in a mineral can be separated into two components: trapped and in situ. The trapped component is composed

of atmospheric neon mixed with mantle and crustal neon and it is retained in fluid- and melt- inclusions. The in situ component accumulates in the mineral lattice and it is composed by cosmogenic and nucleogenic neon. Discrimination of the cosmogenic neon and correction for the non-cosmogenic component can be accomplished using a neon three isotope diagram (Niedermann et al., 1994; Niedermann, 2002) (Figure 2.11).

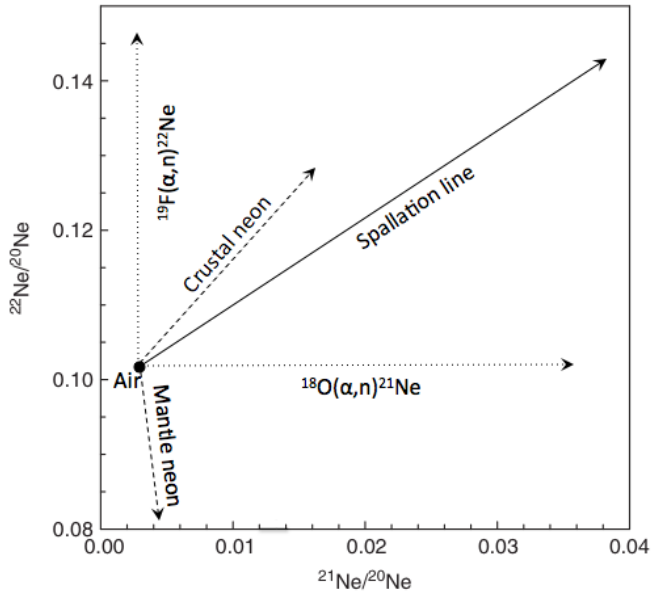

Figure 2.11. Neon three-isotope diagram showing the mixing lines of air derived neon with the different neon components (modified from Niedermann 2002). The spallation line represents the mixing between air-derived neon and pure cosmogenic neon. The slope of the spallation line depends on the composition of the target mineral and it has been experimentally determined for quartz and pyroxene (see text). The contributions from nucleogenic ^{21}Ne and ^{22}Ne represented by the dotted lines shift in the horizontal and vertical directions respectively. The dashed lines represent the mixing between air composition and mantle and crustal component defined by data from Sarda et al. (1988) and Kennedy et al. (1990) respectively.

Based on the principle that cosmogenic neon in a mineral is characterized by a unique cosmogenic $^{21}Ne/^{22}Ne$ ratio, any mixture of the cosmogenic and atmospheric signature must lie on the atmospheric-cosmogenic mixing line (spallation line). Plotting in a three-isotope space ($^{21}Ne/^{20}Ne$ vs. $^{22}Ne/^{20}Ne$) the mixing lines of atmospheric neon with all the neon components (cosmogenic, crustal, mantle and nucleogenic) is a commonly used approach for discrimination of the cosmogenic component as any non-cosmogenic source can be identify by deviations from the spallation line (Niedermann, 2002). If the neon isotopic composition of a sample plots to the right of the spallation line indicating a mixture of atmospheric Ne, cosmogenic Ne and nucleogenic Ne, the concentration of $^{21}Ne_{cos}$ in the sample can be calculated using the following equation:

$$^{21}Ne_{cos} = (^{20}Ne)_{melt} \times \frac{(^{21}Ne/^{22}Ne)_{cos}\,[\,(^{21}Ne/^{20}Ne)_{air} - (^{21}Ne/^{20}Ne)_{melt}]}{m \qquad [(^{21}Ne/^{20}Ne)_{air} - (^{21}Ne/^{20}Ne)_{cos}]} \qquad [2.13]$$

where m is the slope of the of the spallation line that depends on cosmogenic $^{21}Ne/^{20}Ne$ and $^{22}Ne/^{20}Ne$ relative production ratios (Niedermann, 2002). The slope of the spallation line is dependent on the specific elemental reaction cross-sections of the three isotopes and therefore on the mineral composition (Niedermann, 2002). It has been determined experimentally for quartz, pyroxene (augite) and olivine. The values given to the slope of the quartz spallation line are 1.120 ± 0.020 (Niedermann et al., 1993) and 1.143 ± 0.038 (Schäfer et al. 1999). In the case of pyroxene spallation line 1.055 ± 0.017 (Bruno et al., 1997) and 1.069 ± 0.035 (Schäfer et al., 1999) are the calculated slopes. And for olivine the slope is 1.03 ± 0.03 (Fenton et al., 2009). The reproducibility on the spallation line slopes for quartz and pyroxene demonstrate robustness on the calculation of the spallation line. The slopes of he spallation line for the three different minerals confirm the difference on the production rate relative to Mg content although the uncertainties on the slope of the spallation line of olivine and that of pyroxene make the spallation lines for the two minerals indistinguishable.

2.3.2 Mantle-derived Ne

Relative to atmospheric neon the mantle component is enriched in ^{20}Ne and ^{21}Ne (Sarda et al., 1988; Graham, 2002) (see Figure 2.11). In the case of exposure dating, samples are typically sub aerial exposed rocks that have adsorbed or trapped high amounts of atmospheric neon relative to their mantle signature. Therefore the mantle component can usually be ignored for cosmogenic applications (Dunai, 2010). Although mantle Ne concentrations are unlikely to be high in quartz they can be present in mantle rocks (Sarda et al., 1993) or trapped in fluid- and melt- inclusions together with atmospheric Ne (Hetzel et al., 2002).

2.3.3 Nucleogenic Ne ($^{21}Ne_{nuc}$)

The α particles produced by $^{238,235}U$ and ^{232}Th decay interact with neighbouring nuclei producing $^{21}Ne_{nuc}$ form the reactions $^{18}O(\alpha,n)^{21}Ne$ and ^{22}Ne from the reaction $^{19}F(\alpha,n)\ ^{22}Na(\beta^+)^{22}Ne$. To a lesser extent, nucleogenic ^{21}Ne can also be produced by neutrons from the U and Th decay from the reaction $^{24}Mg(n,\alpha)^{21}Ne$. Crustal rocks are commonly enriched in U and Th, consequently the crustal fluids trapped in minerals are usually enriched in ^{21}Ne and ^{22}Ne relative to air.

The neon isotopic composition depends on the O/F ratio of the fluid source region and the preferential release of the ^{22}Ne relative to ^{21}Ne from minerals (Kennedy et al., 1990; Ballentine and Burnard, 2002). Being trapped in the melt and fluid inclusions, the crustal nucleogenic component can be also released by in vacuo crushing. Nucleogenic neon can also be produced in the mineral lattice. The main minerals used in cosmogenic neon studies are quartz and olivine, which typically have low U and Th concentrations. Mineral inclusions and neighbouring minerals with high U and Th concentrations can be source of α particles producing nucleogenic neon. α particles only travel a few tens of microns being sufficient the removal of the rims of the mineral grains (by acid etching) to reduce the nucleogenic component (Dunai, 2010).

In order to discriminate between the cosmogenic and non-cosmogenic components, two techniques can be utilized. The non-cosmogenic trapped component can be released by in vacuo crushing of the sample. Melting of the sample will release all the gas in the lattice and trapped in the melt- and fluid- inclusions. Assuming negligible excess ^{20}Ne, the $^{21}Ne_{cos}$ can be calculated (Niedermann, 2002):

$$^{21}Ne_{cos} = [(^{21}Ne/^{20}Ne)_{melt} - (^{21}Ne/^{20}Ne)_{crush}] \times {}^{20}Ne_{melt} \quad [2.14]$$

Another method for discrimination of cosmogenic Ne is stepwise heating (Niedermann, 2002). In olivine and pyroxene at temperatures < 900˚C the trapped Ne is effectively degassed and only minor amounts of cosmogenic Ne are released (Schaefer, 2000). The total of the cosmogenic Ne is released at temperatures of 1600-1800˚C. This allows for determination of the cosmogenic Ne through partial separation of trapped and cosmogenic neon by stepwise heating at ~ 900˚C and ~ 1600-1800˚C (Niedermann, 2002).

2.3.4 $^{21}Ne_{cos}$ production rate

Cosmogenic neon is produced by spallation reactions of high-energy and fast neutrons with muons being responsible of ~ 3.6 % of the $^{21}Ne_{cos}$ production in quartz (Balco and Shuster, 2009a; Fernandez-Mosquera et al., 2010). The main target elements of cosmogenic neon production in mafic minerals are Mg, Si, Al and Ca with fast neutrons (0.1 to 10 MeV) being responsible for the production in Mg by the reaction $^{24}Mg(n,\alpha)^{21}Ne$ and high-energy neutrons (10 MeV to 10 GeV) responsible for the production of the other elements. Therefore cosmogenic neon production is strongly dependent the on the mineral

chemical composition (Schäfer et al., 1999; Masarik, 2002; Kober et al., 2005). Since the production in Mg is dominant relative to other elements the variability of Mg content in mafic minerals is key to accurately estimate their $^{21}Ne_{cos}$ production rate.

2.3.4.1 Theoretical models of $^{21}Ne_{cos}$ production rate in mafic minerals

The theoretical models of elemental production of $^{21}Ne_{cos}$ for the main target elements (Schäfer et al., 1999; Masarik, 2002 and Kober et al., 2005) predict production rate variations between elements greater than those of $^{3}He_{cos}$. Schäfer et al. (1999) modelled the elemental production of Mg, Al and Si but did not consider production in Na, Ca and Fe. The production rates for these elements are the ones that differ the most between Masarik (2002) and Kober et al. (2005) calculations. Taking the elemental compositions as weight fractions, the $^{21}Ne_{cos}$ production rate using Masarik (2002) (Equation 2.15) and Kober et al. (2005) (Equation 2.16) can be calculated:

$$^{21}Ne_{cos}=102[Na]+175.1[Mg]+62.4[Al]+41.7[Si]+1.8[Ca]+0.187[Fe] \quad [2.15]$$

$$^{21}Ne_{cos}=208[Na]+189[Mg]+60[Al]+44[Si]+17[Ca]+1[Fe]+1[Ni] \quad [2.16]$$

The models of Masarik (2002) and Kober et al. (2005) calculate $^{21}Ne_{cos}$ production in Mg ~4.2-4.4 times higher than that in Si and 936-189 times higher than in Fe. Differences in the elemental production rates of Kober et al. (2005) and Masarik (2002) are a consequence of the use of different reaction cross-sections. Applying the two models to the average composition of commonly used olivine (Fo_{81}) and pyroxene (En_{43}), the ratio between cosmogenic production in pyroxene and olivine is ~0.55 and ~0.58 using Masarik (2002) and Kober et al (2005) calculations respectively.

2.3.4.2 Calibration studies of $^{21}Ne_{cos}$ production in olivine and pyroxene

Empirical determination of the $^{21}Ne_{cos}$ production rate in mafic minerals has been the aim of few studies (Poreda and Cerling, 1992; Amidon et al., 2009; Fenton et al., 2009; Schimmelpfenning et al., 2011). Poreda and Cerling (1992) reported a SLHL scaled by Lal (1991) $^{21}Ne_{cos}$ production rate of 45 ± 4 atoms/g/yr for olivine Fo_{81} from 17.8 ka (K-Ar dated) basalts from the Tabernacle Hills, Utah (~40°N). Amidon et al. (2009) reported cosmogenic production of $^{21}Ne_{cos}$ of 34.1 ± 3.2 atoms/g/yr for pyroxene En_{42} from eroded

610 ka rhyolite from the Coso volcanic field, California (~36˚N). The apparent exposure age for the samples was calculated by ^{10}Be and extrapolated for the $^{21}Ne_{cos}$ production rate calculation. Fenton et al. (2009) reported production rates for olivine Fo_{81-84} and pyroxene En_{43-44} of 48-51 and 23 atoms/g/yr respectively. Schimmelpfenning et al. (2011) published a calibration of $^{21}Ne_{cos}$ production in olivine and pyroxene from the same sample from Kilimanjaro (~3˚S) reporting $^{21}Ne_{cos}(px)/^{21}Ne_{cos}(ol)$ ratios of 0.50-0.53 for olivine Fo_{81} and pyroxene En_{41-43}. This is in agreement with ratios of 0.45-0.48 previously reported by Fenton et al. (2009) and with the ~0.55 and ~0.58 values calculated using the theoretical models of Masarik (2002) and Kober et al (2005). Empirical calibration studies have demonstrated the compositional control of the production rate of $^{21}Ne_{cos}$ in mafic minerals and validate the use of composition scaling using theoretical elemental production rates (Fenton et al., 2009).

2.3.4.3 $^{3}He_{cos}/^{21}Ne_{cos}$ relative apparent production rates in mafic minerals

Cross calibration of production rates of $^{3}He_{cos}$ and $^{21}Ne_{cos}$ is typically used for exposure dating of young exposed surfaces as it has revealed the most accurate method for dating late Holocene, low-K basalts (Poreda and Cerling, 1992; Schäfer et al., 1999; Gillen et al., 2010; Schimmelpfenning et al., 2011; Fenton and Niedermann, 2014; Espanon et al., 2014). The analysis of the two stable isotopes is used to assess the validity of the cosmogenic exposure ages based on their production rate ratios. Poreda and Cerling (1992) evaluated the relative production of $^{3}He_{cos}$ and $^{21}Ne_{cos}$ in olivine and pyroxene from experimental data on lavas from western United States. Their results showed a linear relationship of $^{21}Ne_{cos}/^{3}He_{cos}$ production with Mg content (Equation 2.17):

$$^{21}Ne_{cos}/^{3}He_{cos} = 0.0038\ (Fo_{\%}) + 0.10 \qquad [2.17]$$

where $Fo_{\%}$ represents the Mg content of both olivine and pyroxene expressed as forsterite content. For olivine Fo_{81} Poreda and Cerling (1992) calculated a $^{21}Ne_{cos}/^{3}He_{cos}$ production rate ratio of 0.41 ± 0.05. This was in agreement with the results of Marti and Craig (1987) for Fo_{84} olivine with a production rate ratio of 0.48 ± 0.04. Schäfer et al. (1999) reported $^{21}Ne_{cos}/^{3}He_{cos}$ ratio of 0.23 for pyroxene (Fo_{32}) samples from Antarctica, which conforms the linear relationship from production and Mg content determined by Poreda and Cerling (1992). Applying the available theoretical models of elemental production to olivine (Fo_{81}) and pyroxene (Fo_{25}), the $^{21}Ne_{cos}/^{3}He_{cos}$ ratios are 0.49 and 0.35

for olivine using Masarik (2002) and Kober et al. (2005) models respectively and 0.21 and 0.14 in the case of pyroxene. The empirical data fall between the Masarik (2002) and Kober et al. (2005) calculations following the pattern observed for $^{3}He_{cos}$ production.

Recent inter-calibration studies by Fenton et al. (2009), Gillen et al. (2010), Schimmelpfenning et al. (2011) and Fenton and Niedermann (2014) reported $^{21}Ne_{cos}/^{3}He_{cos}$ ratios for different altitudes (18 m to 4 km) and locations (Australia, Tanzania and Western United States) that are consistent with the Poreda and Cerling (1992) results and give a solid empirical estimation of the $^{21}Ne_{cos}/^{3}He_{cos}$ relative production rate ratios. Figure 2.12 compiles previously reported $^{21}Ne_{cos}/^{3}He_{cos}$ ratios from different locations (low latitudes like Tanzania, high latitudes like Antarctica and a collection of mid latitude locations in the Northern and Southern hemisphere) and compares them to the Mg content of the minerals analysed.

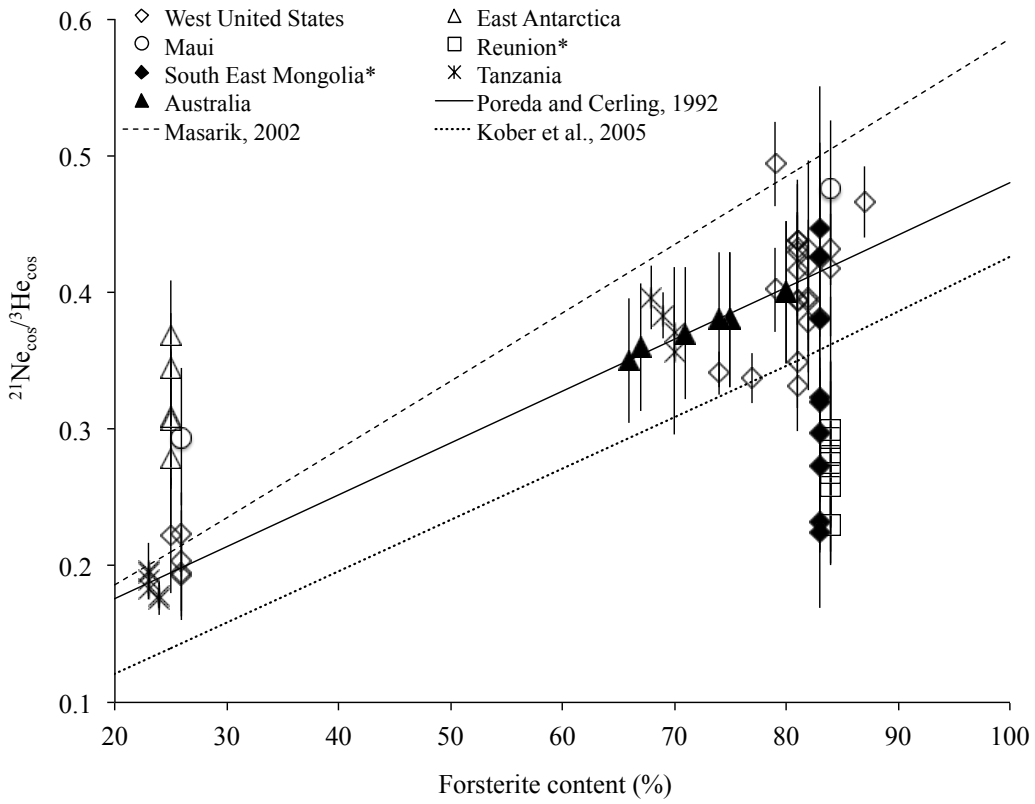

Figure 2.12. Plot of previously reported $^{21}Ne_{cos}/^{3}He_{cos}$ ratios for different locations (Maui: Marti and Craig, 1987; Reunion and South Mongolia: Staudacher et al., 1993; Western United States: Poreda and Cerling, 1992; Fenton et al., 2009; Fenton and Niedermann, 2014; Tanzania: Schimmelpfenning et al., 2011; Australia: Gillen et al., 2010 and East Antarctica: Bruno et al., 1997) relative to Mg content reported as forsterite content in %. Pyroxene compositions are plotted as normalized to forsterite content following Poreda and Cerling (1992). The continuous line represent the relative production rate at SLHL proposed by Poreda and Cerling (1992) and the discontinuous and dotted lines are theoretical lines calculated using Masarik (2002) and Kober et al. (2005) elemental productions respectively. *Forsterite content of the olivines from Reunion and South East Mongolia are assumed to be the same as those measured for Reunion olivines by Furi et al. (2011).

The majority of the studies concentrate on samples at elevations ~1.5 to 2 km with the exception of the work of Schimmelpfenning et al. (2011) who analysed lavas form different altitudes from Kilimanjaro (Tanzania) and reported consistent $^{21}Ne_{cos}/^{3}He_{cos}$ ratios of 0.37 ± 0.02 and 0.19 ± 0.01 for olivine and pyroxene respectively, observing no altitude dependence on the relative production of the two isotopes at this low latitude (~3˚S). Previous studies analysing $^{3}He_{cos}$ in garnet, apatite and zircon in combination with $^{10}Be_{cos}$ in coexisting quartz from the Himalayas (~27˚N) at elevations of 2.8 to 4.8 km reported exponential increase of the $^{3}He_{cos}/^{10}Be_{cos}$ ratio with elevation and hypothesized that tertiary protons and neutrons produced by spallation reactions in rocks having sufficient energy to produce $^{3}He_{cos}$ but not enough energy to produce $^{10}Be_{cos}$ (Gayer et al, 2004; Amidon et al., 2008). Although the mechanisms are still not well understood they could be a consequence of different excitation functions for $^{3}He_{cos}$ and $^{10}Be_{cos}$ (Amidon et al., 2008). Blard et al. (2013) analysed $^{3}He_{cos}$ in pyroxene and $^{10}Be_{cos}$ in quartz from the Bolivian Altiplano (~20˚S) at elevations above 4.8 km and observed no increase in the $^{3}He_{cos}/^{10}Be_{cos}$ ratio with elevation concluding that the effect observed by Gayer et al. (2004) and Amidon et al. (2008) could be related to specific production mechanisms in accessory minerals that are still not well understood or to a regional effect unique to the Himalayas. In order to fully understand the mechanisms of production of cosmogenic isotopes at high elevations more studies are required. In this work I am aiming to compare the relative production rate of $^{3}He_{cos}$ and $^{21}Ne_{cos}$ at high elevations (~3.2 km) in Antarctica.

2.3.5 $^{21}Ne_{cos}$ applications

Cosmogenic neon is largely used for exposure dating quartz in slowly eroding landscapes (Bruno et al., 1997; Schäfer et al., 1999; Dunai et al., 2005) where it can provide information unavailable from cosmogenic radionuclides. The combination of $^{21}Ne_{cos}$ with ^{10}Be and ^{36}Al provides the possibility of resolving complex exposure/erosion histories of old and slowly eroding surfaces (Kober et al., 2007; Strasky et al., 2009; Balco and Shuster, 2009a) and providing valuable information for landscape evolution applications (Strobl et al., 2012). Cosmogenic neon in olivine and pyroxene can be used for exposure dating young basalts (700 ka to as young as 5 ka) (Amidon et al., 2009; Espanon et al., 2014; Fenton and Niedermann, 2014) in combination with $^{3}He_{cos}$.

2.4 Combination of stable and radioactive nuclides for complex exposure determination

The application of combination of stable (^{21}Ne) and radioactive (^{10}Be, ^{26}Al) cosmogenic nuclides to burial dating constitutes the major contribution of this method to Earth science applications (Balco and Shuster, 2009b). Burial dating using stable and radionuclides relies on the different type of accumulation of the two nuclides. Stable and radionuclides accumulate in a surface over time at a constant rate as long as they are exposed. Stable nuclides stop accumulating when they are shielded from cosmic rays (buried). Radionuclides decay during the time of accumulation at a rate that depends on their half-lives and continue decaying when samples are buried. The use of this technique allows for a wider age range and has a better accuracy in comparison to the use of two radionuclides of different half-lives. The age range of the combination of ^{26}Al and ^{10}Be is ~0.5 to 6 Ma, combining ^{10}Be with ^{21}Ne the burial dating can be effective up to the Miocene (Balco and Shuster, 2009b; Di Nicola et al., 2012). $^{21}Ne_{cos}$ is quantitatively retained in quartz over geological time (Kober et al., 2005) and ^{21}Ne can be measured precisely at low concentrations in quartz (Schaefer et al., 2009), therefore ^{10}Be-^{21}Ne is a good pair for resolving complex exposure histories in quartz bearing surfaces. ^{10}Be and ^{21}Ne in quartz has been used to resolve complex histories of burial and to understand denudation rates (Kober et al., 2007; Strobl et al., 2012; Di Nicola et al., 2012).

The ratio of the concentration of stable and radioactive cosmogenic nuclides in a sample can be used to estimate erosion rate and burial histories (Lal and Arnold, 1985; Lal, 1991; Gosse and Phillips, 2001). Plotting the ^{21}Ne/^{10}Be ratio as a function of ^{10}Be concentration for a constant irradiation history, with and without erosion, allows determining the lines that define constant exposure with no erosion and erosion for infinite exposure or saturation line. The area between these two theoretical lines defines different quantities of steady-state erosion and the area above saturation defines the complex exposure domain that implies periods of lower or no exposure to cosmic rays. The area under the line of simple accumulation with no erosion is defined as the forbidden zone as there are no possible combinations of the concentrations of the two isotopes that could give such values (Lal, 1991) (Figure 2.13). The lines that define the erosion and burial domains, from the ^{21}Ne-^{10}Be diagram, are based on theoretical production rates of ^{21}Ne and ^{10}Be and therefore they are mineral dependent. This method has been used mostly in quartz bearing surfaces but it could also be applied to mafic environments where the stable isotope of

preference is $^{3}He_{cos}$. Consequently, the ^{3}He-^{10}Be systematics have potential for resolving complex exposure histories from olivine bearing bedrock.

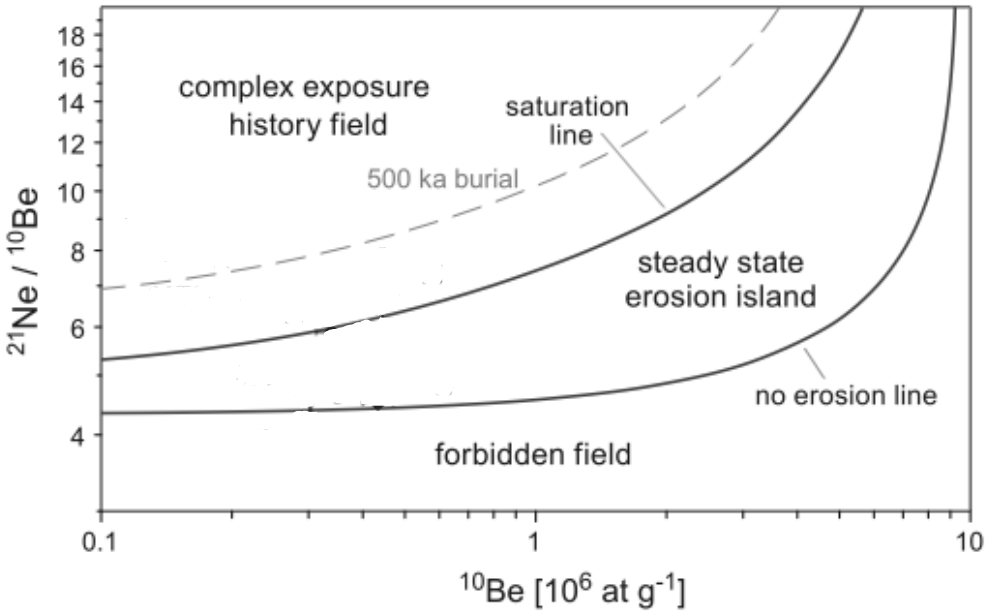

Figure 2.13. Theoretical increase of the $^{21}Ne/^{10}Be$ ratio as a function of ^{10}Be concentration for a constant irradiation history, with and without erosion (modified from Strobl et al., 2012). The line of simple accumulation with no erosion and that of saturation (erosion for infinite accumulation time) define the steady state erosion island, if the samples fall within that area, the erosion rate can then be calculated. The field above the saturation line defines complex exposure history, therefore if samples fall within that domain, a maximum burial age can be determined. The dashed line in grey shows an example of a 500 ka burial isochrones.

2.4.1 $^{10}Be_{cos}$ in olivine

^{10}Be has a half-life of 1.39 ± 0.02 Ma (Chmeleff et al., 2010) and is a useful nuclide to calculate surface exposure ages and erosion rates. ^{10}Be is mainly produced by spallation reactions from O, Mg, Al, Si and Fe (Lal, 1991). The application of ^{10}Be has been restricted to surfaces containing quartz (Nishiizumi et al, 1990; Goethals et al, 2009) although; the long half-life of ^{10}Be might have important implications for dating of burial events in surfaces composed of mafic igneous rocks. The cross calibration of stable isotopes and radionuclides widens the applications of ^{10}Be on Earth sciences. This has been most widely applied in Antarctica where ^{21}Ne, ^{10}Be and ^{26}Al from quartz bearing surfaces are combined to determine rates of erosion and landscape change (i.e. Van der Wateren et al., 1999; Oberholzer et al., 2003; Di Nicola et al., 2009; Di Nicola et al., 2012; Mukhopadhyay et al., 2012; Middleton et al., 2012).

$^{10}Be_{cos}$ is also produced in olivine and its analysis can be used to unravel exposure histories of mafic surfaces. To date the use of $^{10}Be_{cos}$ in olivine has been limited to a few

studies that involved the estimation of the $^{10}Be_{cos}$ to determine exposure ages and erosion rates of Hawaiian surfaces in combination with ^{26}Al, ^{36}Cl and ^{3}He (Nishiizumi et al, 1990), studying river profile evolution (Seidl et al, 1997) and estimating production rate using samples from Mount Etna (Blard et al, 2008). The main limitation for measuring *in situ* produced ^{10}Be for cosmogenic exposure dating is the complete removal of the meteoric ^{10}Be (Brown et al., 1991). $^{10}Be_{cos}$ is also produced in the atmosphere at a rate three orders of magnitude higher than that of in situ production in surface minerals (Monaghan et al., 1986). Meteoric ^{10}Be can be adsorbed by minerals in the surface through weathered mineral zones. If meteoric ^{10}Be is not removed completely it can be the cause of unresolvable ^{10}Be excess (Ivy-Ochs et al. 1998). In the case of quartz sequential chemical dissolution can efficiently remove the meteoric component (Kohl and Nishiizumi, 1992). When analysing phenocrysts this becomes more complex as meteoric ^{10}Be can be present along fractures in phenocrysts where secondary minerals accumulate (Schott and Berner, 1985). Ivy-Ochs et al. (1998) concluded that meteoric ^{10}Be stored in small (few microns) secondary minerals within weathered pyroxenes cannot be effectively removed by sequential dissolution in HF. Blard et al. (2008) developed a cleaning procedure that removes the meteoric component effectively. Nishiizumi et al. (1990) successfully removed the meteoric ^{10}Be by HF dissolution and established the feasibility of simultaneous use of stable and radioactive cosmogenic nuclides to determine exposure ages and erosion rates in basaltic and andesitic bedrock demonstrating the feasibility of ^{3}He and ^{10}Be in olivine for exposure dating and erosion rate determination and opening the possibilities of this isotope combination for burial dating applications.

2.5. Context of this work

Cosmogenic isotopes are produced by spallation reactions from high energy and fast neutrons and the concentration of a stable cosmogenic isotope in a sample is proportional to its exposure time. In order to use cosmogenic nuclides for exposure dating accurate measurement of the cosmogenic nuclide concentration in a sample is required. Complete degassing of the mineral grains is therefore key in the analytical process. In this work I have develop a laser technique to fully degas olivine and pyroxene samples in order to achieve high precision measurements of cosmogenic ^{3}He. The potential of the degassing technique has also been investigated by measuring young exposed samples. For this purpose I undertook fieldwork to the Kula Volcanic Province to collect fresh lava flow samples from different volcanoes in the area in order to exposure date these lava flows.

The use of a diode laser allows for degassing of individual grains and therefore a case study of detrital gold from different locations around Scotland was performed to evaluate the different sources of ^{3}He production in native gold and explore the use of gold for cosmogenic exposure dating of individual detrital grains (Chapter 4).

The production rate of $^{3}He_{cos}$ and $^{21}Ne_{cos}$ vary as a consequence of different elemental composition. In mafic minerals those differences are directly related to the Mg content especially in the case of $^{21}Ne_{cos}$. In this work $^{3}He_{cos}$ and $^{21}Ne_{cos}$ concentrations in different coexisting mafic minerals (olivine, orthopyroxene, clinopyroxene and spinel) are analysed and the results are compared with the theoretical models of Masarik (2002) and Kober et al. (2005). The relative production of $^{3}He_{cos}$ and $^{21}Ne_{cos}$ at high elevation in West Antarctica is also investigated and compared to the theoretical models as well as with previously published $^{3}He_{cos}/^{21}Ne_{cos}$ ratios (Chapter 5).

The use of stable and radioactive cosmogenic isotopes has proven a reliable method to unravel the exposure history of long exposed landscapes. Here I am combining $^{3}He_{cos}$ and $^{10}Be_{cos}$ in olivines from West Antarctica (Chapter 6).

3. Noble gas mass spectrometry

3.1 Introduction

A significant component of my PhD study has been dedicated to the setting up and characterization of the Helix SFT mass spectrometer in the noble gas laboratory at SUERC (continuation of the work started by Dymock, 2014). Some analyses performed during part of this PhD were undertaken using the MAP 215-50 mass spectrometer at SUERC. A description of this mass spectrometer is provided in Appendix A.

This chapter aims to fully characterise the state of the art *ThermoFisher Scientific* Helix SFT dual collector mass spectrometer at SUERC that has been specifically constructed for the simultaneous collection of helium isotopes, ^{3}He and ^{4}He. This chapter describes the instrument and basic performance (peak stability, backgrounds, sensitivity and stability for isotope ratio measurements) providing much of the background for the analytical measurements that are detailed in the subsequent chapters.

3.2 Helix SFT mass spectrometer

3.2.1 Background

Development of mass spectrometry began in the early 1900's (Thomson, 1913; Dempster, 1918; Alvarez and Cornog, 1939) with the most important advances in technology and performance taking place in the 1940's when the first mass spectrometer with an electron impact source was designed and constructed (Nier, 1947). Since then advances in magnetic sector mass spectrometry have allowed the application of noble gas mass spectrometry to Earth sciences (e.g. Aldrich and Nier, 1948; Reynolds, 1956; Hohenberg, 1980; Sano and Wakita 1988; Sano et al., 2008). In the late 1980's noble gas mass spectrometry experienced a major improvement with the development of the VG5400 and MAP 215-50 dual collector mass spectrometers, both provided with a Faraday cup and an electron multiplier. Sano and Wakita (1988) performed high precision measurements of He isotopes in terrestrial samples using a VG5400 mass spectrometer reporting a ^{3}He

detection limit of 8 x 10^5 atoms, about 25 times lower than previous system (Sano et al. 1982). Stuart and Turner in 1992 made high precision abundance and isotopic composition measurements of noble gases in ancient terrestrial fluids using a MAP 215-50 mass spectrometer reporting ^{4}He measurements with 1σ uncertainties as low as 1%. Data collection was typically performed by measuring isotopes individually changing the magnetic field strength or the source acceleration voltage according to the correspondent isotope mass over charge, so called "peak jumping" mode.

Simultaneous collection of isotopes was first applied to stable isotope mass spectrometry (Nier, 1947). However, multicollection is a challenge when applied to static vacuum mass spectrometry due to the need for electron multiplier detectors rather then Faraday cups. In the early part of this century several new multicollector noble gas mass spectrometers were designed, constructed and brought to market, allowing for more precise measurement of isotopic ratios (Sano et al, 2008; Mark et al., 2009; Coble et al., 2011).

3.2.2 Helix SFT description

The Helix SFT (split flight tube) mass spectrometer is an all-metal bidirectional focusing high-dispersion magnetic sector gas source instrument. It has a 35 cm radius, 120˚ extended geometry that has been specifically designed for simultaneous collection of the two helium isotopes, ^{3}He and ^{4}He. The electronics (source, magnet control, power supplies, and collector) are controlled by an embedded computer using *ThermoFisher Scientific* Qtegra software (version 15.006); which allows for fully automated data collection.

The mass spectrometer has a reported internal volume of ~1400 cc. It has a Nier-type electron bombardment source with x and z focusing and is provided with a coiled tungsten filament for ionisation. Two external source magnets are used to collimate the electron beam. All source parameters (HV, focus, electron volts, ion repeller, trap and X and Z steering) are computer controlled and monitored by electronic read backs.

A *SAES* GP50 getter (operated at room temperature) and a stainless steel finger filled with activated charcoal (cooled to -196°C using liquid N) were installed close to the source to minimize the partial pressure of residual gases during He isotope analysis. This is

in addition to the existing *SAES* NP10 getter provided with the instrument that is also operated at room temperature.

The electromagnet is fabricated from high purity (>99.9%) soft iron and has a translational and rotational adjustment in three planes. This allows for individual adjustment of peak shapes and alignment of the peak coincidence for precise $^{3}He/^{4}He$ ratio measurements. The magnetic field is controlled by a temperature-stabilized Hall probe that controls the magnet power supply.

The high mass spur is fitted with an electronically suppressed Faraday detector with an amplifier circuit equipped with a 10^{12} ohm resistor. The low mass spur is provided with a discrete dynode *Balzers* SEV-217 copper-beryllium ion counting electron multiplier (ion counting efficiency > 70%). It incorporates a 5 cm 90˚ electrostatic analyser (ESA) that acts as a filter allowing only ions with fixed mass over charge (m/z) (Herbet and Johnstone, 2003). This improves abundance sensitivity performance; at 1 x 10^{-7} mbar the contribution from m/z = 4 at m/z = 3 is < 1 ppb.

Ultra-high vacuum (~10^{-10} mbar) is achieved by the use of a 40 l/s noble-gas-specific ion pump. During bake-out the pressure is monitored by an ion gauge mounted adjacent to the ion pump.

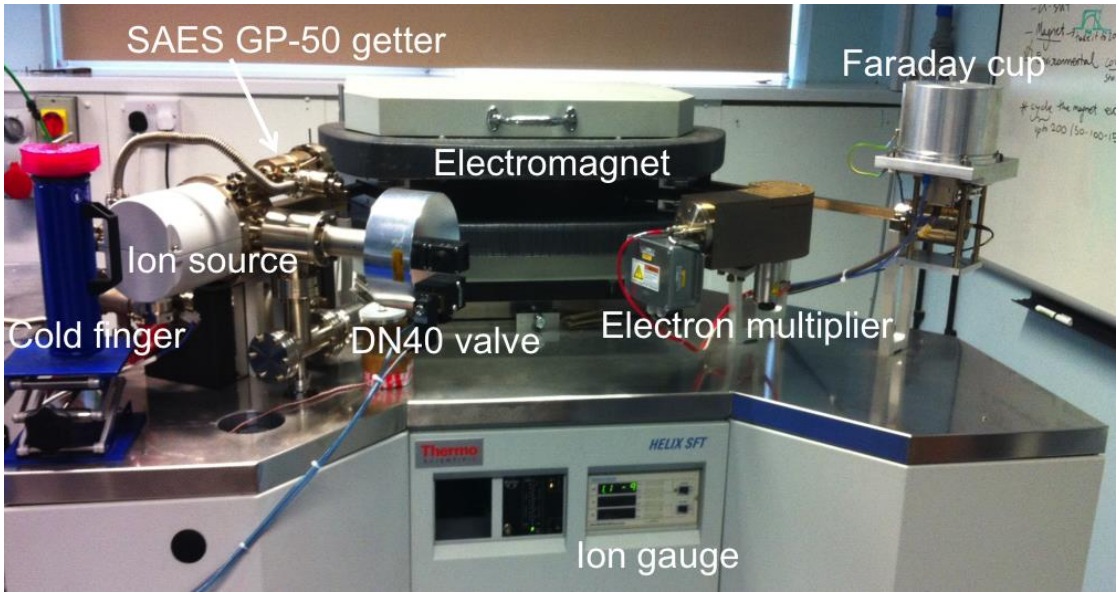

Figure 3.1. Helix SFT mass spectrometer features.

3.2.3 Purification line

An all-metal ultra-high vacuum line (~370 cc internal volume) was constructed and attached to the mass spectrometer soon after delivery. It allows for purification of the noble gases from reactive gases extracted from mineral samples prior to mass spectrometer measurement (Figure 3.2). The line is equipped with two *SAES* GP50 getters both operated at 250ºC to remove the active gases (H_2, O_2, N_2, CO, H_2O, CH_4). An activated charcoal-filled stainless steel finger is mounted on the main manifold block of the purification system. It is generally cooled to -196°C using liquid nitrogen and is used to remove the heavy noble gases (Ar, Kr and Xe). A 5-litre bottle containing helium standard gas HESJ (Matsuda et al., 2002) with $^3He/^4He$ ratio of 20.63 ± 0.10 R_A (R_A being the $^3He/^4He$ ratio of air 1.39 x 10^{-6}) allows for the determination of mass spectrometer sensitivity and ratio reproducibility. It includes an automated 0.1 cc pipette.

Gas extraction from mineral samples can be undertaken by *in vacuo* crushing and/or sample heating/melting. Crushing is performed in an all-metal multi-sample hydraulic crusher. Samples can be heated using either a resistance-heated double vacuum furnace and a variety of lasers (e.g. 75 W diode laser and 25 W CO_2 laser). The noble gases trapped in fluid/melt inclusions are released by crushing. In the case of basalt phenocrysts the magmatic $^3He/^4He$ ratio is measured from melt inclusions (Kurz, 1986). In ore minerals crushing releases the noble gases from hydrothermal fluid inclusions (e.g. Stuart et al. 1994). Samples are heated in order to release the lattice-hosted noble gases. In the case of exposed samples, this technique is used to identify and determine the cosmogenic He and Ne component (Kurz, 1986; Craig and Poreda, 1986). The importance of completely degassing samples is discussed in section 3.3.

Ultra-high vacuum is achieved by 70 l/s turbo-molecular pump (*Pfeiffer* HiCube 80) with a baking two-stage diaphragm pump and a 30 l/s triode ion pump (*Varian*, Starcell). Two types of valves are used on the line. Manual *Varian* DN16CF valves are located on the two GP50 getters, the cold finger trap, the furnace, the laser and the crusher. The mass spectrometer inlet valve, the calibration bottle pipette valves and the pump valves system are automated *VAT* pneumatic DN16CF valves. These valves are computer controlled allowing for fully automated calibrations and cold blank determinations. The valves are controlled and sequenced by the Mass Spec software (developed by Alan Deino, Berkeley Geochronology Center).

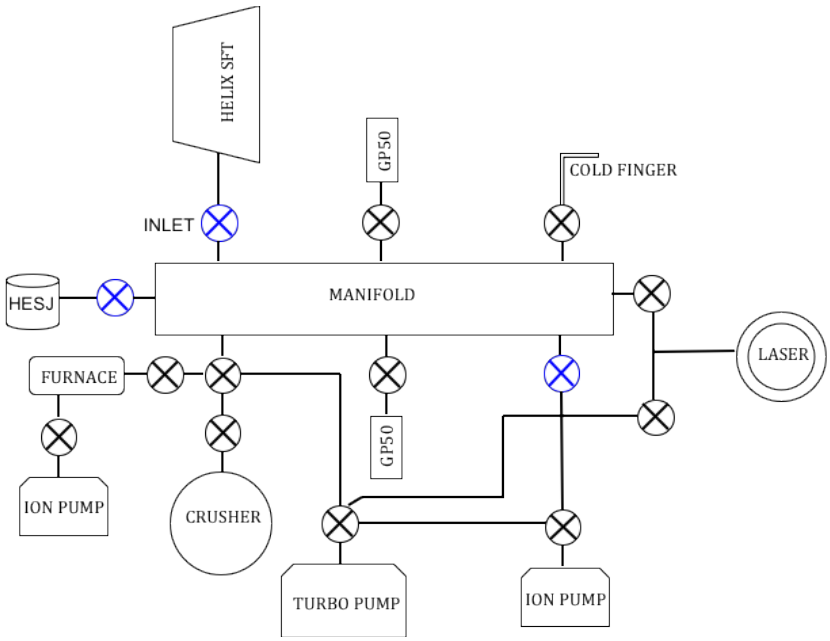

Figure 3.2. Diagram of the ultra-high vacuum purification line. The line can be isolated from the extraction units, which all can be independently pumped into the turbo pump. A secondary ion pump is used to keep the outer volume of the furnace under vacuum. Manual *Varian* DN16CF valves are black, the automated *VAT* pneumatic DN16CF valves are blue.

3.3 Helix SFT performance

The instrument source is operated at high voltage (typically 4.5 kV). This produces high resolution, reduces beam dispersion and provides the best peak shape and sensitivity (Wallington, 1970; Mabry et al., 2012). The source parameters have been determined by manual tuning to achieve optimum peak shape for high sensitivity operation. The tuning has been performed at the maximum beam size that will be measured at the mass spectrometer following the procedures recommended by Burnard and Farley (2000) and Mabry et al. (2012). Maximum beam size is achieved by expansion into the extraction line a 0.1 cc pipette of (Matsuda et al., 2002) standard gas. Typical source parameter values used for performing the analysis during this work are shown in Table 3.1.

Table 3.1. Typical source parameter settings. The voltages are all relative to the 4.5 kV acceleration voltage. The extraction lens and Z settings are % of acceleration voltage (4.5 kV) and the X setting is % of the extraction voltage.

Source parameter	*Typical value*
Trap current	250 µA
Trap voltage	15.68 V
Electron energy	74.13 eV
Ion repeller	-5.24 V
Extraction lens	61.30%
Z-symmetry	-18.10%
Z-focus	84.10%
X-symmetry	-8.97%

3.3.1 Data acquisition

The intensity of the ion beams of both ^{3}He and ^{4}He are typically measured in a 20-cycle run setup in the experiment editor mode of the Qtegra software with 33.55 seconds integration time. Both ^{3}He and ^{4}He are collected simultaneously so that changes in environmental conditions (such as room temperature) impacts both ion beams simultaneously, improving the quality of the data of $^{3}He/^{4}He$ ratio. A bidirectional scan for peak centring on ^{4}He at mass 4.003 is performed after gas inlet and equilibration (30 seconds). The ^{4}He peak centre scan is performed on the Faraday cup, the magnetic field is kept constant and the acceleration voltage is varied. A 0.5 second integration time is used with the peak centre taking 120 seconds (Figure 3.3). Data acquisition begins after the ^{4}He peak position is set with time zero (t = 0) set at the start of the peak centre. Each cycle has an integration time of 33.55 seconds. The total time for data collection is typically 15 minutes. The 20 data points for both peaks (intensity versus time) are regressed to inlet time (t = 0) using the integrated experiment editor of Qtegra software. Typical data collection output from HESJ standard He (Matsuda et al., 2002) is shown in Figure 3.4.

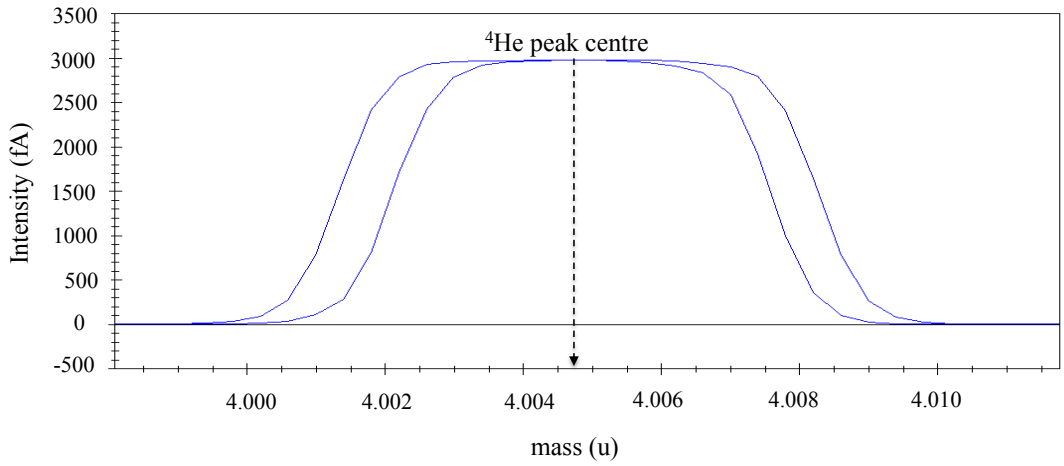

Figure 3.3. Typical Faraday peak shape for 3.13 x 10^{12} atoms of ^{4}He. The variation in peak location is for scanning the acceleration voltage up and down at a fixed magnetic field prior to sample analysis. The peak top is determined as the average of the two peak centres. The acceleration voltage is then fixed at 4.5 kV and the magnetic field is changed to the equivalent peak centre position. The difference between the two peaks is 40 ppm of the peak centre and it is a consequence of the slow response of the resistors.

The split flight tube is specifically designed for the simultaneous collection of ^{3}He and ^{4}He. The ^{4}He is measured on the high mass spur by a Faraday detector. The Faraday amplifier offset is measured at the beginning of the day by switching off the magnetic field for 60 seconds. The measured offset or correction (typically ~2.871 fA) is applied to subsequent measurements. A 1 mm slit in front of the collector permits a mass resolving power of ~600 (see Figure 3.5).

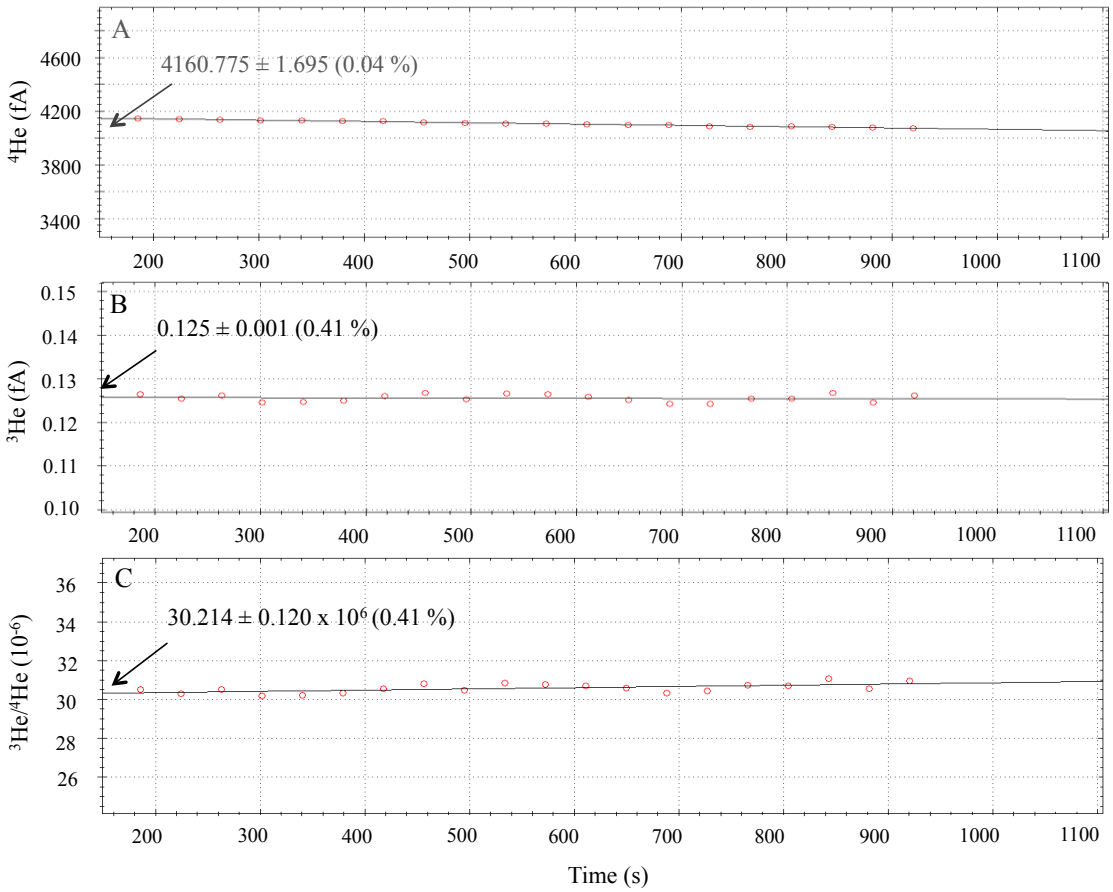

Figure 3.4. Plots of the raw data generated during a 20-cycle analysis of 0.1 cc pipette of the HESJ He standard. (A) Data from ^{4}He peak measured in a Faraday cup and regressed to inlet time, and (B) data from ^{3}He peak measured by an electron multiplier. The data define an exponential fit with a significantly greater uncertainty (0.37 %) at the t = 0 intercept than the ^{4}He (0.06%). (C) ^{3}He/^{4}He ratio. Scatter in the ^{3}He/^{4}He ratio calculated from isotope data. The scatter is consistent with the ^{3}He signal.

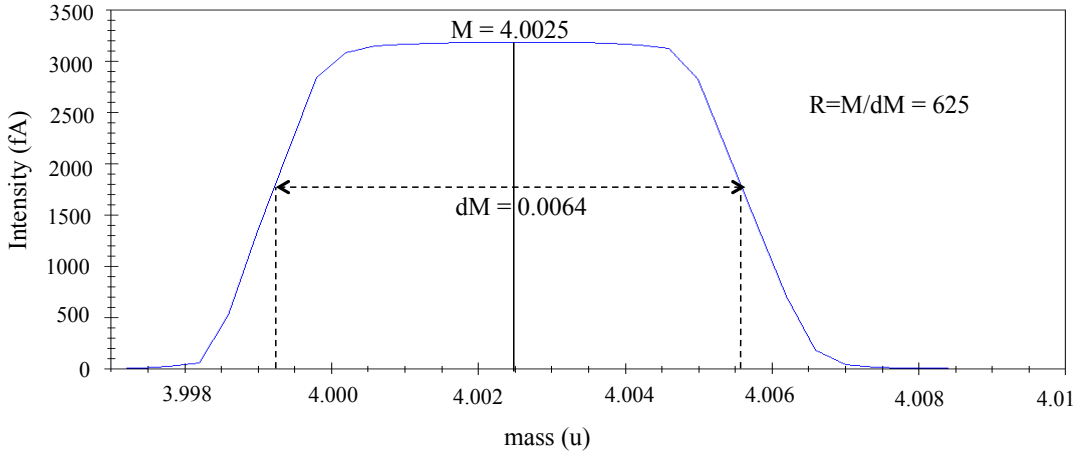

Figure 3.5. Resolving power calculated from scanning over ^{4}He in the Faraday cup. The mass at the centre of the peak (M) is 4.0025 and the difference of mass units at 50 % of the peak intensity (dM) is 0.0064. This results on a resolving power (R) of 625.

^{3}He is measured by focusing the ion beam (via an ESA unit attached to the low mass spur) on to an electron multiplier (*Balzers* SEV-217), which is run in digital (ion counting) mode. The low mass spur of the Helix SFT is off axis with a collector slit that allows for mass resolving power of ~850 (see Figure 3.6). This is adequate for full resolution of $^3He^+$ from HD^+-$^3H^+$ doublet with a valley intensity of < 1% of the peak heights (see Figure 3.7).

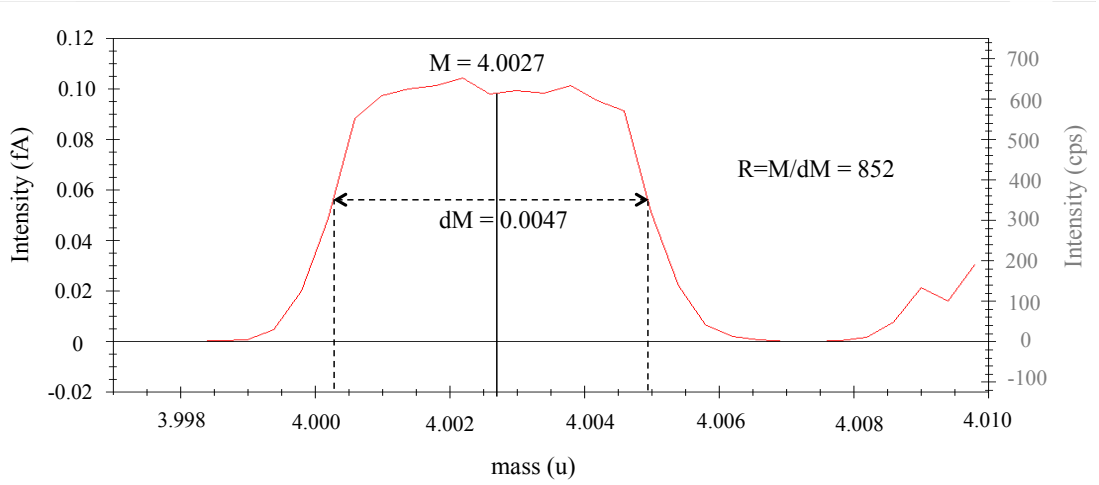

Figure 3.6. Resolving power calculated from scanning over ^{3}He in the electron multiplier. The mass at the centre of the peak (M) is 4.0022 and the difference of mass units at 50 % of the peak intensity (dM) is 0.0047. This results on a resolving power (R) of 852. Scan is performed over mass 4 in the Faraday cup, which corresponds to mass 3 in the multiplier.

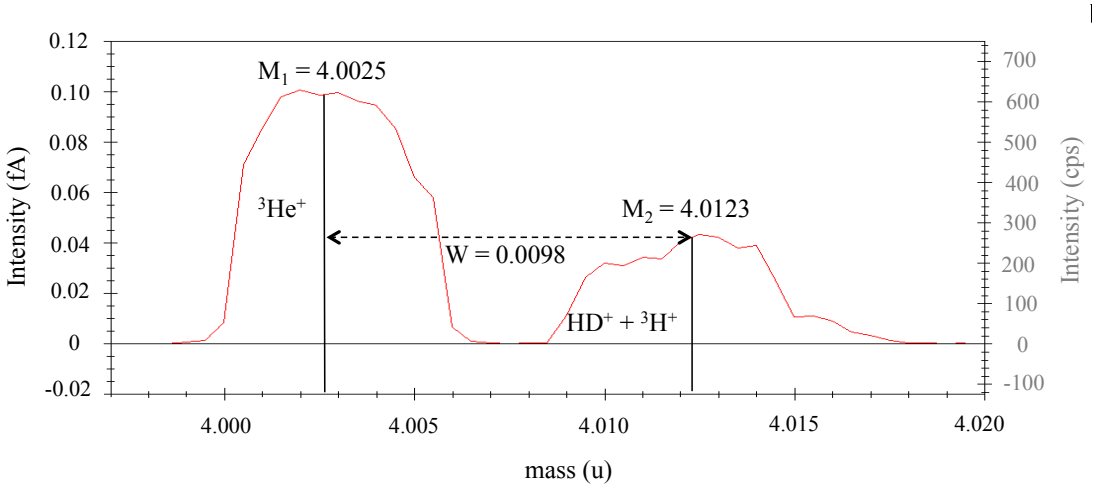

Figure 3.7. Wide scan over ^{3}He in the electron multiplier showing the separation between the $^3He^+$ peak and the HD^+-$^3H^+$ doublet. The separation between the peaks is 0.0098 mass units and the valley intensity is < 1% of the ^{3}He intensity. HD-H_3^+ is typically ~2 x 10^6 atoms. Scan is performed over mass 4 in the Faraday cup, which corresponds to mass 3 in the multiplier.

The electron multiplier is operated at 2040 V, which is the optimum voltage for the maximum measured signal (0.12 fA) determined by continuous measure of the electron multiplier signal over a voltage range from 1500 to 3000 V (Figure 3.8). The collector dark noise (typically ~3 x 10^{-6} fA) is measured by switching the magnetic field off and

measuring the dark counts over 60 seconds and averaging this into counts per second (cps). The electron multiplier generates a signal in counts per second (cps) and a factor of 1.48 x 10^{-4} (given by the manufacturer, *Balzers*) is applied to transform that signal into fA to allow for calculation of absolute ratios. The dead time correction for the ion counter is 30 ns provided by the manufacturer (*Balzers*) and corrected for by the computer-controlled application (Qtegra).

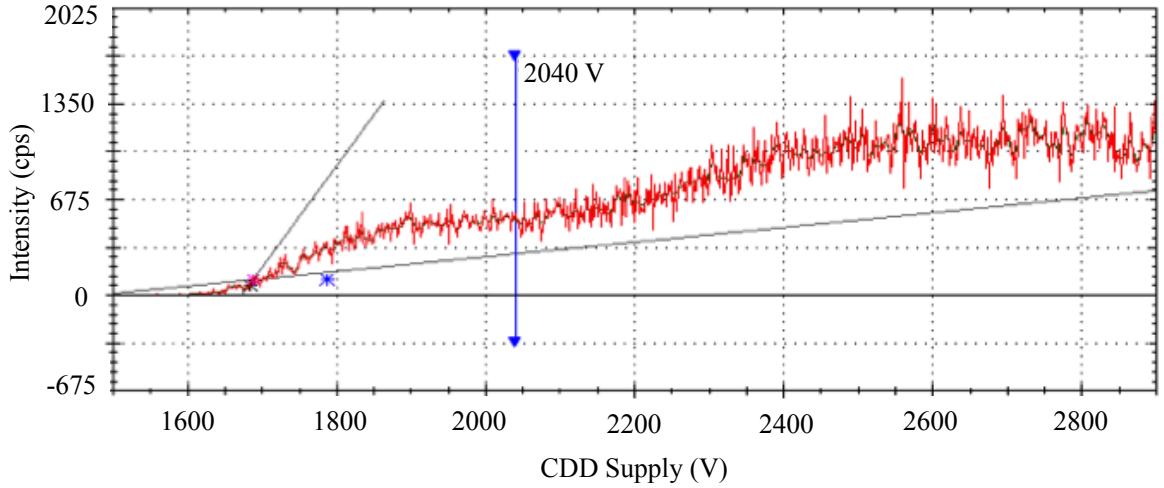

Figure 3.8. Plot of beam intensity vs. CDD (Compact Discrete Dynode) voltage for a constant ^{3}He signal (660 cps). The signal intensity (red line) shows variation with voltage supply changes and a plateau that determines the voltage at which the electron multiplier is most stable. The blue vertical line indicates the optimum voltage at which the electron multiplier is operated determined by the plateau in the signal intensity.

3.3.2 Peak stability

In order to assess the stability of the ^{3}He and the ^{4}He peaks, peak side stability has been evaluated. To quantify the peak side stability 10 consecutive mass scans over the peak were performed over a total time of 15 minutes (this is the time of data acquisition). Each scan is performed consecutively over a 90 second period with a 4 second integration time. The drift of the magnetic field during the time of data collection can be calculated as the displacement of the side of the ^{4}He and ^{3}He peaks at 50 % of the peak signal.

Peak drift is typically 0.0003 atomic mass units (amu). The width of ^{4}He and ^{3}He peaks is 0.005 and 0.003 amu, respectively. Drift of the magnet over 900 seconds represents 6 % of the ^{4}He peak width and 10 % of the ^{3}He peak width demonstrating that the magnet is stable enough to perform accurate measurements of ^{4}He and ^{3}He. The two peaks are measured simultaneously over a 900 second period and the peak side drift

represents 10 % of the width of the smaller peak (^{3}He) allowing for the two peaks to be coincident for the total data acquisition time (see Figure 3.9).

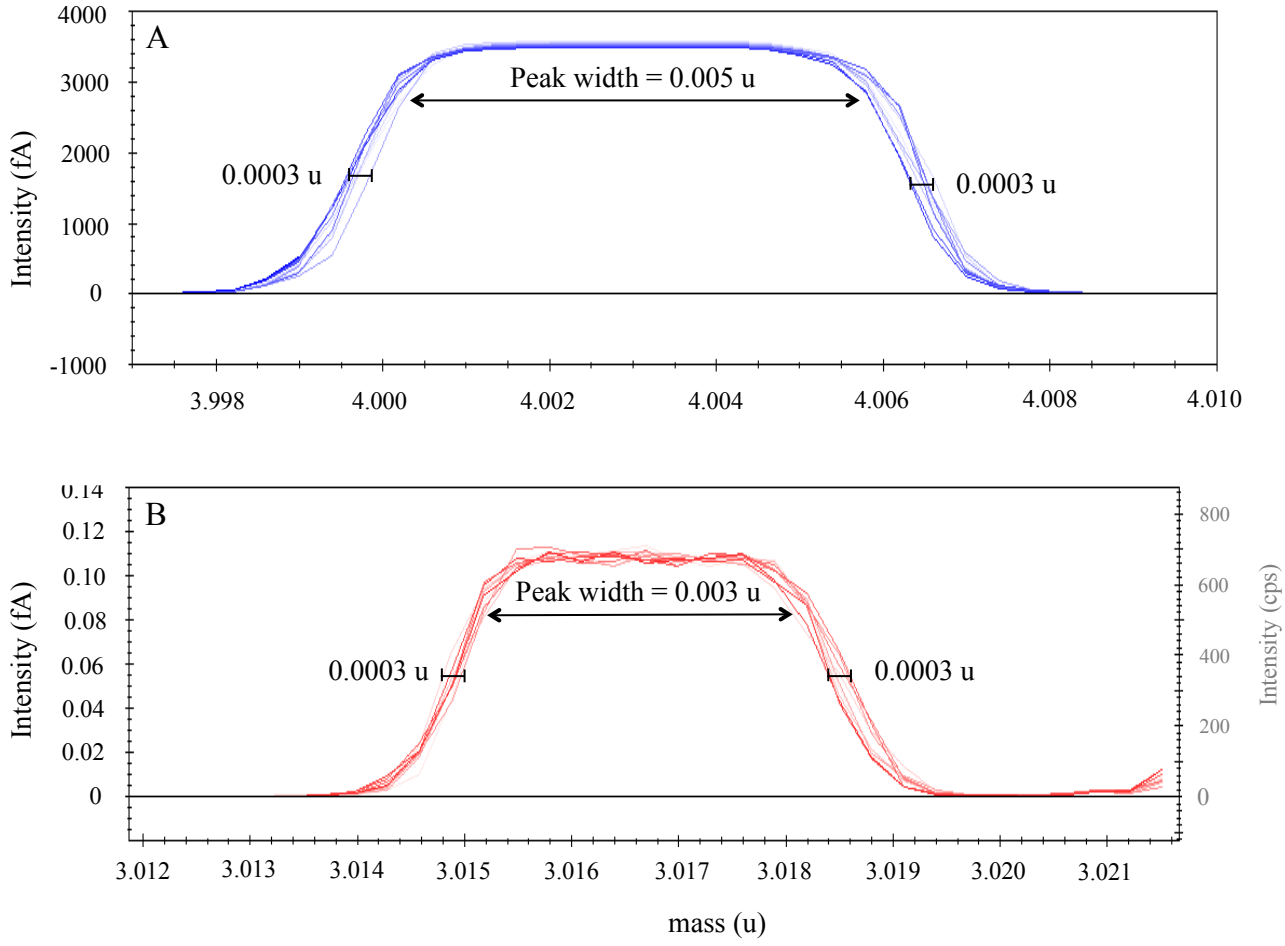

Figure 3.9. Ten consecutive scans over ^{4}He in the Faraday cup (A) and ^{3}He in the electron multiplier (B) to assess the peak side stability. Values of the peak width and peak side drift are given in mass units. The two peaks are measured simultaneously and the peak side drift represents 10 % of the width of the smaller peak (^{3}He).

3.3.3 Peak coincidence

Multicollection requires the two helium isotope beams to be focussed onto both detectors during analysis. Peak coincidence is achieved by adjusting the screws in the pole pieces to move the magnet; this reshapes the magnetic field allowing for mass 3 to be collected in the electron multiplier at the same time that mass 4 is focused onto the Faraday cup. Separate pole pieces control the shape of the peaks individually. The different pole pieces are shown in Figure 3.10 and the resultant coincidence of the ^{4}He and ^{3}He peaks are shown in Figure 3.11.

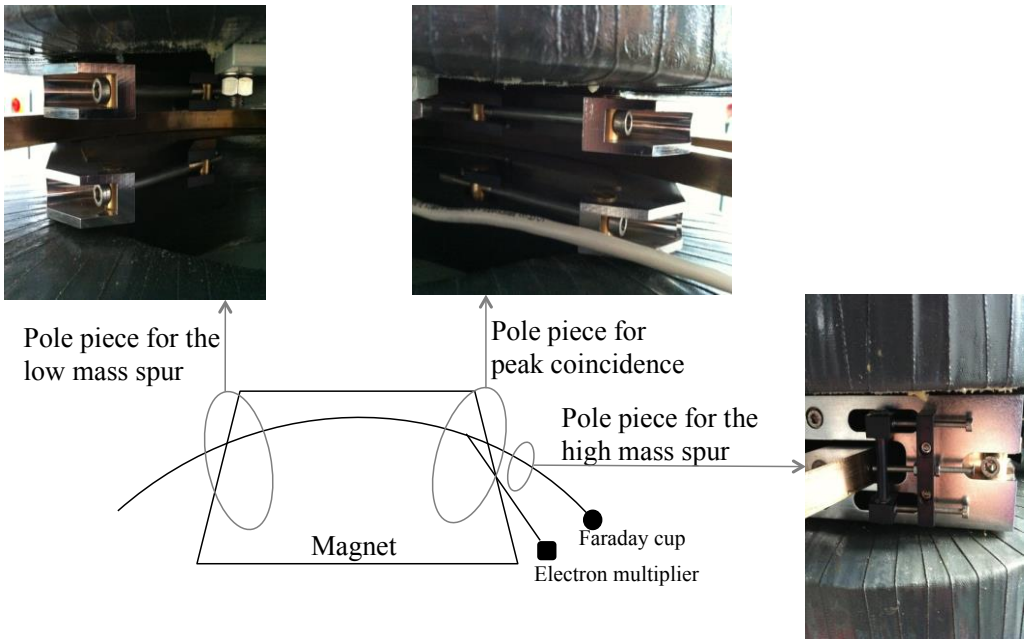

Figure 3.10. Photographs showing the location of the magnet pole pieces. The magnet is provided with two pole pieces: (1) the pole piece on the right hand side of the magnet is used to adjust the peak shape of the low mass spur and (2) the pole piece on the left hand side is used to achieve coincidence of the two peaks. A third pole piece is situated on the flight tube split into the Faraday cup and is used to adjust the shape of the peak of the high mass spur.

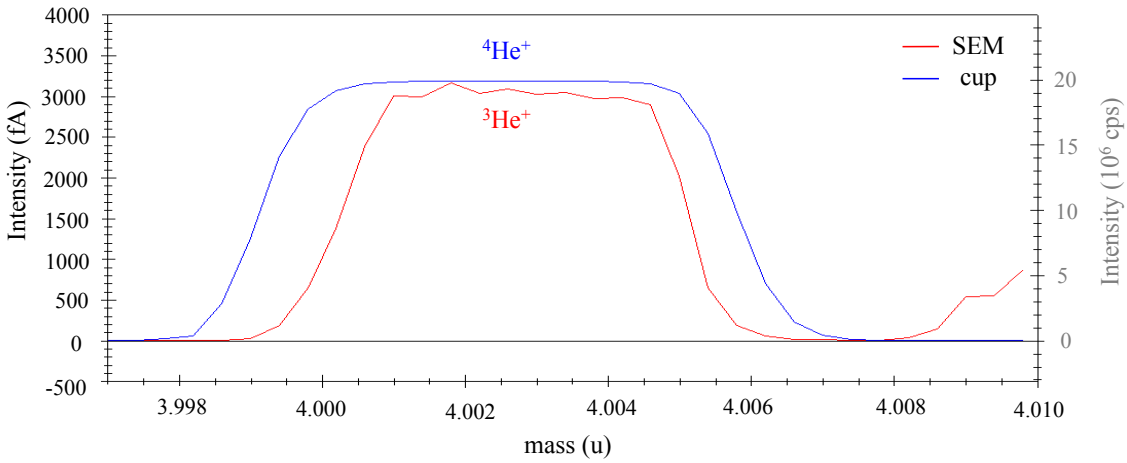

Figure 3.11. Scan over mass 4.003 in the Faraday cup showing the coincidence of the ^{4}He (blue) and ^{3}He (red) peak centres. The gas used for this scan is HESJ (Matsuda et al., 2002) gas standard. The scan is performed by changing the magnetic field. The intensity of ^{3}He peak is scaled to 2 x 10^4 times.

The magnetic field intensity of 0.42156 V is sufficient to focus the two peaks. Establishing the necessary magnet stability at such low field intensities for multicollection has been one of the major challenges in setting up the instrument. The magnetic field remains stable when no peak jumps are performed maintaining the peak coincidence. However, after single peak jumping differential displacement between the two masses occurs due to hysteresis of the magnetic field causing the loss of ^{3}He-^{4}He peak coincidence (Figure 3.12). This is a systematic problem with the Helix SFT, acknowledged by the manufacturer and in conversation with other users. To overcome this issue a routine to

reset the magnet and cancel the effects of hysteresis is performed. This consists of jumping the magnetic field from the ^{3}He-^{4}He position (4.003 mass units) in steps to the maximum value (the sequence expressed in mass units is: 4, 10, 20, 50, 95, 4 each step last ~15s) and return to the field where ^{3}He and ^{4}He are found. After performing this procedure the ^{3}He and ^{4}He peaks are coincident. This effect produced by peak jumping is avoided by jumping to peaks changing the acceleration voltage at fixed magnet intensity.

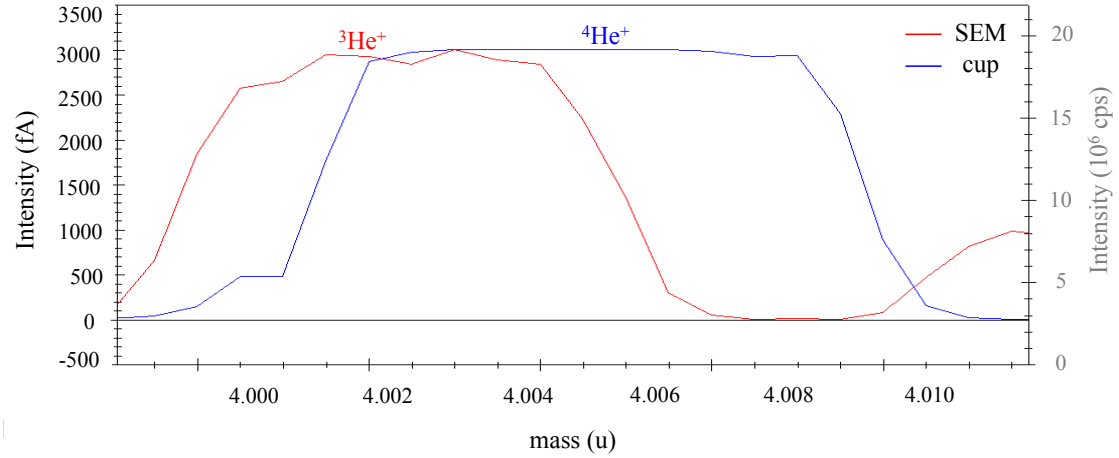

Figure 3.12. Loss of coincidence as a consequence of peak jumping. Resetting the magnet recovers the coincidence of the two peaks. The intensity of ^{3}He peak is scaled to 2 x 10^{4} times.

The low magnetic field strength at which ^{3}He and ^{4}He are measured causes a drift in both directions when no peak jumps are performed. This drift can be ± 0.2 % of the magnetic field strength and appears to be independent of time (see Figure 3.13). The drift of the magnetic field is a direct consequence of the low magnetic field strength and it is not observed when operating at higher masses (i.e. ^{40}Ar, Mark et al., 2009).

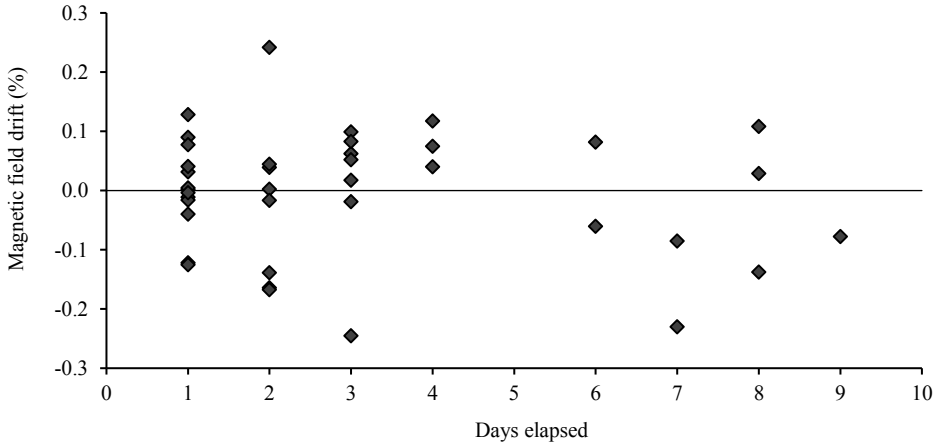

Figure 3.13. Plot of the magnetic field position drift for the ^{4}He and ^{3}He peak centre against time. Positive values indicate that the position of the peak moved towards higher magnetic field intensity and negative values indicate that the position of the peak moved towards lower intensity. Continuous line separates positive and negative drifting with the magnetic field drifting ± 0.2 %.

3.4. Mass spectrometer sensitivity calibration

The mass spectrometer sensitivity has been determined by repeated analysis of known amounts of the HESJ standard He (Matsuda et al., 2002). The HESJ reservoir was prepared at SUERC and calibrated against ^{4}He (7.56 ± 0.02 x 10^{10} atoms per pipette) from a 'check' bottle that has been externally calibrated by University College of London. Sensitivity of 1.38 ± 0.002 x 10^{-9} fA/atom ^{4}He (1σ uncertainty) was determined from the analysis of 12 aliquots from the 'check' bottle (Figure 3.14). The results obtained are normally distributed with an uncertainty of 0.12 % and a mean squared weighted deviation (MSWD) of 0.19. The uncertainty of the sensitivity for each individual measurement (~0.28 %) is dominated by the uncertainty of the given atoms per pipette (0.26 %). This is higher than the reproducibility of the ^{4}He measurements and it is the reason of the low MSWD (< 1).

The sensitivity measurement includes the volume of the purification line and therefore is representative of the sensitivity of the whole system. The sensitivity of the instrument is calculated by applying a factor of 0.75 to the system sensitivity value in order to account for the exclusion of the volume of the purification line and it is equal to 1.84 ± 0.003 x 10^{-9} fA/atom. Since the calibration gas and sample gas are always equilibrated in the same volumes the sensitivity values used in this work are those of the system sensitivity.

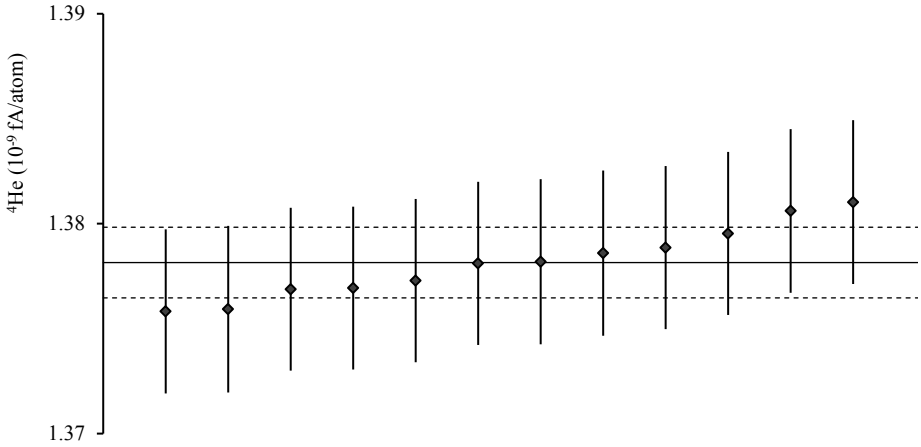

Figure 3.14. ^{4}He results from analysis of the externally calibrated "check" bottle showing the sensitivity of the source for ^{4}He in fA/atom. The continuous line represents the average and the dotted line delimits the uncertainty (1σ). The results obtained from the mass spectrometer analysis are normally distributed with a MSWD of 0.19.

The sensitivity obtained from the analysis of the 'check' bottle was used to determine the amount of He in the HESJ standard reservoir. The concentration of ^4He in a pipette volume of 0.1 cc was determined as follows:

$$S4 = I4_{check}/{}^4He_{check} \quad [3.1]$$

$${}^4He_{HESJ} = I4_{HESJ} / S4 \quad [3.2]$$

Where, S4 is the ^4He sensitivity in fA/atom; $I4_{check}$ and $I4_{HESJ}$ are the ^4He intensities in fA from pipettes of the 'check' bottle and the HESJ bottle respectively and $^4He^*_{check}$ and $^4He_{HESJ}$ are the concentrations of ^4He in atoms/pipette from the 'check' bottle and the HESJ bottle respectively.

^4He concentration of $3.127 \pm 0.003 \times 10^{12}$ atoms/pipette in the HESJ bottle was determined from the average of 17 measurements of individual pipettes (Figure 3.15). The results obtained from the mass spectrometer analysis are normally distributed with an uncertainty of 0.11 % and a MSWD of 0.81. The uncertainty of an individual measurement (~0.12 %) is dominated by the uncertainty of the sensitivity (~0.12 %). The uncertainty of the sensitivity and that of the ^4He atoms/0.1 cc pipette are similar and they represent the instrument's ability to reproduce a measurement.

The ^3He concentration of $8.97 \pm 0.01 \times 10^7$ atoms/pipette in the HESJ bottle was determined from the $^3He/^4He$ ratio of the HESJ standard gas 20.63 ± 0.1 R_A (Matsuda et al., 2002).

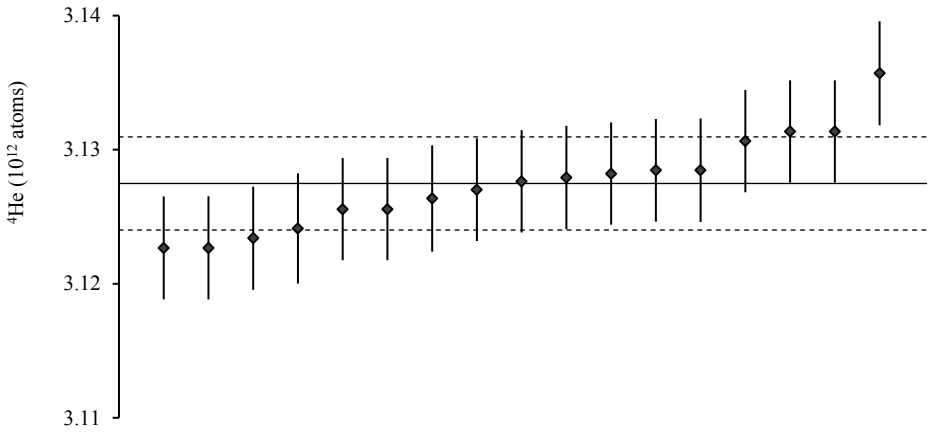

Figure 3.15. ^4He results from analysis of in-house HESJ gas bottle showing the ^4He measurement in atoms in 0.1 ccSTP. The continuous line represents the arithmetic mean and the dotted line delimits the uncertainty (1σ). The results are normally distributed with a MSWD of 0.81.

3.5. Mass spectrometer backgrounds

To characterise the mass spectrometer a series of static mass spectrometer backgrounds (n = 14) were performed over the course of July 2015. The mass spectrometer was isolated from the pumps and ^{4}He and ^{3}He signals were measured in the normal way. The intercepts of each run yield average static background levels of 1.68 ± 0.19 x10^8 and 5.0 ± 1.9 x 10^3 atoms (1σ) (Figure 3.16). Mass spectrometer backgrounds are measured routinely at the start of a day of analyses.

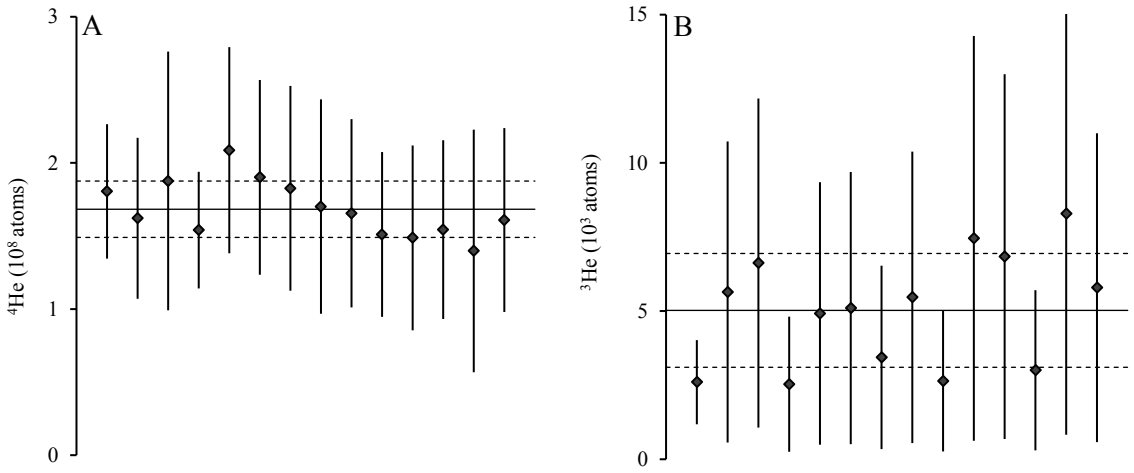

Figure 3.16. Results of static mass spectrometer background measurements (n=14) of (A) ^{4}He and (B) ^{3}He. The average of all the ^{4}He and ^{3}He intensities is represented by the continuous line and the uncertainty by the dotted lines. The uncertainty is taken as 1 σ . The 1 σ uncertainties of the individual background experiments vary from 30 to 60 % for ^{4}He and from 60 to 90 % for ^{3}He.

3.6. Analysis of HESJ gas standard

The sensitivity of the mass spectrometer is a measure of the source ionization capacity, the ion extraction and detector efficiency. Changes in these parameters will result in changes in the mass spectrometer sensitivity as well as the mass discrimination (Mabry et al, 2012). The HESJ calibration gas was used to track the sensitivity changes in order to determine the precision and accuracy of measured He abundances and isotope ratios (Figure 3.17).

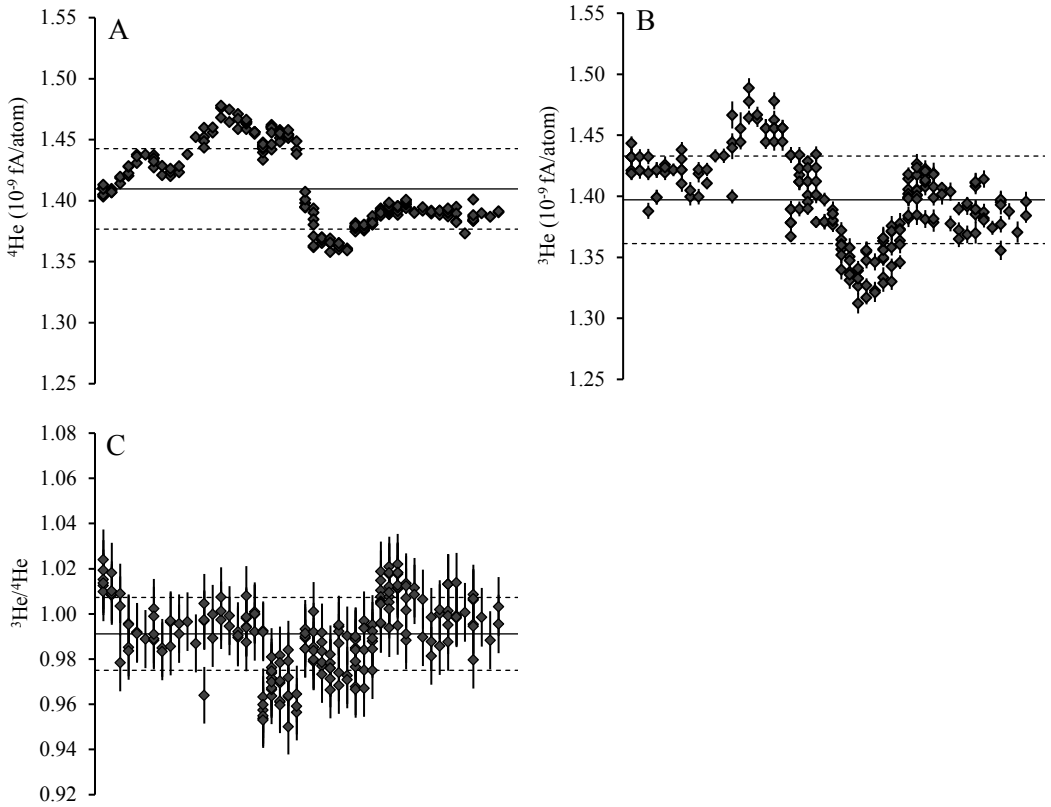

Figure 3.17. Data from the analysis of (A) ^{4}He signal and (B) ^{3}He in HESJ calibration gas over a five months period (May-November 2015). (C) shows the ^{3}He/^{4}He variation. The continuous line represents the arithmetic mean and the dotted line delimits the standard deviation (1σ).

The mean sensitivity of ^{4}He is 1.41 ± 0.03 x 10^{-9} fA/atom (2.3 % relative standard deviation, 1σ) and ^{3}He is 1.40 ± 0.04 x 10^{-9} fA/atom (2.6 % relative standard deviation, 1σ). The standard deviation of individual measurement of ^{4}He is ~0.01 %. The MSWD of the ^{4}He data is 132. The standard deviation of a ^{3}He individual measurement is ~0.4 % yielding a MSWD of 30. The relative standard deviation for the average ^{3}He/^{4}He ratio is 1.6 % with individual measurement uncertainty being ~0.4 % (governed by the ^{3}He uncertainty) yielding a MSWD of 11. The high MSWD (> 1) is related to the scatter in the data being greater than the expected analytical noise. The scatter in the data seems to be generated by changes in the ionization efficiency of the source producing an over dispersion of the data with respect to the individual analytical uncertainty. The smaller variation of the ratio is indication of the stability of the collectors and reflects the consistency of the source relative discrimination.

Sensitivity over 49 calibration shots performed over the course of 8 consecutive days yields smaller standard deviations, ± 0.22% and ± 1.14% for ^{4}He and ^{3}He respectively (Figure 3.18). In this case the variation of the ^{3}He/^{4}He ratio is ±1.03%, mostly dominated by the variability in the measurement of the smaller ion beam. The respective MSWDs

(1.2, 5.4 and 3.8 for ^{4}He, ^{3}He and ^{3}He/^{4}He ratio) are smaller and close to unity demonstrating the stability of the source efficiency over short periods of time (~1 week). The data seems to be still over dispersed in relation to the analytical uncertainty. The main source of such dispersion appears to be related to a memory effect due to consecutive calibration analysis. Calibration gas analyses are routinely performed during the analysis period and sensitivity values are chosen according to the period of analysis.

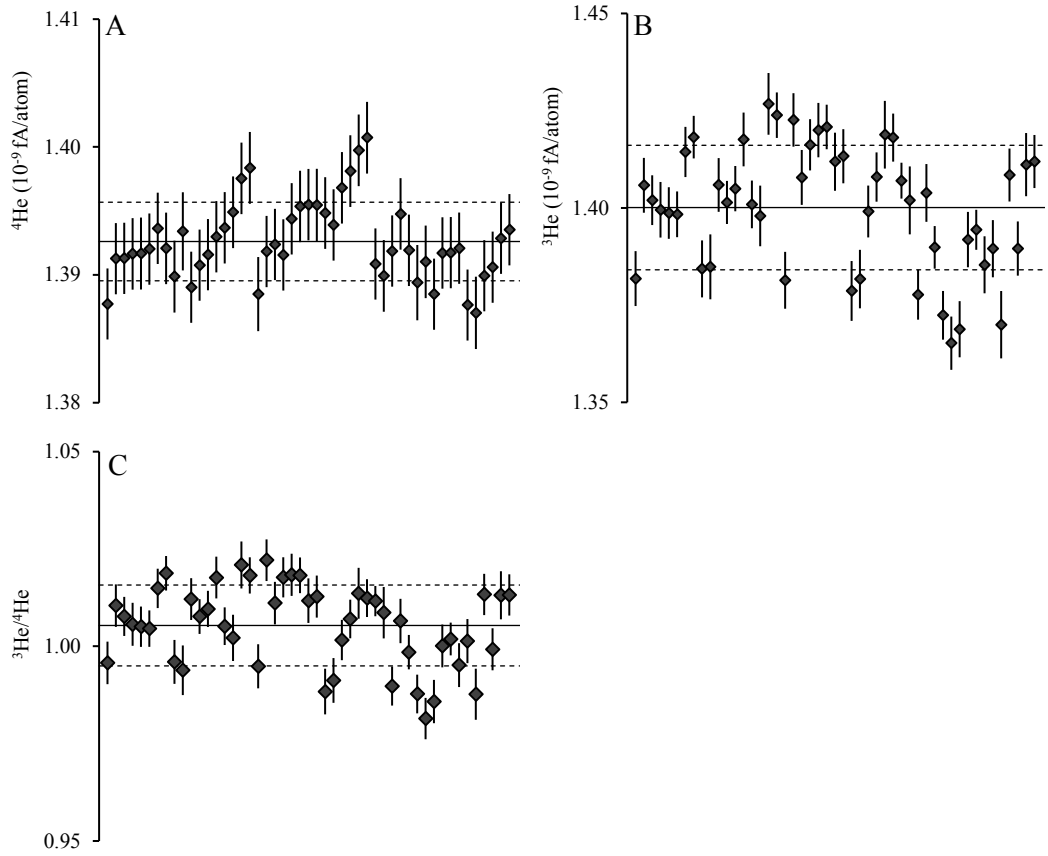

Figure 3.18. (A) ^{4}He., (B) ^{3}He and (C) ^{3}He/^{4}He variation from the analysis of 49 calibration shots over 8 consequtive days in September 2015. The ccontinuous line represents the average and dotted line delimits the standard deviation (1σ).

Sensitivity over the course of one day yields standard deviations ranging from 0.09-0.22 % for ^{4}He and 0.86-1.25 % for ^{3}He. A memory effect is observed when several calibration measurements are performed causing an apparent increase in sensitivity for both ^{4}He and ^{3}He beams (see Figure 3.19). The uncertainty of the weekly reproducibility seems to be governed by the uncertainty of the daily reproducibility.

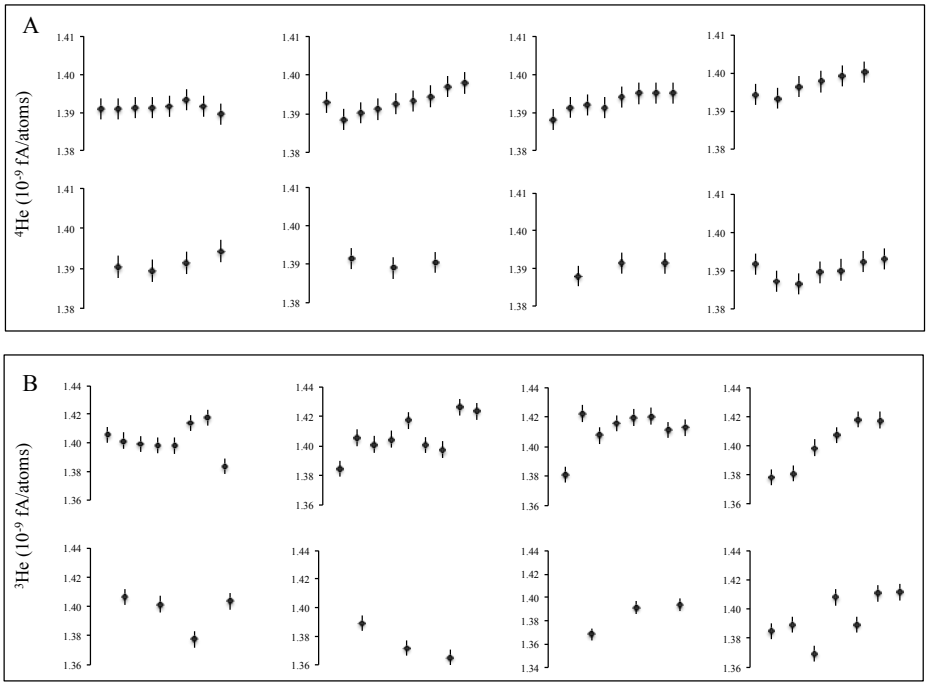

Figure 3.19. Plots of the (A) ^{4}He and (B) ^{3}He sensitivity variation over the course of a day over 8 consequtive days.

Sensitivity stability is crucial when determining the absolute concentration of cosmogenic He in a sample for precise chronology determinations. During sample analysis the uncertainty in the sensitivity constrains our ability to reproduce measurements and determines the limit of the uncertainty of all measurements.

3.6.1. Uncertainties in He measurement

Quantifying uncertainties in the He isotope measurements is imperative in order to fully understand the limitations of the data. The regression of the raw data to inlet time typically yield 1σ uncertainties of 0.2 % and 0.4 % for ^{4}He (3 x 10^{12} atoms, 4,414 fA) and ^{3}He (9 x 10^7 atoms, 0.126 fA) respectively in individual He calibration shots. The uncertainty in the ^{3}He/^{4}He ratio is governed by the ability to measure the small ^{3}He ion beam. The uncertainty increases with decreasing beam intensities more significantly for ^{3}He than ^{4}He (Figure 3.20). A 10^2–fold decrease in the ^{4}He signal on the Faraday cup (~2 x 10^{10} atoms) results in a modest increase in uncertainty from 0.01 % to 0.06 %. The uncertainty in the measurement of the multiplier ^{3}He signal is 100 times higher than that of the Faraday and increases significantly as beam intensity drops. For instance, for a 10^2 drop in the ^{3}He signal (~2 x 10^6 atoms) increases measurement uncertainty from 0.4 % to ~3.0 %.

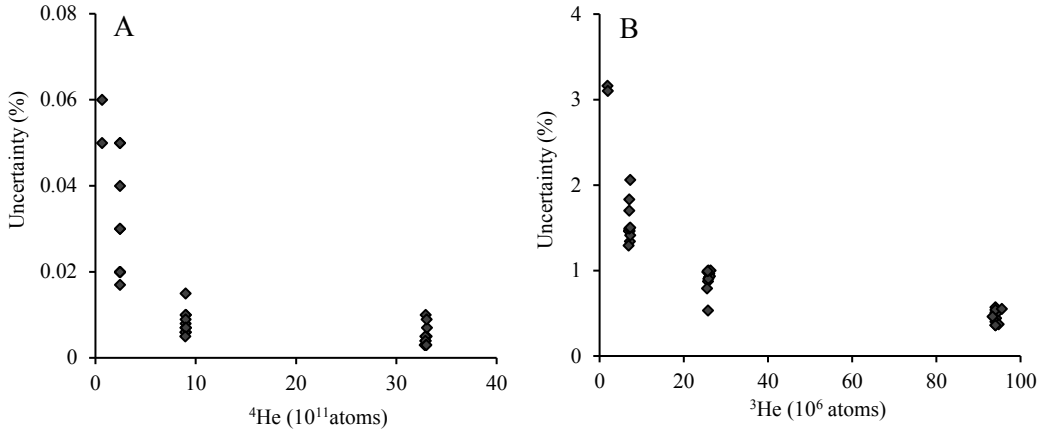

Figure 3.20. Plots showing 1 σ uncertainty of the measurements of different ion beam sizes using the Faraday cup (A) and the electron multiplier (B) over a near 100-fold variation in beam size. A number of 11 expansion experiments have been performed 9 of them consisting on three expansions and two of them consisting on four expansions.

The relative standard deviation of the ^{4}He in the Faraday cup over multiple calibrations per day is on average 0.25 ± 0.11 %. The relative standard deviation of similar ^{3}He measurements using the electron multiplier is on average 0.85 ± 0.43 %. The higher variation in the uncertainty of the measurements performed by the electron multiplier is a consequence of its lower stability and the samller beams, which could not be meassured using a Faraday cup.

3.6.2 Linearity of the source

A series of measurements of varying amounts of the HESJ standard gas have been performed in order to assess the effect of helium partial pressure on the sensitivity and mass fractionation (Figure 3.14). The analysis of the HESJ standard involves the expansion of 0.1 cc from the calibration reservoir (~3 x 10^{12} atoms of ^{4}He and ~9 x10^7 atoms of ^{3}He) into the extraction line and, ultimately the mass spectrometer. In the analyses shown in Figure 3.21 a single calibration shot was expanded from the extraction line into the mass spectrometer over 50 seconds, then the extraction line was isolated and the remaining gas stored in the line for re-expansion into the mass spectrometer after the analysis of the initial expansion. This was repeated several times and results in a 27 % decrease in He each time.

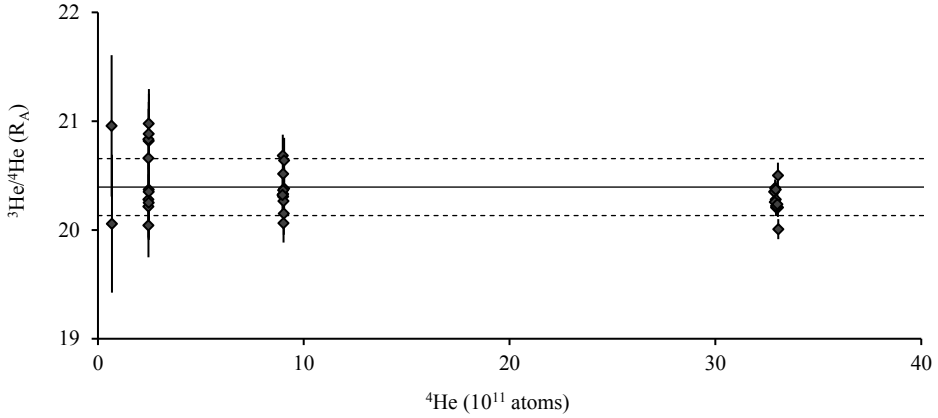

Figure 3.21. Plot showing how the $^3He/^4He$ changes with the size of the ^4He signal. The samples reported in later chapters typically have ^4He in the range 10^{10} to 10^{12}, which is the range covered by this experiment. The continuous line represents the arithmetic average and dotted line delimits the uncertainty (1σ). Eleven expansion experiments have been performed; 9 involved three expansions and two of them consisted of four expansions.

There is no significant difference in the measured $^3He/^4He$ for a range of ^4He intensities varying from 3.3 x 10^{12} to 6.7 x 10^{10} atoms. The measured $^3He/^4He$ ratio is on average 20.72 ± 0.27 R_A and the recommended value for the $^3He/^4He$ of the HESJ bottle is 20.63 ± 0.1 R_A revealing minimal helium isotopic depletion (< 0.5 %).

Data from the average of the $^3He/^4He$ ratio for each of the expansion steps are summarised in Table 3.2. The reproducibility of the $^3He/^4He$ ratio decreases with the amount of ^4He analysed and the relative standard deviation varies from 0.64 to 1.58% (note that 3.10 % is the product of only two experiments and therefore it is not been used in the comparison). Figure 3.22 shows the increase of the uncertainty when the amount of gas analysed is reduced (27 % per expansion) varying from 0.4 % to 4 %. This variation of the uncertainty of the $^3He/^4He$ is governed by the uncertainty of the ^3He.

Table 3.2. Summary of the average $^3He/^4He$ ratio different amounts of HESJ (Matsuda et al., 2002) calibration gas. (RSD: relative standard deviation)

^4He (10^{11} atoms)	*1σ*	*Number of experiments*	*$^3He/^4He_{average}$ (R_A)*	*1σ*	*RSD (%)*
32.97	0.07	11	20.28	0.13	0.64
9.01	0.03	11	20.37	0.19	0.92
2.47	0.01	11	20.52	0.32	1.58
0.67	0.01	2	20.51	0.64	3.10

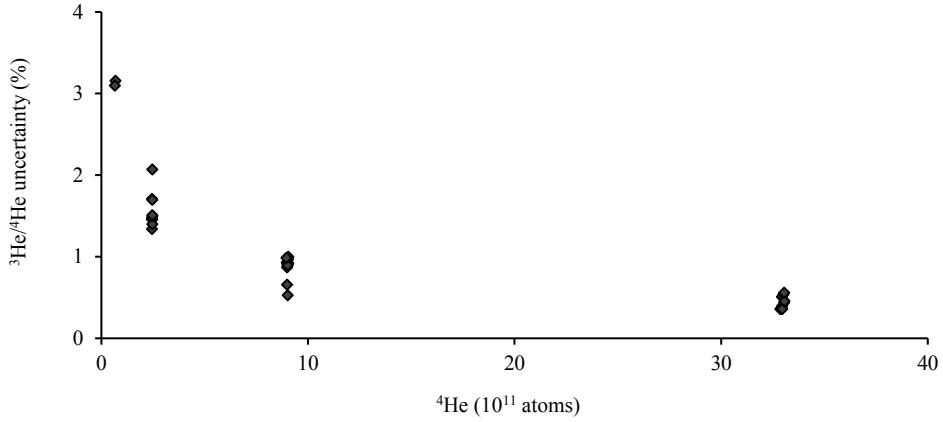

Figure 3.22. Plot showing the uncertainty of the ^{3}He/^{4}He measured in different amounts of HESJ (Matsuda et al., 2002)**.**

3.7. Summary

The Helix SFT has been specifically design for simultaneous collection of helium isotopes (^{3}He and ^{4}He). Multicollection reduces the time of analysis. This, in conjunction with a high-sensitivity Faraday collector and an electron multiplier, results in an improvement of the standard gas precision of approximately 3 times better than that obtain from peak jumping collection using the MAP 215-50 at SUERC (Dymock, 2014). Future development of the instrument will include the incorporation of measurements of ^{20}Ne at the end of every analysis to assess the contribution from air when analysing natural samples. This can be currently performed manually but it will require further work in order to be incorporated in the routine analyses.

The low detection limit of the two collectors enables for more precise measurements (reproducibility of 0.22% and 1.14% for ^{4}He and ^{3}He respectively) of small amounts of gas opening a possibility to accurately measure small amounts of sample. Data from measurements of mineral standards are presented in the following chapter where the gas extraction technique for cosmogenic ^{3}He analysis is described.

4. Helium extraction for accurate dating with cosmogenic noble gases

4.1 Introduction

Cosmogenic nuclides accumulate through time in minerals that are exposed to cosmic rays at the Earth surface. The determination of the absolute concentration of a cosmogenic nuclide in a mineral allows determination of its exposure time, if the production rate is known (Gosse & Phillips, 2001; Lal, 1991). Dating surface exposure using cosmogenic ^{3}He ($^3He_{cos}$) requires the precise determination of an absolute concentration of helium (^{3}He and ^{4}He) in minerals. It is therefore crucial that the cosmogenic He is completely extracted from the mineral. The concentration of cosmogenic helium in a mineral is directly proportional to its exposure duration and the latitude and altitude at which the mineral has been exposed to cosmic rays (Gosse & Phillips, 2001; Lal, 1991). Therefore, the amount of mineral needed to generate a measurable He signal depends on the sample location and exposure history. Using lasers to degas noble gases from minerals is often faster and more efficient than double-walled ultra-high vacuum furnaces (Foeken et al., 2006). However, the ability of particular lasers to couple with minerals often limits lasers to fully degas large volumes.

In this chapter I test the ability of different laser methods to degas cosmogenic He from olivine (xenolith MH.2; see Chapter 5) and pyroxene (global mineral standard CRONUS, Blard et al., 2015). Both contain high ^{3}He concentrations (~10^8 atoms/g) therefore < 20 mg of sample are generally sufficient to generate measurable signals. In the first case study, these laser-degasing methods are tested on olivine and pyroxene from Holocene basalts from the Kula Volcanic Province Western Turkey where large sample masses (~200 mg) are required to generate a measurable ^{3}He signal (~10^5 atoms). In the second case study, the ability of the near-visible wavelength laser is tested for He extraction from individual grains of detrital gold in the search for cosmogenic He.

4.2 Analysis methods and techniques

Direct heating of minerals using a laser reduces noble gas blanks compared to conventional furnaces due to its smaller volume; it permits the analysis of smaller amounts of material and speeds up analysis time (Megrue, 1967; York et al., 1981; Sharp, 1990; Foeken et al., 2006). Laser heating was first applied to noble gas extraction of meteorites using a pulsed ruby laser (690 nm; Megrue, 1967). Since then several types of lasers have been developed and become routinely used. The most commonly used laser types for noble gas analysis are diode lasers with ~800 nm radiation wavelength (e.g. Foeken et al., 2006), CO_2 lasers with 10.6 μm radiation wavelength (e.g. Sharp, 1990; Barfod et al., 2014) and Nd:YAG with 1064 nm radiation wavelength (e.g. House et al. 2000). The choice of the laser is based on the mineral that needs to be heated.

The near-visible wavelength lasers (e.g. diode lasers of range wavelength 750-850 nm) couple well with opaque minerals (e.g. pyroxene) and metals. However they do not couple well with transparent minerals (e.g. quartz, sanidine, apatite and olivine), which either require encapsulation (e.g. Foeken et al. 2006) or the addition of opaque mineral/melt to induce melting (e.g. Foeken et al. 2009a). Diode lasers are widely used for (U+Th)/He thermo chronology applications (e.g. House et al. 2005; Foeken et al. 2006). They are also used for cosmogenic ^{3}He dating (e.g. Foeken et al., 2012; Shuster et al., 2012) offering an alternative to double-walled ultra-high vacuum induction furnaces. In this work two different diode lasers were used: (1) 25 W 808 nm diode laser (FDL25, *Laservall S.p.A.*; Foeken et al., 2006) and (2) 75 W 800 nm diode laser (*Photon Machines*).

CO_2 lasers have a wavelength radiation of 10.6 μm that is absorbed by all oxygen-bearing compounds. This allows for heating of silicates and oxides (Sharp, 1990) and they are widely used for stable isotope (e.g. Sharp, 1990; Sharp, 1992, Bao and Thiemens, 2000) and $^{40}Ar/^{39}Ar$ geochronology studies (e.g. Spell et al., 2001, Smith et al., 2011). This type of laser offers a potential advantage with respect to the near-visible diode lasers as it can couple directly with olivine grains. In this work a 25 W 10.6 μm CO_2 laser (*Synrad Inc.*, Series 48-2, Barfod et al., 2014) was used to degas pyroxene and olivine minerals.

To find the best technique to use for He extraction from minerals I have tested three different laser methodologies: (1) direct heating of mineral grains using near-visible diode

laser, (2) near-visible diode laser heating of grains in encapsulated Pt foil, and (3) direct heating of mineral grains using a CO_2 laser.

For laser degassing of samples the olivine and pyroxene mineral grains were placed on a copper pan in a stainless steel laser cell. Pt packets used in this study are 5 mm long and 2 mm wide and have a maximum capacity of ~15 mg. The choice of the window for the laser cell depends on the laser wavelength. A standard 3 mm thick sapphire (Al_2O_3) window is used for the diode laser experiments. Sapphire gives ~85 % transmission for 800-808 nm wavelengths and is preferred over quartz glass as the diffusion-in of atmospheric He is negligible. In order to protect the laser cell window from absorption of volatilised material from the melted mineral grains a 3 mm thick sapphire coverslip is placed on top of the copper pan. 20 minutes blanks from the sapphire window laser cell are typically 2 x 10^9 and 4 x 10^4 atoms of ^{4}He and ^{3}He respectively. This represents < 1 % of the He from the Mount Hampton samples (see Chapter 5 and 6). The diode laser is capable of heating samples to over 1300˚C.

The CO_2 laser required the use of a doubly pumped ZnSe window (MacIntosh and Heizler, 1994). ZnSe cannot be welded to stainless steel so it is sandwiched between two aluminium gaskets leaving a space at the edge of the window that needs to be continuously pumped to avoid leakage of the atmosphere into the cell. ZnSe windows typically transmit 70% of the energy of 10.6 μm wavelength. To protect the laser cell window a KBr coverslip (95% transmission for 10.6 μm) was used. 20 minutes blanks from the pumped laser cell are ~1.1 x 10^9 and ~4.8 x 10^4 atoms of ^{4}He and ^{3}He respectively representing < 1 % of the gas from Mount Hampton samples (Chapter 5). Temperatures over 1200˚C can be reached using a CO_2 laser.

After the degassing of the minerals the gas released was cleaned for 15 minutes by two *SAES* GP50 getters operated at 250ºC to remove the active gases and by an activated charcoal-filled stainless steel finger cooled to -196°C using liquid nitrogen to remove the heavy noble gases. The gas is then let into the mass spectrometer for He isotope analysis. Any partial pressure of residual gases during the analysis is minimized by a *SAES* GP50 and a *SAES* NP10 getters operated at room temperature and a stainless steel charcoal cold finger at -196°C close to the ion source.

4.3. Blanks

Achieving low and stable blank levels is imperative for precise results. In order to achieve low blank levels in the laser system baking of the laser cell after loading samples is required. The laser extraction system was baked to ~100˚C for 12 hours in order to minimize the blank. It was noted that over-baking could result in the partial degassing of pyroxene samples (Figure 4.1).

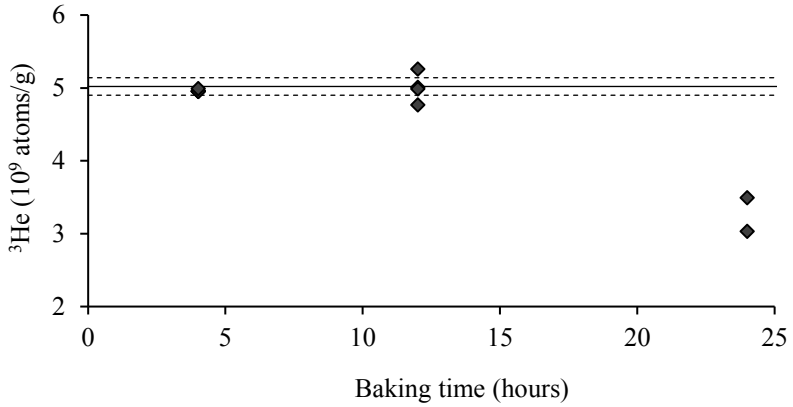

Figure 4.1. Plot of ^{3}He concentration from CRONUS pyroxene standard versus laser cell bake-out time. The samples were encapsulated in Pt packets and degassed using a diode laser. Continuous line represents the published global average (Blard et al., 2015) and dotted line delimits the uncertainty (2σ).

Laser pans are baked using a heat lamp mounted above the pan. Baking for 24 hours appears to partially degas the CRONUS pyroxene standard, losing up to 40 % of the ^{3}He. Through trial and error it was determined that placing the heat lamp ~500 mm above the laser cell for 4 hours achieves low blank levels without degassing samples (maximum external temperature ~120˚C). Measuring the blank levels of the laser extraction methods requires reproducing the same conditions as those of sample analysis. Previously degassed pyroxene minerals have been used to characterize the blank levels. The laser chamber is 'baked' for 12 hours at ~100˚C after a new batch of samples is loaded in order to achieve adequate blank levels.

To assess the blank levels of the doubly-pumped laser window used for degassing samples with the CO_2 laser, three degassed pyroxene samples have been heated for up to 20 minutes. The average blank levels are $6.8 \pm 0.7 \times 10^8$ atoms of ^{4}He and $4.76 \pm 2.3 \times 10^4$ atoms of ^{3}He. This represents less than 1% of the signal produced by analysis of Mount Hampton samples (typically ~10^6 atoms).

The blank levels of the sapphire window laser chamber used for heating with the diode laser have been assessed in three ways: (1) direct heating of degased pyroxene minerals, (2) heating degassed pyroxene samples encapsulated in Pt tubes and (3) heating empty Pt tubes. The samples have been heated for 30 minutes at 20 W laser intensity (Table 4.1).

Table 4.1. Average blank levels of ^{4}He and ^{3}He (n=4) of the sapphire laser chamber used for diode laser heating. All uncertainties are reported as 1σ.

Type of experiment	*^{4}He (10^8 atoms)*	*^{3}He (10^4 atoms)*
Unencapsulated degassed pyroxene	6.5 ± 0.6	4.8 ± 1.8
Encapsulated degassed pyroxene	3.36 ± 0.12	2.9 ± 1.1
Empty Pt packet	3.0 ± 0.8	2.6 ± 0.9

The blank levels of the sapphire window laser chamber represent less than 1 % of the amount of ^{4}He and ^{3}He measured from analysis of encapsulated samples using the diode laser. The measured ^{3}He blanks are of the same order of magnitude than those reported from conventional furnaces and the measured ^{4}He blanks from the laser chamber are similar to those obtained from the single vacuum furnace designed by Zimmermann et al. (2012) and about an order of magnitude lower than those obtained from conventional furnaces (Honda et al., 1993; Niedermann et al., 1997; Aciego et al., 2007; Blard et al., 2015).

4.4 Helium extraction results

4.4.1 Pyroxene

To assess the effectiveness of the different lasers for degassing pyroxene grains several aliquots of CRONUS pyroxene mineral standard (Blard et al., 2015 and references therein) were degassed using three different techniques.

(1) Direct laser heating of the mineral grains. Typically this required ~20 W for 15 minutes (~80% of the 25 W diode laser and ~30% of the 75 W laser)
(2) Laser heating of mineral grains encapsulated in Pt packets. This required 20 W for 15 minutes using the diode laser (see Figure 4.2).
(3) Direct CO_2 laser heating of the mineral grains. Typically this required 20-25 W for 15 minutes (see Figure 4.3).

Prior to comparing the degassing capability of the three gas extraction methods their performance over time was assessed in order to establish appropriate degassing times. There is no significant difference in the ^{3}He released during heating of encapsulated pyroxene mineral with the diode laser for times in excess of 5 minutes although, there is significant dispersion of the ^{4}He concentrations when degassing for 30 minutes. This can be explained by the release of atmospheric ^{4}He from the copper pan and cover slip, and potentially He from adjacent samples. Consequently a heating time of 15 minutes was chosen as standard way of degassing encapsulated pyroxene up to 35 mg. The average concentration of ^{3}He and ^{4}He ($4.97 \pm 0.14 \times 10^{9}$ and $3.67 \pm 0.45 \times 10^{13}$ atoms/g respectively) overlaps the reported concentrations ($5.02 \pm 0.12 \times 10^{9}$ and $3.6 \pm 0.18 \times 10^{13}$ atoms/g; Blard et al., 2015) suggesting that complete degassing of the pyroxene is achieved using this technique (Figure 4.2).

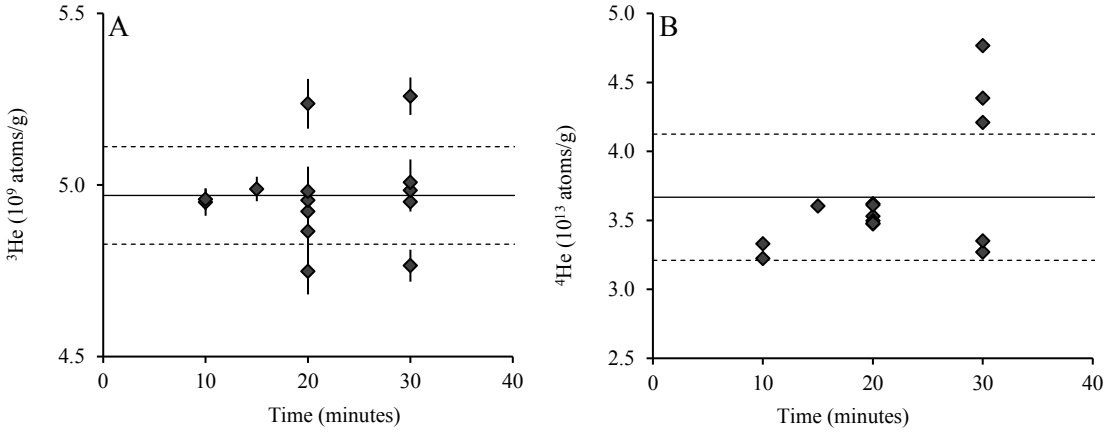

Figure 4.2. Plot of (A) ^{3}He and (B) ^{4}He concentrations measured after heating of CRONUS pyroxene using diode laser on Pt encapsulated samples (20 W) versus heating time (10 to 30 minutes). The continuous line represents the arithmetic mean and the dotted line delimits the standard deviation (1σ).

No significant difference is observed when using the CO_2 laser for degassing pyroxene mineral grains for up to 40 minutes. The average concentration of ^{3}He and ^{4}He ($4.77 \pm 0.24 \times 10^{9}$ and $3.51 \pm 0.17 \times 10^{13}$ atoms/g respectively) overlap those previously reported by Blard et al., (2015) suggesting that complete degassing of the pyroxene is achieved using the CO_2 laser (Figure 4.3).

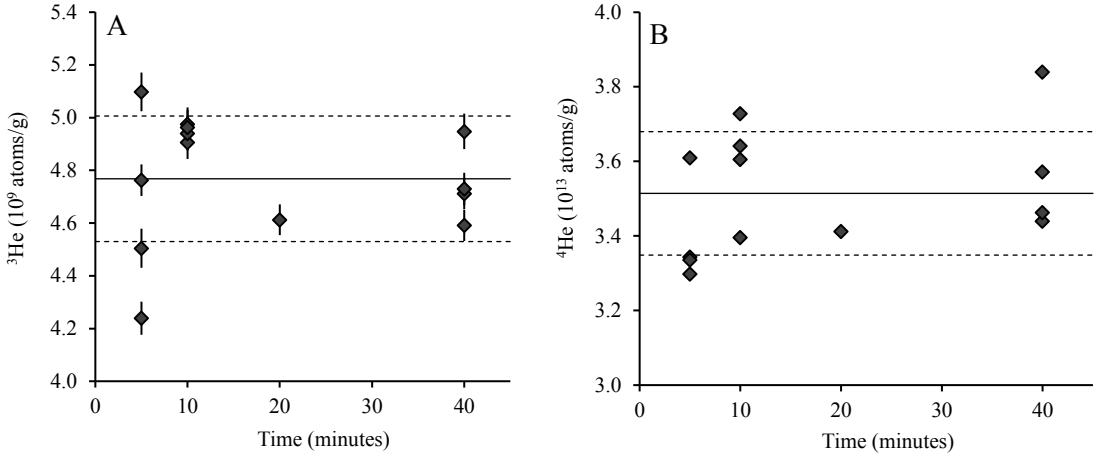

Figure 4.3. Plot of (A) ^{3}He and (B) ^{4}He concentrations measured after heating of CRONUS pyroxene using a 25 W CO_2 laser at 95 % of the power for between 5 and 40 minutes. The continuous line represents the average and the dotted line delimits the standard deviation (1σ).

A compilation of the results obtained using the three different techniques and the correspondent weighted mean values is shown in Figure 4.4 (data from the analysis are reported in Appendix B). When using diode laser directly on unencapsulated sample, the weighted mean values are $4.98 \pm 0.05 \times 10^9$ and $3.56 \pm 0.12 \times 10^{13}$ atoms/g of ^{3}He and ^{4}He respectively; when samples are encapsulated and heated with a diode laser the weighted mean values of ^{3}He and ^{4}He are $4.97 \pm 0.02 \times 10^9$ and $3.50 \pm 0.12 \times 10^{13}$ atoms/g and weighted mean values of $4.90 \pm 0.12 \times 10^9$ and $3.57 \pm 0.10 \times 10^{13}$ atoms/g of ^{3}He and ^{4}He are obtained when using CO_2 laser directly on unencapsulated samples (all uncertainties are 2σ). It is clear that the three laser techniques are capable of completely degassing of less than 50 mg pyroxene samples.

The ^{3}He released from diode laser heating of unencapsulated samples yielded one low measurement that could be a consequence of incomplete degassing of the sample maybe caused by the mineral grains placed into a non-mono-layer distribution causing poor heating of the grains that are on the lower layer. The same effect could also explain the three low outliers from the CO_2 laser heating of unencapsulated samples. In the case of diode laser heating of encapsulated grains two low outliers have been excluded suggesting incomplete degassing of the samples, in this case the shape of the Pt packet can influence the coupling with the diode laser causing the packet to reach lower temperatures. Two aliquots in Pt packets degassed using the diode laser yielded extremely high ^{3}He concentrations considered to be outliers. These high values could be a consequence of electron multiplier noise and they are not considered when calculating the weighted mean.

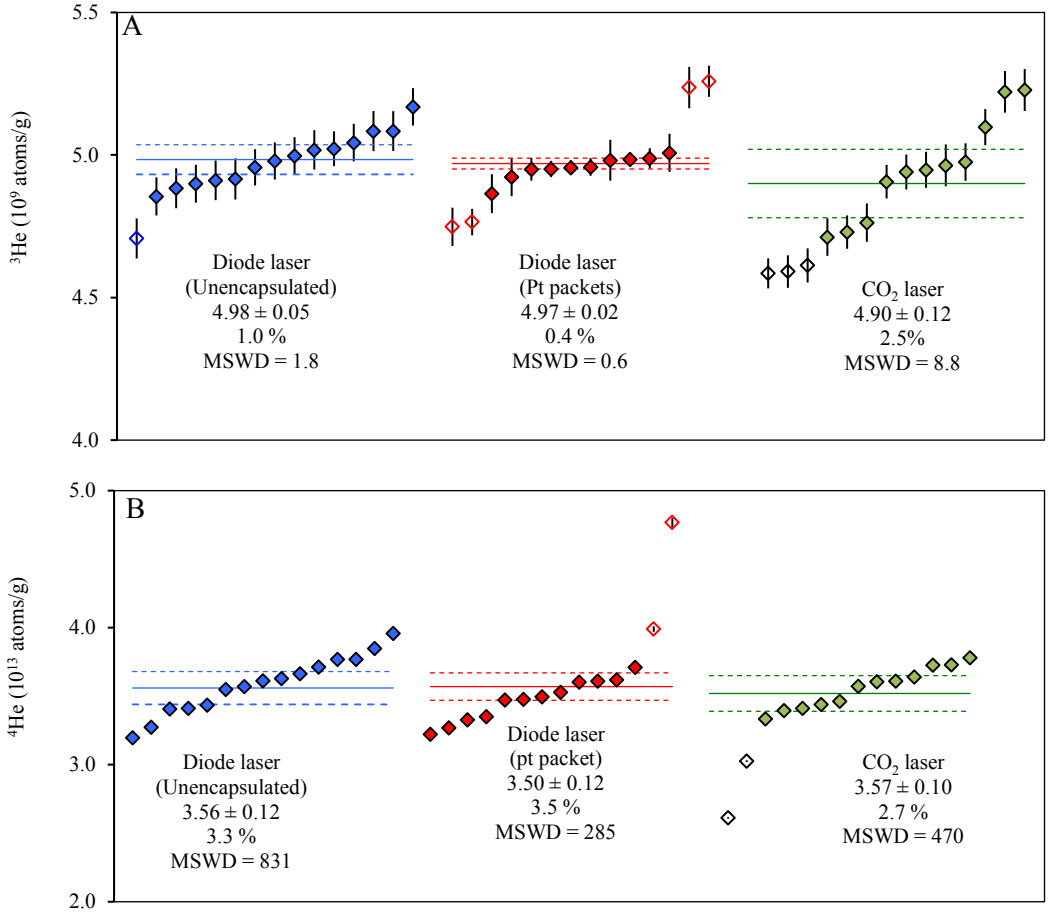

Figure 4.4. Plot of (A) ^{3}He and (B) ^{4}He concentrations from heating CRONUS pyroxene standard by three different laser techniques: (1) unencapsulated minerals heated with a 25 W 808 nm diode laser at 80 % of the power for 30 minutes (blue); (2) minerals encapsulated in Pt packets and heated with a 75 W 800 nm diode laser at 30 % of the power for 30 minutes (red) and (3) unencapsulated minerals heated with a 25 W CO_2 laser at 95 % of the power for up to 40 minutes (green*). The individual analytical uncertainties are at 1σ level. The weighted mean, the uncertainty of the mean (2σ), the relative standard deviation and MSWD are shown. The continuous lines represent the weighted mean value for each group and the dotted lines delimit their standard uncertainty (2σ). The empty symbols in the plots have not been included in the weighted mean calculation as they are considered outliers.

The mean squared weighted deviations (MSWD) of the He concentration data provide information about the dispersion of the dataset. Schaefer et al. (2016) determined the homogeneity of the ^{3}He concentration of CRONUS pyroxene standard (< 2% for sample masses 10-55 mg), therefore the MSWD of the three sets of experiments is an indicator of the precision of the technique. Heating unencapsulated samples with the CO_2 laser yielded a MSWD of 8.8 indicating over-dispersion of the data regarding the analytical uncertainty. This reflects the difficulty of homogeneously heating the mineral grains with CO_2 laser when the grains are in direct contact with each other, the CO_2 laser is more effective for heating individual grains and it looses degassing capacity as the grains are in contact or form layers due to their poor conductivity (Bard et al., 2014). Diode laser heating of encapsulated and unencapsulated samples yielded MSWDs of 0.6 and 1.8

respectively, these values are very close to unity reflecting the robustness of the heating techniques and confirming the appropriate determination of the analytical uncertainties.

The ^{4}He concentrations of the CRONUS pyroxene have MSWD in excess of 200 (Figure 4.4). These may reflect the heterogeneity of the ^{4}He at the sample scale (< 15 mg) caused by small mineral inclusions within the pyroxene grains and/or accessory minerals such as zircons or monazite containing high radiogenic ^{4}He (Schaefer et al., 2016). The ^{4}He released by diode laser heating of encapsulated samples yielded one extremely high concentration, which is considered an outlier. This may be due to ^{4}He released by overheating of the copper pan releasing trapped ^{4}He due to high temperatures (>1400˚C). Two low ^{4}He outliers have been excluded from the CO_2 laser heating data. These could reflect incomplete degassing of the samples. Radiogenic He is released at significantly higher temperature than cosmogenic He in many minerals. In the case of olivine the radiogenic He is released at ~1200˚C whilst the cosmogenic He is typically released below 800˚C (Trull et al., 1991). Heating the CRONUS pyroxene to 1200˚C for 20 minutes typically liberates the cosmogenic and radiogenic He (Blard et al., 2015).

Degassing of ~15 mg of orthopyroxene from the Mount Hampton xenoliths (Chapter 5) using both the ~800 nm lasers revealed that encapsulated samples systematically yielded more cosmogenic ^{3}He than unencapsulated grains (Figure 4.5). This may have been due to difficulty in heating the unencapsulated grains due to absorption of the laser energy by melted pyroxene deposited onto the coverslip during heating. Encapsulation of samples avoids this effect producing more reliable results.

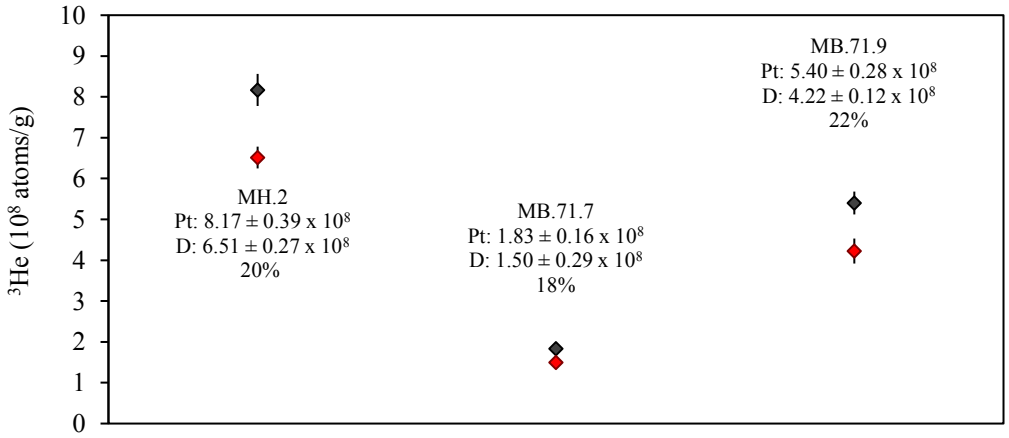

Figure 4.5. Plot of ^{3}He concentrations from orthopyroxene from Mount Hampton xenoliths. The samples heated directly with the 800 nm laser (red diamond, D) released 18-22% less ^{3}He than those encapsulated in Pt packets (black diamond, Pt).

Diode laser heating of unencapsulated grains seemed to be a reliable technique to fully degas CRONUS pyroxene samples but failed to completely degas other natural samples due to sputter of material onto the coverslip. Diode laser heating of encapsulated minerals in Pt packets seems to be the most consistent technique for complete degassing pyroxene samples of ~15 mg with a precision of 0.4 % and a MSWD close to unity. Therefore this has been the preferred technique for the analysis of small samples used in this research (i.e. Mount Hampton xenoliths).

4.4.2.Olivine

Olivine cannot be heated directly by the near visible wavelength diode lasers. I have tested three different laser degassing methods: (1) diode laser heating of olivine grains mixed with degassed pyroxene which acts as a flux transferring heat to the olivine (Foeken et al., 2009a), (2) diode laser heating of grains encapsulated in Pt packets and (3) Direct CO_2 laser heating of olivine grains.

For this study olivine from the MH.2 xenolith ($^3He/^4He$ ~1,500 R_A) from Mount Hampton (Chapter 5) was used in order to test the degassing ability of the three methods. Aliquots of 3 to 30 mg were used for the experiments. This yielded low ^4He beams (~10^9 atoms); which were the same order of magnitude as the blank (the low ^4He concentrations are consequence of no radiogenic ^4He present in the samples as they are inclusion-free xenocrysts). The high ^3He intensities (>10^7 atoms), consequence of long exposure at high latitude and altitude, are three orders of magnitude higher than the blank (^3He and ^4He data are compiled in table 5.4). For this reason only ^3He is considered for assessing the degassing effect of the three different methods: (1) diode laser heating of olivine plus pyroxene flux, 20 W for 30 minutes at ~80% power (analysed using the MAP 250-15, Appendix A); (2) minerals encapsulated in Pt packets, heated by diode laser at 20 W for 30 minutes, and (3) direct heating CO_2 laser at 22 W for up to 40 minutes, the amount of ^3He released by degassing using this technique does not increase with time (Figure 4.6).

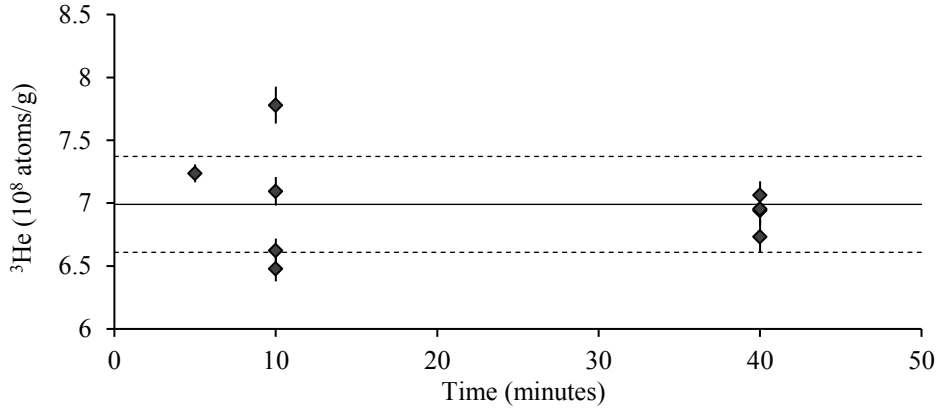

Figure 4.6. Plot of ^{3}He concentrations from MH.2 olivine heated using 25 W CO_2 laser for between 5 and 40 minutes. The continuous line represents the average and dotted line delimits the uncertainty (1σ). The concentration of ^{3}He (6.99 ± 0.38 x 10^8 atoms/g, n=8) yielded by heating is independent of heating time.

^{3}He concentrations released using the three degassing techniques are compared in Figure 4.7 (He isotope data are reported in Appendix B). In this case, the absolute amount of cosmogenic ^{3}He released from the samples is unknown. Therefore, repeated analyses of several aliquots are required in order to accurately calculate $^3He_{cos}$ concentration in the sample and assess which degassing method is the most adequate to fully degas olivine grains. The three degassing methods yielded MSWD values higher than unity, ranging from 4.5 when heating encapsulated minerals to 10.8 for CO_2 laser heating. Therefore, the uncertainty of the different datasets has to be inflated in relation to the distribution of the data in order to provide an accurate estimation of the uncertainty. To calculate a more accurate uncertainty the 2σ uncertainty of the weighted mean is multiplied by the square root of the MSWD to account for the over-dispersion of the data.

Diode laser heating of encapsulated grains yielded a weighted mean ^{3}He concentration of 7.91 ± 0.36 x 10^8 atoms/g. This represents the highest $^3He_{cos}$ concentrations with the lowest 2σ uncertainty (4.6 %) suggesting that this is the most appropriate method for complete degassing of olivine in comparison with the other two methods. This is coherent with the findings from the analysis of CRONUS pyroxene standard. The olivine plus pyroxene flux released ~85% of the ^{3}He released from the previous method; with a weighted mean concentration of 6.71 ± 0.38 x 10^8 atoms/g and the CO_2 laser heating of unencapsulated olivine sample released 88% of the ^{3}He released from diode laser heating of encapsulated grains, with a weighted mean concentration of 6.98 ± 0.85 x 10^8 atoms/g (uncertainties reported as 2σ).

Adding pyroxene flux to olivine grains seems to not completely degas the olivine grains. The idea of this technique is based on heat transfer from melted pyroxene covering olivine grains. It seems that the poor thermal conductivity of the minerals leave the interior of the olivine grains at lower temperature than that necessary to diffuse out all the cosmogenic ^{3}He. When analysed the remaining material after laser heating under a binocular microscope it is observed that some of the grains underneath the melted pyroxene are still intact suggesting that those grains may not have reached enough temperature to completely release all the $^{3}He_{cos}$ in the mineral lattice. In the case of CO_2 laser it seems that the grains have not achieved the required temperature to completely diffuse out all the cosmogenic ^{3}He. The temperature loss produced by the contact between mineral grains could be the main cause of incomplete degassing and high dispersion of the data. Helium diffusion in olivine requires 15% higher temperature than in pyroxene (965-1385˚C in olivine and 770-1170˚C in pyroxene, Trull, 1989; Trull and Kurz, 1993), it is this 15% increase what makes the difference between fully degassing pyroxene using CO_2 laser and not fully degassing olivine with the same technique. Diode laser heating of encapsulated samples simulates the effect of a furnace producing homogenous heating of the sample. The temperature reached by the interior of the packet is ~1300˚C as inspection of the packets under binocular microscope after laser heating of pyroxene confirmed that the mineral grains inside have been melted. This assures that the olivine within the Pt packets can reach enough temperature to be completely degassed. Added to this, the dataset generated by this method is the most precise with 4.6% 2σ uncertainty. These reassure the validity of the method and the accuracy of the ^{3}He concentration.

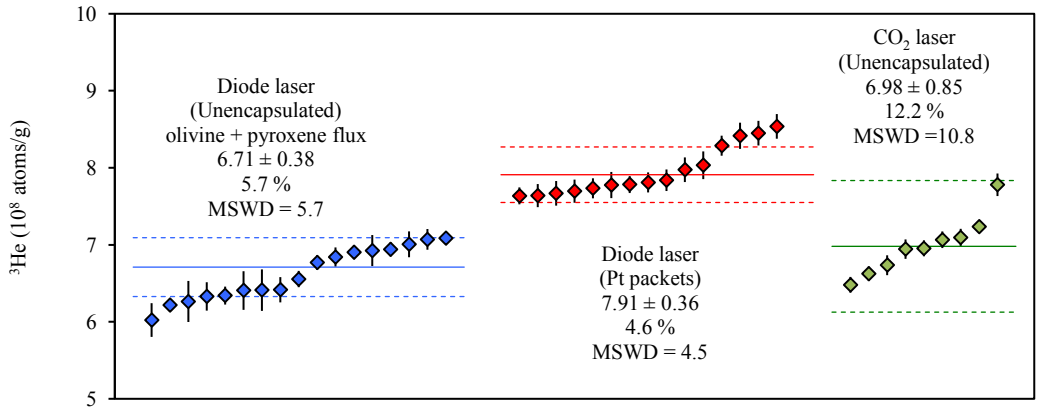

Figure 4.7. Plot of ^{3}He concentrations from MH.2 olivine degassed using: (1) mixed with degassed pyroxene flux heated with a 25 W 808 nm diode laser measured in the MAP 250-15 (blue); (2) encapsulated in Pt packets and heated with a 74 W 800 nm diode laser (red) and (3) heated directly with a 25 W CO_2 laser (green). Analytical uncertainties are at 1σ. The weighted mean, the inflated uncertainty (2σ), the relative standard dviation and MSWD are shown. The continuous lines represent the value of the weighted means for each individual group and the dotted lines delimit their inflated (x $MSWD^{1/2}$) 2σ uncertainties.

Figure 4.8 shows the ^{3}He concentration from the three different degassing methods for sample weights smaller than 30 mg. The data shows that when using the diode laser in unencapsulated sample plus pyroxene flux and the CO_2 laser, the techniques fail on fully degas the samples independently of the weight of the sample. The samples are complete degassed only when encapsulated in Pt packets and heated with the diode laser. The weight of the sample is constrained by the Pt packet size and it is up to 15 mg.

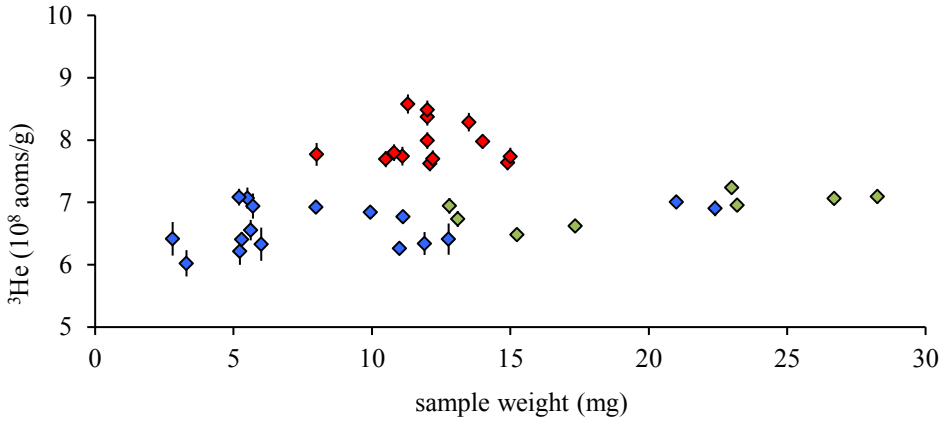

Figure 4.8. ^{3}He concentrations from MH.2 olivine plotted against sample weight degassed using three different techniques: (1) unencapsulated minerals mixed with degassed pyroxene flux heated with a 25 W 808 nm diode laser (blue); (2) minerals encapsulated in Pt packets and heated with a 74 W 800 nm diode laser (red) and (3) unencapsulated minerals heated with a 25 W CO_2 laser (green). Analytical uncertainties are 1σ.

4.5. Mineral standards

Determining the precision of the measurement of cosmogenic He exposure age requires an assessment of all the analytical factors that govern the He concentration in minerals. This is not completely quantified by, for instance, mass spectrometric analysis of repeated measurements of the He standard. The two mineral samples used for the degassing experiments (previous section) can be legitimately assumed to have homogenous cosmogenic He distribution. Repeated analysis of them will provide a way to quantify the effect of the random uncertainty introduced by sample weighing, partial He extraction and variability in blank correction.

4.5.1. CRONUS pyroxene standard

In order to assess the reproducibility of the methodology for analysis of natural samples a series of CRONUS pyroxene standard 12 aliquots of 10-19 mg have been analysed. The samples were encapsulated in Pt packets and degassed using a diode laser, the data collected are regressed to time zero and blank corrected (Figure 4.9).

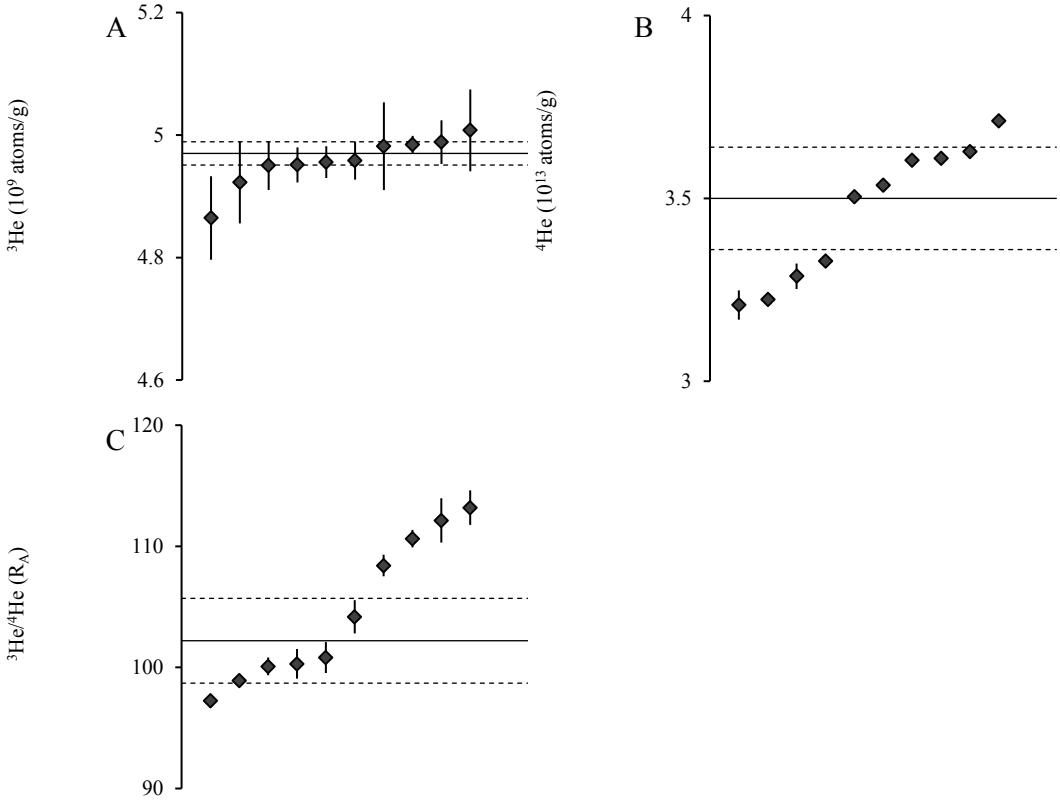

Figure 4.9. (A) ^{3}He concentration, (B), ^{4}He concentration and (C) ^{3}He/^{4}He ratio of CRONUS pyroxene standard degassed using a diode laser to heat encapsulated samples. Continuous line represents the value of the weighted mean and the dotted line delimits the 2σ uncertainty.

The weighted mean and 2σ uncertainties of ^{3}He and ^{4}He concentrations are 4.97 ± 0.02 x 10^9 and 3.52 ± 0.09 x 10^{13} atoms/g respectively. The average ^{3}He/^{4}He is 102.2 ± 3.5 R_A. These values are in agreement with the published global average (^{3}He 5.02 ± 0.12 x 10^9 atoms/g, ^{4}He 3.60 ± 0.18 x 10^{13} atoms/g, ^{3}He/^{4}He = 102 ± 4 R_A) (Blard et al., 2015). The datasets from the different laboratories that participated to the inter-laboratory comparison and the data obtained from this work are compiled in Figure 4.10 (data used for this compilation are reported in Appendix B).

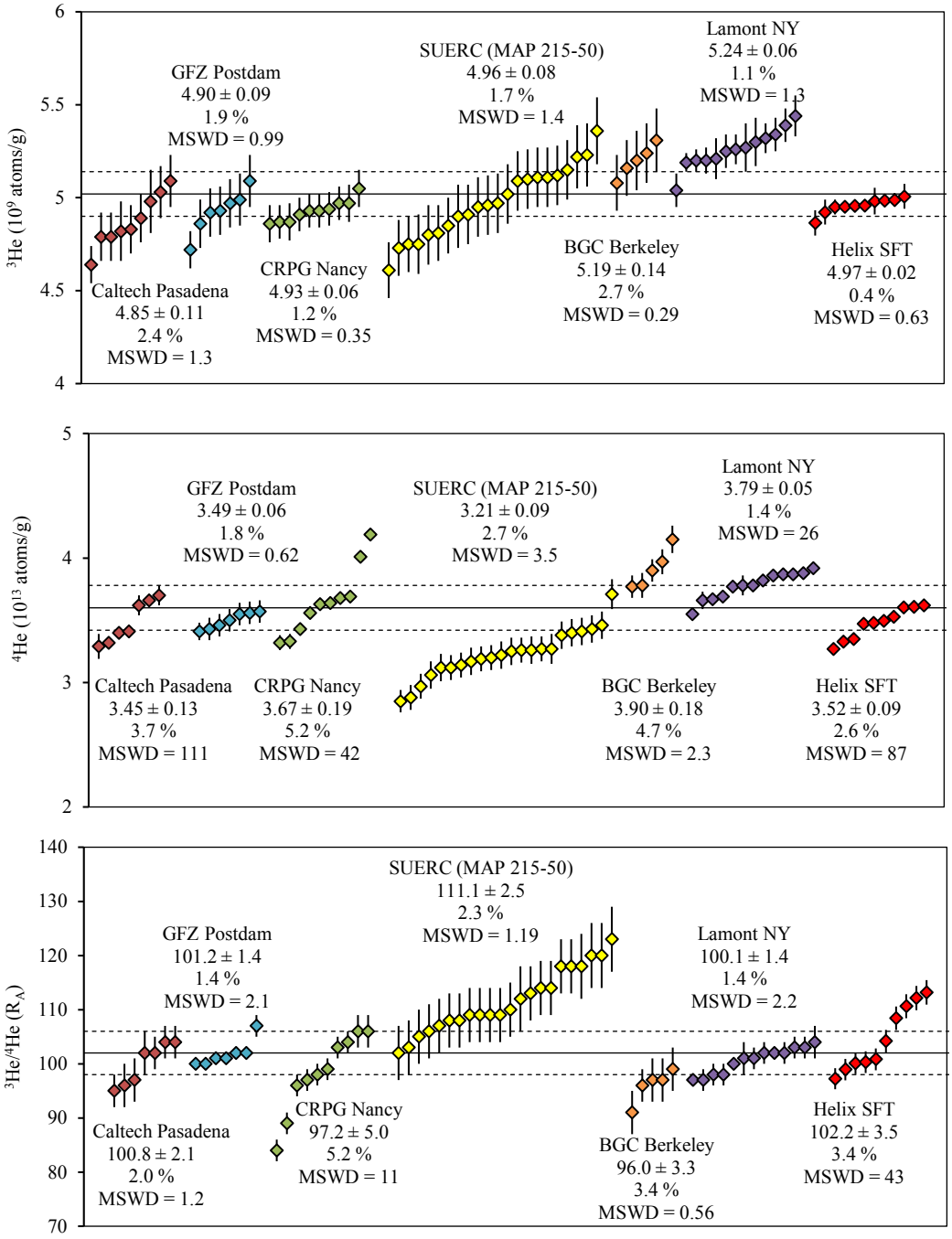

Figure 4.10. Compilation of the CRONUS pyroxene helium isotope data from six different laboratories (Blard et al., 2015) including the results from this study (red diamonds). For each laboratory the weighted mean, the uncertainty of the mean (2σ), the relative standard deviation and MSWD are given. The continuous line represents the value of the reported global average (Blard et al., 2015) and the dotted line delimits the uncertainty (2σ).

The ^{3}He concentrations obtained from this work overlap the average and show that the precision to which we can measure low mass samples with the diode laser and Helix SFT is consistent with global average (Blard et al., 2015). The analysis of CRONUS pyroxene with the Helix SFT at SUERC yielded the most precise ^{3}He dataset amongst all the laboratories with a 2σ uncertainty of 0.4% and a MSWD of 0.6. The dataset of ^{4}He concentrations showed an over dispersion of 2.6% with a MSWD of 87 and consequently the ^{3}He/^{4}He dataset showed an over dispersion of 3.4% with a MSWD of 43. The scatter in

the ^{4}He data is most likely caused by small mineral inclusions within the pyroxene grains and/or accessory minerals such as zircons or monazite containing high radiogenic ^{4}He (Schaefer et al., 2016) and the extremely high MSWD is also a consequence of the high precision to which ^{4}He can be measured with the Helix SFT (0.22%, see Chapter 3) leading underestimation of the uncertainty of the individual measurements when analysing natural samples.

Heating of encapsulated samples of ~15 mg with a diode laser has proven to be the technique that produces the most reproducible dataset. Laser degassing of samples consists of heating each sample on its own individual well in contrast with the furnace where the same volume is used to heat several samples, one at the time, increasing the chances of residual gas being released from degassed samples in the furnace volume. Dataset produced at SUERC in the MAP 215-50 show higher ^{3}He dispersion than this work and generally lower ^{4}He concentrations. In that case, unencapsulated samples were degassed for 5 minutes using a diode laser (Blard et al., 2015) leading to higher dispersion possibly produced by random partial degassing of samples (see section 4.4.1). This effect is avoided by encapsulating the samples in Pt packets.

The weight of the sample used for the analysis of CRONUS pyroxene standard from all the laboratories varies between 2 to 100 mg with the majority of the laboratories analysing samples of 10 to 25 mg (Figure 4.11).

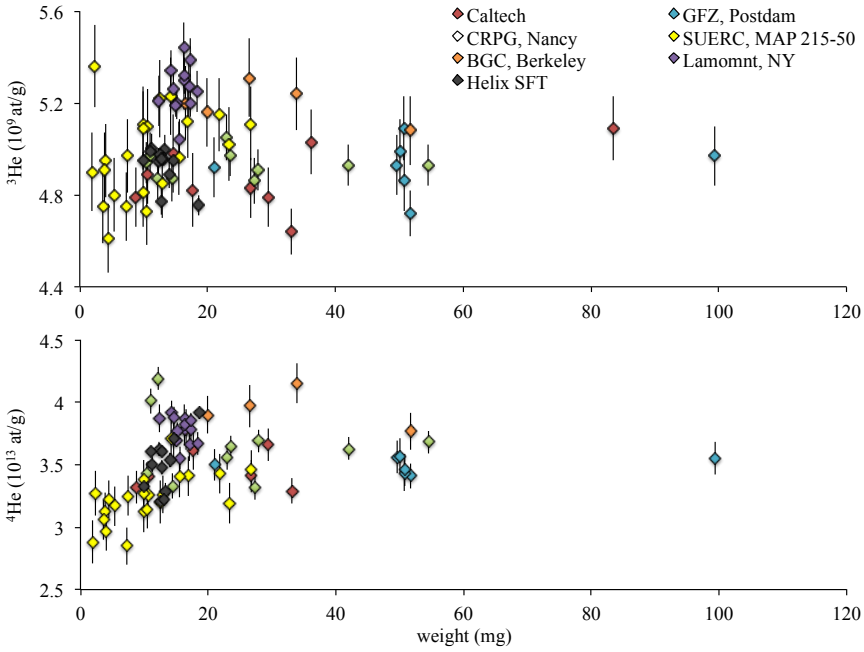

Figure 4.11. Plot of the CRONUS pyroxene helium isotope data from six different laboratories (Blard et al., 2015) including the results from this study (grey diamonds) against sample weight.

The weight of the sample does not seem to be associated with any variation on the concentration of ^{3}He revealing the homogeneity of the CRONUS pyroxene as shown by Schaefer et al. (2016). ^{4}He is more variable with smaller samples (< 15 mg) yielding generally lower ^{4}He and more disperse concentrations; which agrees with the recommendations of Schaefer et al. (2016) of using preferably samples of weight > 15 mg to avoid high ^{4}He dispersion.

4.5.2. MH.2 olivine

One study of my PhD consists of the analysis of crystals from peridotite xenoliths from Mount Hampton (Chapter 5). The xenoliths contain homogeneous high purity inclusion-free crystals with ^{3}He/^{4}He up to 10,000 Ra, indicating that all the ^{3}He is cosmogenic. In order to quantify how well the He concentration can be measured in olivine for this study, I have used repeated measurements of He in inclusion-free olivine crystals from the MH.2 xenolith. The results obtained from the analysis of 15 aliquots of 8-15 mg of the MH.2 olivine sample are shown in Figure 4.12 and compiled in Table 4.2. All samples were encapsulated in Pt packets and degassed using a diode laser.

For this study only ^{3}He concentrations have been considered. ^{4}He is highly variable (0.5 to 30 x10^{11} atoms/g) reflecting subtle variation in the radiogenic and magmatic He concentrations (see Chapter 5 for further details). The high ^{3}He concentrations (7.6 to 8.5 x 10^{8} atoms/g) yield ^{3}He/^{4}He ratios that are 200 to 10,000 times the air ratio. The results are normally distributed with a weighted mean and 2σ uncertainty that accounts for data over-dispersion (x MSWD$^{1/2}$) of 7.91 ± 0.36 x 10^{8} atoms ^{3}He/g and MSWD of 4.5.

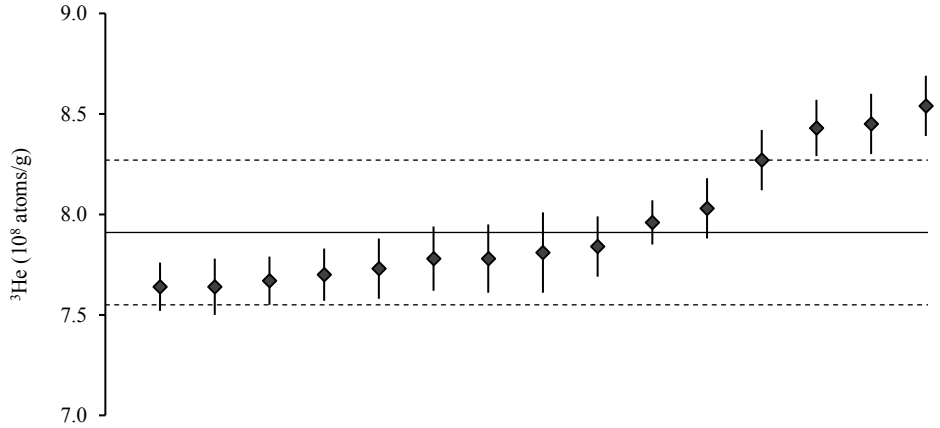

Figure 4.12. Variation in the ^{3}He concentration of 15 aliquots of MH.2 olivine standard degassed using a diode laser to heat encapsulated samples. The continuous line represents the value of the weighted mean and the dotted line delimits the uncertainty (2σ).

Table 4.2. Helium isotope results from the analysis of 15 aliquots of MH.2 olivine. All the ^{3}He is assumed to be cosmogenic. Uncertainties reported are the propagated 1σ.

Weight (mg)	*^{4}He (10^{11}at/g)*	±	*^{3}He (10^{8} at/g)*	±	*^{3}He/^{4}He (R_A)*	±
14.9	0.51	0.01	7.64	0.12	10693	245
17	2.25	0.27	7.64	0.14	2032	40
15	0.47	0.01	7.67	0.12	11543	279
12.2	1.1	0.03	7.70	0.13	5001	157
10.5	2.74	0.33	7.73	0.15	2032	40
15	4.94	0.59	7.78	0.16	1131	23
11.1	4.57	0.54	7.78	0.17	1227	26
8	7.59	0.91	7.81	0.2	740	19
10.8	7.28	0.87	7.84	0.15	775	20
14	1.16	0.01	7.96	0.11	4902	101
12	4.4	0.53	8.03	0.15	1312	26
13.5	5.25	0.02	8.27	0.15	1469	33
12	28.52	0.1	8.43	0.14	211	4
12	30.3	0.06	8.45	0.15	202	3
11.3	1.21	0.02	8.54	0.15	5130	138

The over-dispersion of ^{3}He results related to the analytical uncertainties observed for MH.2 olivine is in contrast with the observations from CRONUS pyroxene were the dispersion of the dataset was in agreement with the analytical uncertainties. The over-dispersion of the MH.2 olivine accounts for random uncertainty due to potential differences in the degassing of the samples. The higher He diffusion temperature in olivine with respect to pyroxene could be the source of the observed dispersion. Comparing the amount of ^{3}He released from each sample with the sample weight (Figure 4.13) there is no clear evidence that partial degassing of samples is associated with the weight of the sample as the samples yielding the highest ^{3}He concentrations are those of middle range masses (11 to 14 mg). Slight variations on shape of the Pt packets could lead to differences in reflectivity and coupling with the laser causing differences on the maximum temperature reached by the sample. The shape of the packet could also influence the amount of Pt surface that is in contact with the copper pan affecting the amount of heat loss. These effects are not as noticeable when degassing pyroxene due to the lower He diffusion temperature. The 4.5% uncertainty calculated for the weighted mean accounts for this effect and therefore it defines how well encapsulated olivine samples can be degassed with a diode laser and measured with the Helix SFT.

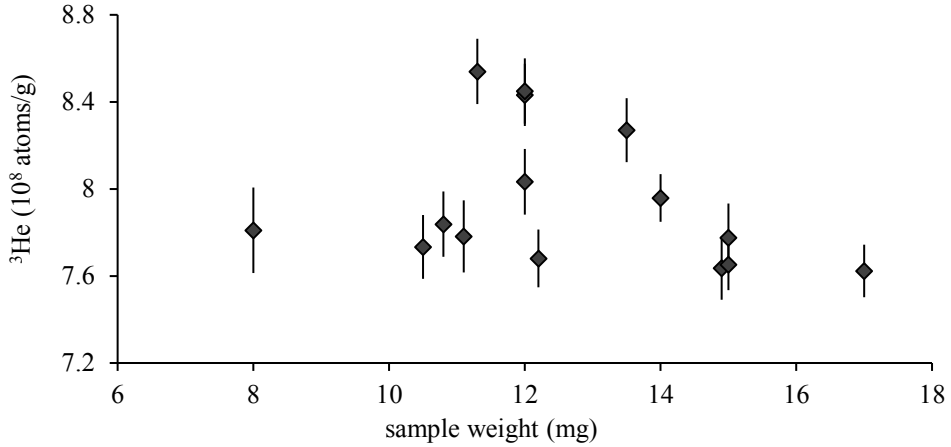

Figure 4.13. Plot of the MH.2 olivine ^{3}He data against sample weight

4.5.3. Measurement uncertainty

The analysis of several aliquots of CRONUS pyroxene mineral standard and MH.2 olivine has revealed a potential source of random uncertainty caused by the shape of the Pt packets influencing the temperature achieved by the sample and consequently the total degassing of the minerals. Therefore, it is imperative for accurate estimation of the uncertainty to incorporate this random uncertainty to the analytical uncertainty. The ability to reproduce a measurement of a natural sample sets the limits to how well a single measurement can be performed. In this case, the precision achieved using the diode laser on encapsulated samples (0.4% and 4.6% at 2σ for pyroxene and olivine respectively) is amongst the best cosmogenic ^{3}He can be measured and with the current uncertainties in production rates and scaling factors (10-15%; Balco et al., 2008) the final interpretation of the results will not be affected by the measurement uncertainty.

To assess the consistency of the ^{3}He uncertainty the data obtained from pyroxene and olivine analyses have been normalized to the weighted mean and compared with the different sample weights used. Figure 4.14 shows the CRONUS pyroxene helium isotope data normalized to the weighted mean for the different sample weights used (10 to 15 mg). The results show the internal consistency with 0.4% 2σ uncertainty for ^{3}He concentrations. The results for ^{4}He concentrations show higher scatter with 4.0% 2σ uncertainty of the weighted mean and reflect the over-dispersion of the data with respect to the analytical uncertainties. Since the ^{4}He concentrations in CRONUS pyroxene standard are heterogeneous due to variable amounts of radiogenic ^{4}He (Schaefer et al., 2016) the uncertainty of ^{3}He (± 0.4%) defines how well a single pyroxene aliquot of weight < 15 mg

can be degassed with a diode laser when encapsulated in Pt foil and measured with the Helix SFT.

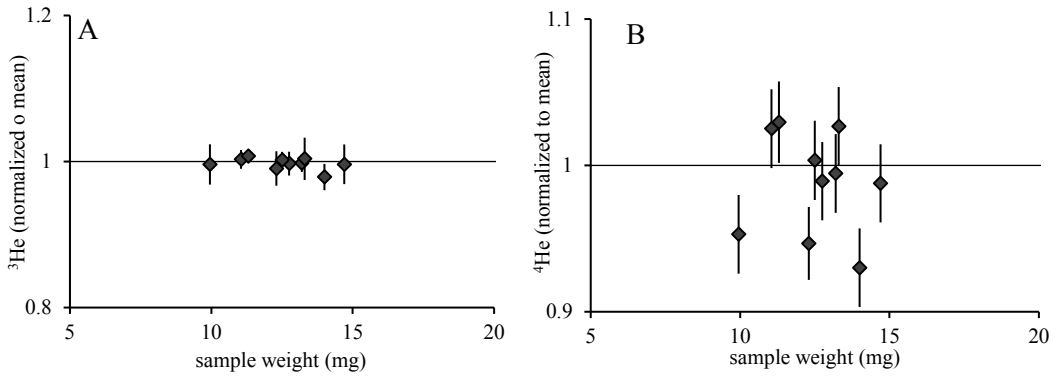

Figure 4.14. (A) ^{3}He and (B) ^{4}He of CRONUS pyroxene normalized to the weighted mean relative to sample weight with 2σ uncertainties.

In the case of olivine, the ^{3}He data from MH.2 have been normalized to the weighted mean for the different sample masses used (8 to 15 mg) and the uncertainties considered include the over-dispersion of the data by multiplying the uncertainty by the square root of the MSWD. The results show internal consistency of 4.6% (2σ), which includes the random uncertainty related to the shape of the packets (Figure 4.15). This suggests that the analysis of ^{3}He of single olivine aliquots have an uncertainty no better than ± 4.5% when degassed with a diode laser encapsulated in Pt foil and measured with the Helix SFT.

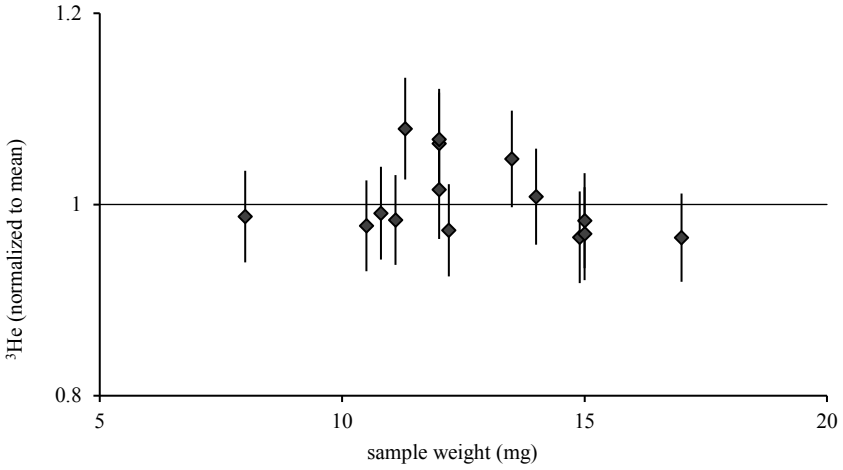

Figure 4.15. Variation of ^{3}He in MH.2 olivine normalized to the weighted mean with 2σ uncertainties including the over-dispersion of the data (xMSWD$^{1/2}$).

4.5.4 Summary

Analysis of CRONUS pyroxene standard validates the analytical technique showing that for homogeneous samples of ~10^9 atoms/g ^{3}He concentrations they can be measured with a precision of 0.4% (2σ uncertainty). The results demonstrate that the Helix SFT at SUERC is capable of producing data that are as accurate and precise as other mass spectrometer in other laboratory in the world.

The analysis of MH.2 olivine determines the precision to which we can measure He from olivine samples. With 2σ uncertainty of 4.6% sets a limit to how well we can measure single olivine aliquots. The higher uncertainty of the MH.2 olivine standard is a consequence of the difficulty of completely degassing olivine grains. Our ability to reproduce any measurement depends on the ability to fully degas the sample, which is related to the sample mineralogy because of the differences on the diffusion temperature of $^3He_{cos}$ in different minerals.

Using a diode laser to degas up to 20 mg of encapsulated mineral has proven a useful technique yielding low blanks and generating high precision data from high ^{3}He concentration mafic minerals. Therefore, this is the technique used for degassing the mineral samples from Mount Hampton for $^3He_{cos}$ analysis (the results are presented in Chapters 5 and 6).

Cosmogenic He has proved useful for determining the exposure age of Quaternary basaltic volcanism when other techniques (e.g. ^{14}C) cannot be applied (Craig and Poreda 1986, Ammon et al., 2009; Foeken et al., 2009b; Marchetti et al., 2014; Espanon et al., 2014; Heineke et al., 2016). Typically this work is done on olivine and pyroxene phenocrysts. The low cosmogenic ^{3}He concentration requires significantly larger sample masses (0.5 to 2g) than measured in this section, and degassing is usually facilitated by double-walled furnaces. In the next section I test the ability of laser extraction for degassing He from olivine and pyroxene from Holocene basalts from Western Turkey.

4.6. Case study 1: surface exposure dating of Holocene basalts

Determining the eruption age of Holocene lava flows is essential for understanding the temporal history of volcanic activity that may pose a hazard to indigenous populations. In the Kula Volcanic Province (KVP, Figure 4.16) in Western Turkey the most recent volcanism appears to have occurred in the last ~10 ka (Westaway et al., 2004, 2006; Heineke et al., 2016). While the age of all most recent phases of volcanic activity in the populated KVP have not been determined, the low erosion rate, the preservation of uneroded lava tops and the availability of pyroxene and olivine phenocrysts makes the province a useful natural laboratory for employing the ^{3}He exposure dating technique and testing the laser extraction. The production rate of cosmogenic ^{3}He in the Kula region (~700 m, 38˚N, 28˚E) (similar to that at SLHL, 120 atoms/g/year, Goehring et al., 2010) combined with Holocene flow ages (e.g. Westaway et al., 2004, 2006; Heineke et al., 2016) suggests that a minimum of 200 mg of olivine/pyroxene is required to generate 10^{5} atoms of ^{3}He.

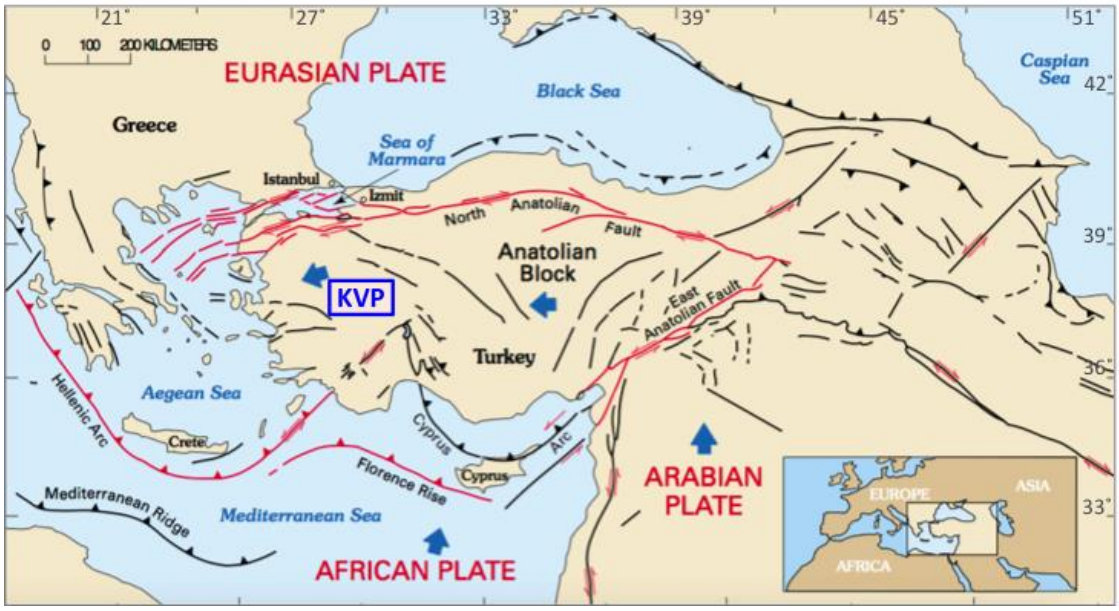

Figure 4.16. Map showing the location of the Kula Volcanic Province (KVP) and the main faults and trenches (modified from Holzer, 2000)

4.6.1. Introduction

The KVP is part of the Aegean-Western Anatolia Volcanic belt. The region is in extension in response to forces generated from the subduction of the African plate beneath its southern margin (Meijer and Wortel, 1997). The magmatism in the area developed in

three distinct phases of volcanic activity. The oldest phase, from Early to Mid Miocene, consists of tuffs and ignimbrites associated with lava domes, flows and volcanic breccias (Yanev et al., 1998). A second volcanic cycle occurred approximately 6 Ma after and consists mainly of alkali basalt flows (Robert et al., 1992). The most recent phase occurred during the Late Pliocene and Quaternary when basaltic volcanism emanates from monogenetic cinder cones. It consists of lava flows, generally of aa-type, and pyroclastics that rest on a sequence of thin and wide lava flows forming a basal plateau (Innocenti et al., 2005). The KVP covers an overall surface of ~200 km^2 with an estimated volume of eruption products of ~2.5 km^3 (Bunbury et al., 2001).

The latest volcanic phase of the KVP is subdivided in three different groups (β2-β4) based on similar geomorphological style (i.e. weathering and stratigraphic age) of the basalts (Hamilton and Strickland 1841, Canet and Jaoul, 1946, Richardson-Bunbury, 1996 and references therein). The β2 group extends mostly over the eastern part of the volcanic field with ages of 1.3-0.9 Ma (Westaway et al., 2004, 2006) and originated prior to the incision of the modern Gediz gorge. The estimated volume of this volcanism is ~0.5 km^3 (Bunbury et al., 2001). The younger β3 basalts (240-80 ka, Westaway et al., 2004, 2006) typically show well-developed soils that may be used for agriculture and occupy the largest area of the Kula volcanic field with a volume together with β4 basalts of ~2 km^3 (Bunbury et al., 2001). The β4 basalts appear fresh in the field and are the youngest of all the groups. Several studies have dated the most recent volcanism in the KVP. Ercan et al. (1985) reported K-Ar ages of 25 ± 6 ka for β4 basalts. Based on recalculation of K-Ar ages, geological evidence and the absence of historical records of volcanism around Kula, Westaway et al. (2006) suggested that eruption of these flows occurred until late Holocene (7 ± 2 ka). Based on luminescence dating of fluvial sediments an age of 3 to 2.6 ka was obtained for a lava flow near the locality of Kula (van Gorp et al., 2013). The most recent dating study applied cosmogenic ^3He exposure dating of several lava flows across the KVP, the data suggested that the β4 basalts erupted only over the last 3 ka (Heineke et al., 2016) and that the β3 phase occurred up until 11 ka contrary with what was suggested by previous studies (Westaway et al., 2004, 2006). Westaway et al. (2004, 2006) based on K-Ar ages of some flows around the Gediz river proposed a shorter time span for the β3 flows with ages ranging from ~240 ka to ~80 ka and older starting age for the β4 flows ~60 ka (Westaway et al., 2004) with the youngest volcanism occurring in the last 7 ± 2 ka (Westaway et al., 2006).

4.6.2. Sample sites and description

Fieldwork was performed in order to collect samples from different lava flows from the most recent eruption phase (β4) in the KVP with the use of satellite images the main volcanic cones were identified. For this study five different lava flows from three volcanic cones have been studied (Figure 4.17).

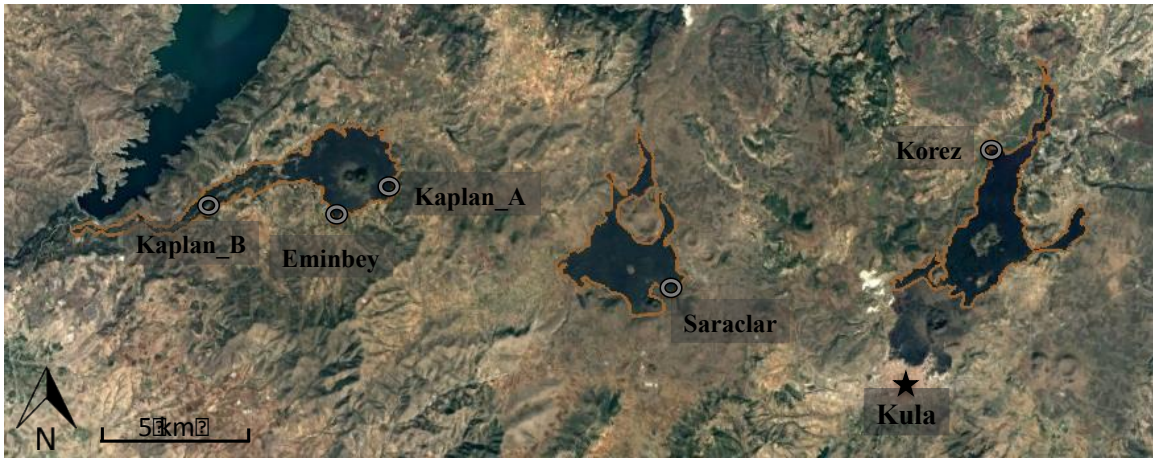

Figure 4.17. Satellite image of the Kula Volcanic Province showing the location of the samples used in this study. The city of Kula is indicated for geographical reference.

All the flows sampled are aa-type consisting on basanites containing olivine and pyroxene phenocrysts. All the samples were taken from well-preserved surfaces with topographic shielding less than 10º. The samples were named according to their proximity to different villages and were taken from different lava flows identified by field inspection. Figure 4.18 shows field photographs of the sampled areas. The high level of preservation of the surfaces studied lead to classify all the basalts sampled as part of the β4 volcanic phase (Figure 4.18b-f) and only one of the flows sampled (Kaplan_B) showed some vegetation with no signs of agriculture development (Figure 4.18a). Therefore all the samples can be considered to be part of the β4 volcanic phase based on the classification of Richardson-Bunbury (1996). Samples Kaplan_A, Eminbey and Kaplan_B correspond to different flows with Kaplan_B being identify as the oldest of the three based on field observations. Saraclar sample was collected from a sub-horizontal surface at the base of the cone. Korez sample was taken from ~8 km North from the city of Kula in the eastern part of the volcanic area.

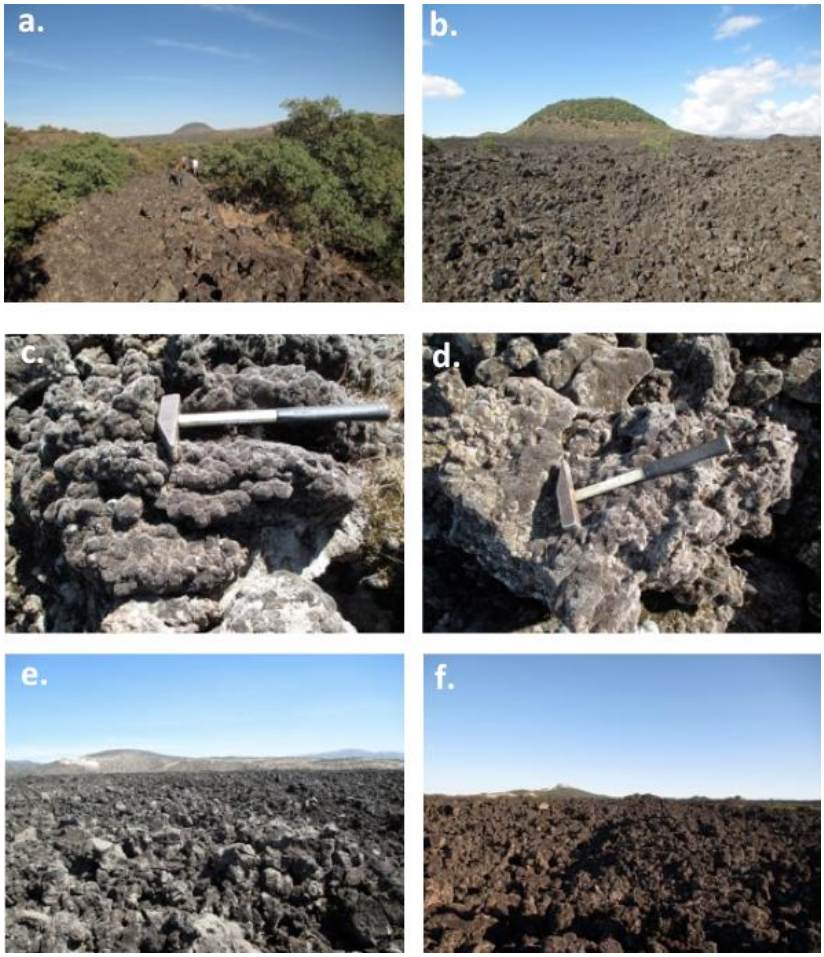

Figure 4.18. Photographs of some of the sites and well-preserved aa lava surfaces sampled. (a) Kaplan_B lava flow. (b) Kaplan_A lava flow. (c) Aa surface sampled from Kaplan_A flow. (d) Aa surface sampled from Eminbey lava flow. (e) Saraçlar flow. (f) Körez flow.

4.6.3. Sample preparation and analytical techniques

Pyroxene and olivine phenocrysts of 500 to 1000 μm were separated from crushed samples by hand picking. The mineral concentrates were ultrasonically cleaned in 20% HNO_3, distilled water and finally in analar acetone. Samples of approximately 600 mg were crushed in an all-metal hydraulic crusher to separate the magmatic ^3He component (see Appendix B for description of the crushing technique). Data from the crushing step are shown in Table 4.3.

Table 4.3. Data of $^3He/^4He$ ratios from crushing experiments of n.4 olivine samples from KVP. An average $^3He/^4He$ ratio is calculated and presented in this table. Uncertainties are reported as propagated 1σ.

Sample name	*Mineral*	*^4He (10^{11}atoms)*	±	*$^3He/^4He$ (R_A)*	±
Körez	ol	1.044	0.015	7.71	0.31
Saraclar	ol	2.487	0.035	7.88	0.22
Kaplan_B	ol	0.457	0.006	7.3	0.45
Eminbey	ol	0.457	0.006	7.44	0.43
Average				***7.58***	***0.26***

The $^{3}He/^{4}He$ ratios obtained from crush extraction agree within 1σ uncertainty yielding an average of 7.58 ± 0.26 R_A; which reflects the mantle origin of the magmatic source. The data are consistent with an asthenosphere source, rather than lithosphere source (Kurz et al., 1982). This is in agreement with the average 7.67 ± 0.10 R_A reported by Heineke et al. (2016). These data confirm the findings of Alici et al. (2002) that characterised the Quaternary volcanism in Kula as associated with thinning of the lithosphere and upwelling of asthenospheric melts with the lavas not experiencing significant contamination on their way to the surface. The average $^{3}He/^{4}He$ ratio from crushing is used to quantify the $^{3}He_{cos}$ assuming negligible contribution from the radiogenic component using the following equation (Craig and Poreda 1986, Kurz 1986, see Chapter 2 for details):

$$^{3}He_{cos} = [(^{3}He/^{4}He)_{melt} - (^{3}He/^{4}He)_{crush}] \times {}^{4}He_{melt} \quad [4.1]$$

Semi-quantitative major-element analyses of the mineral separates from four of the samples have been performed using scanning electron microscopy (ISAAC, University of Glasgow). The results are presented in Table 4.4. The olivine separates show high level of homogeneity with ~2% (1 σ) consistency in composition between grains and forsterite contents of Fo_{84-85}. Pyroxene separates show more compositional variability (~10%, 1 σ) with enstatite contents of En_{43-46}.

Table 4.4. Results from semi-quantitative analysis of major-element composition for olivine (ol) and pyroxene (px) separates reported as oxides (wt %). The results are normalised to 100.N 3 to 5 mineral grains were analysed from each sample and the data presented here are the average of 3 measurements per grain. Each grain showed a variability of ~1% (1σ) showing homogeneity throughout the mineral grain.

Sample	*Mineral*	*Na_2O*	*MgO*	*Al_2O_3*	*SiO_2*	*K_2O*	*CaO*	*MnO*	*TiO_2*	*CrO*	*FeO*	*NiO*
Korez	ol	0.24	45.09	-	39.81	-	0.22	0.24	-	-	14.17	0.23
	ol	0.26	43.69	-	39.35	-	0.22	0.29	-	-	16.09	0.11
	ol	0.24	45.46	-	40.05	-	0.20	0.24	-	-	13.63	0.19
	ol	0.23	44.80	-	39.82	-	0.22	0.21	-	-	14.61	0.10
Eminbey	ol	0.22	42.82	-	39.12	-	0.22	0.28	-	-	17.25	0.10
	ol	0.25	45.10	-	39.94	-	0.24	0.19	-	-	14.13	0.15
	ol	0.29	43.96	-	39.69	-	0.19	0.23	-	-	15.44	0.19
	ol	0.25	45.04	-	39.95	-	0.23	0.26	-	-	14.13	0.13
	px	0.89	13.44	8.16	47.77	0.05	22.43	-	1.79	0.25	5.22	-
	px	2.41	13.54	15.35	39.44	1.53	12.51	-	5.60	0.03	9.59	-
	px	2.30	13.94	15.25	39.48	1.73	12.62	-	5.67	0.04	8.97	-
Kaplan_B	ol	0.23	45.43	-	39.87	-	0.23	0.22	-	-	13.88	0.14
	ol	0.25	42.91	-	39.37	-	0.15	0.29	-	-	16.93	0.09
	ol	0.24	44.81	-	39.80	-	0.21	0.19	-	-	14.55	0.19
	px	0.96	13.84	8.51	47.95	0.05	21.66	-	1.67	0.77	4.59	-
	px	0.89	12.04	9.95	45.51	0.05	22.30	-	2.47	0.06	6.73	-
	px	2.43	13.60	15.16	39.59	1.57	12.57	-	5.47	0.06	9.55	-
Saraclar	ol	0.20	45.39	-	39.88	-	0.23	0.21	-	-	13.89	0.19
	ol	0.26	45.13	-	39.89	-	0.27	0.24	-	-	13.99	0.22
	ol	0.22	44.97	-	39.99	-	0.25	0.22	-	-	14.24	0.11
	px	2.28	13.54	15.19	39.48	1.82	12.48	-	5.48	0.03	9.71	-
	px	2.23	13.84	15.14	39.79	1.87	12.47	-	5.28	0.05	9.32	-
	px	0.73	13.27	7.96	47.19	0.03	22.96	-	2.12	0.29	5.45	-

4.6.4. Extraction of cosmogenic ^3He

To generate a measurable ^3He signature ~200 mg of sample are required. The higher weight with respect of the standards challenges the degassing technique. Therefore, three different degassing techniques have been also tested to extract the cosmogenic ^3He from olivine and pyroxene separates from the Kula volcanic province. The different laser procedures described in previous sections have been used and adapted to the higher amounts of mineral used. To avoid sputtering of material onto the coverslip due to the high amount of material (~200 mg) laser cells with wells of 10 mm depth were used. The higher amount of material required rules out the possibility of encapsulate the minerals in Pt packets as the weight of the sample is restricted to ~15 mg and the use of several packets will require 10-15 packets per sample which will imply the use of the laser continuously for ~150 minutes with the risk of releasing atmospheric ^4He trapped in the copper pan leading to underestimation of the $^3He/^4He$ ratios. Therefore, for degassing pyroxene separates, the mineral grains were heated directly using the CO_2 and the 75w 800 nm diode lasers in order to distinguish which technique is more appropriate for such high amount of material. In the case of olivine three methods were employed: direct heating of grains using the CO_2 laser, diode laser heating of unencapsulated grains mixed with degassed pyroxene flux and diode laser heating of encapsulated samples in Mo packets. The choice of a different metal to encapsulate the samples is simply due to availability, Mo and Pt have similar thermal properties and there is no relevant increase in the blank levels ($4.8 \pm 0.9 \times 10^4$ atoms of ^3He).

4.6.4.1 Pyroxene results

Results from the degasing of pyroxene grains from KVP are summarised in Table 4.5 and shown Figure 4.19. Four aliquots from two samples (3 from Kaplan_A and 1 from Eminbey) have been degased using the CO_2 laser for 20 minutes, the remaining samples were degassed using the 75W diode laser and two different heating times were employed (20 and 50 minutes) in order to assess whether longer heating times favour the complete degassing of the samples. Up to 2 consecutive heating experiments were performed per aliquot when CO_2 laser was used. The amount of He released on the second heating step was in all cases lower than the blank or very close to blank level and therefore the amount of He released on the first heating step is considered to be the total He in the sample.

Several aliquots from each sample (with the exception of Korez, only one aliquot was analysed) have been degassed using the diode laser.

Table 4.5. Results from the degasing of pyroxene mineral samples from KVP. Several aliquots of each sample have been analysed. The technique of degassing is specified. The ^{4}He concentration is expressed in 10^{11} atoms/g and the ^{3}He and $^3He_{cos}$ in 10^6 atoms/g. The uncertainties are reported as 1σ.

Sample name	*Degasing*	*Weight (mg)*	*^{4}He*	±	*Blank (%)*	*^{3}He*	±	*Blank (%)*	*^{3}He/^{4}He (R_A)*	±	*$^3He_{cos}$*	±
Kaplan_A	CO_2 laser	85.3	2.42	0.10	3	3.95	0.44	14				
			-	-		-	-					
			2.42	0.10	3	3.95	0.44	14	11.65	1.39	1.37	0.17
Kaplan_A	CO_2 laser	163.9	2.12	0.03	2	2.07	0.22	14				
			0.08	0.17	49	0.20	0.17	141				
			2.12	0.03	2	2.07	0.22	14	6.98	0.74	-	-
Kaplan_A	CO_2 laser	62.3	1.99	0.03	5	2.71	0.55	28				
			0.08	0.02	131	-	-					
			1.99	0.03	5	2.71	0.55	28	9.75	1.99	0.60	0.12
Kaplan_A	Diode laser	193.2	3.41	0.06	3	4.21	0.27	6	8.80	0.59	0.58	0.05
Kaplan_A	Diode laser	224.8	3.45	0.15	3	4.46	0.26	5	9.22	0.68	0.79	0.07
Kaplan_A	Diode laser	196.8	2.54	0.17	4	3.39	0.17	7	9.51	0.79	0.68	0.08
Eminbey	CO_2 laser	186.2	3.43	0.05	1	4.46	0.25	6				
			0.12	0.01	29	0.24	0.13	105				
			3.43	0.05	1	4.46	0.25	6	9.29	0.53	0.81	0.05
Eminbey	Diode laser	202.5	7.69	0.12	1	9.00	0.36	3	8.34	0.36	0.82	0.05
Eminbey*	Diode laser	270	2.10	0.12	4	2.52	0.15	7	8.58	0.73	0.29	0.03
Kaplan_B	Diode laser	210.7	2.11	0.05	5	4.42	0.28	5	14.96	1.01	2.16	0.17
Kaplan_B*	Diode laser	220.2	5.03	0.16	2	5.48	0.19	4	7.76	0.37	0.13	0.01
Saraclar	Diode laser	206.1	0.63	0.04	17	0.98	0.18	23	11.04	2.18	0.30	0.06
Saraclar	Diode laser	146.8	1.21	0.06	13	1.59	0.27	20	9.37	1.67	0.30	0.06
Saraclar	Diode laser	109.4	1.57	0.08	13	1.66	0.33	26				
			-	-		-	-					
			1.57	0.08		1.66	0.33		6.89	1.89	-	-
Korez	Diode laser	124.3	0.20	0.26	90	0.55	0.10	68	19.87	26.54	0.34	0.64

Since the samples are very young and the weight of the sample used is minimal the percentage that the blank represents from the amount of gas released is calculated. All of the samples analysed were heated for 20 minutes apart from * that were heated for 50 minutes. To calculate the concentrations of $^3He_{cos}$ the average ratio from the crush is used (7.58 ± 0.26 R_A; R_A= 1.39 x 10^{-6}); two of the aliquots analysed yielded ^{3}He/^{4}He ratios lower tan the crushed ratio therefore no $^3He_{cos}$ is calculated.

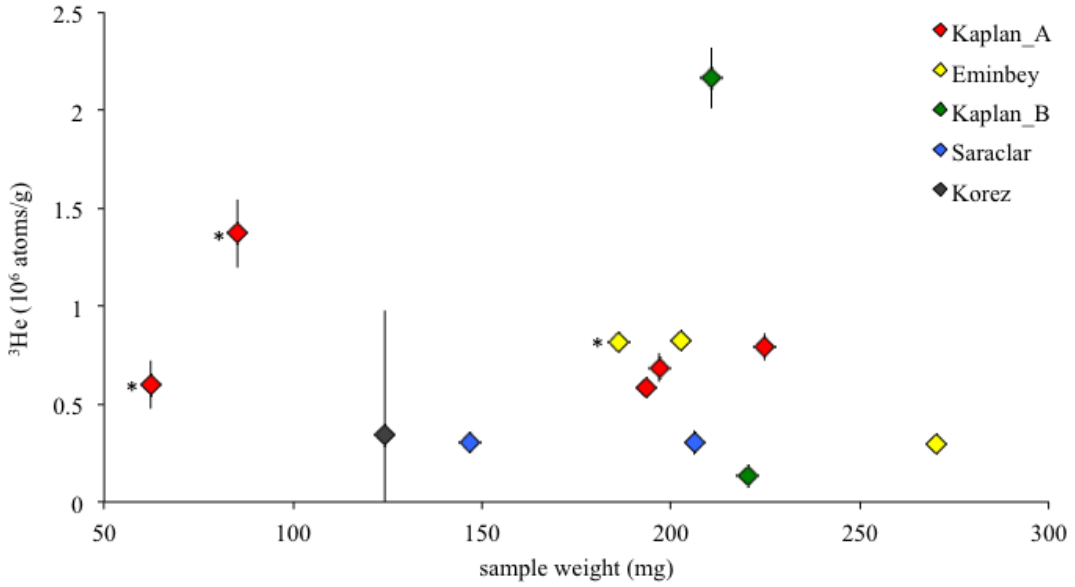

Figure 4.19. Plot of the $^3He_{cos}$ concentration of pyroxene samples against sample weight. All the aliquots were degassed using the diode laser with the exception of * which were degassed using the CO_2 laser.

In the case of sample Kaplan_A, three aliquots were degassed using a CO_2 laser and three using a diode laser. In the case of CO_2 laser heating the results are less consistent than those obtained with the diode laser. One aliquot yielded lower $^3He/^4He$ ratio than the magmatic ratio therefore $^3He_{cos}$ could not be calculated, one aliquot yielded twice as much $^3He_{cos}$ than the concentration measured using the diode laser and a third aliquot yielded $^3He_{cos}$ concentration that agrees with the results obtained from diode laser heating. The consistency on the results from the diode laser heating suggests that the extremely high $^3He_{cos}$ concentration observed in one of the CO_2 heated aliquots is somehow bias (due to high influence of the blank level) and will not be used for age calculations. The blank level of the CO_2 laser represents >14% of the amount of ^3He released by the samples in contrast with the diode laser blank that represents < 7% of the total ^3He causing that the results from CO_2 laser heating are more strongly affected by variability in the blank levels.

Three aliquots from Eminbey sample were analysed, one of which was degassed using the CO_2 laser with the blank representing 6% of the total ^3He released and the $^3He_{cos}$ concentration in agreement with one of the two aliquots degassed using the diode laser, the other aliquot degassed using the diode laser released 35% less $^3He_{cos}$ suggesting that only partial degasing of the sample has been achieved maybe due to the high amount (270 mg) of sample analysed, therefore this result will not be used for age calculations.

Two aliquots from Kaplan_B where analysed, both heated using a diode laser. One of the aliquots was heated over a 20 minutes period and the other was heated for 50 minutes. Both samples released similar amount of ^3He with the one heated for longer time releasing over 2 times the amount of ^4He maybe related to over-heating of the copper pan due to the longer heating time. Consequently the $^3He_{cos}$ calculated from the sample heated for longer is 60% lower that the sample heated for 20 minutes and therefore will not be used for age calculations.

Three aliquots from Saraclar sample were analysed. All the aliquots were heated using the diode laser with the blank level representing >13% and >20% of the total ^4He and ^3He released. One of the aliquots yielded a $^3He/^4He$ ratio below the magmatic ratio and therefore no $^3He_{cos}$ has been calculated. The other two samples yielded $^3He_{cos}$ concentrations that are in agreement within uncertainty.

One aliquot from Korez sample was heated using the diode laser. This sample comes from the most recent lava flow and released low amounts of He with the blank

representing 90% and 68% of the ^{4}He and ^{3}He respectively therefore no meaningful age can be calculated from it.

The diode laser has proved a more robust method for degassing pyroxene of weights > 50 mg although it has a limitation on fully degassing sample weights of > 250 mg. In this study the young age of the samples limits how much the blank level influences the results and therefore it is revealed the difficulty of using laser degassing for cosmogenic exposure age calculation of young basalts.

4.6.4.2 Olivine results

Olivine from three of the samples (Kaplan B, Eminbey and Saraclar) were analysed using three different techniques described above and the results are shown in Table 4.6 and Figure 4.20. Two aliquots from two samples (one from Kaplan_B and one from Eminbey) were wrapped in Mo foil and heated using a diode laser. One aliquot from Eminbey was heated using a CO_2 laser and two aliquots from two samples (one from Kaplan_B and one from Saraclar) were mixed with pyroxene flux and heated with the diode laser. Up to 2 consecutive heating experiments were performed per aliquot (except in the case of Saraclar). The amount of He released on the second heating step was in all cases lower than the blank or very close to blank level and therefore the amount of He released on the first heating step is considered to be the total He in the sample.

Table 4.6. Results from the degasing of olivine mineral samples from KVP. Several aliquots of each sample have been analysed. The technique of degassing is specified, CO_2 laser is used directly on the mineral grains and diode laser requires the adding of pyroxene flux or encapsulating the grains in Mo packets. The ^{4}He concentration is expressed in 10^{11} atoms/g and the ^{3}He and $^3He_{cos}$ in 10^6 atoms/g. Uncertainties are reported as 1σ.

Sample name	*Degasing*	*Weight (mg)*	*^{4}He*	±	*Blank (%)*	*^{3}He*	±	*Blank (%)*	*^{3}He/^{4}He (R_A)*	±	*$^3He_{cos}$*	±
Kaplan_B	Mo Packet	193	0.29	0.00	66	0.98	0.20	25				
			-	-		-	-					
			0.29	0.00		0.98	0.20		23.76	4.76	0.66	0.13
Kaplan_B	Diode+Px	52.49	2.94	0.17	14	4.77	0.66	19				
			-	-		-	-					
			2.94	0.17		4.77	0.66		11.59	1.75	1.64	0.26
Saraclar	Diode+Px	189.46	21.16	0.31	1	4.91	0.24	5	1.66	0.08	-	-
Eminbey	Mo Packet	240.5	0.96	0.01	16	1.36	0.21	15				
			0.07	0.00	223	0.20	0.12	102				
			0.96	0.01		1.36	0.21		10.12	1.56	0.34	0.05
Eminbey	CO_2 laser	208.39	1.12	0.02	3	1.32	0.15	17				
			0.09	0.01	36	0.17	0.12	130				
			1.12	0.02		1.32	0.15		8.45	0.99	0.13	0.02

Since the samples are very young and the weight of the sample used is minimal the percentage that the blank represents from the amount of gas released is calculated. All of the samples analysed were heated for 20 minutes. To calculate the concentrations of $^3He_{cos}$ the average ratio from the crush is used (7.58 ± 0.26 R_A; R_A= 1.39 x 10^{-6}); one sample yielded ^{3}He/^{4}He ratios lower tan the crushed ratio.

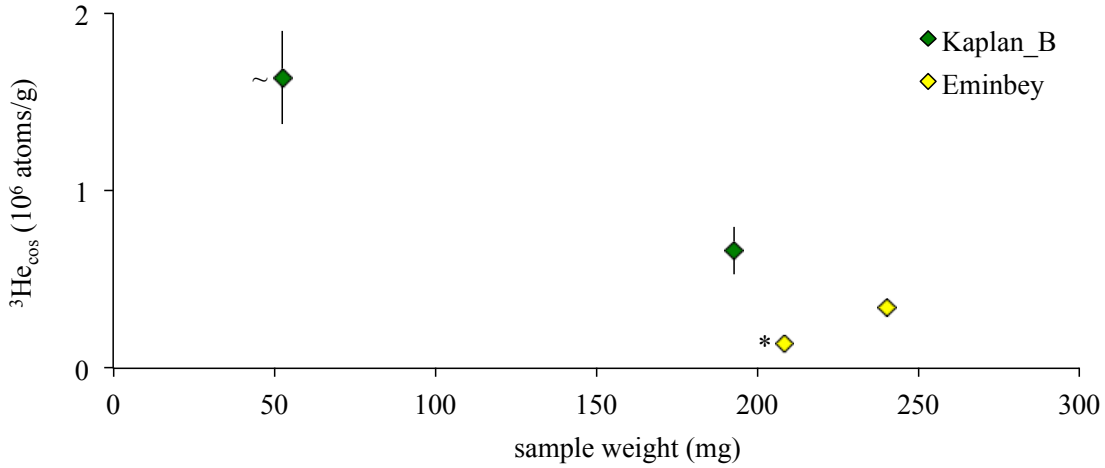

Figure 4.20. Plot of the $^3He_{cos}$ concentration of olivine samples against sample weight. Two aliquots were wrapped in Mo foil and heated with the diode laser, the aliquot showing ~ was added pyroxene flux and degassed using the diode laser and the aliquot with * was degassed using the CO_2 laser.

Two aliquots of the sample Kaplan_B sample were degassed using the diode laser. One aliquot was wrapped in Mo foil and the other aliquot was mixed with pyroxene flux. The aliquot mixed with pyroxene flux yielded 20% less $^3He_{cos}$ than the pyroxene separate. The diode laser beam couples well with the pyroxene flux that melts and covers the olivine transferring heat into it. After degassing the specimen was studied using a binocular microscope. It was observed that the pyroxene flux covered the uppermost layer of the olivine grains but deeper grains were not in contact with pyroxene causing partial degasing of the sample. The aliquot wrapped in Mo foil was 40% lower than that released from the one mixed with degassed pyroxene flux. In order to be able to hold >200 mg of material the Mo packets have to be quite large leaving a large surface (~4 cm^2) in contact with the copper pan causing heat loss and therefore incomplete degassing of the sample. This is also observed in the case of Eminbey were the aliquot wrapped in Mo foil yielded 60% less $^3He_{cos}$ than the pyroxene separate. In this case heating of olivine with the CO_2 laser yielded a $^3He_{cos}$ concentration 80% lower than that obtained from pyroxene, this could be caused by not achieving enough temperature to diffuse He from olivine when heated with the CO_2 laser. In the case of Saraclar (only one aliquot analysed) the high ^4He (20 times higher than previously measured in pyroxene) compared to ^3He (4 times higher than measured in pyroxene) was released yielding a low $^3He/^4He$ ratio (1.66 R_A). In this particular case the only explanation for such extremely high ^4He is contamination of the degassed pyroxene flux possibly by absorption of air as the degassed pyroxene flux is powdered increasing the specific surface to interact with olivine but also being susceptible to air absorption.

In summary, the experiments suggest that complete degassing of olivine samples of weight >50 mg using laser heating is not feasible and limits this technique to olivine samples with exposure ages older than 20 ka. Consequently the results obtained from pyroxene separates are the only ones that will be used for age calculation. A summary of the $^{3}He_{cos}$ concentrations that will be used for age calculations is shown in table 4.7. Laser degassing of >50 mg of olivine and pyroxene samples has proved to be more challenging than degasing ~15 mg samples. In addition, the low He concentrations have proved difficult to reproduce.

Table 4.7. Summary of the $^{3}He_{cos}$ results used for age calculations.

Sample name	*Degasing*	*Weight (mg)*	*$^{3}He_{cos}(10^{6}$atoms/g)*	±
Kaplan_A	CO2 laser	62.3	0.6	0.12
Kaplan_A	Diode laser	193.2	0.58	0.05
Kaplan_A	Diode laser	224.8	0.79	0.07
Kaplan_A	Diode laser	196.8	0.68	0.08
Average			*0.66*	*0.09*
Eminbey	CO2 laser	186.2	0.81	0.05
Eminbey	Diode laser	202.5	0.82	0.05
Average			*0.82*	*0.01*
Kaplan_B	Diode laser	210.7	2.16	0.17
Saraclar	Diode laser	206.1	0.3	0.06
Saraclar	Diode laser	146.8	0.3	0.06
Average			*0.3*	*0.01*

The data has been chosen based on analytical evidences (see text). Arithmetic mean and 1σ uncertainties have been calculated for the samples where several aliquots were analysed. The relative standard deviations of the average of the results of several aliquots from the same sample vary from 1% in the case of Saraclar and Eminbey up to 14% in the case of sample Kaplan_A.

4.6.5. Surface exposure dating

Cosmogenic ^{3}He exposure ages are calculated using equation 4.1. The magmatic $^{3}He/^{4}He$ ratio is taken as an average of the results from crushing the mineral separates. The ratio obtained is 7.58 ± 0.26 R_A. The $^{3}He_{cos}$ concentrations obtained from laser degassing the samples were computed using the CRONUScalc online calculator (*http://web1.ittc.ku.edu:8888/2.0*; version 2.0; Marrero et al., 2016) to calculate minimum apparent exposure ages for the different lava flows. For age calculation the time- and nuclide-dependent scaling factor proposed by Lifton et al. (2014) (LSDn, *Sa*) was used and the apparent exposure ages obtained are summarised in Table 4.8.

Table 4.8. Summary of the sample locations and the apparent exposure ages calculated from $^{3}He_{cos}$ concentrations.

Sample	*Latitude*	*Longitude*	*Elevation*	*$^{3}He_{cos}$ (10^{6} atoms/g)*	±	*Production rate (atoms/g/year)*	*Exposure age (ka)*	±
Kaplan_A	38.60	28.45	624	1.37	0.17	137.92	3.94	0.77
	38.60	28.45	624	0.51	0.11	137.92	3.83	0.28
	38.60	28.45	624	0.58	0.04	137.92	5.17	0.44
	38.60	28.45	624	0.79	0.07	137.92	4.49	0.51
Average							***4.36***	***0.61***
Eminbey	38.60	28.42	605	1.37	0.09	135.69	5.40	0.27
	38.60	28.42	605	0.82	0.04	135.69	5.42	0.27
Average							***5.41***	***0.19***
Kaplan_B	38.60	28.38	419	2.16	0.16	115.47	***16.30***	***1.22***
Saraclar	38.58	28.56	731	0.31	0.06	150.99	1.83	0.49
	38.58	28.56	731	0.3	0.05	150.99	1.80	0.31
Average							***1.82***	***0.29***

The production rate of $^{3}He_{cos}$ is that of spallation scaled using the LSDn (Lifton et al., 2014) scaling factor. The data have been calculated using the scheme of Marrero et al. (2016). All the uncertainties are the propagated 1σ internal uncertainty. The uncertainty of the average of samples Eminbey and Saraclar are calculated as propagated 1σ uncertainty and not taken as standard deviation, the standard deviation of both samples is 0.01, which is not representative of the uncertainty of the measurements as only two aliquots are considered.

The apparent exposure ages obtained for the different β4 flows taken as an average of the results obtained from the analysis of various aliquots of pyroxene range from 1.82 ± 0.29 ka for Saraclar flow up to 16.3 ± 1.22 ka for Kaplan_B flow. The sample from Korez that cannot be dated due to limitations of the analytical technique must have an apparent exposure age of < 1.8 ka (the age of Saraclar flow that sets the limits of the analytical procedure).

4.6.5.1 Comparison of exposure ages with previously published ages

The most recent published exposure ages (Heineke et al., 2016) used cosmogenic ^{3}He and ^{10}Be to date the most recent phases of volcanism in the KVP demonstrating that in the case of dating young basalts, cosmogenic nuclides are a reliable alternative to K-Ar and ^{40}Ar-^{39}Ar dating. Therefore, for the purpose of this study I compare the $^{3}He_{cos}$ data obtained from laser degasing of pyroxene separates from five lava flows with the $^{3}He_{cos}$ data published by Heineke et al. (2016) from furnace degasing of olivine from six lava flows (Figure 4.21).

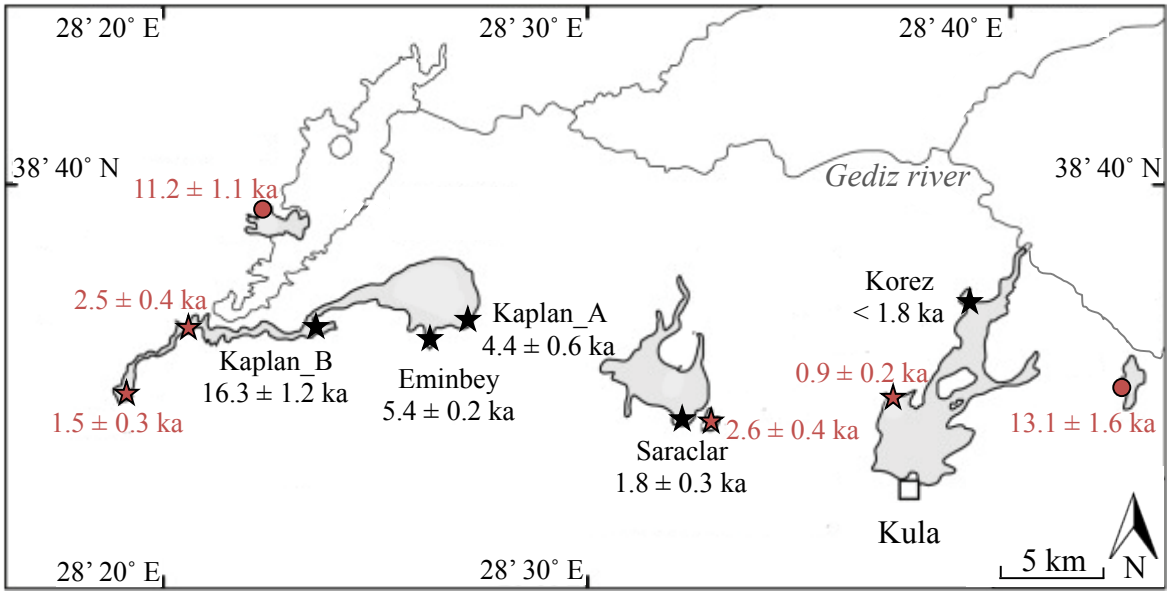

Figure 4.21. Simplified map of the KVP showing the apparent exposure ages of Heineke et al. (2016) (red) and those from this study (black). The stars represent the lava flows corresponding to the β4 volcanic phase and the circles the lava flows from the β3 phase. (Map modified from Heineke et al., 2016).

Comparing the data obtained for the β4 lava flows to those of Heineke et al. (2016) the flow from Korez, although an age could not be determined with the laser technique, it can be estimated to be younger than 1.8 ka. This is in agreement with the 0.9 ±0.2 ka reported by Heineke et al (2016) and it supports the idea of an over-estimation of the K-Ar ages (7 ± 2 and 4 ± 2 ka) of Westaway et al. (2006) based on samples taken from the north of the same flow, due to minor amounts of excess Ar.

The exposure ages obtained from Saraclar lava flow (1.8 ± 0.3 ka) agree within 2σ uncertainty with those reported by Heineke et al. (2016) for the same lava flow. In the case of Kaplan_A and Eminbey flows the exposure ages estimated from this study (4.4 ± 0.6 and 5.4 ± 0.2 ka) are slightly higher than those obtained from Heineke et al. (2016) from samples taken from the easternmost flows of the same area (2.6 ± 0.4 ka). Sample Kaplan_B records an exposure age of 16.3 ± 1.2 ka. The different exposure ages from the area of Kaplan suggest that this volcano has been active since c. 16.3 ka with different episodes of volcanic activity with the last episode occurring c. 1.5 Ka.

The older age obtained in sample Kaplan_B is closer to the ages estimated by Heineke et al. (2016) for the two β3 lava flows (11.2 ± 1.1 and 13.1 ± 1.6 ka). Sample Kaplan_B was described from field observations to present some vegetation development and also appear to be overlapped in certain areas by younger flows, which is in agreement with it being an older exposed flow. The development of some bushes and grass cannot be

used as criteria for classifying the flow as β3, it requires the development of soil and the surface to be eroded enough for agriculture exploitation (Richardson-Bunbury, 1996). Therefore, Kaplan_B flow is classified as β4 in agreement with the description of Richardson-Bunbury (1996). The exposure ages determined from this study suggest that the β4 volcanism has been taken place over the past 16 ka. The new data generated from this study suggest that either the β3 and β4 eruption phases occurred simultaneously or the flows classified as β3 by Heineke et al. (2016) were actually β4 as described by Richardson-Bunbury (1996).

4.6.6. Summary

The use of cosmogenic ^{3}He for determining the exposure age of Holocene surfaces has been a commonly used technique since 1990's (Kurz et al., 1990; Foeken et al., 2009b; Fenton and Niedermann, 2014; Heineke et al., 2016). All the studies used 300 mg to 1 g of material (olivine and pyroxene), which was degassed using a furnace. This is the first attempt to use a laser for dating Holocene lava flows using a relatively small amount of material (< 250 mg). The idea was to be able to analyse several aliquots of the same sample and try different laser degassing methods.

The use of a laser for complete degassing of samples with weights ranging from 50 mg to 250 mg for cosmogenic ^{3}He analysis has proved challenging, especially in the case of olivine were no reliable measurements were obtained due to incomplete degassing. Degassing pyroxene minerals using a laser seems to be a technique that still has room for improvement, as not all the samples analysed were completely degassed but the results have revealed to be of the same quality as those obtained by using a furnace and are encouraging for further development of this technique. Maybe the use of a copper pan with bigger and deeper wells or a better encapsulation of the grains in the case of olivine could be future routes to continue developing this technique.

4.7 Case study 2: Cosmogenic ^{3}He in detrital gold from Scotland

The use of the laser has been proven an effective method for degassing small amounts of sample allowing for the technique to be used in individual grains. This gas extraction technique rules out the possibility of metals alloying with the furnace liner. In

this case study I want to test the capability of the laser to degas individual gold grains from different locations in Scotland in order to unravel their time at the surface using cosmogenic ^{3}He. The cosmogenic nuclide concentration of individual detrital mineral grains has the potential to provide information about the duration of transport-storage and the long-term recycling rate of detrital grains in a fluvial system. In the case of detrital minerals, cosmogenic ^{3}He concentrations may shed light on the processes of transport and accumulation that generate alluvial placer deposits.

Quantitative release of He from metals requires melting (Shukolyukov et al., 2012). The temperature of gold melting (1068°C) is easily attained by near-visible diode laser heating of opaque mineral grains (see section 4.2). Laser heating has several advantages over conventional UHV furnace for degassing gold grains; lower blank, volume reduction and avoids alloying gold with the furnace liner which will radically shorten the component lifetime and may lead to catastrophic vacuum failure (Bochsler et al., 1978; Nier and Schlutter, 1988). In addition, up to 21 single grains can be loaded per laser pan (Figure 4.22) facilitating rapid analysis due to short pump down time. Further, laser heating has the potential to be automated, which would allow analysis of one pan in a ~24 hour period. Here I report He isotope analysis of individual gold grains from various alluvial deposits across Scotland (Sutherland, Kowegreens Burn, Westwater, Cononish, Aberfeldy, Ochil Hills, Leadhills and Glengaber Burn), with the purpose of determining whether cosmogenic ^{3}He has accumulated and retained in the gold grains.

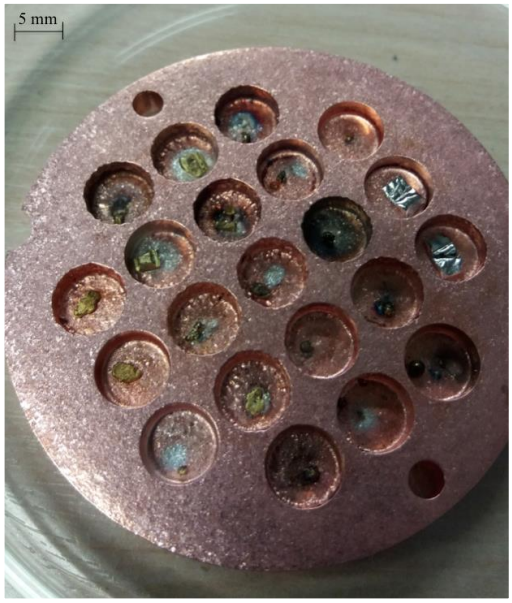

Figure 4.22. Photograph of a Cu laser pan loaded with 19 native gold samples and two processed empty Pt packets used for bank measurements.

4.7.1. Gold mineralisation in Scotland

Gold mineralisation in Scotland is largely hydrothermal in origin, likely Caledonian in age (Chapman et al., 2000a, Mark et al., 2011). In Scotland, most alluvial gold is derived from orogenic mineralization with evidence of epithermal and mesothermal gold (Chapman, 2007). The different sources of gold mineralization in Scotland are typically distinguished based on the Ag content and the relative proportions of sulphides, sulpharsenides and tellurides as inclusions (Chapman et al., 2000a). Chapman (2007) compiled the Ag content from placer and orogenic gold from Scotland (Figure 4.23).

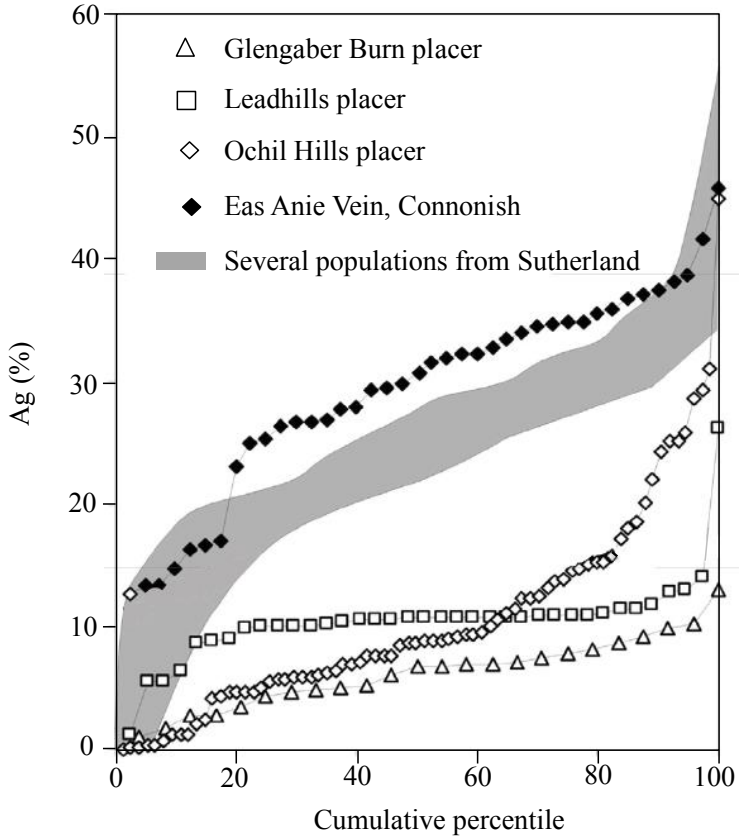

Figure 4.23. Examples of Ag content for in-situ and alluvial placer gold for orogenic vein gold and epithermal gold from different locations in Scotland (modified from Chapman, 2007).

Placer gold grains present a wide range of Ag content indicative of differences in composition throughout the mineralization system. The alluvial gold in the Leadhills area is probably derived from direct erosion of mineralized rock with at least four distinct mineralization sources associated with mesothermal shear zones, mafic and ultramafic rocks enriched with Ni and Cu and associated with oxidizing solutions along faults and zones of weakness. The distributions of the different types of gold reflect a limited glacial and drainage transport (Leake et al., 1998). This limited transport was also observed in

alluvial gold from the Glengaber burn, where two distinct sources of gold mineralization were identified on the basis Ag contents with the mineralization most likely controlled by deep-seated discordant NNW-trending structures that allowed the mineralization fluids to move from deep crustal levels (Chapman et al., 200b). Three distinct types of gold mineralization are identified in the alluvial gold from the Ochil Hills that correspond to different emplacement temperatures. These correspond to low-sulphidation epithermal mineralization with (i) a wide range of Ag (5-15%), (ii) low range of Ag content (5-9%) and (iii) a less abundant type with low Ag content (<5%) (Chapman et al., 2005). Although no bedrock occurrences have been identified for the Ochil Hills placer gold, the different microchemical compositions are confined to specific drainage systems suggesting the transport has also been limited (Chapman et al., 2005, 2006). The source of mineralization of placer gold in Sutherland has been identified as a low-sulphidation epithermal source (Crummy et al., 1997; Chapman, 2007).

4.7.2. Sample description and methodology

All the alluvial gold samples in this study were donated by Mr Peter Davidson and formed part of the collection of the National Museum of Scotland. The samples consist on panned gold grains and nuggets (n = 36) in size range 1 to 8 mm diameter from 8 main localities around Scotland (Sutherland, Tyndrum, Argyll, Aberdeenshire, Leadhills, Moffat, Aberfeldy and Ochil Hills) (Figure 4.24). In addition three sulphide samples from two localities (Leadhills and South Aberdeenshire) were donated by the Dr. John Faithful from the Hunterian Museum and Art Gallery in Glasgow and Dr. Clive Rice from Aberdeen University, and analysed in order to quantify the magmatic He content.

All grains were loaded into 21-hole Cu pans and pumped for 12 hours. Individual gold grains were degassed using the 808 nm, 75 W diode laser at ~40% power for 15 minutes and the gas released from the heating of the samples was analysed using the Helix SFT mass spectrometer (see Chapter 3). The results were blank corrected with blank levels for ^{4}He and ^{3}He being $5.9 \pm 0.9 \times 10^{8}$ and $1.5 \pm 0.2 \times 10^{4}$ atoms respectively. Blank levels represent <1% of the ^{4}He and between 2% and 95% of the ^{3}He released.

Eight gold grains from the same localities were dissolved in 5 cycles of freshly prepared *aqua regia* (8 ml 0.8M HNO_3 and HCl at 1:3) at 100˚C, each cycle lasting 5 hours. The samples were subsequently dried and then re-dissolved in 20 ml of 0.8M HNO_3

then Li content analysed using the ICP-MS (Agilent 7500ce) at SUERC. Ten blanks were prepared simultaneously following the same procedures. Li concentration standards (Specpure® trace element certified) at 5, 10 and 20 ppm were also analysed. The results obtained from the analysis of Li in gold samples are presented in Appendix B3 and discussed in section 4.7.4.3.

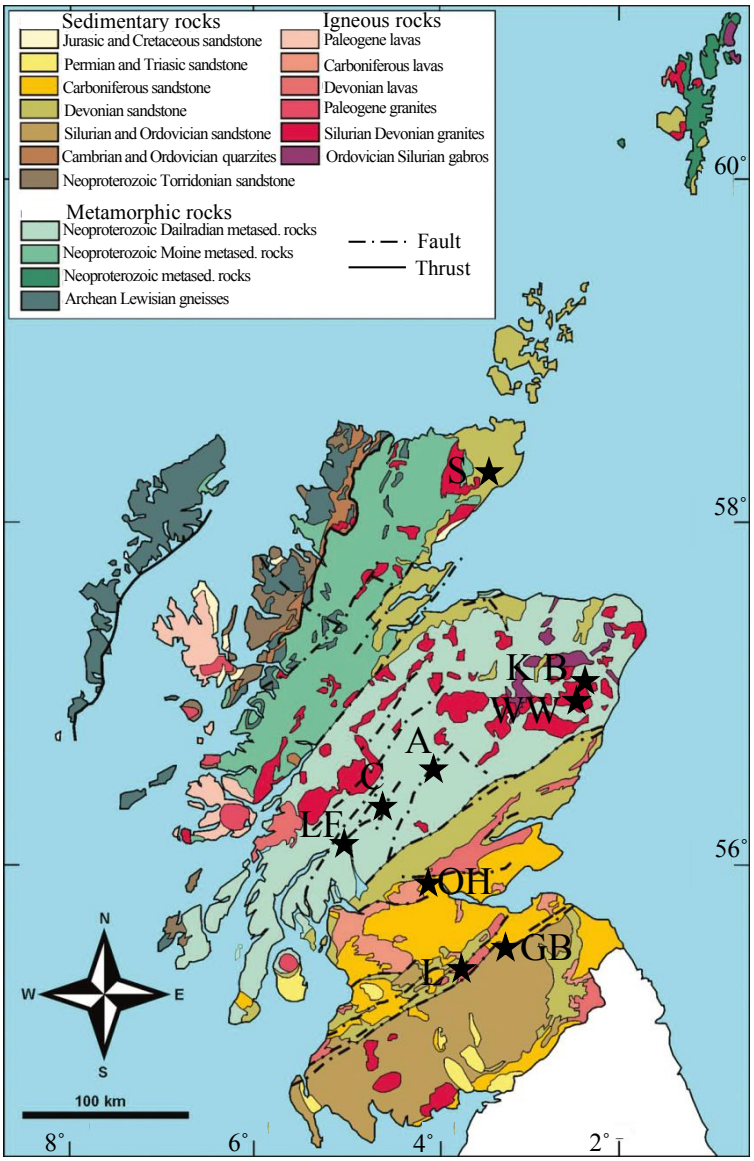

Figure 4.24. Geological map of Scotland with the different locations of the alluvial gold grains. S: Sutherland, KB: Kowegreens Burn, WW: Westwater, C: Crom Alt Brun, LF: Loch Fyne, A: Aberfeldy, OH: Ochil Hills, L: Leadhills, GB: Glengaber Burn.

4.7.3. He isotopes results

Table 4.9 compiles the results of He isotopes analysis of 36 grains from 8 different locations across Scotland.

Table 4.9. Helium isotope data from detrital gold grains from eight locations in Scotland. Up to 3 grains from the same locations were analysed. The uncertainties are reported as 1σ.

Sample name	*Location*	*Area*	*Weight (mg)*	*^{4}He (10^{13} atoms/g)*	±	*^{3}He (10^7 atoms/g)*	±	*^{3}He/^{4}He (R_A)*	±
KB.1	Kidonan Burn	Sutherland	17.1	3.23	0.03	9.88	0.43	2.23	0.10
KB.2	Kidonan Burn	Sutherland	28.7	59.13	0.10	1.46	0.09	0.02	0.00
KB.3	Kidonan Burn	Sutherland	9.0	15.13	0.03	0.49	0.12	0.02	0.01
S.1	Suisgill Burn	Sutherland	23.8	4.21	0.02	1.81	0.12	0.31	0.02
S.2	Suisgill Burn	Sutherland	6.1	2.45	0.01	1.16	0.24	0.34	0.07
S.3	Suisgill Burn	Sutherland	12.5	299.43	0.51	0.55	0.10	0.00	0.00
C.1	Crom Alt Burn	Tyndrum	21.0	1.66	0.02	0.69	0.10	0.30	0.04
C.2	Crom Alt Burn	Tyndrum	68.1	0.49	0.01	0.19	0.02	0.29	0.02
C.3	Crom Alt Burn	Tyndrum	35.1	2.26	0.01	0.51	0.06	0.17	0.02
LF.1	Loch Fyne	Argyll	54.0	2.73	0.01	1.97	0.08	0.52	0.02
LF.2	Loch Fyne	Argyll	18.6	1.06	0.01	0.5	0.08	0.34	0.05
WW.1	Westwater	Aberdeenshire	17.3	0.09	0.01	-	-	-	-
WW.2	Westwater	Aberdeenshire	19.3	0.41	0.01	0.84	0.08	1.50	0.15
WW.3	Westwater	Aberdeenshire	3.5	8.14	0.01	4.97	0.49	0.44	0.04
WW.4	Westwater	Aberdeenshire	27.2	0.55	0.01	0.57	0.07	0.77	0.09
WW.5	Westwater	Aberdeenshire	18.0	0.9	0.01	1.27	0.11	1.03	0.09
WW.6	Westwater	Aberdeenshire	25.2	1.12	0.01	5.98	0.18	3.91	0.12
WW.7	Westwater	Aberdeenshire	27.9	1.63	0.01	0.77	0.08	0.34	0.04
WW.8	Westwater	Aberdeenshire	7.1	14.12	0.02	1.31	0.24	0.07	0.01
WW.9	Westwater	Aberdeenshire	14.2	1.41	0.01	4.33	0.21	2.24	0.11
KoB.1	Kowegreens Burn	Aberdeenshire	27.2	4.09	0.01	1.06	0.13	0.19	0.02
KoB.2	Kowegreens Burn	Aberdeenshire	1.4	3.24	0.01	0.1	0.51	0.02	0.12
L.1a*	Wintage Glen	Leadhills	10.1	9.34	0.02	1.82	0.24	0.14	0.02
L.1b	Wintage Glen	Leadhills	46.7	4.14	0.01	1.39	0.08	0.24	0.01
Average				*6.74*	*3.67*	*1.6*	*0.3*		
L.2	Wintage Glen	Leadhills	10.8	6.46	0.01	0.25	0.07	0.03	0.01
L.3	Wintage Burn	Leadhills	16.5	0.35	0.01	0.92	0.09	1.91	0.19
L.4	Wintage Burn	Leadhills	27.9	0.55	0.01	0.03	0.03	0.04	0.04
L.5	Wintage Burn	Leadhills	12.7	3.5	0.01	0.01	0.03	0.00	0.01
GB.1	Glengaber Burn	Moffat	19.2	0.27	0.01	0.74	0.08	1.99	0.20
GB.2	Glengaber Burn	Moffat	11.9	1.15	0.01	0.04	0.04	0.03	0.02
GB.3	Glengaber Burn	Moffat	37.8	0.16	0.01	0.49	0.11	2.23	0.49
A.1a*	Moness Burn	Aberfeldy	19.2	0.38	0.01	0.1	0.03	0.19	0.06
A.1b	Moness Burn	Aberfeldy	79.7	0.45	0.01	0.12	0.02	0.20	0.03
A.1c	Moness Burn	Aberfeldy	19.3	2.27	0.01	0.12	0.04	0.04	0.01
Average				*1.36*	*1.28*	*0.12*	*0.01*		
OH.1	Thorter Burn	Ochil Hills	37.1	1.15	0.01	2.58	0.14	1.63	0.09
OH.2	Thorter Burn	Ochil Hills	24.6	3.06	0.01	0.09	0.04	0.02	0.01
OH.3	Thorter Burn	Ochil Hills	29.3	127.83	0.22	0.87	0.06	0.01	0.01
OH.4	Birdland Glen	Ochil Hills	17.3	0.41	0.01	1.9	0.19	3.38	0.34
OH.4	Birdland Glen	Ochil Hills	7.0	2.51	0.01	0.4	0.12	0.12	0.04

*Two grains (L.1, A.1) were large enough to be separated into smaller fragments (a, b, c), which were analysed individually and the average and 1σ standard deviation is calculated.

^{4}He concentrations range from 2 x 10^{12} to 3 x 10^{15} atoms/g and ^{3}He concentrations vary from 3 x 10^5 to 1 x 10^8 atoms/g (only one sample failed to produce ^{3}He higher than blank levels). The large variation on the ^{4}He concentrations may be related to the presence of U and Th in the mineral lattice or U- and Th-rich mineral inclusions (i.e. zircon) (Eugster et al., 1995). Over the lifetime of the gold (~400 Ma) decay of U and Th has produced considerable amounts of radiogenic ^{4}He. Since the variation of the ^{4}He concentrations depends on the distribution of U-rich mineral inclusions within the gold

grains ^{4}He concentrations are expected to vary within grains as observed from the analysis of fragments from grains L.1 and A.1 where ^{4}He concentrations varied by 55 % and 95 %.

In the case of ^{3}He the concentrations within an individual grain are fairly homogenous with the concentration obtained from the analysis of three different fragments of A.1 sample having 3 % dispersion and 19 % dispersion in the case of sample L.1. In the case of L.1 sample, aliquot L.1b weighed 4.6 times more than aliquot L.1a and released 24 % less ^{3}He. Observation under binocular microscope after heating revealed that the gold grain was not melted and therefore the low ^{3}He concentration may be a consequence of incomplete melting. This reveals the difficulty of melting large grains, especially those which morphology is spherical; this could be solved by flattening the grains and breaking them into smaller fragments.

$^{3}He/^{4}He$ ratios vary from 0.01 to 3.9 R_A. Typically, $^{3}He/^{4}He$ in orogenic gold deposits, released by *in vacuo* crush extraction, are up to 0.4 R_A (Burnard, 2012). The high $^{3}He/^{4}He$ of some Scottish gold grains hints at an excess of ^{3}He that may be cosmogenic in origin, not least because *in situ* radiogenic ^{4}He is expected to have lowered $^{3}He/^{4}He$.

4.7.4. Unravelling the source of ^{3}He

In order to quantify the cosmogenic ^{3}He content of the gold grains the contribution of air-derived He, magmatic ^{3}He and nucleogenic ^{3}He have been investigated.

4.7.4.1. Air derived ^{3}He ($^{3}He_{air}$)

To quantify the contribution of air-derived ^{3}He, ^{20}Ne was measured in three samples. The results are summarized in Table 4.10. The He contribution from air is calculated based on atmospheric $^{4}He/^{20}Ne$ ratio of 0.29 ± 0.01 (Porcelli et al., 2002 and references therein) and the air derived ^{3}He concentration is calculated using the atmospheric $^{3}He/^{4}He$ ratio of 1.39×10^{-6} (Mamyrin et al., 1970). Air-derived ^{4}He and ^{3}He represent less than 0.08 % and less than 0.13 % of the respective totals in the three grains analysed. Assuming air-derived ^{3}He concentration of $1.66 \pm 0.30 \times 10^{4}$ atoms/g, the ^{3}He contribution from air can be calculated for the rest of the samples analysed. With the exception of two L.4 grains and GB.1 (6 and 28 %) air-derived ^{3}He represents less than 2 % of the measured ^{3}He.

Table 4.10. He isotopes and ^{20}Ne from 3 gold grains.

Sample name	*Weight (mg)*	^{4}He	±	^{3}He	±	^{20}Ne	±	$^{4}He_{air}$	±	$^{4}He_{air}$ *(%)*	$^{3}He_{air}$	±	$^{3}He_{air}$ *(%)*
WW.3	7.1	14.12	0.02	1.31	0.24	4.15	0.21	11.97	0.02	0.008	1.664	0.30	0.13
WW.3	14.2	1.41	0.00	4.33	0.21	3.12	0.19	8.98	0.02	0.064	1.249	0.06	0.03
OH.2	29.3	127.83	0.22	0.87	0.06	1.64	0.07	4.71	0.01	0.000	0.655	0.04	0.08

The ^{4}He concentration is expressed in 10^{13} atoms/g, ^{3}He in 10^{7} atoms/g and ^{20}Ne in 10^{10} atoms/g. The air-derived $^{4}He_{air}$ and $^{3}He_{air}$ are expressed in 10^{9} and 10^{4} atoms/g respectively. Uncertainties are reported as 1 σ . The air-derived $^{4}He_{air}$ and $^{3}He_{air}$ are calculated based on atmospheric $^{4}He/^{20}Ne = 0.29 \pm 0.01$ and $^{3}He/^{4}He = 1.39 \times 10^{-6}$ (Porcelli et al., 2002 and references therein).

4.7.4.2. Magmatic ^{3}He ($^{3}He_{mag}$)

Scottish gold has likely precipitated from ancient hydrothermal fluids. Hydrothermal fluids very commonly contain mantle-derived He (e.g. Turner and Stuart, 1992), and can retain a small proportion of it for 100's millions of years in, for instance, hydrothermal sulphide minerals (e.g. Davidheiser-Kroll et al. 2014). While it has yet to be shown that hydrothermal gold retains mantle-derived ^{3}He in fluid inclusions, the signature from the hydrothermal source needs to be assessed before definitive statements regarding cosmogenic He can be made. In the absence of shielded gold samples, sulphides associated with the source mineralization of gold could provide an insight of the ^{3}He content of the cogenetic gold. Two samples of pyrite from the main stage vein mineralisation in the Leadhills area, and one sample of pyrite associated with the gold mineralisation in the Dalradian series from the area of Aberdeenshire, have been analysed. $^{3}He/^{4}He$ ratios range from 0.04 to 2.3 R_A and ^{3}He concentrations vary from 0.3 to 4.4 x 10^{7} atoms/g (Table 4.11). The average ^{3}He concentration (2.0 ± 1.5 x 10^{7} atoms/g) provides an estimation of the magmatic ^{3}He concentration in the gold grains.

Table 4.11. Helium isotopes from hydrothermal pyrite released by melting. The uncertainties are reported as 1σ.

Sample name	*Mineral*	*Area*	*Weight (mg)*	^{4}He *(10^{13} atoms/g)*	±	^{3}He *(10^{7} atoms/g)*	±	$^{3}He/^{4}He$ *(R_A)*	±
NMS 010_1	Py	Leadhills	4.5	0.10	0.00	0.30	0.16	2.3	1.2
NMS 010_2	Py	Leadhills	5.18	1.51	0.00	1.35	0.23	0.65	0.11
NMS 06	Py	Leadhills	2.7	0.38	0.00	0.86	0.36	1.63	0.68
SHIB_1	Py	Aberdeenshire	9.05	12.41	0.02	2.71	0.30	0.16	0.02
SHIB_2	Py	Aberdeenshire	10.81	37.22	0.06	2.19	0.20	0.04	0.00
SHIB_3	Py	Aberdeenshire	11.64	17.18	0.03	4.40	0.30	0.19	0.01
Average						*1.97*	*1.48*		

It can be seen in Figure 4.25 that the ^{3}He concentration in samples KB.1, WW.3, WW.6 and WW.9 are higher than the upper limit of the hydrothermal He concentration, providing evidence for the presence of excess ^{3}He in these grains potentially of cosmogenic origin. This is supported by the high $^{3}He/^{4}He$ of these grains (2.1 to 3.3 R_A)

despite the likelihood that 400 Ma of radiogenic ^{4}He has grown into those grains due to U and Th decay.

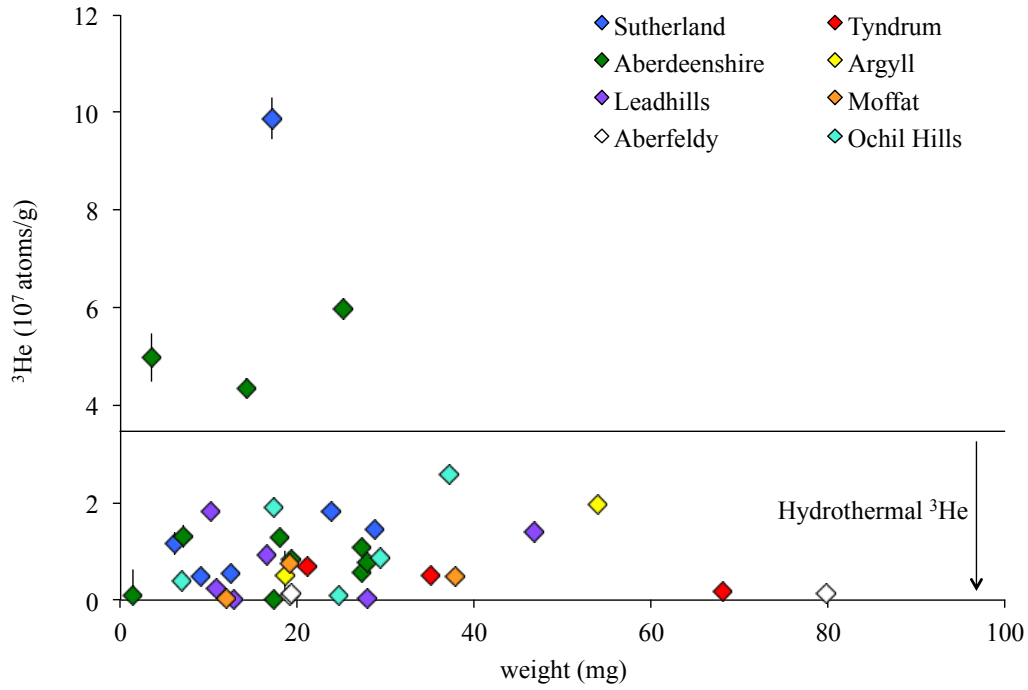

Figure 4.25. Plot of the ^{3}He concentrations in Scottish gold. The black line represents the maximum $^{3}He_{mag}$ derived from hydrothermal fluids.

4.7.4.3. Thermal neutron produced ^{3}He ($^{3}He_{nuc}$)

$^{3}He_{nuc}$ is produced by the thermal neutron absorption reaction $^{6}Li(n, \alpha)^{3}H(\beta^{-})^{3}He$ where the $^{3}He_{nuc}$ production rate for a neutron flux of 1 neutron/cm^2/yr is 6.13 x 10^{-6} atoms/g/yr/ppm of Li (Lal, 1987). At the Earth's surface the $^{3}He_{nuc}$ production is dominated by cosmogenic thermal neutron flux with the radiogenic neutron flux becoming important only at depths below 2000 g/cm^2 (Lal 1987). In the case of gold, this depth is ~1 m. The potential that Scottish gold has accumulated $^{3}He_{nuc}$ for up to 400 Ma requires the contribution to be quantified. The radiogenic neutron production rate of $^{3}He_{nuc}$ is ultimately controlled by U and Th decay (production of neutrons) and the concentration of neutron absorbers (e.g. H, B, Be, Li) within the rock (Farley et al., 2006). In the case of gold, if the production rate for radiogenic neutron produced $^{3}He_{nuc}$ is assumed to be similar to that of a crustal rock (~0.02 atoms/g/year/ppm; Farley et al., 2006) over 400 Ma the Li content necessary to generate the ^{3}He signature can be calculated (see Figure 4.26). Most of the grains require < 3 ppm Li in order to generate the measured ^{3}He concentration,

although the four samples with highest ^{3}He concentrations (KB.1, WW.3, WW.6, WW.9) require Li concentrations that vary from 5 to 12 ppm.

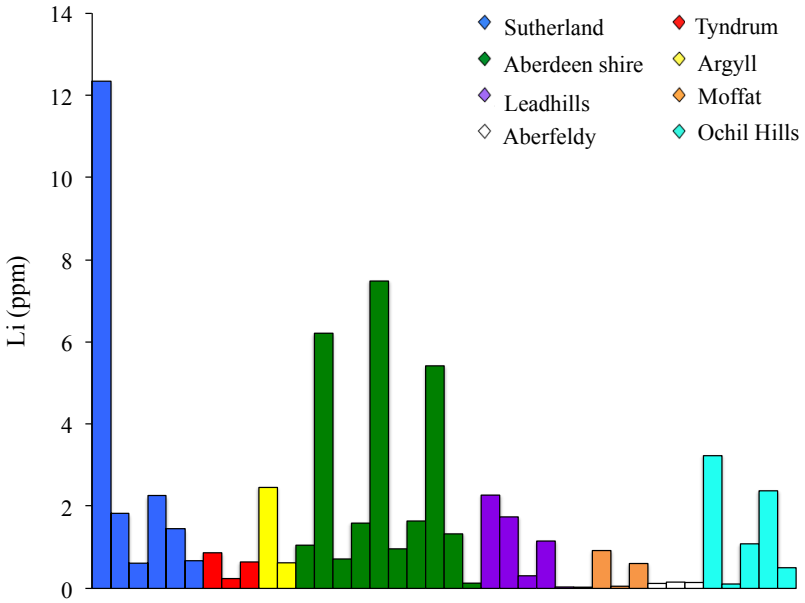

Figure 4.26. Plot of the theoretical Li concentrations in ppm required to generate the $^{3}He^{*}$ signature. Calculations are based on the radiogenic neutron production rate of $^{3}He_{nuc}$ of ~0.02 atoms/g/year/ppm (Farley et al., 2006) over 400Ma.

In order to quantify the proportion of the measured ^{3}He that is nucleogenic in origin, the Li content of 8 gold grains from 6 locations was measured, along with 10 blanks. Five gold grains were divided into several fragments, and samples KB.4 and WW.9 were fragments of grains that were previously analysed for He. Table 4.12 compiles the results of the Li concentration (details of the calculation and the results from Li standards are presented in Appendix B3). The Li content of the blanks ranged from 8 to 583 ng (n = 10). The large variation in the blank makes it difficult to estimate the blank with confidence and therefore the Li concentrations in the samples can only be estimated by giving a maximum and a minimum value based on the maximum and minimum blanks obtained. No samples yielded Li concentrations above the highest blank thus the minimum Li content is 0 ppm. Considering the lowest blank as the limit to calculate the maximum Li content in the gold, the results reflect a variation on the Li content from 3 ppm up to 47 ppm. The high Li content would have generated a ^{3}He signature of c. 5 times higher than the highest ^{3}He measured in the samples. In the cases where more than two aliquots from the same sample have been analysed the Li concentrations obtained have a variation of up to 85 %. The high variation in the blanks is also reflected in the Li concentrations obtained within a single gold grain. In the case of the variation observed within a single grain one could think of this being a consequence of heterogeneous distribution of Li if, for instance,

Li is stored in fluid inclusions. However, since this is also observed in the blank measurements it seems that these variations could be a consequence of an analytical artefact potentially caused by residual Li in glassware and pipettes or by random release of residual Li accumulated in the mass spectrometer system. Further investigation is required in order to be able to accurately measure the Li concentration in the gold samples.

Table 4.12. Li concentrations from 8 gold grains from 6 different localities.

Sample name	*Area*	*Weight (mg)*	*Li (ng)*	±	*Li (ppm)max*	±
Blank_1			78.3	0.7		
Blank_2			88.5	1.2		
Blank_3			93.5	1.1		
Blank_4			55.2	0.6		
Blank_5			83.6	0.8		
Blank_6			97.8	1.0		
Blank_7*			8.1	0.1		
Blank_8			582.6	6.0		
Blank_9			163.4	1.8		
Blank_10			51.9	0.6		
KB.4	Sutherland	4.0	196.2	1.8	47.02	0.45
C.4-1	Tyndrum	21.7	110.6	1.1	4.72	0.05
C.4-2	Tyndrum	23.0	302.7	2.8	12.81	0.12
C.4-3	Tyndrum	21.5	73.8	0.8	3.05	0.04
LF.3-1	Tyndrum	32.4	324.2	4.1	9.76	0.13
LF.3-2	Tyndrum	19.7	279.8	2.9	13.79	0.15
LF.3-3	Tyndrum	23.6	84.4	0.9	3.23	0.04
LF.3-4	Tyndrum	11.6	131.2	1.2	10.60	0.10
WW.9	Aberdeenshire	13.5	149.8	2.0	10.50	0.15
L.6-1	Leadhills	25.6	514.5	5.6	19.78	0.22
L.6-2	Leadhills	25.3	215.1	2.0	8.18	0.08
L.6-3	Leadhills	23.6	238.9	2.9	9.78	0.12
L.6-4	Leadhills	11.6	99.5	1.0	7.88	0.09
L.7-1	Leadhills	25.7	87.0	0.9	3.07	0.03
L.7-2	Leadhills	41.3	191.3	2.0	4.43	0.05
L.7-3	Leadhills	34.0	87.1	0.8	2.32	0.02
GB.1	Moffat	3.8	135.6	1.2	33.55	0.33
A.2-1	Aberfeldy	20.3	554.5	5.2	26.92	0.26
A.2-2	Aberfeldy	27.5	220.4	2.0	7.72	0.07
A.2-3	Aberfeldy	18.4	94.5	1.1	4.69	0.06

Li (ppm)max is the maximum Li content calculated based on the minimum blank (*), the minimum limit for the Li content is 0 ppm based on the maximum blank (blank_8).

The current uncertainties associated with the Li content in gold restrict the ability to determine with confidence the Li concentrations in the samples and consequently hinders the identification of the nucleogenic component. In order to calculate the nucleogenic ^{3}He produced in the gold samples analysis of the residual gold from the degassing step is required as well as further development of the determination of the technique to determine Li concentrations in gold.

4.7.4.4. Cosmogenic ^3He ($^3He_{cos}$)

If we consider that the detrital gold grains have been exposed at maximum since the last glacial maximum (22 ka, Bowen et al., 2002) a $^3He_{cos}$ concentration can be calculated. This requires the knowledge of $^3He_{cos}$ production rate. In the case of gold, the $^3He_{cos}$ production rate has not been determined, either empirically or theoretically. The production rate of $^3He_{cos}$ decreases with increasing atomic mass (Masarik, 2002; Kober et al., 2005). Given the high atomic mass of gold (197 amu) it seems logical to think that the production rate should be lower than that of Fe (~39 atoms/g/year; Masarik, 2002), which is the element with highest atomic mass for which a production rate has been determined. Assuming $^3He_{cos}$ production rate in gold that is the same as Fe, a maximum $^3He_{cos}$ concentration of 8.58 x 10^5 atoms/g gold can be determined. This represents 1 to 2 % of the total ^3He concentration present in the samples that yielded the highest concentrations (KB.1, WW.3, WW.6 and WW.9). The old mineralization age of Scottish gold (~400 Ma) in combination with the variable Li concentration suggests that it will be difficult to isolate the LGM cosmogenic ^3He component.

If no contribution from nucleogenic ^3He is assumed, then the excess ^3He present in samples KB.1, WW.3, WW.6 and WW.9 can be considered to be of cosmogenic origin, recording minimum apparent exposure ages of 0.23 to 1.7 Ma. To generate this ages it is required that the samples have been at the surface through several glacial cycles suggesting that glacial erosion has not completely removed these heavy grains of sediment. This is in agreement with previous observations that the gold have experiment limited glacial and fluvial transport based on chemical composition of gold grains across Scotland (Leake et al., 1998; Chapman et al., 2000b; Chapman et al., 2005; Chapman et al., 2006).

4.7.5 Summary

This study has demonstrated that ^3He can be extracted and measured in individual gold grains showing the potential for using $^3He_{cos}$ in detrital minerals from regions where exposure is longer than the a few 10's thousands of years. Isolating the $^3He_{cos}$ requires refinement of the determination of the Li concentrations in gold in order to quantify the $^3He_{nuc}$ contribution.

For the purpose of using ^{3}He concentrations in gold for cosmogenic exposure dating it is imperative that the $^{3}He_{cos}$ production rate in gold is determined so that exposure durations can be accurately calculated. In order to fully understand the residence time of an alluvial gold deposit analysis of more grains per site will be required. The technique of extracting and measuring ^{3}He from individual grains has the potential to be automated and therefore to allow for analysis of tens to hundreds of grains from the same deposit in a relatively short time.

4.8. Conclusions

The data presented in this chapter confirm that lasers can be used to completely degas $^{3}He_{cos}$ from small mass of minerals (~15 mg). This has several advantages over conventional UHV furnaces (Fenton and Niedermann, 2014). It has been applied in a preliminary study of 36 single detrital gold grains. Automation of the laser degassing process will allow for rapid sample throughout, and the generation of large data sets required for provenance studies.

Dating young exposed lava flows using the diode laser has produced ages that are reproducible and enable the timescale of the eruptive events in the Kula Volcanic Province to be determined. The results are in agreement with previously reported ages (Heineke et al., 2016) confirming the potential of this technique for cosmogenic ^{3}He analysis (Foeken et al., 2009b). However, for larger sample weights (> 50 mg) the laser degassing has limitations that must be refined if it is to be applicable for determining short exposure.

5. Chemical control of cosmogenic ^{3}He and ^{21}Ne production rate

5.1 Introduction

Cosmogenic ^{3}He and ^{21}Ne are quantitatively retained in mafic minerals (e.g. olivine and pyroxene) for tens of millions of years and are extensively used for exposure age and erosion rate determinations of a variety of geological surfaces in a range of basic igneous rocks (Poreda and Cerling, 1992; Bruno et al., 1997; Schaefer et al., 1999; Fenton et al., 2002; Margerison et al., 2005; Kounov et al., 2007; Gayer et al., 2008; Foeken et al., 2009; Evenstar et al., 2009; Fenton and Niedermann, 2014; Espanon et al., 2014). Converting $^{3}He_{cos}$ and $^{21}Ne_{cos}$ concentrations in minerals to exposure ages and erosion rates require accurate and precise nuclide production rates. Production rates of $^{3}He_{cos}$ and $^{21}Ne_{cos}$ are typically obtained from studies of co-genetic olivine and pyroxene from uneroded surfaces in basalt flows that have been independently dated (e.g. Poreda and Cerling, 1992; Fenton et al., 2009; Foeken et al., 2009; Blard et al., 2013).

Cosmogenic ^{3}He and ^{21}Ne in terrestrial minerals is dominantly produced by spallation reactions induced by high-energy neutrons on O (^{3}He only), Mg, Al, Si, Na, Ca and Fe (Lal, 1991; Gosse and Phillips 2001; Niedermann, 2002). Thus both nuclides have the potential to be used to determine the exposure history of many minerals (e.g. olivine, pyroxene (Fenton et al., 2013; Fenton and Niedermann, 2014), Fe-Ti oxides (Bryce & Farley, 2002; Kober et al., 2005; Shuster et al., 2012), apatite, zircon (Farley et al., 2006, Amidon et al., 2009) that cannot be studied with the workhorse radionuclides ^{10}Be and ^{26}Al. The production rate of $^{3}He_{cos}$ and $^{21}Ne_{cos}$ in minerals is strongly governed by the mineral chemical composition (Masarik, 2002; Kober et al., 2005). The need to quantify elemental production rates is clear.

The difficulty in finding adequately dated rock surfaces that contain the array of appropriate minerals makes it difficult to determine production rates in the standard manner. Previous attempts based on numerical models of particle fluxes in the Earth's atmosphere and cross-sections for the relevant nuclear reactions (Schaefer et al. 1999,

Masarik 2002, Kober et al. 2005) are summarized in sections 2.2 and 2.3. The theoretical models for production of cosmogenic ^{3}He present higher discrepancy than those proposed for Ne. In the case of cosmogenic ^{3}He differences on the assumption of the relative $^{3}He/^{3}H$ production ratio are the cause of up 60% difference in the production rate in mafic minerals between the two theoretical models. Masarik (2002) assume the $^{3}He/^{3}H$ production to be 1 while Kober et al. (2005) assume the relative production ratio to be that calculated by Leya et al. (2004) which in some cases is up to 3 times higher than unity. In the case of cosmogenic Ne the theoretical production rates of Mg and Si given by the two models are similar and consequently the theoretical production rate of mafic minerals are similar too.

This study aims to quantify the compositional dependence of the relative production of $^{3}He_{cos}$ and $^{21}Ne_{cos}$ in olivine, orthopyroxene, clinopyroxene and spinel from xenoliths from the summit (> 3,300 m) of the Mount Hampton volcanic edifice, Antarctica. The samples were selected specifically as a previous study (Moriera and Madureira, 2005) demonstrated they should contain high concentration (~10^{9} atoms/g of ^{3}He and ~10^{8} atoms/g of ^{21}Ne). To understand the composition dependence, the major element composition and cosmogenic ^{3}He and ^{21}Ne concentrations have been determined in different minerals. The data were compared to theoretical mineral production rates calculated using element-specific production rates of Masarik (2002) and Kober et al. (2005) to test the accuracy of the theoretical models.

5.2 Geological setting

The Marie Byrd Land (MBL) volcanic province consists of eighteen high elevation (> 3000 m) polygenetic shield and strato-volcanoes that protrude through the West Antarctic Ice Sheet (WAIS) (Le Masurier, 1990a). The volcanoes consist predominantly on felsic alkaline lavas (phonolite, trachyte and rhyolite in composition) with basanite and hawaiite present most commonly as parasitic vents and basal flows at the larger volcanoes (Le Masurier and Rex, 1989; Le Masurier 1990a; 1990b; Panter et al., 1994). The MBL is located in the southern flank of the West Antarctic Rift System, which extends ~4000 km from the western Ross Sea to the Antarctic Peninsula and is the only rift system on Earth that is covered by a continental-scale ice sheet (Le Masurier, 1990b; Panter et al., 1994; Paulsen and Wilson, 2010).

The volcanoes in the Marie Byrd Land appear to form a linear chain that joins to the perimeter of the province. The Executive Committee range (ECR) is a prominent volcanic chain that extends 100 km in a north-south direction in the centre of the MBL. It is formed by five major volcanoes. Volcanic activity has migrated southwards in the past 13.7 Ma (Le Masurier and Rex, 1989). The ECR volcanism has been described as a sequential release of magmas along a relict fracture system reactivated during Cenozoic extension of the West Antarctic Rift System (Le Masurier and Rex, 1989; Panter et al., 1994).

Mount Hampton is the northern-most volcano in the Executive Committee Range. It is one of the oldest volcanoes in the MBL with the main period of activity being the late Miocene (Le Masurier and Rex, 1989). The summit is 3,323 m above sea level and it is exposed as a nunatak ~1000 m above the WAIS level. Mount Hampton is one of two closely coalesced volcanoes: Mount Hampton and Whitney Peak. It is a shield volcano structure with 10-15˚ constructional slopes and shows no particular features of erosional dissection (Le Masurier, 1987). It is composed of phonolites with feldspar and augite phenocrysts and parasitic cone basanites that contain assemblages of xenoliths, the most common being spinel lherzolite (LeMasurier and Kawachi, 1987). The location of the MBL, the ECR and the area of study within Mount Hampton are shown in Figure 5.1.

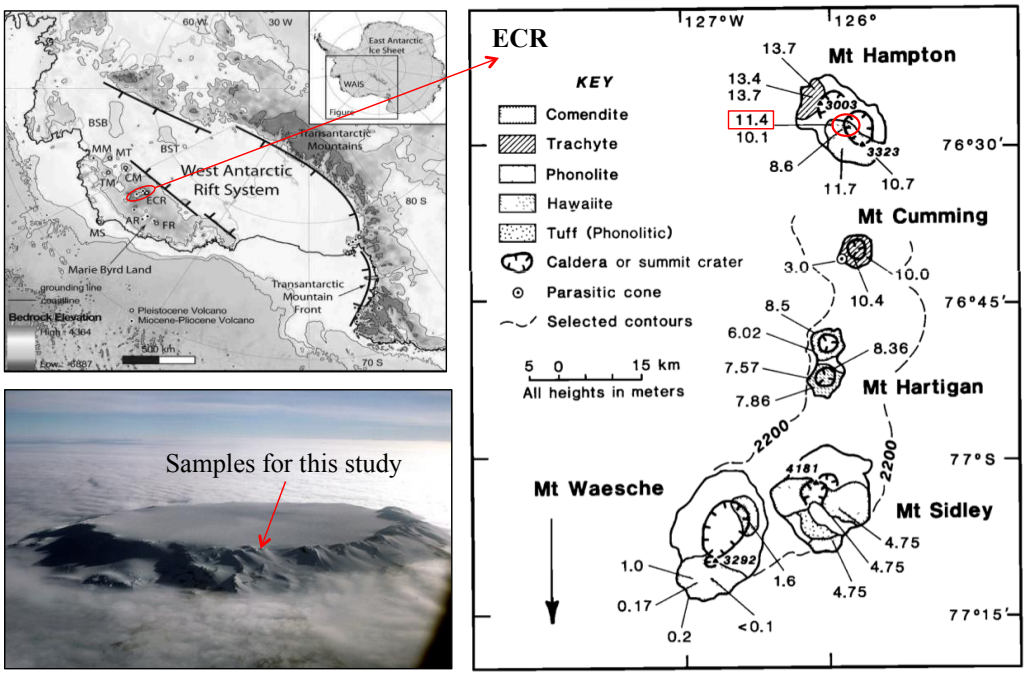

Figure 5.1. Maps and photograph of the location of Mount Hampton within the Executive Committee Range (ECR). Top left: Bed elevation map of Antarctica showing the location of the ECR within the Marie Byrd Land in the WAIS interior. Modified from Paulsen and Wilson (2010). Bottom left: Aerial photograph of Mount Hampton showing the sampling area for the xenoliths analysed in this study. Photograph donated by Prof. John Smellie, University of Leicester. Right: Geologic map of the ECR showing K-Ar ages. Modified from Le Masurier and Rex (1989).

5.3 Sample description

The samples studied in this thesis consist of seven lherzolite xenoliths from Mount Hampton (76˚ 30S 126˚W). Four xenoliths (MB.71.7, MB.71.8, MB.71.9 and MB.71.10) were provided by Prof. John Smellie from University of Leicester; two (MH.1 and MH.2) were provided by Prof. John Gamble from University of Cork and one (MM) was provided by Prof. Manuel Moreira from Institut de Physique du Globe de Paris, Université Paris. The samples were collected during the second season of the Antarctic expedition WAVE (West Antarctic Volcano Exploration) in January 1991. The samples were provided with the information that all samples were separated by a few meters and collected from the same surface near the Mount Hampton summit (~3200 m above sea-level) although the exact location of the samples is unknown. The samples were collected from loose scoriaceous material at the Mount Hampton summit. They consist on loose xenolith samples that are likely products of the same eruption that occurred at 11.4 Ma (LeMasurier and Rex, 1989). Photographs of the xenoliths and a petrographic description of thin sections are included in Appendix C.

5.4 Chemical and mineralogical composition

Semi-quantitative elemental composition analysis of all the samples was performed using scanning electron microscope analysis (SEM) at *ISAAC* at University of Glasgow. More precise measurements were made on minerals from five samples (MH.1, MH.2, MB.71.7, MB.71.8, MB.71.9) analysed by electron probe micro analyser at the *EPMA Facility* at School of Geosciences, University of Edinburgh for accurate chemical composition. Three analyses were performed on each grain, typically five to ten grains per mineral. The chemical compositions determined by SEM were within 2% of the value measured by EPMA.

The composition of each xenolith mineral expressed in relative Mg content is shown in Table 5.1. All the xenoliths present similar relative Mg contents with olivine compositions varying from Fo_{90} to Fo_{91}, orthopyroxene compositions ranging from En_{89} to En_{90} and clinopyroxene compositions ranging from En_{49} to En_{51}. Spinel shows more variability between xenoliths in particular related to the amounts of Cr and Al.

The average major element composition of each mineral from each xenolith is shown in Table 5.2 and all the major element data of the mineral grains are reported in Appendix C. Typically the minerals have homogenous composition with MgO weight % variations between the rim and the core of the individual grains of < 1% (1σ) and grain-to-grain variation of < 1% (1σ). In the case of FeO the variations between the rim and core of the grains and the grain-to-grain variations are typically < 3% (1σ). The compositional homogeneity will have minimal effect on variation of ^{3}He and ^{21}Ne production rates.

Table 5.1. Summary of the mineral composition for the different xenoliths from Mount Hampton.

Sample name	Olivine	Orthopyroxene	Clinopyroxene	Spinel
MH.1	Fo_{91}	En_{90}	En_{51}	Sp_{57}
MH.2	Fo_{90}	En_{90}	En_{50}	Sp_{68}
MB.71.7	Fo_{91}	En_{90}	En_{50}	Sp_{66}
MB.71.8	Fo_{90}	En_{90}	En_{50}	Sp_{58}
MB.71.9	Fo_{90}	En_{89}	En_{49}	Sp_{70}
MB.71.10	Fo_{90}	En_{89}	En_{50}	
MM	Fo_{91}	En_{89}	En_{50}	Sp_{41}

Compositions are expressed as forsterite (Fo(100*Mg/Mg+Fe)) in the case of olivine; enstatite (En(100*Mg/Mg+Fe+Ca)) for orthopyroxene and clinopyroxene and spinel (Sp(100*Mg/(Mg+Fe+Cr)) for spinel.

Table 5.2. Summary of the major-element composition for the different minerals from Mount Hampton xenoliths. Elemental compositions are reported as oxides (wt %) and are the average composition of 5 to 10 grains (3 measurements per grain). The results are normalised to 100. All the data obtained from EPMA and SEM are reported in Appendix C.

Sample	*Mineral*	*Method*	*MgO*	*FeO*	*SiO2*	*CaO*	*TiO2*	*MnO*	*Na2O*	*Al2O3*	*NiO*	*Cr2O3*
MH.1	ol	EPMA	50.91	8.94	39.52	0.08	0.00	0.12	0.01	0.02	0.40	0.00
MH.2	ol	EPMA	49.99	8.86	40.48	0.09	0.01	0.12	0.01	0.03	0.42	0.00
MB.71.7	ol	EPMA	50.94	9.11	39.30	0.07	0.01	0.13	0.00	0.02	0.41	0.00
MB.71.8	ol	EPMA	49.99	8.70	40.67	0.08	0.00	0.13	0.00	0.02	0.41	0.00
MB.71.9	ol	EPMA	49.19	10.63	39.56	0.06	0.01	0.14	0.00	0.02	0.38	0.00
MB.71.10	ol	SEM	48.42	9.90	41.02	0.00	0.00	0.22	0.00	0.00	0.43	0.00
MM	ol	SEM	49.52	9.15	41.33	0.00	0.00	0.00	0.00	0.00	0.00	0.00
MH.1	opx	EPMA	34.50	5.71	54.63	0.96	0.03	0.12	0.08	3.86	0.11	0.00
MH.2	opx	EPMA	32.74	5.47	55.83	0.98	0.05	0.12	0.08	4.61	0.12	0.00
MB.71.7	opx	EPMA	34.48	5.81	54.45	0.83	0.09	0.13	0.10	4.00	0.10	0.00
MB.71.8	opx	EPMA	33.89	5.53	55.99	0.95	0.02	0.13	0.04	3.34	0.11	0.00
MB.71.9	opx	EPMA	33.80	6.86	53.35	0.76	0.13	0.15	0.10	4.74	0.10	0.00
MB.71.10	opx	SEM	32.74	6.25	55.76	0.83	0.00	0.00	0.00	3.82	0.00	0.60
MM	opx	SEM	31.91	5.43	53.80	1.01	0.00	0.00	0.00	6.41	0.00	1.45
MH.1	cpx	EPMA	17.22	2.53	52.78	21.56	0.10	0.08	1.02	4.65	0.05	0.00
MH.2	cpx	EPMA	16.72	2.74	52.54	21.13	0.16	0.08	1.05	5.54	0.05	0.00
MB.71.7	cpx	EPMA	16.39	2.48	52.50	21.12	0.33	0.08	1.47	5.58	0.05	0.00
MB.71.8	cpx	EPMA	17.65	2.38	53.19	22.32	0.06	0.08	0.57	3.70	0.05	0.00
MB.71.9	cpx	EPMA	15.45	2.99	51.89	20.67	0.57	0.09	1.67	6.64	0.04	0.00
MB.71.10	cpx	SEM	15.49	2.83	51.85	19.88	0.78	0.00	1.83	5.94	0.00	1.41
MM	cpx	SEM	16.30	2.42	50.33	20.40	0.00	0.00	0.86	7.27	0.00	2.41
MH.1	sp	SEM	11.87	6.46	0.00	0.00	0.00	0.00	0.00	61.37	0.00	20.31
MH.2	sp	EPMA	20.61	10.09	0.12	0.00	0.00	0.11	0.00	52.65	0.37	16.05
MB.71.7	sp	SEM	13.52	4.33	0.00	0.00	0.00	0.00	0.00	64.45	0.00	17.69
MB.71.8	sp	EPMA	18.91	11.24	0.11	0.00	0.00	0.15	0.00	40.81	0.25	28.54
MB.71.9	sp	EPMA	20.75	11.15	0.10	0.00	0.00	0.10	0.00	57.81	0.39	9.70
MM	sp	SEM	10.35	7.29	0.00	0.00	0.00	0.00	0.00	42.26	0.00	40.10

SEM- Scanning Electron Microscopy, undertaken at *ISAAC* at University of Glasgow. Data from SEM analysis are used in the cases where no EPMA was performed. EMPA- Electron Microprobe Analysis, undertaken at University of Edinburgh.
ol-olivine; opx-orthopyroxene; cpx-clinopyroxene; sp-spinel

5.5 Noble gas determination methods

All xenoliths yielded enough olivine, clinopyroxene and orthopyroxene, and six yielded enough spinel, for He and/or Ne isotope analysis. All the samples were crushed and sieved and mineral concentrated from the 125-250 μm and 250-500 μm fractions were separated by hand-picking under binocular microscope and only inclusion free grains were selected. The mineral separates were cleaned in analar acetone.

Helium isotope analyses were performed using the Helix SFT described in Chapter 3. Aliquots of 5-15 mg were encapsulated in Pt tubes and degassed using a diode laser following the procedures described in Chapter 4. For this work the 250-500 μm mineral grains were crushed to < 100 μm to promote degassing during laser heating. Samples were heated to ~1300˚C. The magmatic ^{3}He contribution was determined on olivine (~300 mg) from xenolith MH.1 on gas released by *in vacuo* crushing using an all-metal multi-sample hydraulic crusher described in Appendix B.

The Ne isotope composition of minerals from six xenoliths (MH.1, MH.2, MB.71.7, MB.71.8, MB.71.9 and MB.71.10) was analysed using the MAP 215-50. These procedures are described in Appendix A. Aliquots of 30-90 mg were wrapped in Mo foil and degassed using a resistance-heated double vacuum furnace described in Appendix B. Only one sample (MB.71.7) yielded sufficient spinel for Ne isotope measurement. Orthopyroxene and clinopyroxene aliquots from 3 of the samples (MH.2, MB.71.8 and Mb.71.9) were degassed using a diode laser directly on to unencapsulated grains (see Chapter 4 for details). All samples were heated to ~1300˚C for 20 minutes.

5.6 Results

5.6.1 Helium isotopes

Duplicate measurements generally show reproducibility of < 4% with 6 samples showing > 10% dispersion. ^{3}He concentrations range from 1.4 x 10^{8} to 1.8 x 10^{9} atoms/g. These are amongst the highest ^{3}He concentrations measured in terrestrial samples; previously only measured in high altitude, low erosion rate landscapes such as Antarctica

and the Atacama desert (e.g. Schaefer et al., 1999; Margerison et al., 2005, Moreira and Madureira, 2005; Evenstar et al., 2009; see Figure 5.2).

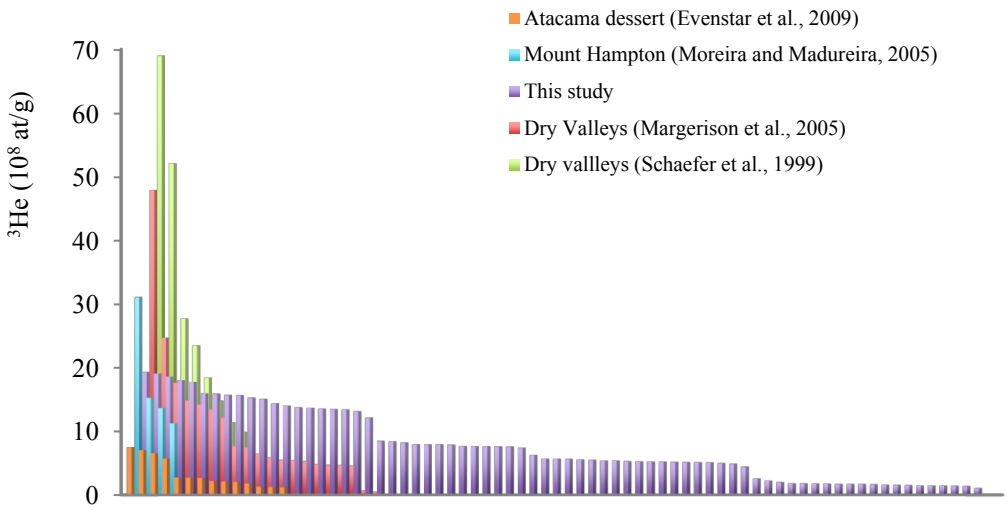

Figure 5.2. Histogram of the highest cosmogenic ^{3}He concentrations measured on Earth amongst which the data from Mount Hampton xenoliths used in this study are found.

$^{3}He/^{4}He$ ratios obtained from complete degassing of the samples generally range from 0.024 to 52 x 10^{3} R_A. These are amongst the highest $^{3}He/^{4}He$ measured in terrestrial samples and are comparable to the cosmic ray dominated signatures measured in meteorites (e.g. Bogard and Cressy, 1973; Cressy and Bogard, 1976).

Determining the $^{3}He_{cos}$ concentrations in minerals from old rocks requires accounting for the contribution of nucleogenic and inherited (mantle-derived) ^{3}He (Margerison et al. 2005). The Li content of olivine and pyroxene from mantle xenoliths is typically low (< 2 ppm) (Seitz et al., 2004; Ryan and Kyle, 2004). The concentration of nucleogenic ^{3}He produced from the $^{6}Li(n,\alpha)^{3}H(\beta)^{3}He$ reaction in 11.7 Ma considering a production rate of 0.04 atoms/g/year (Dunai et al., 2007 and references therein) represents < 0.3% of the measured ^{3}He. Thus nucleogenic ^{3}He can be excluded.

The high $^{3}He/^{4}He$ ratios obtained from heating the samples suggest that no discernible radiogenic ^{4}He from the decay of U and Th is present in the samples. MH.1 olivine was crushed in vacuum to determine the magmatic He concentration. It yielded 3.85 ± 0.67 x 10^{5} ^{3}He atoms/g with a $^{3}He/^{4}He$ ratio of 9.02 ± 1.64 R_A. Given the likely high cosmogenic He concentration, it can be assumed that the crush-released ^{3}He is a mixture of mantle and cosmogenic sources. Panter et al. (2000) characterized the basalts from the Marie Byrd Land to have a strong HIMU signature with no evidence of crustal

contamination. Assuming a $^3He/^4He$ ratio of 6.5 ± 0.6 R_A for the magmatic He (Parai et al., 2009 and references therein), and 1.8 ± 0.5 x 10^5 R_A for cosmogenic He (Wieler, 2002) the contribution of each component can be determined (Table 5.3).

Table 5.3. Helium isotope data from in vacuum crushing of olivine from MH.1 xenolith.

MH.1 olivine				
Weight (mg)	*Crushed (mg)*	*^4He (10^{10} at/g)*	*^3He (10^5 at/g)*	*$^3He/^4He$ (R_A)*
284	105	3.07 ± 0.16	3.85 ± 0.67	9.02 ± 1.64
Magmatic component		3.07 ± 0.85	2.77 ± 0.81	6.5 ± 0.6
Cosmogenic component		-	1.08 ± 0.29	1.8 ± 0.6 x 10^5

The magmatic and cosmogenic components have been calculated assuming a HIMU mantle source (Panter et al., 2000) with a $^3He/^4He$ ratio of 6.5 ± 0.6 R_A (Parai et al., 2009 and references therein) and a cosmogenic $^3He/^4He$ ratio of 1.8 ± 0.5 x 10^5 R_A (Wieler, 2002). The calculated cosmogenic ^4He represents 0.02 ppb of the total ^4He released from crushing. Uncertainties are reported as 1σ.

The magmatic ^3He (2.77 ± 0.81 x 10^5 atoms/g) represents < 0.2% of the total ^3He released from the heating step therefore its contribution can be neglected. The $^3He_{cos}$ released from crushing (1.08 ± 0.29 x 10^5 atoms/g) represents < 0.1% of the total $^3He_{cos}$ in a sample. This demonstrates that the crushing method at SUERC does not release a significant proportion of the cosmogenic He (cf. Blard et al 2006). The low contribution of non-cosmogenic ^3He (magmatic and nucleogenic) implies that all the ^3He released from degassing the samples can be considered to be cosmogenic in origin. The measured ^3He concentrations and $^3He/^4He$ ratios of all samples are presented in Table 5.4.

Table 5.4. Helium isotope data of the different minerals from 7 lherzolite xenoliths from Mount Hampton.

Sample name	*Mineral*	*weight (mg)*	*$^3He_{cos}$ (10^8 atoms/g)*	±	*$^3He/^4He$ (R_A)*	±
MH.1	Ol	9.7	15.77	0.19	8,429	198
MH.1	Ol	11.2	15.73	0.19	15	1
MH.1	Opx	10.7	15.97	0.17	17,148	819
MH.1	Cpx	8.7	12.62	0.19		
reheat*			2.53	0.07		
total			***15.15***	***0.20***	***1,883***	***34***
MH.1	Sp	16.1	12.19	0.15		
reheat			0.61	0.03		
total			***12.80***	***0.16***	***52,442***	***6,030***
MH.1	Sp	1.9	13.08	0.36		
reheat			0.53	0.07		
total			***13.61***	***0.36***	***6,758***	***354***
MH.2	Ol	12.0	8.43	0.14	211	4
MH.2	Ol	13.5	8.12	0.15		
reheat		13.5	0.15	0.02		
total			***8.27***	***0.15***	***1,469***	***33***
MH.2	Ol	12.1	7.44	0.12	5,849	156
MH.2	Ol	14.0	7.96	0.11	4,902	101
MH.2	Ol	12.2	7.68	0.13	5,001	157
MH.2	Ol	14.9	7.62	0.12	10,693	245
MH.2	Ol	15.0	7.65	0.12	11,543	279
MH.2	Ol	11.3	8.52	0.15		
MH.2	Ol	16.6	7.91	0.13	2,330	48
MH.2	Ol	17.0	7.70	0.10		
reheat			-	-		
total			***7.70***	***0.10***	***2,698***	***47***
MH.2	Opx	11.8	7.96	0.11		
reheat			0.00	0.01		
total			***7.96***	***0.11***	***33,208***	***3,750***
MH.2	Cpx	17.3	7.98	0.13	4,618	101

Sample name	*Mineral*	*weight (mg)*	*$^{3}He_{cos}$ (10^{8} atoms/g)*	±	*$^{3}He/^{4}He$ (R_A)*	±
MH.2	Cpx	12.7	5.52	0.12		
reheat			0.23	0.03		
total			***5.75***	***0.12***	***3,879***	***138***
MH.2	cpx	12.40	5.16	0.09		
reheat			-	-		
total			***5.16***	***0.09***	***4,280***	***137***
MH.2	cpx	10.50	4.46	0.08	4,952	119
MH.2	cpx	14.90	5.01	0.07	5,727	251
MH.2	cpx	13.00	7.67	0.08	1,283	21
MH.2	sp	11.80	6.00	0.13		
reheat			0.31	0.04		
total			***6.31***	***0.13***	***4,604***	***159***
MH.2	sp	7.20	5.41	0.37		
reheat*			0.55	0.04		
total			***5.96***	***0.37***	***7,462***	***833***
MB.71.7	ol	6.40	2.24	0.06	7	1
MB.71.7	ol	13.70	1.78	0.05		
reheat			0.01	0.00		
total			***1.79***	***0.05***	***24***	***1***
MB.71.7	ol	9.50	1.77	0.06	134	5
MB.71.7	opx	14.40	1.71	0.05	1,037	36
MB.71.7	opx	11.50	1.81	0.06		
reheat			-	-		
total			***1.81***	***0.06***	***2,385***	***121***
MB.71.7	cpx	12.80	1.60	0.04		
reheat			0.04	0.01		
total			***1.64***	***0.04***	***414***	***12***
MB.71.7	cpx	15.40	2.01	0.05	170	5
MB.71.7	cpx	11.60	1.71	0.06		
reheat			0.00	0.01		
total			***1.71***	***0.06***	***183***	***7***
MB.71.7	sp	9.50	1.82	0.05	175	6
MB.71.7	sp	2.80	1.38	0.10		
reheat			-	-		
total			***1.38***	***0.10***	***46***	***4***
MB.71.8	ol	12.30	18.10	0.21		
reheat			0.84	0.04		
total			***18.94***	***0.21***	***2,524,337***	***3,415,283***
MB.71.8	ol	16.40	18.47	0.19		
reheat			0.20	0.02		
total			***18.67***	***0.19***	***1,126***	***18***
MB.71.8	opx	11.10	19.40	0.21	97,445	7,938
MB.71.8	cpx	8.70	17.83	0.27	10,604	281
MB.71.8	cpx	6.10	19.16	0.31	8,810	226
reheat			0.03	0.03		
MB.71.8	sp	12.90	13.83	0.44		
total			***13.86***	***0.44***	***9,392***	***321***
MB.71.8	sp	2.40	12.84	0.68		
reheat			0.35	0.05		
total			***13.19***	***0.68***	***9,614***	***944***
MB.71.9	ol	18.00	5.26	0.09	432	9
MB.71.9	ol	12.90	5.11	0.08		
reheat			0.01	0.01		
total			***5.13***	***0.08***	***543***	***11***
MB.71.9	ol	14.90	5.68	0.09	396	8
MB.71.9	ol	12.40	5.40	0.11	174	4
MB.71.9	opx	13.00	5.69	0.17	679	23
MB.71.9	cpx	11.70	5.19	0.07		
reheat			0.00	0.00		
total			***5.19***	***0.07***	***293***	***5***
MB.71.9	cpx	14.80	5.59	0.09	173	4
MB.71.9	cpx	14.20	5.48	0.09		
reheat			0.00	0.00		
total			***5.48***	***0.09***	***227***	***4***
MB.71.9	cpx	10.60	5.31	0.10		
reheat			-	-		
total			***5.31***	***0.10***	***397***	***9***
MB.71.9	cpx	8.60	4.96	0.12		
reheat			0.32	0.02		
total			***5.27***	***0.12***	***247***	***7***
MB.71.9	sp	15.00	4.91	0.09	935	20
MB.71.9	sp	15.60	4.88	0.08		
reheat*			0.83	0.04		
total			***5.71***	***0.09***	***502***	***10***
MB.71.9	sp	8.50	4.79	0.11		
reheat*			0.44	0.04		
total			***5.24***	***0.12***	***383***	***10***

Sample name	*Mineral*	*weight (mg)*	*$^{3}He_{cos}$ (10^{8} atoms/g)*	±	*$^{3}He/^{4}He$ (R_A)*	±
MB.71.9	sp	6.00	5.03	0.12		
reheat			0.11	0.02		
total			***5.14***	***0.12***	***702***	***20***
MB.71.10	ol	13.00	2.58	0.06	532	14
MB.71.10	ol	13.40	1.56	0.05	783	30
MB.71.10	ol	8.00	1.53	0.06	35	2
MB.71.10	ol	12.60	1.47	0.04	63	2
MB.71.10	ol	10.60	1.46	0.04	449	14
MB.71.10	opx	11.70	1.72	0.06		
reheat			-	-		
total			***1.72***	***0.06***	***596***	***21***
MB.71.10	opx	8.70	1.43	0.08	832	52
MB.71.10	cpx	13.30	1.67	0.05	138	4
MB.71.10	cpx	12.00	1.47	0.05	169	6
MB.71.10	cpx	9.10	1.05	0.05		
reheat			0.02	0.01		
total			***1.06***	***0.05***	***107***	***8***
MM	ol	15.40	14.81	0.21		
reheat			0.56	0.03		
total			***15.36***	***0.21***	***14,199***	***275***
MM	ol	15.70	13.68	0.17		
reheat			0.07	0.01		
total			***13.75***	***0.17***	***21,225***	***780***
MM	opx	16.10	14.08	0.23		
reheat			-	-		
total			***14.08***	***0.23***	***6,428***	***140***
MM	opx	13.80	16.03	0.25	8,164	191
MM	cpx	11.60	14.47	0.20	260	4
MM	sp	8.50	13.53	0.23	4,056	98
MM	sp	9.40	13.49	0.16		
reheat			0.11	0.02		
total			***13.59***	***0.16***	***2,566***	***44***

The uncertainties reported are the propagated analytical 1σ uncertainties. 40% of the samples have been reheated. Typically < 5% of the total ^{3}He concentration (7 samples didn't release any ^{3}He) was released on the reheat with the exception of 4 samples (*) that released > 5%.
ol-olivine; opx-orthopyroxene; cpx-clinopyroxene; sp-spinel

5.6.2 Neon isotopes

Neon isotope data from olivine, orthopyroxene, clinopyroxene and spinel are presented in Table 5.5 and plotted on a conventional three-isotope diagram in Figure 5.2. The samples degassed using the diode laser generally released less air-derived Ne than those degassed using the double-walled vacuum furnace. In the case of sample MB.71.9, two aliquots of orthopyroxene were analysed using the diode laser and the furnace with the aliquot degassed using the furnace releasing one order of magnitude higher ^{20}Ne and consequently one order of magnitude lower $^{21}Ne/^{20}Ne$ ratio. The cosmogenic ^{21}Ne ($^{21}Ne_{cos}$) concentrations measured in the samples degassed using the laser was ~20% higher than that obtained using the furnace with the exception of orthopyroxene from MH.2 and MB.71.8 where the $^{21}Ne_{cos}$ concentrations from laser and furnace degassing agree within uncertainty. The results from laser degassing have not been used for $^{21}Ne_{cos}$ production rate variation with elemental composition.

Table 5.5. Neon isotope data of the different minerals from 6 lherzolite xenoliths from Mount Hampton.

Sample name	*Mineral*	*Weight (mg)*	*$^{21}Ne_{cos}$ (10^{8} atoms/g)*	±	*$^{21}Ne/^{20}Ne$ (10^{-2})*	±	*$^{22}Ne/^{20}Ne$ (10^{-2})*	±
MH.1	ol	75.9	5.61	0.19	7.98	0.10	18.59	0.16
MH.1	opx	45.3	4.42	0.15	4.57	0.06	13.16	0.18
MH.1	cpx	28.3	3.07	0.13	1.75	0.04	11.72	0.14
MH.2	ol	84.3	3.37	0.11	3.39	0.04	13.67	0.08
MH2	ol	29.1	3.19	0.11	1.63	0.02	11.66	0.10
MH.2 *	opx	59	2.41	0.10	20.04	0.36	32.45	0.68
MH.2	opx	65	2.60	0.10	1.72	0.03	11.80	0.06
MH.2 *	cpx	94.5	1.42	0.05	10.99	0.20	23.73	0.51
MH.2	cpx	26.1	1.82	0.07	1.82	0.04	12.72	0.30
MB.71.7	ol	53.1	0.57	0.04	0.71	0.02	10.52	0.10
MB.71.7	opx	47.7	0.48	0.03	0.59	0.03	10.24	0.13
MB.71.7	cpx	40.3	0.40	0.02	0.47	0.02	10.59	0.19
MB.71.7	sp	14.4	0.79	0.22	0.49	0.05	10.21	0.09
MB.71.8	ol	53	7.97	0.25	5.61	0.05	16.18	0.08
MB.71.8 *	opx	75.6	6.07	0.29	85.04	2.30	105.26	3.15
MB.71.8	opx	36.2	6.20	0.23	7.63	0.13	19.40	0.36
MB.71.8*	cpx	41.6	3.97	0.21	37.24	1.17	54.15	1.86
MB.71.8	cpx	13.9	4.81	0.21	1.53	0.04	11.95	0.18
MB.71.9	ol	57.4	2.38	0.08	1.38	0.02	11.17	0.06
MB.71.9*	opx	75.7	1.52	0.07	19.99	0.51	32.32	1.00
MB.71.9	opx	70.1	1.89	0.06	1.77	0.02	12.18	0.06
MB.71.9 *	cpx	66.5	1.05	0.04	5.22	0.11	17.27	0.36
MB.71.10	ol	71.5	0.55	0.03	1.08	0.04	10.98	0.12
MB.71.10	opx	74.6	0.39	0.01	0.60	0.02	10.59	0.13

The uncertainties reported are the propagated analytical 1σ uncertainties. Samples have been degassed using a furnace with the exception of * that have been degassed using the diode laser. The results shown in this table have been corrected for mass spectrometer depletion.
ol-olivine; opx-orthopyroxene; cpx-clinopyroxene; sp-spinel

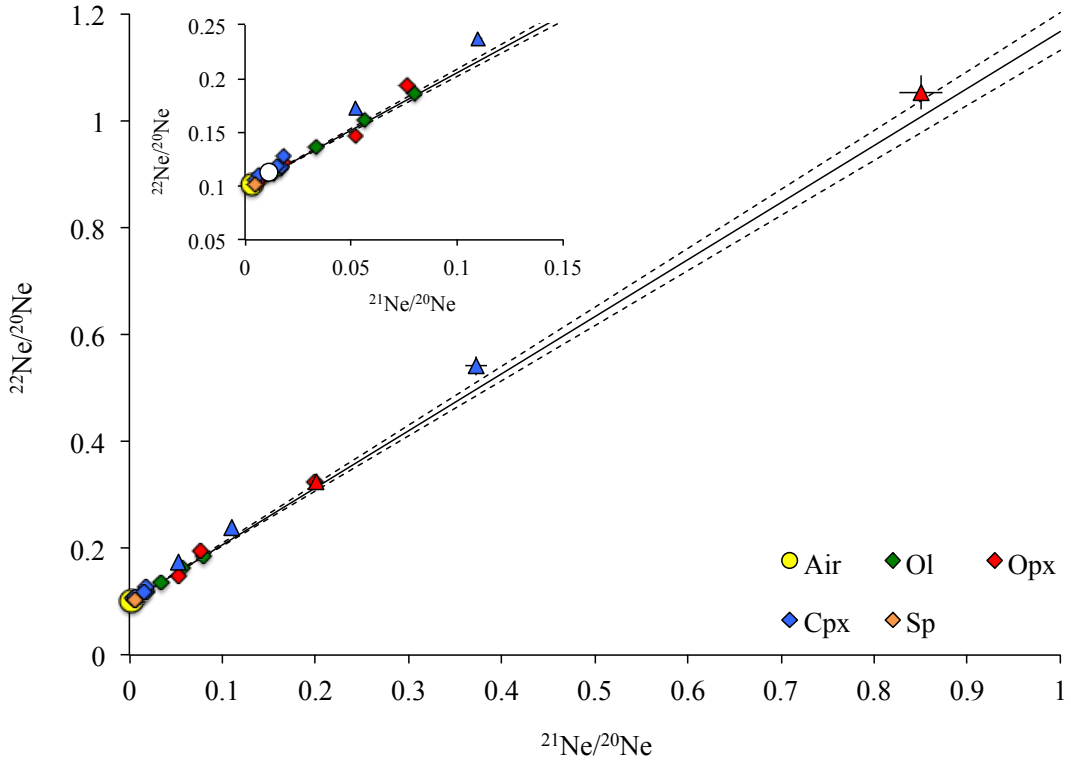

Figure 5.3. Neon isotope data of mineral separates from Antarctic xenoliths. The continuous line is the empirical terrestrial cosmogenic spallation line for pyroxene defined by Schaefer et al., (1999), and the dashed lines represent the 2σ uncertainty. The white circle in the inset figure represents the typical composition of the CREU quartz internal standard (Vermeesch et al., 2015); which defines the limit of the commonly measured $^{22}Ne/^{21}Ne$ ratios. Triangles represent the samples degassed using a diode laser; diamonds are samples that have been degassed using a furnace.

Most data fall within the 2σ uncertainty limits of the air-cosmogenic Ne mixing line produced from spallation reactions as defined by Antarctic pyroxene (En_{43-44}) (Schaefer et al., 1999). All samples show a strong cosmogenic Ne component with almost half of the samples (n = 10) yielding higher $^{21}Ne/^{20}Ne$ and $^{22}Ne/^{20}Ne$ than the cosmogenic Ne-rich CREU quartz mineral standard (Vermeesch et al., 2012); which defines the limit of the commonly measured terrestrial samples. The Ne isotope composition of orthopyroxene from MB.71.8 is comparable to ratios measured in extra-terrestrial material.

Some data do not lie on the air-cosmogenic mixing line. Samples with low air-derived Ne (0.5 to 8 x 10^4 atoms $^{20}Ne/g$) require corrections for $^{40}Ar^{2+}$ and $^{44}CO_2^{2+}$ that are significant (up to 20% in the case of $^{40}Ar^{2+}$ and up to 50% for $^{44}CO_2^{2+}$). It is well established that $^{40}Ar^{2+}$ is dependent on the partial pressure of the mass spectrometer source (first-order relationship between $^{40}Ar^{+}/^{40}Ar^{2+}$ and H^+, Vermeesch et al., 2012). It is not clear what the residual gas species are as He, CO, CH_4 are not routinely measured, although the presence of any of those could potentially increase the partial pressure in the ionization region of the source altering the relative production of $^{40}Ar^{2+}$. An increase of 20% in the $^{40}Ar^{+}/^{40}Ar^{2+}$ is enough to plot the data on the spallation line. It is important to note that variations in the $^{40}Ar^{+}/^{40}Ar^{2+}$ correction do not affect the $^{21}Ne_{cos}$ calculation.

The extremely high $^{21}Ne_{cos}$ concentrations (0.2 to 8 x 10^8 atoms/g) and $^{21}Ne/^{20}Ne$ (up to 0.85) are comparable to the cosmogenic signatures measured in meteorites. As the air standard ($^{21}Ne/^{20}Ne = 0.0029$) is used for mass fractionation determination, small non-linearity in electron multiplier sensitivity may generate large differences in cosmogenic ^{21}Ne concentrations. One eucrite sample (Millbillillie), one Martian shergottite (Tissint) and two L6 chondrites (Strathmore and High Possil) were analysed in order to confirm that analysis of extreme compositions are not affected by calibration at low $^{21}Ne/^{20}Ne$ and $^{22}Ne/^{20}Ne$ (i.e. air). Details of the analysis of the extra-terrestrial samples and the data collected are given in Appendix D.

The neon isotopic compositions corrected for mass spectrometer fractionation are compared with previously published data (Figure 5.4). Data from Millbillillie are compared with previously published data from different fragments (Michel and Eugster, 1989; Miura et al., 1998) and with unpublished data from two independent laboratories: IGGCAS (Institute of Geology and Geophysics Chinese Academy of Science, Beijing) and IGS (Institute of Geological Science, University of Berne) from the same fragment of the eucrite used for an inter-laboratory comparison. The average $^{21}Ne/^{22}Ne$ and $^{20}Ne/^{22}Ne$

ratios from the inter-laboratory comparison are 0.888 ± 0.019 and 0.893 ± 0.023 uncertainty representing 2% and 3% respectively. The agreement of the $^{21}Ne/^{22}Ne$ and $^{20}Ne/^{22}Ne$ ratios from the three laboratories suggests that the correction due to fractionation is correct and corroborates the accuracy of the measured ratios. The results from Strathmore and High Possil are compared with the L6 chondrites inventory (Schultz and Kruse, 1989) with neon isotopic ratios that are within the expected range. Tissint shergottite results were compared with the shergottite inventory (Garrison et al., 1995) with neon isotopic signatures that agree with shielded shergottite compositions. The results from the analysis of different extra-terrestrial material corroborate the validity of the method utilized for neon isotopic composition of the Mount Hampton xenoliths.

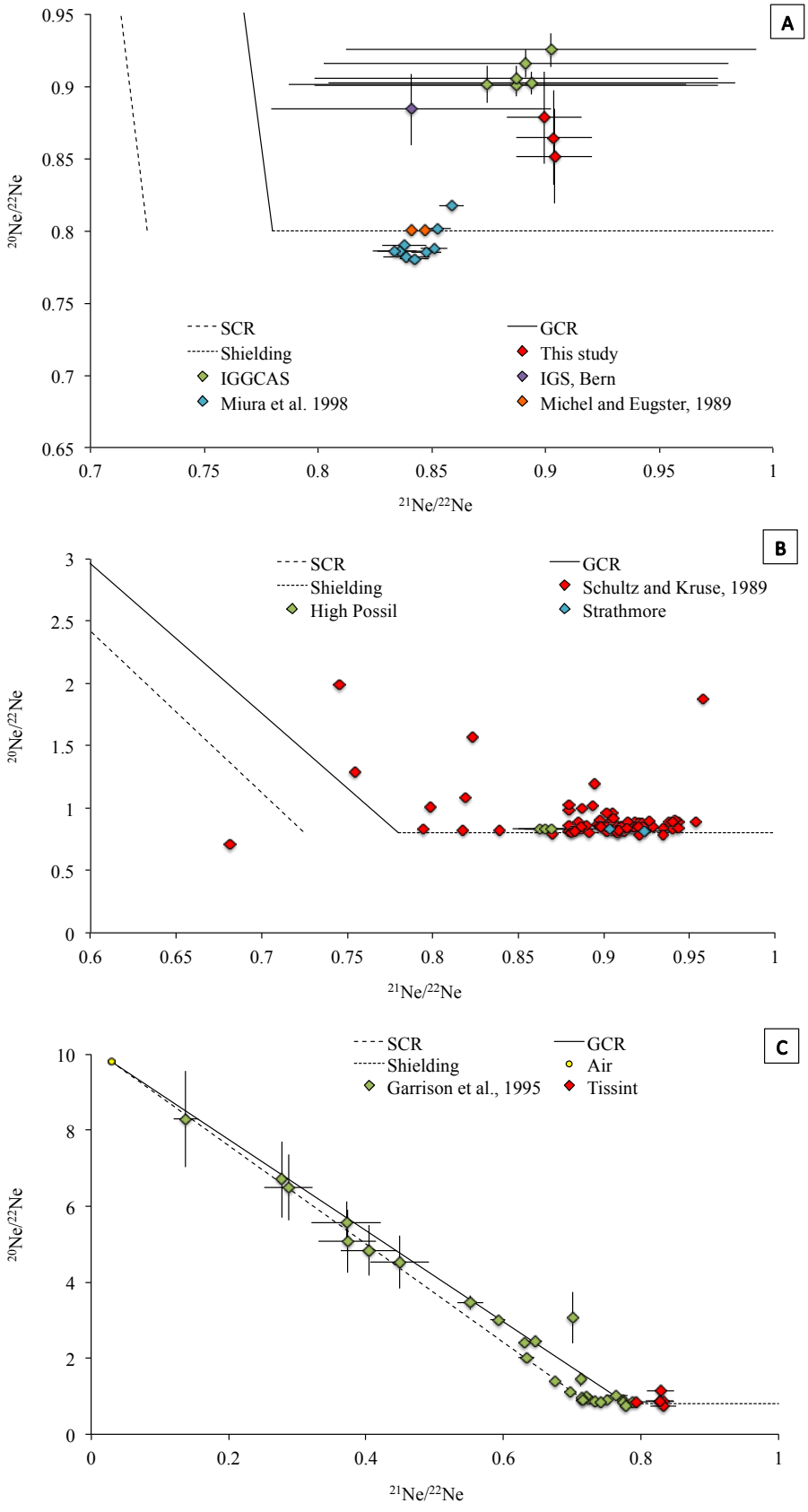

Figure 5.4. Neon isotope data from the analysis of: (A) one eucrite sample (Millbillillie); (B) two L-6 chondrites (High Possil and Strathmore) and (C) one shergottite (Tissint). The results are compared with previously published data and in the case of Millbillillie eucrite also with unpublished data from two laboratories (Chinese and Bern) for an inter-laboratory comparison. The continuous line represents the Galactic cosmic ray (GCR) signature and the discontinuous line the Solar Cosmic Ray (SCR) component with the dotted line representing GCR signature with complete shielding. GCR and SCR mixing lines are taken from Garrison et al., 1995. Theoretical shielding line is taken from Hohenberg et al. (1978). The plotted uncertainties are 1σ.

The Ne isotope composition of the meteorites, the Mount Hampton xenolith results from this work and previously published data from Mount Hampton olivine (Moreira and Madureira, 2005) are plotted in Figure 5.5. The neon isotopic compositions of the xenoliths are spread both sides of the Galactic Cosmic Ray (GCR) line with the majority of them showing terrestrial cosmogenic signature. The GCR Ne in meteorites is produced by spallation reactions induced by primary and secondary high-energy particles (Hohenbergh et al. 1078; Leya et al., 2000) while the production on earth is mostly due to secondary neutrons of lower energy (Gosse and Phillips, 2001). Generally the isotopic compositions of the samples agree within uncertainty with the terrestrial air-spallation mixing line defined by Schaefer et al (1999). These data confirm that the particles responsible for cosmogenic nuclide production at high latitude and altitude are of higher energy that those responsible for production at lower latitudes-altitudes showing in some cases isotopic signatures characteristic of extra-terrestrial material (Lal, 1991; Stone, 2000).

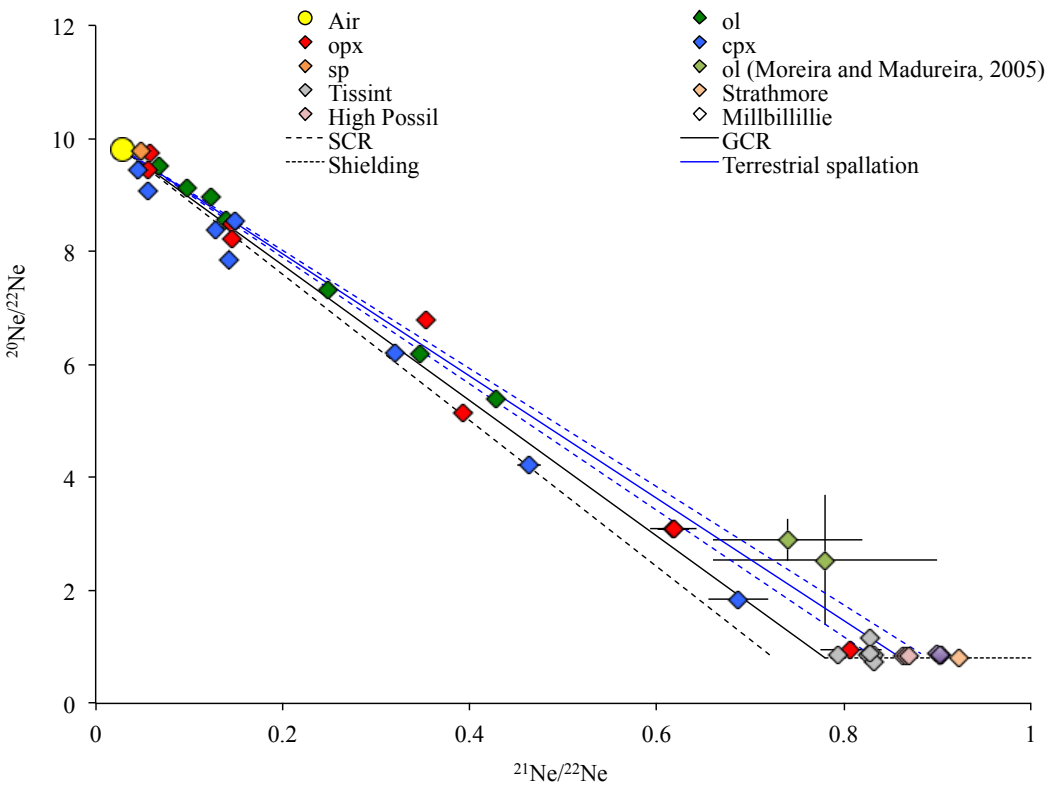

Figure 5.5. Neon isotope data from the analysis of Mount Hampton xenolith minerals plotted in a neon three-isotope diagram and compared with results from the analysis of extra-terrestrial samples and previously reported neon data from Mount Hampton (Moreira and Madurera, 2005). The plotted uncertainties are 1σ. GCR and SCR mixing lines are taken from Garrison et al., 1995. Theoretical shielding line is taken from Hohenberg et al. (1978).
GCR-Galactic Cosmic rays; SCR-Solar Cosmic Rays

The results of $^{21}Ne_{cos}$ concentrations for the different minerals from the xenoliths are compared with previously published data from Mount Hampton (Moreira and Madureira, 2005) in Figure 5.5. The dispersion of the $^{21}Ne_{cos}$ from the different xenoliths

suggest that they have had different cosmic ray irradiation history, consistent with the cosmogenic He data. Generally, olivine from all the xenoliths yielded the highest $^{21}Ne_{cos}$ concentration, more than clinopyroxene and orthopyroxene. Only one spinel sample was analysed (from xenolith MB.71.7) and the $^{21}Ne_{cos}$ concentration of olivine is indistinguishable within uncertainty with that of spinel. Our dataset is in agreement with previously published $^{21}Ne_{cos}$ concentration (Moreira and Madureira, 2005) ratifying the validity of the analytical method.

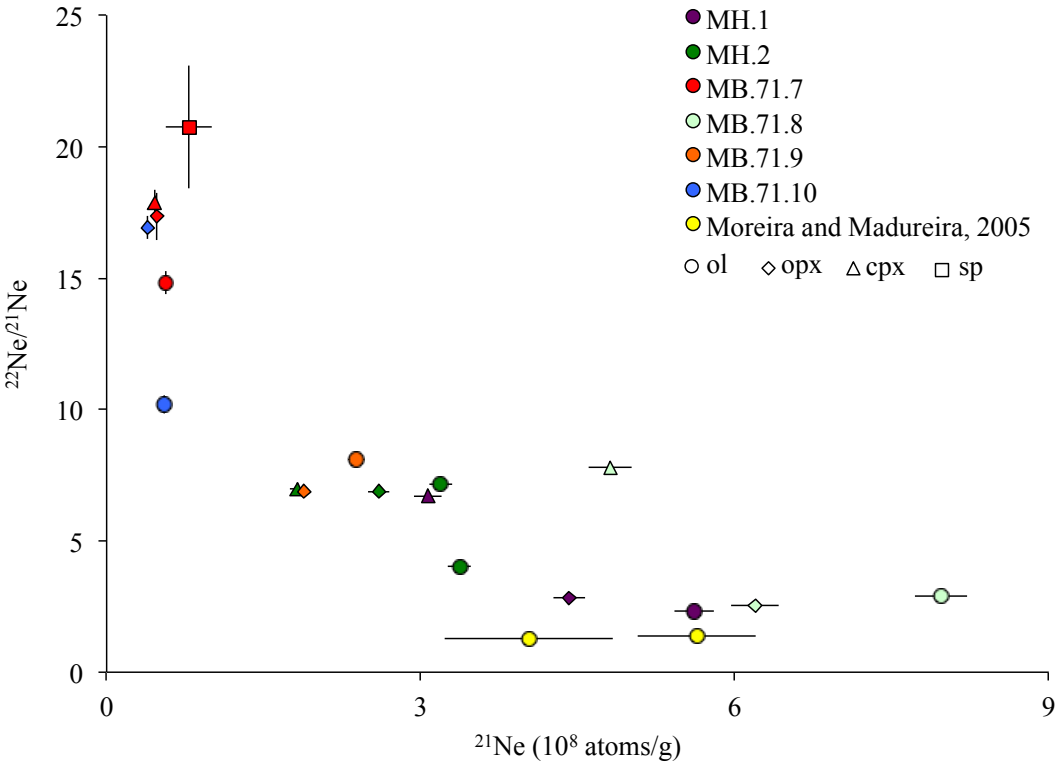

Figure 5.6. Plot of the $^{22}Ne/^{21}Ne$ ratio against ^{21}Ne concentrations for the different minerals analysed from Mount Hampton. Only results from furnace heating have been included in this diagram. The plotted uncertainties are 1σ.

5.7 Mineral chemistry control on the production of cosmogenic ^{3}He and ^{21}Ne

To quantify the compositional control on the production of cosmogenic ^{3}He and ^{21}Ne the experimentally determined concentrations for the different minerals present in a sample have been compared with compositional-based production rates based on the model calculations of Masarik (2002) and Kober et al. (2005).

5.7.1 Production rate calculation based on mineral composition

The production rate of cosmogenic nuclides in minerals is based on the sum of the elemental production rates for a given mineral (Lal, 1991; Masarik, 2002; Kober et al., 2005). In this study I compare olivine, orthopyroxene, clinopyroxene and spinel. The major-element concentrations vary between those minerals (see section 5.4.1) and the $^{3}He_{cos}$ and $^{21}Ne_{cos}$ production rates vary consequently. Theoretical production rates for each of the different minerals present in Mount Hampton xenoliths have been calculated based on the models of Masarik (2002) and Kober et al. (2005) for the major-element concentrations measured on each mineral using Equation 5.1 as follows:

$$Pm = \frac{\sum Xi \times Ai \times Pi}{W} \quad [5.1]$$

where Xi is the molar fraction of the element i (Mg, Fe, Ca, Na, Si, Al, O); Ai is the atomic mass (g/mol); Pi is the production rate (atoms/g/year) of $^{3}He_{cos}$ or $^{21}Ne_{cos}$ from the respective element i (Table 5.6); W is the molecular weight (g/mol) of the mineral of interest and Pm is the total production rate (atoms/g/year) of $^{3}He_{cos}$ or $^{21}Ne_{cos}$ for the mineral of interest.

The element specific production rates for $^{3}He_{cos}$ and $^{21}Ne_{cos}$ from the numerical models of Masarik (2002) and Kober et al. (2005) are summarized in Table 5.6. Production rates of Kober et al. (2005) are generally higher than those of Masarik (2002). In the case of $^{3}He_{cos}$, Kober et al. (2005) calculate production rates that are 20% (Si) to 150% (Fe) higher than those of Masarik (2002). In the case of $^{21}Ne_{cos}$, Kober et al. (2005) calculate production rates that are 5% (Si) to 85% (Ca) higher than those of Masarik (2002) (see section 2.1.5 for details on the two models). These generate different production rates in olivine, orthopyroxene, clinopyroxene and spinel minerals.

The different xenoliths are loose material from the same surface and they record different minimum exposure ages. Therefore, cosmogenic ^{3}He and ^{21}Ne concentrations cannot be used to determine absolute production rates. Here I normalize mineral-specific production rates calculated by Masarik (2002) and Kober et al. (2005) to orthopyroxene, and compare with those determined from the concentrations obtained by the analysis of the Mount Hampton xenolith minerals. For the cosmogenic ^{3}He production rate calculations production from Cr has been assumed to be indistinguishable from Fe due to their similar

atomic masses. Kober et al. (2005) does not provide the production rate of cosmogenic ^{3}He from Ca. Based on the relationship of the production rate given by Masarik (2002) and Kober et al. (2005) for Mg (Kober et al. (2005) calculates 61% higher production rate than Masarik (2002)) the production of Ca for the Kober et al. (2005) model is calculated to be 95 atoms/g/year (the same as Fe).

Table 5.6. Element specific production rates (atoms/g/yr) for $^{3}He_{cos}$ and $^{21}Ne_{cos}$ given by the numerical models of Masarik (2002) and Kober et al. (2005).

		Elemental production rate (atoms/g/yr)							
Nuclide	*Numerical model*	*O*	*Na*	*Mg*	*Al*	*Si*	*Ca*	*Fe*	*Ni*
$^{3}He_{cos}$	*Masarik, 2002*	128.7	-	110.8	102	106	57.7	38.5	-
	Kober et al., 2005	191	-	182	160	129	-	95	91
$^{21}Ne_{cos}$	*Masarik, 2002*	-	102	175.1	62.4	41.7	1.8	0.187	-
	Kober et al., 2005	-	208	189	60	44	17	1	1

5.7.1.1 ^{3}He production rates based on mineral composition

Based on the major-element composition of the different minerals present in each xenolith, theoretical mineral-specific production rates have been determined using the Masarik (2002) and Kober et al. (2005) numerical models. The results are shown in Figure 5.7. The production rates obtained by applying Kober et al. (2005) elemental production rates are 30 to 50% higher than those calculated from Masarik (2002) production rates, which are closer to the empirically determined sea level high latitude (SLHL) production rates, e.g. olivine 120 ± 9.4 atoms/g/year (Goehring et al., 2010 and references therein). Olivine and orthopyroxene have similar chemical compositions and the $^{3}He_{cos}$ production rates cannot be resolved within the current analytical uncertainties (Figure 5.7). On the other hand, $^{3}He_{cos}$ production rate clinopyroxene can readily be resolved from orthopyroxene. This is a consequence of the different Mg content of the two minerals. The calculated ^{3}He production rate in orthopyroxene (En_{89-90}) is ~4% higher than clinopyroxene (En_{49-51}) using elemental production rates of Masarik (2002) and ~14% higher using the production rates of Kober et al. (2005). A wide range of spinel compositions was observed, notably showing variability in Cr and Al contents. The difference in production rate from Fe from the two models means the spinel production rate relative to orthopyroxene and clinopyroxene is different depending on the model used for the production rate calculation. When the Masarik (2002) element production rates are used spinel He concentration should be 5 to 16% lower than orthopyroxene. When the Kober et al. (2005) element production rates are used the production rate from spinel is 9 to 17% higher than clinopyroxene.

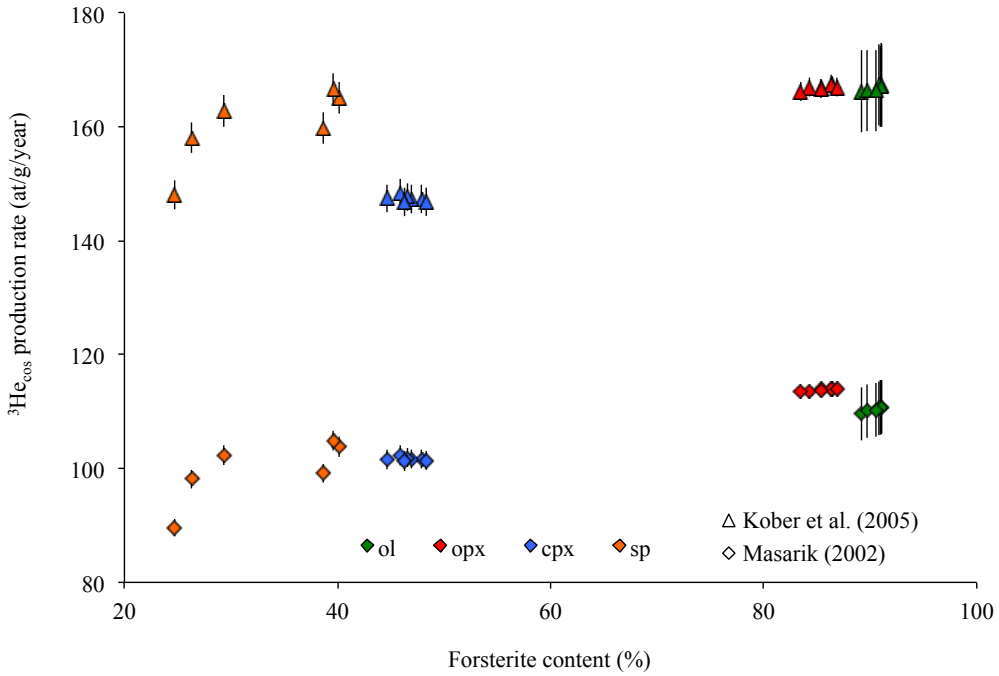

Figure 5.7. Theoretical $^{3}He_{cos}$ production rate calculated using the theoretical elemental production proposed by Masarik (2002) and Kober et al. (2005) for the chemical composition of the Mount Hampton xenolith samples. Pyroxene and spinel compositions are plotted as normalized to forsterite content. The error bars represent the analytical 1σ uncertainty taken from Chapter 4 (1.7% for pyroxene and spinel and 4.3% for olivine).
ol-olivine; opx-orthopyroxene; cpx-clinopyroxene; sp-spinel

5.7.1.2 ^{21}Ne production rates based on mineral composition

The results obtained from applying the elemental production rates from Masarik (2002) and Kober et al. (2005) models to the major-element composition of the different minerals from Mount Hampton are shown in Figure 5.8. In the case of $^{21}Ne_{cos}$ there is no production from O and therefore the production of $^{21}Ne_{cos}$ in mafic minerals is strongly dominated by Mg content (Lal, 1991; Schaefer et al., 1999). The mineral production rates calculated using Kober et al. (2005) element production rates are 1 to 7% higher than those calculated by Masarik (2002). With current analytical uncertainties these differences are indistinguishable. The two theoretical models are in agreement and predict measurable production rate differences between different mafic minerals. The calculated $^{21}Ne_{cos}$ production rate of olivine is 20 to 23% higher than that of orthopyroxene independent of the model. The $^{21}Ne_{cos}$ production rate of olivine is 39-46% higher than that of clinopyroxene using the Masarik (2002) element production rates, and 35-42% higher if the element production rates of Kober et al. (2005) are used. The calculated $^{21}Ne_{cos}$ production rate of olivine is 39-55% higher than spinel using Masarik (2002) element production rates are used and 43-58% higher when Kober et al. (2005) element production rates are used.

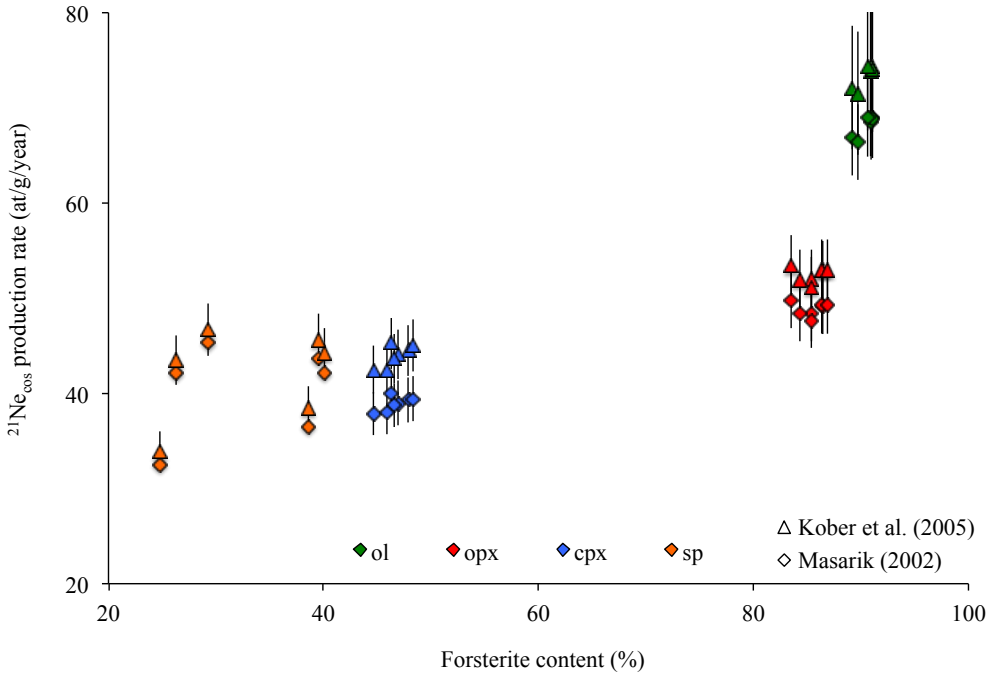

Figure 5.8. Theoretical $^{21}Ne_{cos}$ production rate calculated using the theoretical elemental production proposed by Masarik (2002) and Kober et al. (2005) for the chemical composition of the Mount Hampton xenolith samples. Pyroxene and spinel compositions are plotted as normalized to forsterite content. The error bars represent the analytical 1σ uncertainty taken from Section 5.6.3 (6%).
ol-olivine; opx-orthopyroxene; cpx-clinopyroxene; sp-spinel

5.8 Relative production of cosmogenic ^{3}He and ^{21}Ne in minerals

All the minerals from the same xenolith have had the same cosmic ray irradiation history. Therefore the relative concentrations of $^{3}He_{cos}$ and $^{21}Ne_{cos}$ are representative of the relative production rates. To quantify the chemical composition control on the production rate of $^{3}He_{cos}$ and $^{21}Ne_{cos}$ in olivine, orthopyroxene, clinopyroxene and spinel the measured concentrations of $^{3}He_{cos}$ and $^{21}Ne_{cos}$ have been compared with those calculated using the Masarik (2002) and Kober et al. (2005) models. To simplify this comparison mineral ratios are used. The analytical concentrations for each mineral separate have been normalized to the concentrations of one mineral phase and compared with the corresponding production rate ratios calculated for $^{3}He_{cos}$ and $^{21}Ne_{cos}$ using equations 5.2 and 5.3 respectively.

$$(^{3}He_{mineral}/^{3}He_{opx})_{measured}/(^{3}He_{mineral}/^{3}He_{opx})_{calculated} \quad [5.2]$$

$$(^{21}Ne_{mineral}/^{21}Ne_{ol})_{measured}/(^{21}Ne_{mineral}/^{21}Ne_{ol})_{calculated} \quad [5.3]$$

where, $(^{3}He_{mineral}/^{3}He_{opx})_{measured}$ and $(^{21}Ne_{mineral}/^{21}Ne_{ol})_{measured}$ are the ratios of the cosmogenic nuclide concentrations and $(^{3}He_{mineral}/^{3}He_{opx})_{calculated}$ and $(^{21}Ne_{mineral}/^{21}Ne_{ol})_{calculated}$ are the ratios of the cosmogenic nuclide production rates

calculated from elemental productions model by Masarik (2002) or Kober et al. (2005). The $^{3}He_{cos}$ concentrations measured in olivine, clinopyroxene and spinel (mineral) separates have been normalized to those measured in orthopyroxene (opx) and the $^{21}Ne_{cos}$ concentrations obtained from orthopyroxene, clinopyroxene and spinel (mineral) separates have been normalized to those obtained from olivine (ol). The choice of the normalization mineral is based on the robustness of the degassing technique used to release the cosmogenic signature. In the case of $^{3}He_{cos}$, although all the samples have been degassed using the same Pt encapsulation technique pyroxene is easier to completely degas than olivine and therefore it is the preferred mineral for normalization. In the case of $^{21}Ne_{cos}$ all the olivine samples have been degassed using the furnace, which is more reliable method for complete degassing of more than 50 mg. In the case of $^{3}He_{cos}$ three aliquots of orthopyroxene per sample were analysed and the average value was used for the comparison with 1σ uncertainty of < 3%.

5.8.1 Relative production of cosmogenic ^{3}He in olivine, orthopyroxene, clinopyroxene and spinel

$^{3}He_{cos}$ concentrations from olivine separates are compared to the concentrations from orthopyroxene separates in Figure 5.9. The most robust data comes from xenolith MH.2 where 15 splits of olivine have been measured. Normalized to the average He content of orthopyroxene from MH.2 the ratio generally agrees within analytical uncertainty with the production rate ratios calculated from mineral composition using Masarik (2002) and Kober et al. (2005). In this case the propagated analytical uncertainties (4-6%, 1 σ) do not allow the two numerical models to be resolved. Olivine and orthopyroxene are compositionally similar and the production rate ratios are close. The empirical data corroborate this. The ^{3}He content of orthopyroxene and olivine are indistinguishable within current analytical uncertainties in most samples. Olivine from MB.71.10 yielded slightly lower ^{3}He, compared to orthopyroxene, than expected from both models. This may reflect incomplete degassing of olivines. One aliquot of olivine from MM and three from MH.2 yielded slightly higher ^{3}He than expected from theoretical calculations, in the case of MH.2 the average ^{3}He value agrees within uncertainty with the theoretical calculations (average 1.03 ± 0.04 in the case of Masarik, 2002 and 1.00 ± 0.04 in the case of Kober et al., 2005), in the case of sample MM only two aliquots are analysed and the average ^{3}He agrees within uncertainty with analytical calculations (average 1.06 ± 0.08 in the case of Masarik, 2002 and 1.03 ± 0.08 in the case of Kober et al., 2005).

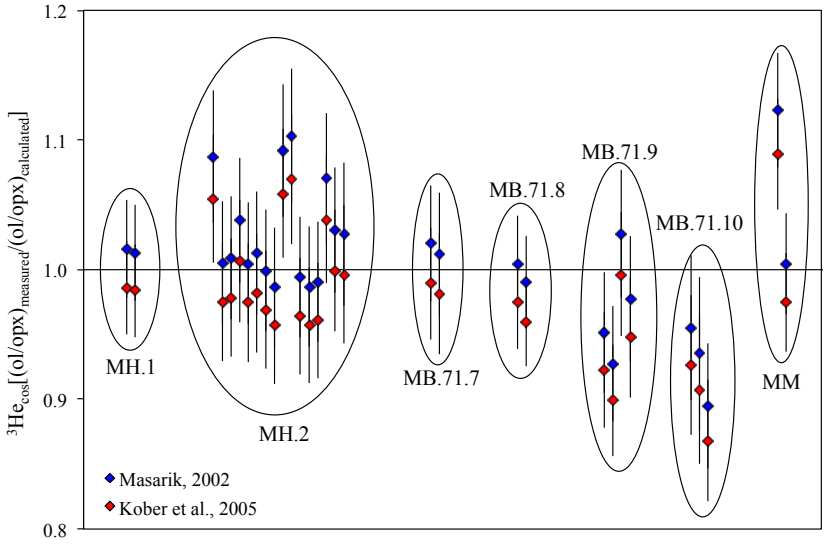

Figure 5.9. Comparison of the $^3He_{cos}$ concentration in olivine (ol) and orthopyroxene (opx) compared to the calculated production rates based on chemical composition using Masarik (2002) (blue diamonds) and Kober et al. (2005) (red diamonds). The horizontal line defines the line for measured data equal to calculated data. All uncertainties are reported as 1σ.

$^3He_{cos}$ measured in clinopyroxene is plotted relative to orthopyroxene in Figure 5.10. The ^3He contents predicted by both models are generally resolvable with the analytical uncertainties (2-5%, 1σ). The majority of the samples yielded $^3He_{cos}$ concentrations, relative to orthopyroxene, that are consistent with those predicted by the Masarik (2002) model. Clinopyroxene from MH.2 and MB.71.10 yielded $^3He_{cos}$ concentrations that are lower (by up to 40%) than the theoretical values. All the clinopyroxene with low $^3He_{cos}$ concentrations released < 4% of the total $^3He_{cos}$ concentrations during reheat, suggesting that incomplete extraction is not the reason. The majority of the clinopyroxene that yielded the low He concentrations were from the same analytical period. These samples were baked for 15 hours, longer than normal procedure. It is likely that these samples were outgassed during the baking process. One aliquot from sample MB.71.7 yielded higher (up to 20%) ^3He concentrations in clinopyroxene, relative to orthopyroxene, than expected. Incomplete degassing of the orthopyroxene seems not a valid option as consistency on the measurements is observed as well as consistency with the olivine results. Variability in the blank is not an option either as the blank represents < 1% of the total ^3He released from the samples. Weight uncertainty (typically ~0.1%) won't justify such variability. With straightforward cause for the extremely high ^3He concentration it can be considered to be an outlier.

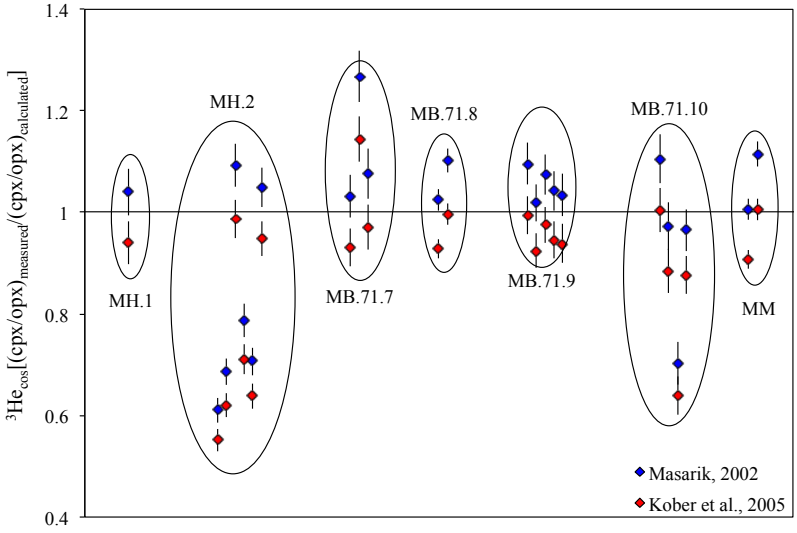

Figure 5.10. Comparison of the ratios of the measured $^{3}He_{cos}$ concentration in clinopyroxene (cpx) and orthopyroxene (opx) and the respective calculated production rates based on chemical composition using Masarik (2002) (blue diamonds) and Kober et al. (2005) (red diamonds). The continuous line defines the line for measured data equal to calculated data.

$^{3}He_{cos}$ concentrations in spinel, relative to orthopyroxene, are generally lower ratios (by up to 20%) than expected from theoretical calculations (Figure 5.11). In some cases the analytical uncertainty is such that the two theoretical models cannot be resolved. Spinel from two xenoliths (MH.1 and MB.71.9) yielded ratios that agree with theoretical calculations of Masarik (2002) with one aliquot of MB.71.9 agreeing with the calculations from Kober et al. (2005) elemental production rates. The low measured relative production in xenoliths may reflect the difficulty of completely degassing spinel. Helium loss during heating is dependent on the factors that control He diffusion, principally the ionic porosity. The ionic porosity of spinel (51.63%, Ando and Oishi, 1974) is lower than pyroxene and olivine (55.44% and 55.90% respectively Zheng and Fu, 1998) consequently the activation energy of spinel is 25% higher than that of olivine (Zheng and Fu, 1998) requiring higher temperatures to completely degas. The production rate of He from Cr has been assumed to be the same as Fe. If this assumption is incorrect the maximum overestimation of the theoretical relative production rate will be between 2% in the case of MB.71.9 up to 11% in the case of MM; which are the spinel minerals showing the lowest and highest Cr content. However, this possible overestimation of the Cr production rate will not justify the low ^{3}He concentrations leaving the difficulty of complete degassing of spinel the main cause of discrepancy.

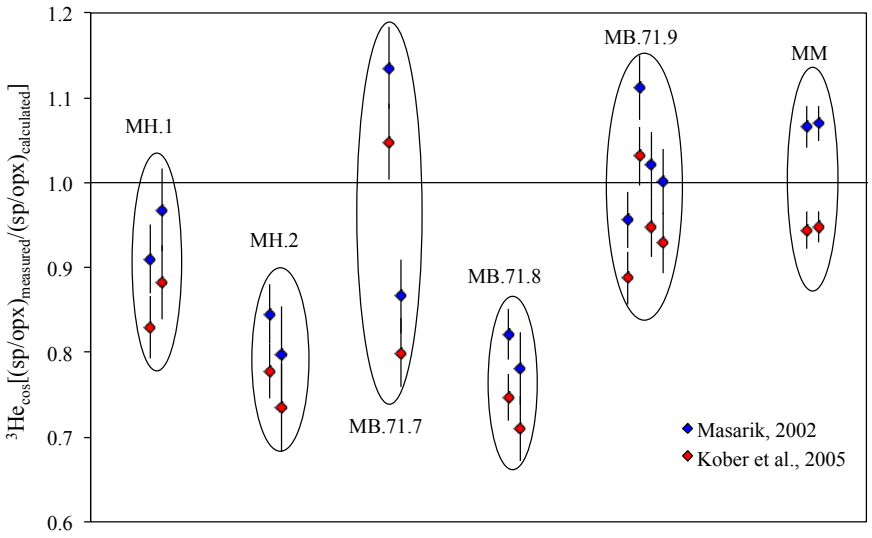

Figure 5.11. Comparison of the ratios of the measured $^3He_{cos}$ concentration in spinel (sp) and orthopyroxene (opx) and the respective calculated production rates based on chemical composition using Masarik (2002) (blue diamonds) and Kober et al. (2005) (red diamonds). The continuous line defines the line for measured data equal to calculated data.

Three spinel samples (MH.2, MB.71.9 and MM) showed up to 15% higher than expected relative production to orthopyroxene. The same observations than previously stated for clinopyroxene apply for the analysis of spinel with the exception that in the case of spinel the available grain size used for analyses corresponds to the 125 to 250 µm fraction and it represents the smallest proportion within the xenoliths (< 5% of the whole rock). With the ejection distance of ^3He and ^3H spallation reaction in olivine being 54-170 µm and 70-220 µm for ^3He and ^3H respectively (Ziegler et al., 2008) implantation of $^3He_{cos}$ produced in the surrounding minerals could be the cause of such high ^3He concentration observed in some spinel samples. Figure 5.12 shows an example of the mineral distribution within the xenoliths, with spinel being of smaller size and surrounded by olivine and orthopyroxene of much bigger sizes, resulting on an effect of implantation of ^3He in the small spinel.

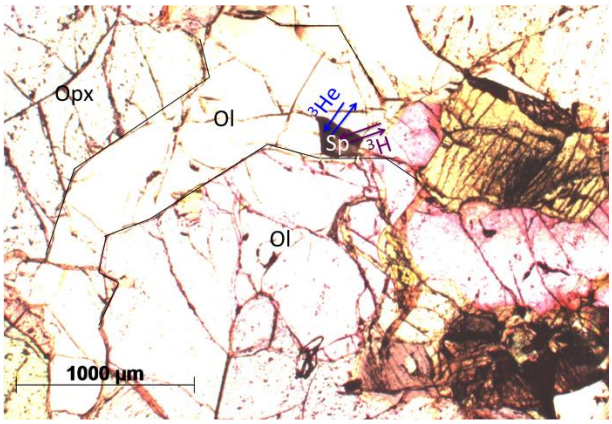

Figure 5.12. Photograph of thin section from sample MB.71.8 showing the distribution of spinel within the xenolith. Spinel of size ~ 200 µm surrounded by orthopyroxene of >1000 µm with implantation of ^3He and ^3H occurring in both directions but only being relevant in the case of spinel due to its smaller size.

If the higher than expected concentrations measured in spinel are a product of implantation then the $^{3}He_{cos}$ in spinel will have been implanted from surrounding orthopyroxene and olivine grains, as those are the most abundant minerals in the rock. The $^{3}He_{cos}$ production rates for olivine and orthopyroxene are indistinguishable within uncertainty and therefore the production rate of orthopyroxene has been used for quantifying the rate of implantation. An estimation of the production rate in spinel due to implantation can be calculated for ^{3}He and ^{3}He ejection distances using the ejection-implantation equation proposed by Blard and Farley (2008) modified for the minerals of interest:

$$P_3 = Sp_3\,[1 - 1.5 \times (S/D) + 0.5 \times (S/D)^3] + Opx_3\,[1.5 \times (S/D) - 0.5 \times (S/D)^3] \qquad [5.4]$$

where, Sp_3 and Opx_3 are the $^{3}He_{cos}$ production rate (atoms/g/year) of spinel and orthopyroxene respectively, S is the stopping distance of the α-nuclei (μm) and D is the diameter of the crystal (μm). Quantifying the rate of implantation requires the knowledge of the $^{3}H/^{3}He$ ratio from spallation production, estimated to be between 1 (Masarik, 2002) and ~0.5 (Kober et al., 2005). For calculating the production rate of ^{3}He due to implantation (P_3), average values for the stopping distances of ^{3}H and ^{3}He have been used and the production rates for spinel and orthopyroxene are based on theoretical values of Masarik (2002) and Kober et al. (2005) and the P_3 assuming all coming from ^{3}H and ^{3}He has been calculated. The two extreme grain diameters have been considered (125 μm and 250 μm) for the calculations and the results are compiled in table 5.7.

For the smaller grains (125 μm) the production in spinel due to implantation is equal to that of orthopyroxene, independent of whether ^{3}H or ^{3}He atoms are implanted. Therefore all the $^{3}He_{cos}$ present in 125 μm spinel grains has been implanted from the surrounding minerals. For the larger grains (250 μm diameter), the production rate due to implantation is 1 to 5 % lower than that of orthopyroxene when using Masarik (2002) theoretical production rates and 1 to 3 % lower than orthopyroxene when using the production rates of Kober et al. (2005). Consequently for 250 μm spinel grains > 95 % of the $^{3}He_{cos}$ has been implanted from the surrounding minerals.

Table 5.7. Calculation of the production rate of ^{3}He in spinel due to implantation from surrounding orthopyroxene grains.

Sample name	*Element*	*D(nm)*	*S(nm)**	*Psp (atoms/g./year)*	*Popx (atoms/g/year)*	*P3*	*P3<Psp (%)*	*P3<Popx (%)*
Masarik (2002)								
MH.1	^{3}He	125	122	98	114	114	16	0
MH.2	^{3}He	125	122	103	114	114	11	0
MB.71.7	^{3}He	125	122	100	115	115	15	0
MB.71.8	^{3}He	125	122	98	115	115	17	0
MB.71.9	^{3}He	125	122	108	114	114	5	0
MM	^{3}He	125	122	97	114	114	18	0
MH.1	^{3}H	125	145	98	114	113	16	1
MH.2	^{3}H	125	145	103	114	114	10	0
MB.71.7	^{3}H	125	145	100	115	114	14	1
MB.71.8	^{3}H	125	145	98	115	114	17	1
MB.71.9	^{3}H	125	145	108	114	114	5	0
MM	^{3}H	125	145	97	114	113	17	1
MH.1	^{3}He	250	122	98	114	109	11	5
MH.2	^{3}He	250	122	103	114	110	7	3
MB.71.7	^{3}He	250	122	100	115	110	10	4
MB.71.8	^{3}He	250	122	98	115	109	12	5
MB.71.9	^{3}He	250	122	108	114	112	4	2
MM	^{3}He	250	122	97	114	108	12	5
MH.1	^{3}H	250	145	98	114	110	13	3
MH.2	^{3}H	250	145	103	114	112	8	2
MB.71.7	^{3}H	250	145	100	115	112	12	3
MB.71.8	^{3}H	250	145	98	115	111	13	3
MB.71.9	^{3}H	250	145	108	114	113	4	1
MM	^{3}H	250	145	97	114	110	14	3
Kober et al. (2005)								
MH.1	^{3}He	125	122	158	169	169	7	0
MH.2	^{3}He	125	122	164	170	170	4	0
MB.71.7	^{3}He	125	122	159	170	170	7	0
MB.71.8	^{3}He	125	122	157	170	170	8	0
MB.71.9	^{3}He	125	122	169	169	169	0	0
MM	^{3}He	125	122	147	170	170	15	0
MH.1	^{3}H	125	145	158	169	169	7	0
MH.2	^{3}H	125	145	160	170	169	6	0
MB.71.7	^{3}H	125	145	162	170	170	5	0
MB.71.8	^{3}H	125	145	153	170	169	11	0
MB.71.9	^{3}H	125	145	162	169	169	4	0
MM	^{3}H	125	145	162	170	169	5	0
MH.1	^{3}He	250	122	158	169	166	5	2
MH.2	^{3}He	250	122	160	170	167	4	2
MB.71.7	^{3}He	250	122	162	170	167	3	2
MB.71.8	^{3}He	250	122	153	170	164	7	3
MB.71.9	^{3}He	250	122	162	169	167	3	1
MM	^{3}He	250	122	162	170	167	3	1
MH.1	^{3}H	250	145	158	169	167	6	2
MH.2	^{3}H	250	145	160	170	168	5	1
MB.71.7	^{3}H	250	145	162	170	168	4	1
MB.71.8	^{3}H	250	145	153	170	166	9	2
MB.71.9	^{3}H	250	145	162	169	167	3	1
MM	^{3}H	250	145	162	170	168	4	1

*****The stopping distances (S) are taken as the average stopping distance for ^{3}H and ^{3}He (Ziegler et al., 2008) and the respective production rates for spinel (Sp_3) and orthopyroxene (Opx_3) are calculated based on the elemental production rates of Masarik (2002) and Kober et al. (2005). Two grain diameters (D) are used with constrain the minimum and maximum spinel grain sizes analysed.

If all the ^{3}He present in the spinel minerals that showed high concentrations have been produced outside the mineral grains (in surrounding olivine and orthopyroxene) then the relative production of spinel with orthopyroxene should be equal to. This is true for two samples (MH.2 and MB.71.9) out of the three that showed high ^{3}He concentrations (Figure 5.13). The high (but not as high as 100% implanted) ^{3}He concentration recorded from spinel from sample MM could be a combination of implanted ^{3}He from surrounding olivine and orthopyroxene and incomplete degassing during the heating step.

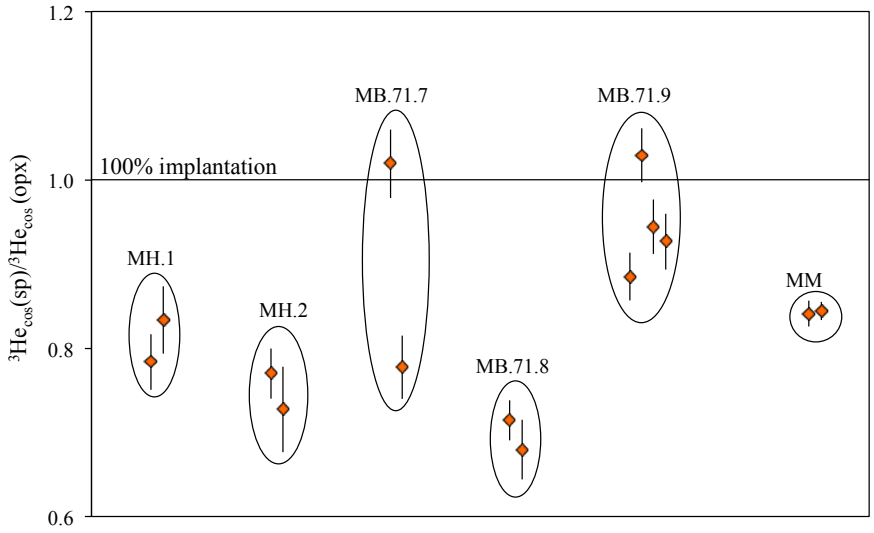

Figure 5.13. Comparison of the measured $^{3}He_{cos}$ concentration in spinel (sp) and orthopyroxene (opx) to test implantation $^{3}He_{cos}$ from the surrounding minerals (mainly orthopyroxene and olivine). Since the production rate of olivine and that of orthopyroxene are indistinguishable with analytical uncertainty the concentration of orthopyroxene is chosen for this comparison. The continuous line represents the line of 100% implantation meaning that all the ^{3}He present in the spinel mineral has been produced outside.

Generally the $^{3}He_{cos}$ data confirms the differences in the production rate related to elemental composition of minerals predicted by the two theoretical models (Masarik, 2002; Kober et al., 2005) although with the current uncertainties it is not possible to distinguish which of the models is the most accurate. The data have also shown the technical difficulty of complete gas extraction from mafic minerals using a diode laser, in particular, fully degassing spinel. These dataset suggests that implantation occurs and it is relevant when small grains are analysed, therefore small grain size fractions (125 to 250 μm) should be avoided especially when the mineral analysed is not the most abundant in the rock.

5.8.2 Relative production of cosmogenic ^{21}Ne in olivine, orthopyroxene, clinopyroxene and spinel

$^{21}Ne_{cos}$ production varies in relation to the amount of Mg present in the mineral (Masarik and Reedy, 1996; Schaefer et al, 1999; Masarik, 2002; Kober et al., 2005). In the case of ^{21}Ne both theoretical models of Masarik (2002) and Kober et al. (2005) predict similar production rates, indistinguishable with the current analytical uncertainties. The data from orthopyroxene and clinopyroxene have been compared with that of olivine in order to assess whether the theoretical models accurately predict the relative production rates of these minerals (Figures 5.14 and 5.15). Only one spinel sample from MB.71.7 was analysed and the $^{21}Ne_{cos}$ concentration obtained is indistinguishable within analytical

uncertainty to that of olivine whilst theoretical models predict a production rate in spinel 50% lower than that in olivine. It will be necessary to analyse more spinel samples in order to accurately interpret this result.

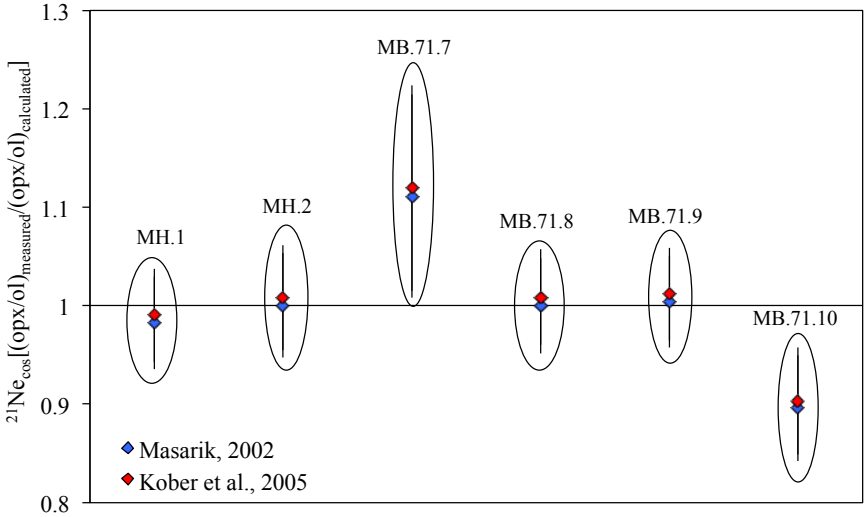

Figure 5.14. Comparison of the ratios of the measured $^{21}Ne_{cos}$ concentration in orthopyroxene (opx) and olivine (ol) and the respective calculated production rates based on chemical composition using Masarik (2002) (blue diamonds) and Kober et al. (2005) (red diamonds). Only the $^{21}Ne_{cos}$ concentrations from furnace degassing of the samples have been used for this comparison. The continuous line defines the line for measured data equal to calculated data.

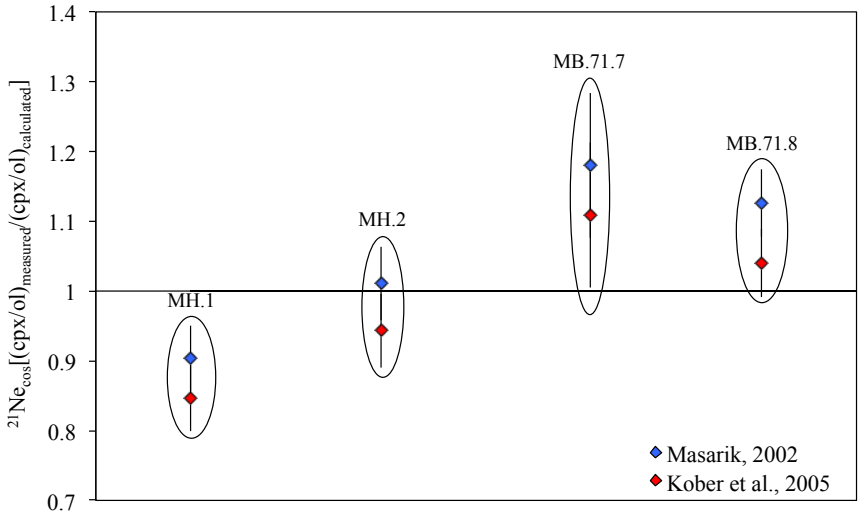

Figure 5.15. Comparison of the ratios of the measured $^{21}Ne_{cos}$ concentration in clinopyroxene (cpx) and olivine (ol) and the respective calculated production rates based on chemical composition using Masarik (2002) (blue diamonds) and Kober et al. (2005) (red diamonds). Only the $^{21}Ne_{cos}$ concentrations from furnace degassing of the samples have been used for this comparison. The continuous line defines the line for measured data equal to calculated data.

Four out of the six orthopyroxene samples and two out of four clinopyroxene samples yielded $^{21}Ne_{cos}$ concentrations relative to olivine that agree with theoretical predictions. In the case of sample MB.71.7 both clinopyroxene and orthopyroxene separates seem to have yielded $^{21}Ne_{cos}$ concentrations relative to olivine ~10% higher than

expected from theoretical calculations suggesting that maybe the olivine sample was not completely degassed. This seems to be also the case for MB.71.10 orthopyroxene and MH.1 clinopyroxene yielding $^{21}Ne_{cos}$ concentrations ~10% lower than expected from theoretical predictions. The $^{21}Ne_{cos}$ data have validated empirically the theoretical elemental productions of Masarik (2002) and Kober et al. (2005). These data has proved the technical difficulty of the analysis of mafic minerals, which require much higher (~70%) temperatures than quartz to be completely degassed.

5.8.3. Scaling for elemental composition

The $^{3}He_{cos}$ and $^{21}Ne_{cos}$ data have confirmed that the $^{3}He_{cos}$ and $^{21}Ne_{cos}$ production rates vary with chemical composition and therefore, this variation has to be considered in order to adequately interpret cosmogenic $^{3}He_{cos}$ and $^{21}Ne_{cos}$ concentrations in exposed rocks. With the current analytical uncertainties it is difficult to distinguish which theoretical model predicts better the chemical composition variations. However, it is clear the importance of quantifying such variations. Here I propose a normalization factor (N) to scale the production rates for elemental composition based on theoretical elemental production rates. Equation 5.5 shows an example for olivine (major elements are Mg, Fe, Si and O):

$$N = \frac{(\chi_{Mg} \text{ x } P_{Mg} + \chi_{Fe} \text{ x } P_{Fe} + \chi_{Si} \text{ x } P_{Si} + \chi_{O} \text{ x } P_{O})_j}{(\chi_{Mg} \text{ x } P_{Mg} + \chi_{Fe} \text{ x } P_{Fe} + \chi_{Si} \text{ x } P_{Si} + \chi_{O} \text{ x } P_{O})_i} \qquad [5.5]$$

where, χ_{Mg}, χ_{Fe}, χ_{Si}, χ_{O} are the respective atoms of Mg, Fe, Si and O present in the olivine from which the production rate is used (i) and the olivine from which the exposure age is calculated (j) and P_{Mg}, P_{Fe}, P_{Si}, P_{O} are the element specific theoretical production rates.

In the case of $^{3}He_{cos}$, the global average production rate (120 ± 16 atoms/g/year) is determined from the average olivine composition of $Fo_{82\pm4}$ (Goehring et al., 2010; Delunel et al., 2016). The Mount Hampton olivine has an average composition of $Fo_{90\pm0.5}$. Based on these compositions a normalization factor of N = 1.031 ± 0.05 using Masarik (2002) theoretical production rates and N= 1.022 ± 0.05 using the theoretical production rates of Kober et al (2005) is obtained. For the same olivine compositions the normalization factor for $^{21}Ne_{cos}$ production is N = 1.088 ± 0.04 irrespective of the theoretical method applied. For Mount Hampton xenoliths, failing to apply the N factor translates into an

underestimation of the exposure ages by ~7% and ~12% for $^{3}He_{cos}$ and $^{21}Ne_{cos}$ respectively.

5.8.4. Relative production rates of ^{3}He and ^{21}Ne in mafic minerals

The $^{21}Ne_{cos}/^{3}He_{cos}$ production rate ratio is strongly dependent on the Mg concentration in the target mineral (Schaefer et al. 1999, Masarik 2002, Kober et al. 2005). The $^{21}Ne_{cos}/^{3}He_{cos}$ ratios measured in the Mount Hampton xenoliths show a relation with the Mg content present in the mineral of study with lower ratios for minerals with lower Mg concentrations (Figure 5.16). Within the xenoliths the $^{21}Ne_{cos}/^{3}He_{cos}$ are distinguishable with analytical uncertainty. Generally, the ratios for orthopyroxene and clinopyroxene are 20 to 25 % and 30 to 40 % lower than for olivine. The average $^{21}Ne_{cos}/^{3}He_{cos}$ ratios obtained are 0.40 ± 0.04 for olivine (Fo_{90-91}); 0.29 ± 0.03 for orthopyroxene (En_{89-90}) and 0.23 ± 0.06 for clinopyroxene (En_{49-51}). The high dispersion of the data, especially for clinopyroxene is a consequence of the difficulty of the degassing technique.

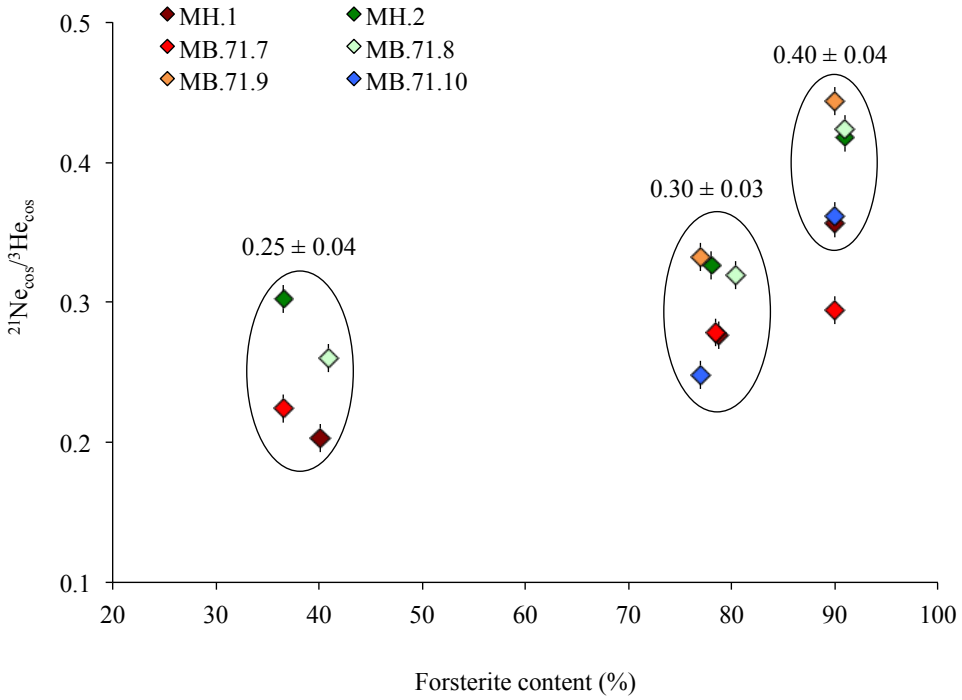

Figure 5.16. $^{21}Ne_{cos}/^{3}He_{cos}$ ratios from the analysis of Mount Hampton xenoliths. The average ratios for olivine, orthopyroxene and clinopyroxene are calculated. Note that the ratio from MB.71.7 olivine has not been included in the average calculation due to incomplete degassing of $^{21}Ne_{cos}$ and therefore it is also excluded from the comparison plot.

To test whether the relative production rate of $^{3}He_{cos}$ and $^{21}Ne_{cos}$ changes with high altitude, high latitude and long exposure, the $^{21}Ne_{cos}/^{3}He_{cos}$ ratios of Mount Hampton

xenoliths are compared with previously published data from volcanic rocks (Marti and Craig, 1987; Poreda and Cerling, 1992; Staudacher et al., 1993; Bruno et al., 1997; Fenton et al., 2009; Schimmelpfenning et al., 2011; Gillen et al., 2010; Fenton and Niedermann, 2014) (Figure 5.17).

Generally the $^{21}Ne_{cos}/^{3}He_{cos}$ ratios for Mount Hampton are in agreement with previously reported ratios from other areas. However, the Mount Hampton dataset seems to fall in the lower spectrum of the compilation, especially in the case of orthopyroxene. The high dispersion on the data from this work and that of the previously published ratios suggests that the relative production rate of $^{21}Ne_{cos}$ and $^{3}He_{cos}$ are technically difficult to determine. Most data conform the relative production rate proposed by Poreda and Cerling (1992) although some data from Mount Hampton and West United States seem to fit the theoretical relative production rate of Kober et al., (2005), which predicts lower $^{21}Ne_{cos}/^{3}He_{cos}$ as a consequence of higher $^{3}He_{cos}$ production rates than the model of Masarik (2002).

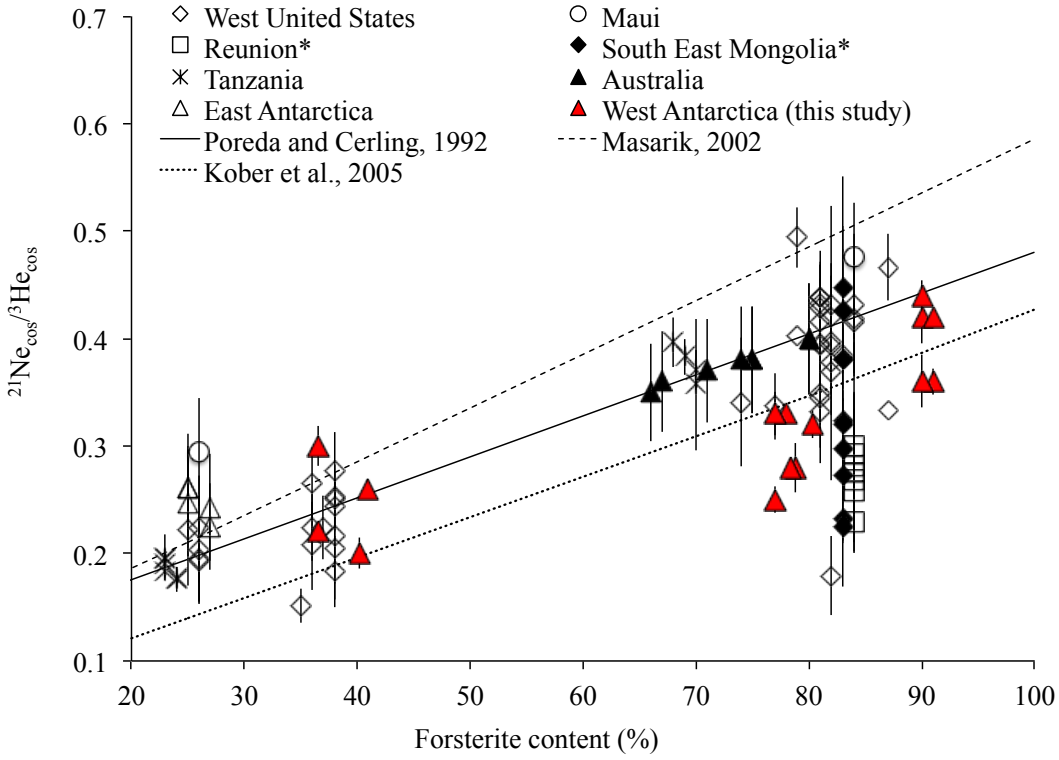

Figure 5.17. Plot of the $^{21}Ne_{cos}/^{3}He_{cos}$ ratios from the analysis of Mount Hampton xenoliths (red triangles) and previously reported $^{21}Ne_{cos}/^{3}He_{cos}$ ratios for different locations around the world (Maui: Marti and Craig, 1987; Reunion and South Mongolia: Staudacher et al., 1993; Western United States: Poreda and Cerling, 1992; Fenton et al., 2009; Fenton and Niedermann, 2014; Tanzania: Schimmelpfenning et al., 2011; Australia: Gillen et al., 2010 and East Antarctica: Bruno et al., 1997) relative to Mg content reported as forsterite content in %. Pyroxene compositions are plotted as normalized to forsterite content following Poreda and Cerling (1992). The continuous line represent the relative production rate at SLHL proposed by Poreda and Cerling (1992) and the discontinuous and dotted lines are theoretical lines calculated using Masarik (2002) and Kober et al. (2005) elemental productions respectively. All the data used are compiled in Appendix C. *Forsterite content of the olivines from Reunion and South East Mongolia are assumed to be the same as those measured for Reunion olivines by Furi et al. (2011).

In the past, analysis of $^{3}He_{cos}$ in garnet, apatite and zircon and $^{10}Be_{cos}$ in coexisting quartz from the Himalayas (~27˚N) at elevations of 2.8 to 4.8 km reported exponential increase of the $^{3}He_{cos}/^{10}Be_{cos}$ ratio with elevation (Gayer et al, 2004; Amidon et al., 2008). The hypothesis to explain these differences in the relative production rate with altitude was based on the idea of tertiary protons and neutrons produced by spallation reactions in rocks at high altitude having sufficient energy to produce $^{3}He_{cos}$ but not enough energy to produce $^{10}Be_{cos}$ (Gayer et al, 2004; Amidon et al., 2008). Another study performed by Blard et al. (2013) analysed $^{3}He_{cos}$ in pyroxene and $^{10}Be_{cos}$ in coexisting quartz from the Bolivian Altiplano (~20˚S) at elevations above 4.8 km and observed no particular increase in the $^{3}He_{cos}/^{10}Be_{cos}$ ratio with elevation concluding that the effect observed by Gayer et al. (2004) and Amidon et al. (2008) could be either related to specific production mechanisms in accessory minerals or to a regional effect unique to the Himalayas.

Schimmelpfenning et al. (2011) analysed lavas form different altitudes (1 to 5.4 km) from Kilimanjaro (Tanzania) reporting consistent $^{21}Ne_{cos}/^{3}He_{cos}$ ratios of 0.37 ± 0.02 and 0.19 ± 0.01 for olivine and pyroxene respectively. They observed no altitude dependence on the relative production of the two isotopes at this low latitude (~3˚S). The Mount Hampton samples come from a surface at ~3 km of altitude and high latitude (~76˚S) where the production rates reach their maximum. The $^{21}Ne_{cos}/^{3}He_{cos}$ ratios from Mount Hampton generally agree within uncertainty with the previously reported $^{21}Ne_{cos}/^{3}He_{cos}$ ratios for olivine and pyroxene (Marti and Craig, 1987; Staudacher et al., 1993; Poreda and Cerling, 1992; Fenton et al., 2009; Fenton and Niedermann, 2014; Schimmelpfenning et al., 2011; Gillen et al., 2010; Bruno et al., 1997) revealing no clear altitude dependence.

5.9 Conclusions

The analysis of xenolith minerals from Mount Hampton have yielded some of the highest $^{3}He_{cos}$ and $^{21}Ne_{cos}$ concentrations recorded in terrestrial samples. The results demonstrated that chemical composition controls the production rate of $^{3}He_{cos}$ and $^{21}Ne_{cos}$ and therefore scaling for composition using theoretical elemental production rates is necessary for accurate cosmogenic nuclide interpretation.

The current analytical uncertainties do not allow for distinguishing which of the two elemental production rate models provides most accurate results. The normalization

factors calculated using the two methods are indistinguishable within uncertainty. Therefore the suggestion from this work is to incorporate a compositional scaling factor for accurate exposure age determination but the choice of theoretical method remains at the discretion of the user.

The $^{21}Ne_{cos}/^{3}He_{cos}$ ratios are consistent with previously reported ratios from other locations at lower altitudes. Consequently the relative production rates of $^{21}Ne_{cos}$ and $^{3}He_{cos}$ seem to be independent of altitude in the case of Mount Hampton.

6. Cosmogenic ^{3}He and ^{10}Be in olivine to unravel the erosion history of Mount Hampton, West Antarctica

6.1 Introduction

The West Antarctic Ice Sheet (WAIS) covers the western side of the Transantarctic Mountains in the Antarctic continent (Figure 6.1). It is the only marine-based ice sheet on Earth and consequently it is susceptible to collapse due to increasing temperatures (Stone et al., 2003; Joughin and Alley, 2011). Determining how the WAIS has responded to temperature variations during Pleistocene interglacials and the Pliocene warm period (when atmospheric CO_2 concentrations may have been higher than present (400 ppm) and temperatures were warmer than today; Raymo et al., 1996; Ravelo et al., 2004) is important for predicting the response of the WAIS to impending global warming (Oppenheimer, 1998; Scherer et al., 1998; Stone et al., 2003) as the collapse of the WAIS could result in an increase of the eustatic sea level of ~3 m (Bamber et al., 2009). The evolution of the Antarctic landscape is strongly affected by past climate (e.g. Summerfield et al., 1999). Studies of the landscape adjacent to WAIS can be used to establish the fluctuations of the WAIS growth contributing to the understanding of past WAIS collapses (Stone et al., 2003; Mukhopadhyay et al., 2012) and the modelling of the future of the WAIS (Pollard and DeConto, 2009; Naish et al., 2009; Ackert et al., 2011; Feldmann and Levermann, 2015).

The aim of this study is to assess the extent to which the exposure history of xenoliths from the top of Mount Hampton (see Chapter 5) records the rate of landscape change above the WAIS. The cosmogenic ^{3}He data from xenolith olivines presented in Chapter 5 have been combined with new measurements of cosmogenic ^{10}Be in the same olivines to unravel the exposure history. Several possible scenarios for the ^{3}He-^{10}Be data are investigated using theoretical models and two main possible scenarios are discussed.

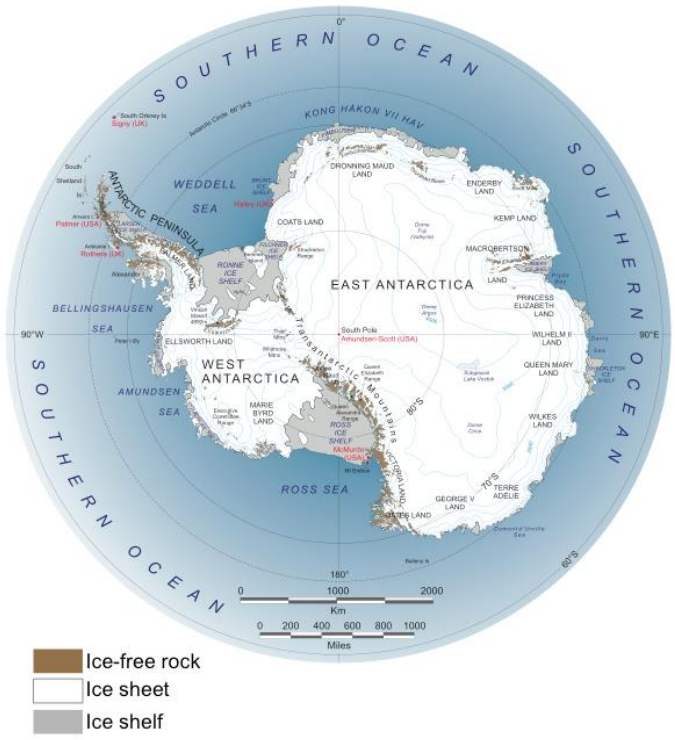

Figure 6.1. Overview map of Antarctica showing the major geographical features of the Antarctic continent. Map taken from http://lima.usgs.gov, British Antarctic Survey.

6.2 Glaciological context

The WAIS was formed during the late Miocene and through the Pleistocene from the coalescence of isolated ice caps that covered a number of islands in the Amundsen Sea and continental blocks during the Oligocene and early Miocene (Anderson and Shipp, 2001). In the early stages glacial erosion was effective especially in inland areas associated with the build up of the ice sheet in Marie Byrd Land (MBL), or with the transition from fluvial to glacial conditions. Glacial erosion is considered to be ineffective after ~15 Ma when the regime changed to a cold-based ice sheet (Rocchi et al., 2006, 2015). The WAIS is the only marine-based ice sheet in the world, and its dynamics make it susceptible to collapse during deglaciation related to warmer climate (Stone et al., 2003; Joughin and Alley, 2011). Fluctuations of the volume of the WAIS have been correlated with global climate conditions (Lisiecki and Raymo, 2005) with possible collapses of the WAIS during the warm periods of the late Pliocene and Pleistocene (Pollard and DeConto, 2009). During the Last Glacial Maximum (LGM) (26 ka to 19 ka, Clark et al., 2009) the WAIS extended to the break of the continental shelf in eastern and central Ross Sea and began to retreat shortly after to its current volume (Anderson and Shipp, 2001; Anderson et al., 2002).

Thickness fluctuations over time have been widely studied (Jensen, 1983; Ackert et al., 1999, 2007; Steig et al., 2001; Anderson et al., 2002; Stone et al., 2003; Pollard and DeConto, 2009; Joughin and Alley, 2011; Mukhopadhyay et al., 2012; Fretwell et al., 2013). The maximum WAIS surface elevation occurred in the early Holocene at ~10 ka (Ackert et al., 1999, 2007; Anderson et al., 2002; Stone et al., 2003). The thickness changes of the WAIS during the Holocene are still uncertain. The O and H isotope composition of the Byrd ice core is a function of past atmospheric pressure (Martinerie et al., 1992), and records ice elevations of 400 to 500 m above the current ice level during the LGM and early Holocene (Jensen, 1983; Steig et al., 1986). Cosmogenic ^{3}He and ^{36}Cl ages of moraines from Mount Waesche in the Executive Committee Range (ECR) have demonstrated that the WAIS expanded ~45 m since the LGM (Ackert et al., 1999). ^{10}Be exposure ages of transported cobbles from the Marie Byrd Land (MBL) suggested that during the LGM the WAIS was ~700 m higher than today near the coast and ~200 m higher in the interior (Stone et al., 2003). A more recent study using cosmogenic ^{21}Ne and ^{10}Be from nunataks in the Ohio Range in the WAIS interior revealed that the thickness of the WAIS has not been above 160 m from the current ice level (~2200 m in the WAIS interior) since the late Miocene (~7 Ma) (Mukhopadhyay et al., 2012). The variations in the ice elevation reported so far indicate that in the WAIS interior the highest volcanic peaks of the Executive Committee Range (ECR) (> 3000 m) have been above the current ice level (~2400 m) since their eruption in the late Miocene (Ackert et al., 1999; Stone et al., 2003; Mukhopadhyay et al., 2012). Mount Hampton sits 200 km from the coast and reaches an elevation of 3,323 m. Thus the summit cannot ever have been covered by the WAIS and it can be considered to be a nunatak since the time of formation (11.4 Ma; Le Masurier and Rex, 1989).

6.3 Cosmogenic ^{21}Ne and ^{10}Be in Antarctica

Combining the stable and radioactive cosmogenic isotopes is a useful tool for unravelling complex exposure histories involving exposure, erosion and burial. The stable nuclide (^{3}He and ^{21}Ne) integrates the total history of exposure of a rock surface to cosmic rays whist the radioactive nuclides (^{10}Be, ^{26}Al, ^{36}Cl and ^{14}C) record only the history governed by their respective half-life (Goose and Phillips, 2001) (see section 2.4 for details on the systematics). This has been most widely applied in Antarctica using ^{21}Ne, ^{10}Be and ^{26}Al in quartz to track ice elevation variations and determine rates of erosion and landscape

change (Van der Wateren et al., 1999; Oberholzer et al., 2003; Di Nicola et al., 2009; Di Nicola et al., 2012; Mukhopadhyay et al., 2012; Middleton et al., 2012).

One of the first applications was to constrain the extent of the glacial advances in Northern Victoria Land in East Antarctica using ^{3}He, ^{21}Ne and ^{10}Be from glacial erratics in ice-free surfaces to determine the rate of erosion for such stable landscape (~0.2 m/Ma) (Oberzholzer et al., 2003). Di Nicola et al. (2009, 2012) used ^{21}Ne, ^{10}Be and ^{26}Al from erratics from two locations in Northern Victoria Land to reconstruct fluctuations of the East Antarctic Ice Sheet (EAIS) since the late Miocene, revealing histories of continuous surface exposure with extremely low (0.05 m/Ma) erosion rates and complex exposure. Combining ^{21}Ne-^{10}Be concentrations from 14 Ma surfaces from pothole and channel features from the Dry valleys in East Antarctica, Middleton et al. (2012) showed surfaces previously considered to have experienced near negligible erosion rate have a more complex history: the pothole and channel features have either experienced large increases in erosion rates (from 0.3 for 11 Ma to 1 m/Ma in the last 3 Ma) or they record the fluctuations of the EAIS.

The combination of ^{21}Ne and ^{10}Be in Antarctica has been restricted to quartz-bearing surfaces. This study applies the same principles to olivine-bearing rocks in order to unravel the exposure history of an apparently uneroded nunatak (Mount Hampton) in the WAIS interior. The cosmogenic ^{3}He database acquired in this study is more extensive than the ^{21}Ne inventory (Chapter 5), so it is used in combination with ^{10}Be in olivine for this study.

6.4 Cosmogenic ^{10}Be in olivine

Cosmogenic ^{10}Be ($^{10}Be_{cos}$) is the most commonly used *in situ* cosmogenic radionuclide (Dunai, 2010). It is often used in conjunction with ^{26}Al for determining erosion rates and burial dating of sediments (Granger et al., 1997; Granger and Muzikar, 2001) and it has also been used in conjunction with ^{26}Al, ^{21}Ne or ^{14}C to unravel complex exposure histories (Lal, 1991; Nishiizumi et al., 1991a; Gosse and Phillips, 2001; Kober et al., 2005; Miller et al., 2006; Di Nicola, 2009). The vast majority of $^{10}Be_{cos}$ studies have used quartz due to its ubiquity at the Earth surface and the simple chemistry. Olivine offers a possible alternative when mafic rocks are the target lithologies (Nishiizumi et al., 1990). The half-life of $^{10}Be_{cos}$ (1.39 ± 0.02 Ma: Chmeleff et al., 2010) is better suited to studies of

long-term exposure of mafic rocks than ^{36}Cl (half life 306 ± 0.2 ka; Goldstein, 1996). However the use of $^{10}Be_{cos}$ in olivine has so far been limited to only few studies where it was used to calculate erosion rates, study river profile evolution and determine production rates (Nishiizumi et al., 1990; Seidl et al., 1997; Blard et al., 2008).

6.4.1 Meteoric ^{10}Be

Cosmogenic ^{10}Be is produced in the atmosphere by neutron spallation of O and N at a rate that is ~10^3 times faster than the *in situ* production rate at Earth surface (Goose and Phillips, 2001; Monaghan et al., 1986). Meteoric ^{10}Be can be adsorbed to the surface of mineral grains and in some cases it can infiltrate though weathered mineral zones. If meteoric ^{10}Be is not removed completely it can be the cause of unresolvable ^{10}Be excess (Ivy-Ochs et al. 1998). In the case of quartz sequential chemical dissolution efficiently removes the meteoric component (Kohl and Nishiizumi, 1992). In mafic minerals meteoric ^{10}Be may be contained within fractures of secondary minerals (Schott and Berner, 1985). Meteoric ^{10}Be cannot be effectively removed from heavily weathered minerals even by sequential dissolution in HF (Ivy-Ochs et al., 2008) and sample-specific procedures are required in order to remove it effectively (Blard et al., 2008). When the minerals do not show signs of weathering the standard sequential chemical dissolution is sufficient to eliminate the meteoric component (Nishiizumi et al., 1990).

6.4.2 Separation and analysis of cosmogenic ^{10}Be in olivine

The olivine xenocrysts from Mount Hampton used in this study are fresh and largely free of alteration and mineral inclusions and have been subjected to sequential chemical dissolution (Brown et al., 1991; Kohl and Nishiizumi, 1992; Cerling and Craig, 1994). Samples of ~1g of olivine of grain size 250-500 μm were handpicked from gently disaggregated xenolith samples. Xenoliths MH.1, MH.2, M.71.7, MB.71.8, MB.71.9 and MB.71.10 (described in Appendix C) were used. The chemical procedures were simultaneously performed in a blank to account for any possible contamination during the process. The procedures for elimination of meteoric component, ^{9}Be carrier addition and dissolution are described below and summarized in Figure 6.2.

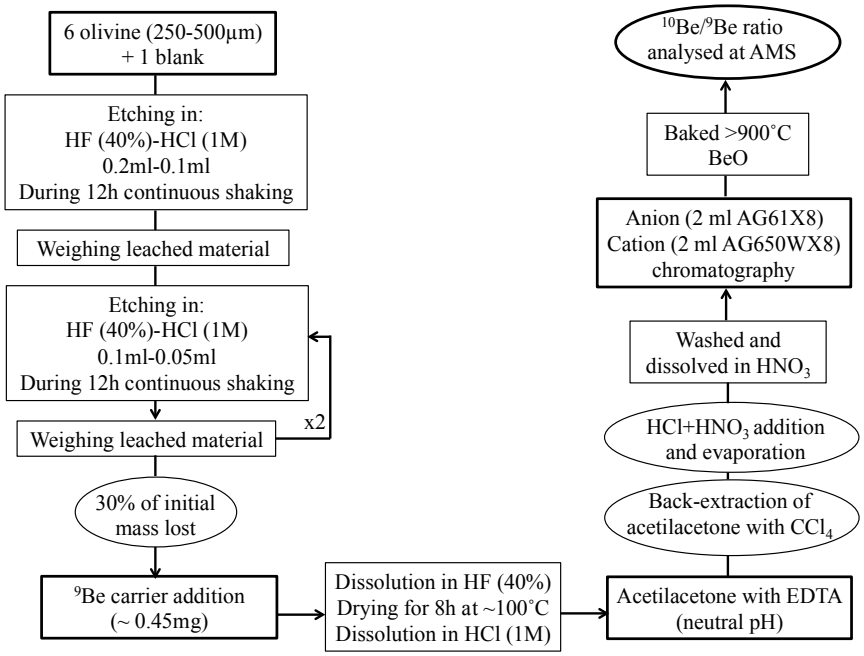

Figure 6.2. Schematic of the procedures followed for ^{10}Be separation in olivine.

To eliminate meteoric ^{10}Be from the surface of the olivine crystals, three sequential HF and HCl dissolutions were performed removing approximately 30% of the initial mass. The olivine cores were then completely dissolved in HF and spiked with ~500 µg of ^{9}Be carrier (Bourlès, 1988; Brown et al., 1992). The high concentration of Fe and Mg (up to 10^9 times the ^{9}Be carrier) required a bulk Be separation step before the final Be extraction by chromatography. Bulk separation was performed using a solvent extraction of beryllium by acetyl acetone at neutral pH in the presence of ethylenediaminetetraacetic acid (EDTA) in order to selectively complex transition metals and to avoid their co-extraction with beryllium by acetyl acetone (Tabushi, 1958; Seidl, 1993; Seidl et al., 1997). The acetyl acetone was recovered by back extraction using CCl_4. The mixture was then evaporated in the presence of concentrated HCl to break the Be-acetyl acetone complex and in the presence of concentrated HNO_3 to fume out the organic residue.

Following the standard protocol for quartz samples (e.g. Wilson et al., 2008), the remaining iron was removed from the Be enriched mixture by adsorption onto 2 ml AG61X8 anion chromatography columns and Be (and other cations) was eluted with 6 M HCl. Cation-exchange chromatography (2 ml AG650WX8 column) was used to separate Ti and B (elution in 0.5M H_2SO_4), Be (elution in 1.2 M HCl) and Al (elution in 4 M HCl). $Be(OH)_2$ was then precipitated with aqueous ammonia solution at pH 8.5. After washing the precipitate with 5 ml of Milli-Q water it was dissolved in one or two drops of concentrated nitric acid. The nitrate in this solution was decomposed at >200ºC, and the

product was baked to beryllium oxide in a muffle furnace at >900ºC. After this process seven cathodes (six samples and one blank) were prepared for ^{10}Be analysis. Data of the sample weights and the ^{10}Be separation steps are included in Appendix E.

6.5 Cosmogenic ^{10}Be results

$^{10}Be/^{9}Be$ ratios of the six samples and the blank prepared were measured using the 5 MV NEC Pelletron accelerator mass spectrometer at SUERC (Xu et al., 2010). ^{10}Be concentrations are based on $^{10}Be/^{9}Be$ ratio of 2.79 x 10^{-11} for NIST Standard Reference Material 4325. The data from the AMS have been corrected for the blank (representing 0.4 to 6 % of the total ^{10}Be measured) and for the ^{9}Be carrier added to calculate $^{10}Be_{cos}$ concentrations (details of the measurements of $^{10}Be/^{9}Be$ are included in Appendix E). ^{10}Be concentrations in the Mount Hampton olivine samples vary from 0.23 to 2.27 x 10^{7} atoms/g (Table 6.1). This represent the highest concentrations ever measured in olivine.

Table 6.1. Cosmogenic ^{10}Be concentrations from olivine separated from spinel lherzolite xenoliths from Mount Hampton. The uncertainties reported are the propagated analytical 1σ uncertainties.

Xenolith	*Weight (g)*	*^{9}Be carrier (µg)*	*^{9}Be (10^{19} atoms)*	*AMS*			*^{10}Be (10^{7}atoms/g)*	*1σ*
				Sample ref	*$^{10}Be/^{9}Be$ (10^{-13})*	*1σ*		
MH.1	0.734	516.01	3.45	b9343	4.849	0.089	2.268	0.042
MH.2	0.673	520.31	3.48	b9344	1.974	0.046	1.009	0.024
MB.71.7	0.731	522.95	3.49	b9345	0.375	0.017	0.169	0.008
MB.71.8	0.748	519.61	3.47	b9347	3.820	0.079	1.764	0.037
MB.71.9	0.756	522.16	3.49	b9348	1.769	0.044	0.807	0.020
MB.71.10	0.769	518.15	3.46	b9349	0.522	0.020	0.226	0.009
Blank	0.000	504.60	3.37	b9350	0.022	0.004		

Comparing the concentration of a stable cosmogenic nuclide ($^{3}He_{cos}$) with a radioactive nuclide ($^{10}Be_{cos}$) measured in the same sample requires accounting for the half-life of the radioactive nuclide (1.378 Ma; Chmeleff et al., 2010; Korschinek et al., 2010) and the mineral and site-specific production rate of each nuclide (Lal, 1991). The production rates used for the comparison of $^{3}He_{cos}$ and $^{10}Be_{cos}$ concentrations from olivine ($Fo_{89\text{-}91}$) from Mount Hampton are scaled for the correspondent latitude, altitude and elevation (76˚30'S, 125˚52'W, 3020 m) using Lal (1991)/Stone (2000) scaling factors and following the scheme implemented by Balco et al. (2008) for ^{10}Be and Marrero et al. (2016) for ^{3}He. The SLHL production rate for $^{3}He_{cos}$ is taken from Goehring et al. (2010) and for $^{10}Be_{cos}$ is taken from Nishiizumi et al. (2007). They have been scaled for chemical composition using the element-specific production rates of Masarik (2002) and the normalization factor (N) described in section 5.5.4. Table 6.2 summarizes the $^{3}He_{cos}$ and $^{10}Be_{cos}$ concentrations and the relevant scaled production rates and normalization factors.

Table 6.2. Compilation of the data of ^{10}Be and ^{3}He from olivine xenoliths from Mount Hampton. The $^{3}He_{cos}$ concentrations are an average of all the aliquots measured with the Helix SFT (see Chapter 5, section 5.4.2).

Sample	*Latitude S*	*Longitude W*	*Elevation (m)*	*Olivine (Fo)*	*^{10}Be (10^{7} atoms/g)*	*1σ*	*$PR^{10}Be\_Qtz$ scaled to Lal(1991)/Stone (2000)*	*N factor*	*^{10}Be Apparent exposure age (ka)*	*1σ*	*$^{3}He(10^{8}$ atoms/g)*	*1σ*	*$PR^{3}He\_Fo_{84}$ scaled to Lal(1991)/Stone (2000)*	*N factor*	*^{3}He Apparent exposure age (ka)*	*1σ*	*$^{3}He/^{10}Be$*	*1σ*
MH.1	76˚ 30'	125˚ 52'	3020	91	2.27	0.04	58.38	0.884	451	40	15.75	0.03	1674.0289	1.031	925	140	69.43	1.29
MH.2	76˚ 30'	125˚ 52'	3020	91	1.01	0.02	58.38	0.883	188	16	7.95	0.32	1674.0289	1.030	467	74	78.79	3.66
MB.71.7	76˚ 30'	125˚ 52'	3020	91	0.17	0.01	58.38	0.883	30	3	1.78	0.01	1674.0289	1.030	104	16	105.26	5.29
MB.71.8	76˚ 30'	125˚ 52'	3020	91	1.76	0.04	58.38	0.883	341	30	18.80	0.19	1674.0289	1.031	1101	170	106.60	2.47
MB.71.9	76˚ 30'	125˚ 52'	3020	89	0.81	0.02	58.38	0.875	149	13	5.37	0.24	1674.0289	1.029	319	51	66.53	3.38
MB.71.10	76˚ 30'	125˚ 52'	3020	90	0.23	0.01	58.38	0.877	41	4	1.52	0.05	1674.0289	1.030	90	14	67.41	3.52

The scaled production rates of ^{10}Be and ^{3}He are calculated using the CRONUS calculators v. 2.3 (Balco et al. ,2008) version 2.3 and Marrero et al. (2016) respectively. The Normalization factor (N) is calculated following the recommendations from section 5.6.1. Apparent exposure ages are calculated following the equations of Lal (1991) assuming zero erosion.

The $^{3}He_{cos}/^{10}Be_{cos}$ ratios vary from 66.5 to 106.6. These are much higher than the expected value from the production rates (~33, Amidon et al., 2009; Blard et al., 2013) and it is shown by the discrepancy between the calculated apparent exposure ages from $^{10}Be_{cos}$ (41 to 451 ka) and $^{3}He_{cos}$ (90 to 1101 ka). The $^{3}He_{cos}$ and $^{10}Be_{cos}$ results do not reflect a simple exposure history. Plotting the data on a $^{3}He_{cos}/^{10}Be_{cos}$ vs.$^{10}Be_{cos}$ diagram reveals complex exposure history for the Mount Hampton nunatak (Figure 6.3).

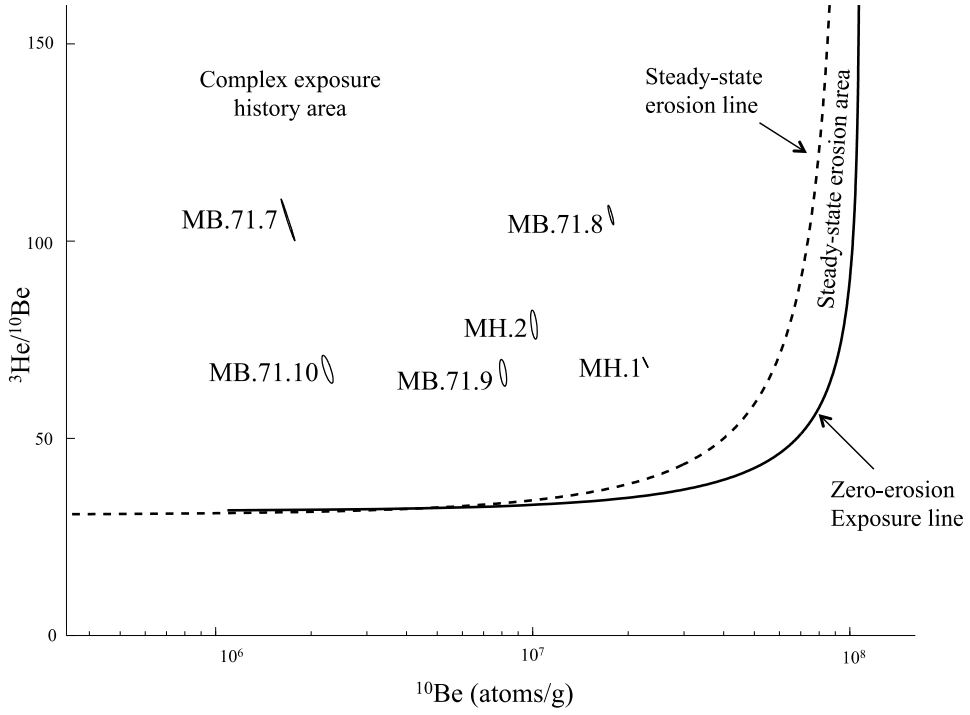

Figure 6.3. Plot of the ^{10}Be concentration vs. $^{3}He/^{10}Be$ for Mount Hampton xenolith olivine. Ellipses represent the 68% confidence interval. The banana-shaped area is known as a steady-state erosion area (Lal, 1991). The continuous line represents the evolution with time of the $^{3}He/^{10}Be$ ratio in the sample with zero erosion. The dotted line represents the steady-state ratios achieved once the rock has been eroded by at least one mean cosmic ray attenuation length at a given constant rate for infinite amount of time. Samples plotting above the steady-state erosion have had a complex exposure history.

The results show significant dispersion of the $^{3}He/^{10}Be$ ratios, indicating that each xenolith has suffered a unique exposure history despite the fact that they are all from the same surface. The samples come from scoriaceous material deposited on top of a lava flow and were collected from the same surface near the summit of Mount Hampton. The irregular topography of the surface and the fact that the xenoliths consisted on loose material can explain the variety of the cosmogenic ^{3}He and ^{10}Be concentrations and the $^{3}He/^{10}Be$ ratios. The samples though were on the same surface at the time of collection, a surface that is known to be 11.4 Ma; which sets the time limit for our interpretations. Understanding the common exposure history of these xenoliths will reveal the erosion patterns of a surface that has been lying above the WAIS since the time of formation.

6.6 Modelling complex exposure history

6.6.1 Cosmogenic ^{3}He and ^{10}Be principles for complex exposure history models

The *in situ* production of cosmogenic nuclides occurs by spallation induced by fast neutrons, negative muon capture and fast muon interactions. The production rate depends directly on depth below Earth surface. The cosmic ray flux is attenuated with mass causing the spallogenic production to decrease exponentially with depth (Goose and Phillips, 2001). At the surface production of $^{3}He_{cos}$ and $^{10}Be_{cos}$ is dominated by spallation by fast neutrons. There is little sign of a significant contribution of ^{3}He from muon production (Farley et al., 2006). In the case of $^{10}Be_{cos}$, the proportion from muon production increases with depth due to their weaker attenuation compared to fast neutrons (Heisinger et al., 2002; Balco et al., 2008).

During the time of surface exposure, $^{3}He_{cos}$ accumulates at a constant rate as a function of the time of exposure. $^{10}Be_{cos}$ accumulates at a rate that is a function of the time of exposure and its decay constant (Lal, 1991). As a consequence, for an exposed surface with zero erosion $^{10}Be_{cos}$ production reaches saturation after 5-6 half-lives while $^{3}He_{cos}$ continues to accumulate. On a surface that is being eroded the saturation is reached earlier, and the rate of accumulation from spallation decreases as a function of the rate of erosion, the density of the rock and the attenuation length according to:

$$^{3}He_{cos}/^{10}Be_{cos} = [P_{3sp} \times (\lambda_{10}+(\varepsilon\rho/\Lambda)]/[P_{10sp} \times \varepsilon\rho/\Lambda] \quad [6.1]$$

where, P_{3sp} and P_{10sp} are the $^{3}He_{cos}$ and $^{10}Be_{cos}$ production rates by spallation from fast neutrons; λ_{10} is the ^{10}Be decay constant (4.62×10^{-7} yr^{-1}, Nishiizumi, 2002); ε is the erosion rate (cm/ka); ρ is the density (g/cm^3) and Λ the attenuation length (g/cm^2) (Lal, 1991).

During burial, $^{3}He_{cos}$ initially present in a sample remains while the $^{10}Be_{cos}$ concentration decreases as a function of its decay constant. Therefore, the $^{3}He_{cos}/^{10}Be_{cos}$ ratio of a sample that has been exposed and buried increases as a function the time of burial according to:

$$^{3}He_{cos}/^{10}Be_{cos} = {}^{3}He_{in}/(^{10}Be_{in} \times e^{-\lambda_{10}T_{burial}}) \quad [6.2]$$

where, $^{3}He_{in}$ and $^{10}Be_{in}$ are the inherited $^{3}He_{cos}$ and $^{10}Be_{cos}$ concentration; λ_{10} is the ^{10}Be decay constant and T_{burial} is the time of burial (Fabel and Harbor, 1999).

When a sample is at a certain depth (z) below the surface for a length of time (T), the production rate of $^{3}He_{cos}$ and $^{10}Be_{cos}$ decreases as a function of depth and time according to:

$$^{3}He = \frac{P_{3sp}}{\frac{\varepsilon\rho}{\Lambda sp}}\left(e^{-\frac{z\rho}{\Lambda sp}}\right)\left(1-e^{-\left(\frac{\varepsilon\rho}{\Lambda sp}\right)T}\right) \quad [6.3]$$

$$^{10}Be = \frac{P_{10sp}}{\lambda_{10}+\frac{\varepsilon\rho}{\Lambda sp}}\left(e^{-\frac{z\rho}{\Lambda sp}}\right)\left(1-e^{-\left(\lambda 10+\frac{\varepsilon\rho}{\Lambda sp}\right)T}\right)+\frac{P_{10fm}}{\lambda_{10}+\frac{\varepsilon\rho}{\Lambda fm}}$$
$$\left(e^{-\frac{z\rho}{\Lambda fm}}\right)\left(1-e^{-\left(\lambda_{10}+\frac{\varepsilon\rho}{\Lambda fm}\right)T}\right)+\frac{P_{10sm}}{\lambda_{10}+\frac{\varepsilon\rho}{\Lambda sm}}\left(e^{-\frac{z\rho}{\Lambda sm}}\right)\left(1-e^{-\left(\lambda_{10}+\frac{\varepsilon\rho}{\Lambda sm}\right)T}\right) \quad [6.4]$$

where, P_{3sp} and P_{10sp} are the $^{3}He_{cos}$ and $^{10}Be_{cos}$ production rates by spallation of fast neutrons; P_{10fm} and P_{10sm} are the $^{10}Be_{cos}$ production rates by spallation of fast muons and negative muon capture and $\Lambda_{sp,fm,sm}$ are the respective attenuation lengths (Goose and Phillips, 2001; Lal, 1991; Balco et al., 2008). One consequence of this is that the $^{3}He_{cos}/^{10}Be_{cos}$ ratio decreases with depth. Thus during complex exposure histories the $^{3}He_{cos}/^{10}Be_{cos}$ ratios reflect the nuclide specific production rate, erosion rate, attenuation length, and the time of exposure (simple or complex).

6.6.2 Complex exposure history models

There are two main mechanisms for generating the observed ^{10}Be-^{3}He systematics: burial under ice and non-constant erosion rate. In the following sections I model two main scenarios that consider cover by ice and erosion change, the different models produced include:

(1) intermittent burial under ice related to glacial-interglacial cycles with burial occurring when the conditions were warmer than currently;
(2) intermittent burial under ice related to glacial-interglacial cycles with burial occurring when the conditions were colder than currently;
(3) Accumulation of cosmogenic signature at depth with instantaneous surface exposure;
(4) Episodic erosion consisting on various erosion episodes;

(5) Episodic erosion consisting on one dramatic change in erosion rate.

Combinations of values have been given to the parameters of each model to calculate different theoretical $^{3}He_{cos}$-$^{10}Be_{cos}$ concentrations. Theoretical concentrations are calculated following the equations of Lal (1991). The sea level high latitude (SLHL) spallation production rate used for $^{3}He_{cos}$ is 124 ± 16 atoms/g/year; which is the production rate in olivine (Fo_{91}) calculated from the global average for olivine $Fo_{84\pm4}$ (120 ± 16 atoms/g/year; Delunel et al., 2016) and production from negative muon capture and fast muon interactions have been assumed to be negligible (Kurz, 1986b; Sarda et al., 1992; Farley et al., 2006). For $^{10}Be_{cos}$ the SLHL production rate used is 3.54 ± 0.28 atoms/g/year; which is the production rate in olivine (Fo_{91}) calculated from quartz (4.01 ± 0.32 atoms/g/year; Brochers et al., 2016). The production rate from fast muons and negative muons is 0.221 atoms/g/year calculated using CRONUS calculators Matlab code v 2.3 (Balco et al. 2008). Table 6.3 summarizes the parameters and variables used to calculate the different complex exposure models.

Table 6.3. List of the different models generated and the parameters used to account for different complex-exposure scenarios.

Model parameters	*Values*	*Notes and references*
Complex exposure*		
^{10}Be production rate for olivine (Fo_{89-91}) at Mount Hampton	51.4 atoms/g/year	Following the scheme of Balco et al. (2008) version 2.3 scaling factor Lal(1991)/Stone(2000) scaled for composition using Masarik (2002)
^{3}He production in olivine (Fo_{89-91}) at Mount Hampton	1725 atoms/g/year	Following the scheme of Marrero et al. (2016) scaling factor Lal(1991)/Stone(2000) scaled for composition using Masarik (2002)
Production rate from fast muons	0.0777 atoms/g/year	Calculated using CRONUS calculators Matlab code v 2.3
Production rate from negative muon capture	0.0992 atoms/g/year	
Attenuation length from neutron spallation	160 g/cm^2	Balco et al. (2008); Gosse an Phillips (2001)
Attenuation length from fast muons	2.60 x 10^3 g/cm^2	Calculated using CRONUS calculators Matlab code v 2.3
Attenuation length from negative muon capture	1.30 x 10^3 g/cm^3	Calculated using CRONUS calculators Matlab code v 2.3
Half life for ^{10}Be	1.378 Ma	Chmeleff et al. (2010); Korschinek et al. (2010)
Rock density	2.67 g/cm^3	
Constant exposure-erosion lines		Calculated applying equations from Lal (1991) for constant exposure at zero erosion and for steady-state erosion for infinite time
Cyclic ice cover models		The same variables have been used to test two different ice cover models:(1) dry-based ice cover in warmer conditions, (2) dry-based ice cover in colder conditions
Time of shielding under ice (years)		Based on $\delta^{18}O$ records (<5.3 Ma Lisiecki and Raymo, 2005; > 5.3 Ma Zachos et al., 2008)
Total duration of complex history	11.4 Ma	Le Masurier and Rex (1989)
Erosion under ice (m/Ma)	Yes/No	Dry-based ice: assumed no erosion while cover by ice and erosion while uncover (Calculated following Balco et al., 2008; Lal., 1991)
$\delta^{18}O$ threshold		Shielding above/below a certain $\delta^{18}O$ threshold
Erosion rate (m/Ma)		Different erosion rates generate different $^{3}He/^{10}Be$ ratios
Erosion rate variation models		Three models have been produced to determine the rate and timing of the change of erosion rate
Accumulation at depth		Accumulation of cosmogenic nuclides at depth.
Accumulation depth (m)		Depth at which the samples have been accumulating cosmogenic signal
Time of accumulation at depth (Ma)		Time of continuous accumulation
Episodic erosion		Material is removed in steps
Average erosion rate (m/Ma)		Erosion rate is taken as an average for the total residence time (11.4Ma)
Material removed from one erosive event (m)		Erosive events are assumed to last an equal length of time
Total duration of complex history	11.4 Ma	Le Masurier and Rex (1989)
Erosion rate change		Erosion rate is assumed to be zero during the time of accumulation at depth prior to the removal of material
Accumulation depth (m)		Material removed to place the samples at the surface
Time when erosion started (m)		This considers the time at depth required to generate the ^{3}He-^{10}Be signature including a time of erosion
Total duration of complex history	11.4 Ma	Le Masurier and Rex (1989)

References for the chosen values are listed where applicable. All the parameters have been calculated using the equations of Lal (1991) modified by Balco et al. (2008) to include muon production. The models have been calculated using Matlab coding. *Parameters of complex exposure common to all the models.

6.6.3 Burial beneath ice

The Mount Hampton summit does not show erosive features indicative of significant ice accumulation (Le Masurier, 1987). It has never been covered by the WAIS (e.g. Mukhopadhyay et al., 2012). Consequently periods of shielding could have only been caused by the formation of a local cold-based alpine glacier. Such cold-based alpine glaciers often do not leave major evidence unlike the wet-based alpine glaciers that typically leave moraines or drift deposits (Denton et al., 1993).

Erosion rates in Antarctica range from a few centimetres/Ma in non-glaciated surfaces from the Dry Valleys (Schafer et al., 1999; Margerison et al., 2005) up to hundreds of m/Ma in glaciated mountaintops near the coast of the WAIS (Andrews and LeMasurier, 1973; Rocchi et al., 2006). In the interior of Antarctica the extreme cold and dryness at high altitudes are not sufficient to leave significant erosion evidence although changes in the erosion rates over long periods of time could be sufficient to vary the cosmogenic nuclide signature revealing erosion patterns that are more complex than the steady-state commonly assumed (Middleton et al., 2012).

In the WAIS interior at elevations >600 m above its current elevation precipitation occurs only on the form of snow (Bromwich, 1988). Shielding by cold-based ice cover could provide sufficient burial to generate complex exposure history signatures. The minimum time of burial and maximum erosion rate required to produce the He-Be data can be modelled (Figure 6.4). The data obtained from this model are presented in Table 6.4.

Table 6.4. Summary of the minimum times of burial and the maximum erosion rates (ε) required for generating the $^{3}He_{cos}$-$^{10}Be_{cos}$ signatures. Uncertainties are reported as 1σ**.**

Sample name	*Time of burial (Ma)*	±	*ε (m/Ma)*	±
MH.1	0.81	0.06	0.71	0.06
MH.2	1.42	0.11	1.73	0.14
MB.71.7	2.34	0.19	6.00	0.48
MB.71.8	1.53	0.12	0.62	0.05
MB.71.9	1.29	0.10	2.22	0.18
MB.71.10	1.51	0.12	6.95	0.56

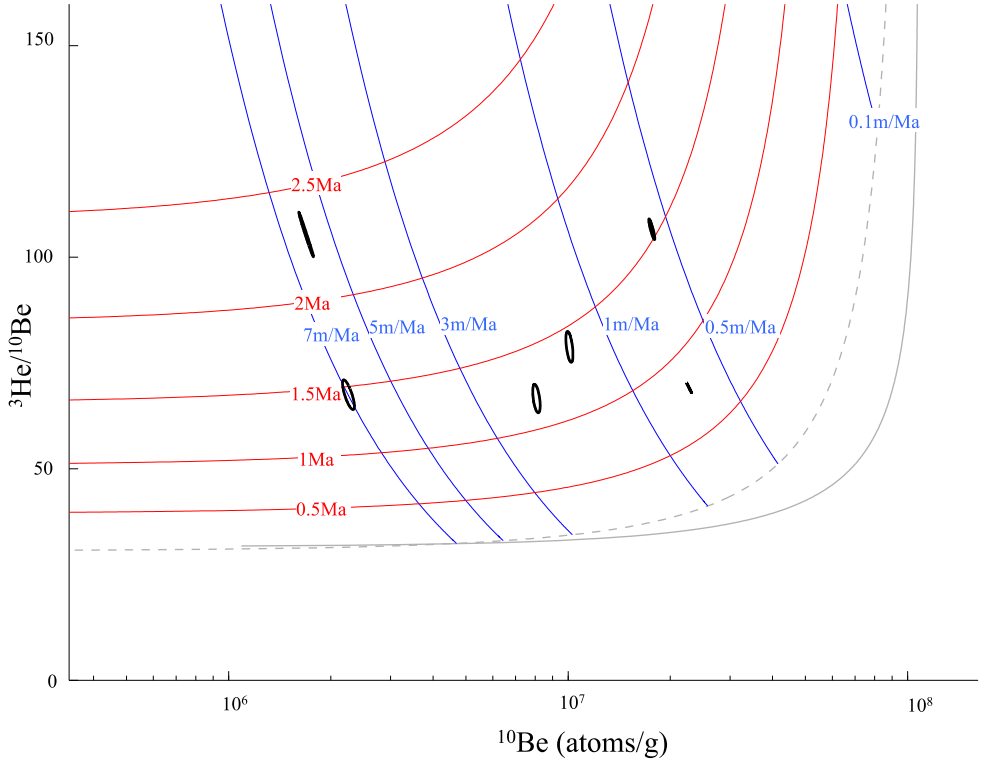

Figure 6.4. Plot of ^{10}Be concentrations against $^{3}He/^{10}Be$. Ellipses represent the 68% confidence interval. The grey continuous and discontinuous lines represent the steady-state erosion area (Lal, 1991; Balco et al., 2008). The red lines represent theoretical lines of different burial times and the blue lines represent theoretical lines of different erosion rates during time of exposure. This is the simplest exposure-burial-model that is widely used to interpret cosmogenic signatures of complex exposure. Theoretical lines have been determined following the equations of Lal (1991) modified by Balco et al. (2008) to account for muon production. Each ($^{3}He/^{10}Be$)-^{10}Be is a combination of minimum burial time and maximum erosion rate.

Continuous burial for up to 2.34 Ma is required to generate the data. Intermittent shielding due to cold-based ice cover could account for the time of burial and generate the observed signals. The parameters used in the previous model have been combined with the $\delta^{18}O$ records for the past 11.4 Ma (Lisiecki and Raymo, 2005; Zachos et al., 2008) to correlate the intermittent ice cover shielding with glacial-interglacial cycles. The shielding of the Mount Hampton nunatak has been modelled under two different conditions: (1) shielding during glacial cycles when conditions are colder, i.e. above a $\delta^{18}O$ threshold, and (2) shielding during interglacial cycles when conditions are warmer, i.e. below a $\delta^{18}O$ threshold (Figure 6.5).

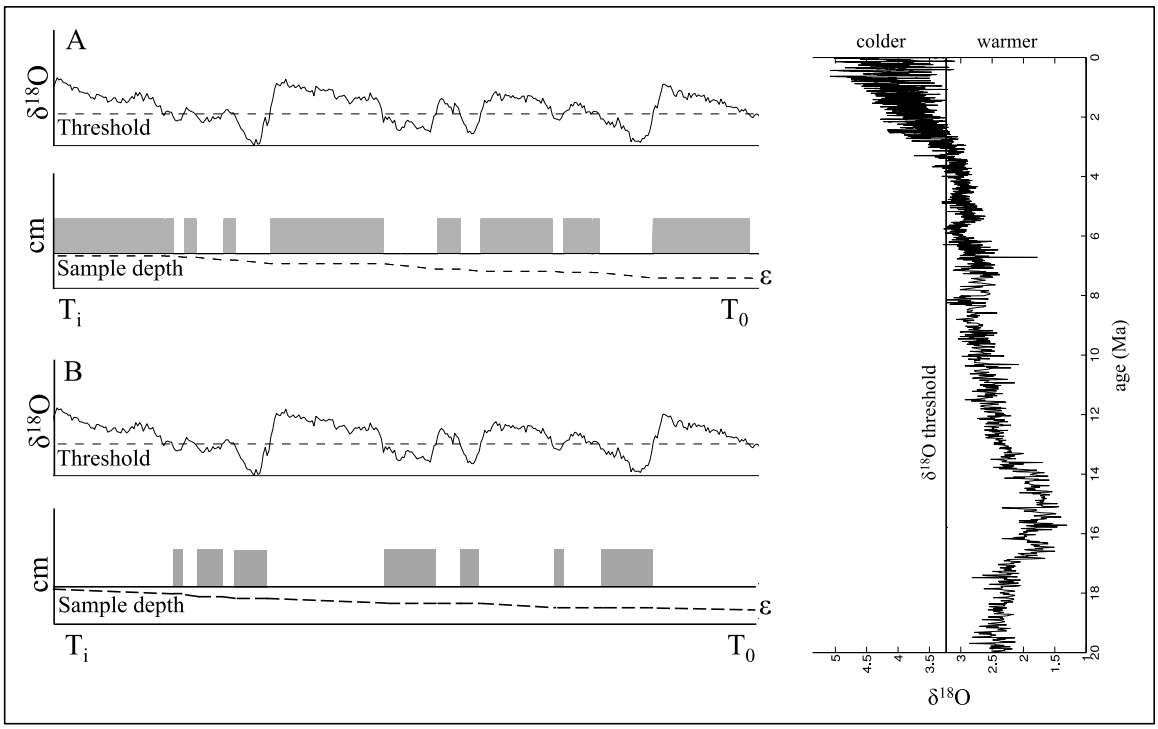

Figure 6.5. Schematic of the two different ice cover models where periods of shielding are related to the benthic $\delta^{18}O$ record (Lisiecki and Raymo, 2005; right side of the diagram). Model A assumes that shielding occurs during cold periods calculating a $\delta^{18}O$ threshold above which ice cover occurs. Model B assumes that shielding occurs during warm periods calculating a $\delta^{18}O$ threshold below which ice cover occurs. Both models assume zero erosion during the time of burial and consider an erosion rate (ε, m/Ma) for the time of exposure.

6.6.3.1 Ice cover during glacial periods

The first model assumes that ice cover (i.e. shielding) developed during glacial cycles when conditions are colder than today (Figure 6.6). The model calculates the $\delta^{18}O$ threshold above which shielding occurs and an erosion rate during the time of exposure. Each $\delta^{18}O$ threshold is associated to a burial time necessary to generate the ^{3}He-^{10}Be signatures assuming a total history of 11.4 Ma. Since all the samples are from the same surface, the burial time due to ice cover has to be the same for all the samples. An average $\delta^{18}O$ of 3.51 ± 0.21 is then taken as that required to generate the ^{3}He-^{10}Be signatures. This suggests that glacial cycles over the past c. 3.5 Ma are capable to generate the ^{3}He-^{10}Be signatures with erosion rates ranging from 0.71 to 6.95 m/Ma during the time of exposure (see Figures 6.6 and 6.7).

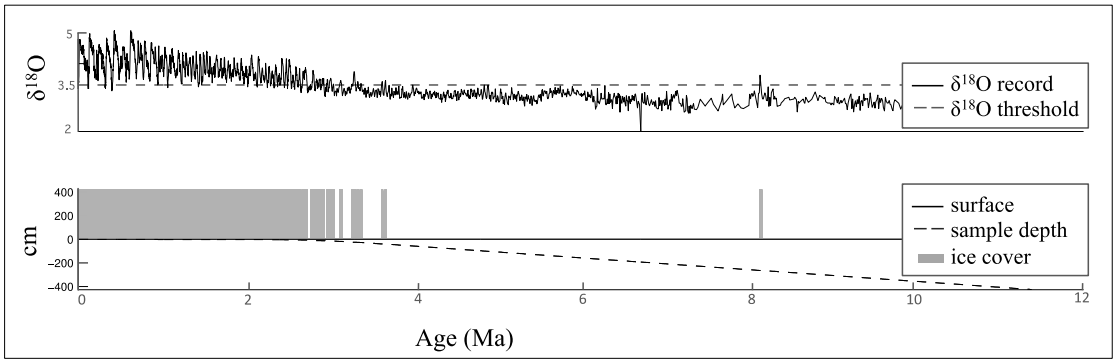

Figure 6.6. Schematic of a cold-based ice glacier forming above $\delta^{18}O$ of 3.5 on the summit of Mount Hampton nunatak. Zero erosion is assumed during the periods of covering.

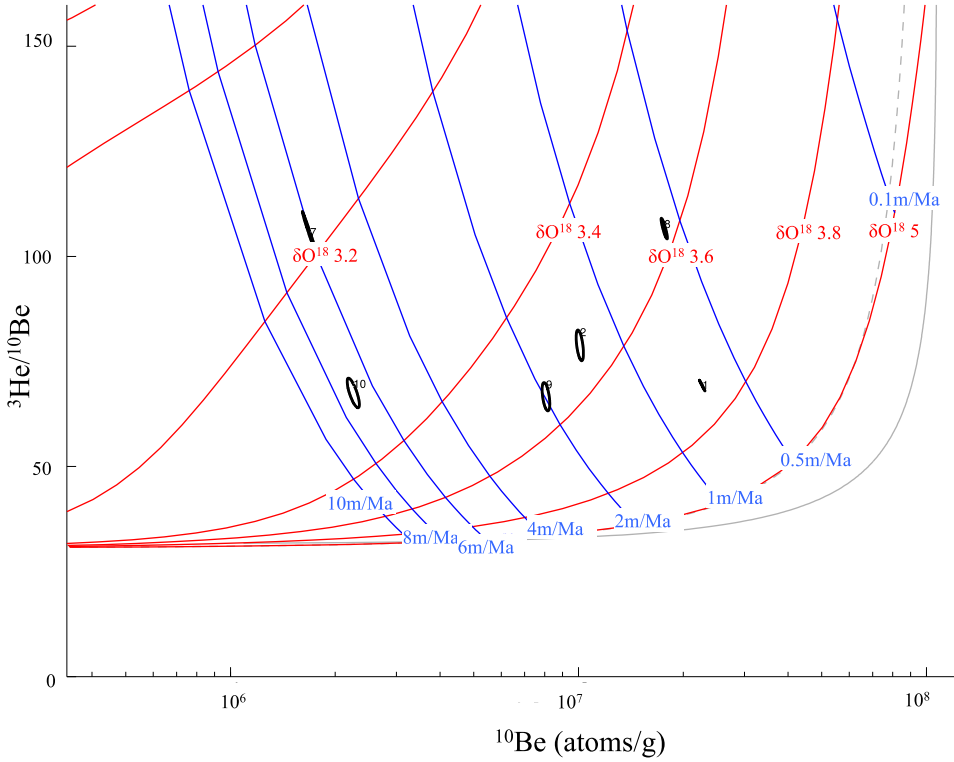

Figure 6.7. Plot of the sample ^{10}Be concentrations against $^{3}He/^{10}Be$. Ellipses represent the 68% confidence interval. The grey continuous and discontinuous lines represent the steady-state erosion area (Lal, 1991; Balco et al., 2008). The red lines represent theoretical lines of different $\delta^{18}O$ threshold above which shielding occurs and the blue lines represent theoretical lines of erosion rate during the time of exposure. Theoretical lines have been determined following the equations of Lal (1991) modified by Balco et al. (2008) to account for muon production and combined with $\delta^{18}O$ records from Lisiecki and Raymo (2005). Each ($^{3}He/^{10}Be$)-^{10}Be pair is a combination of minimum $\delta^{18}O$ threshold and maximum erosion rate.

6.6.3.2 Ice cover during interglacial periods

The model assumes that ice cover is generated during interglacial warm conditions. Theoretical $\delta^{18}O$ thresholds below which ice cover occurs and erosion rates for the time of exposure are calculated. Ice cap formation during warmer interglacial cycles implies that

the Mount Hampton summit has been covered by ice for most of the last few million years (Figure 6.8).

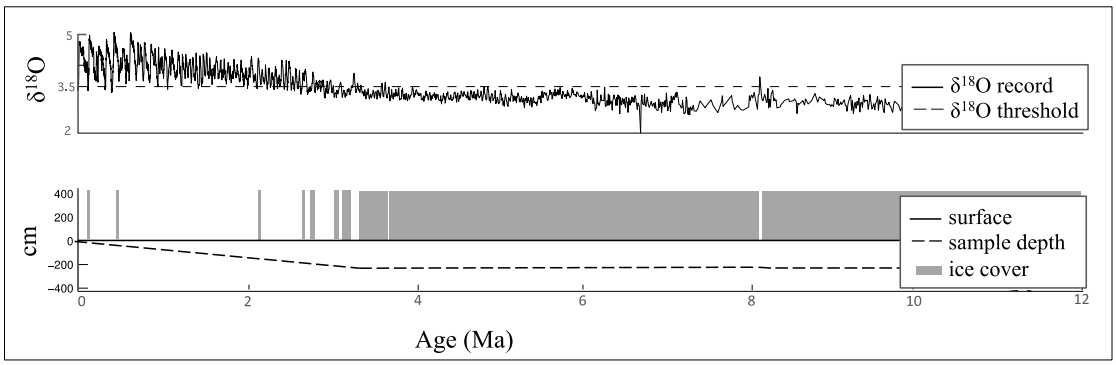

Figure 6.8. Schematic of the times of burial from cold-based ice glacier formation on the summit of Mount Hampton nunatak since the time of formation. Zero erosion is assumed during the periods of covering.

This scenario would generate $^{3}He_{cos}$ and $^{10}Be_{cos}$ concentrations that fall on the steady-state erosion line (i.e. compatible with a simple history of exposure and erosion). None of the $\delta^{18}O$ threshold and maximum erosion rate combinations fit the dataset (see Figure 6.9).

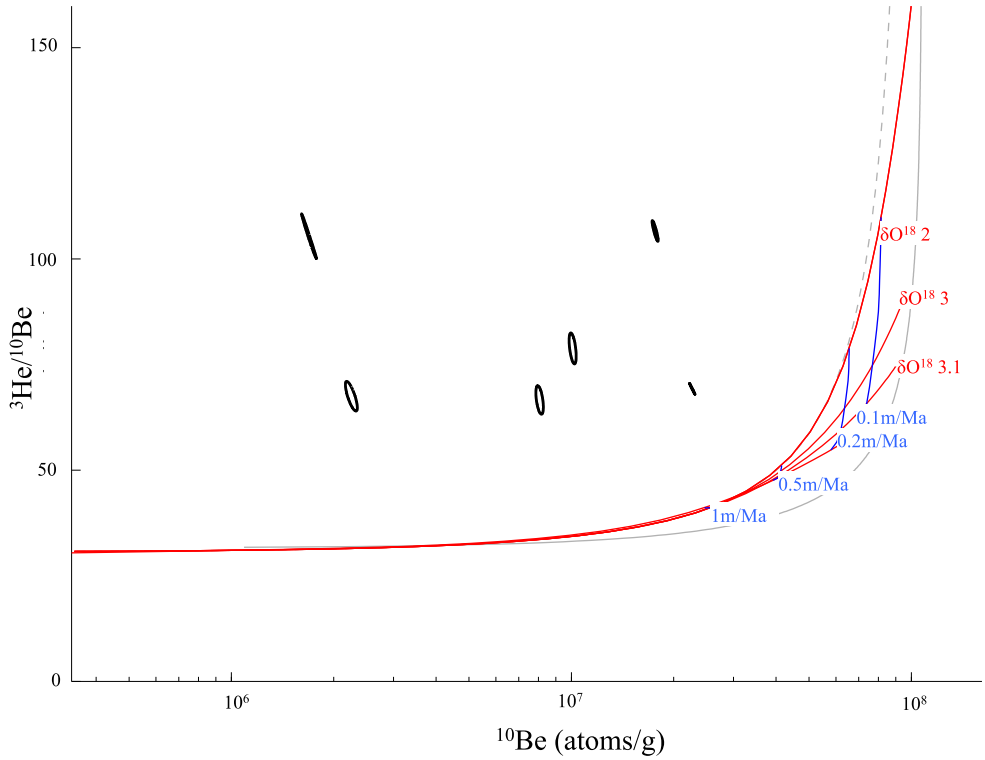

Figure 6.9. Plot of the sample ^{10}Be concentrations against $^{3}He/^{10}Be$. Ellipses represent the 68% confidence interval. The grey continuous and discontinuous lines represent the steady-state erosion area (Lal, 1991; Balco et al., 2008). The red lines represent theoretical lines of different $\delta^{18}O$ threshold below which shielding occurs and the blue lines represent theoretical lines of erosion rate during the time of exposure. Theoretical lines have been determined following the equations of Lal (1991) modified by Balco et al. (2008) to account for muon production and combined with $\delta^{18}O$ records from Lisiecki and Raymo (2005). Each ($^{3}He/^{10}Be$)-^{10}Be pair is a combination of maximum $\delta^{18}O$ threshold and maximum erosion rate.

6.6.4 Erosion rate variation models

6.6.4.1 Accumulation at depth

An alternative explanation for the evolution of the Mount Hampton summit landscape involves long-term variation in erosion rate. In the simplest case the ^{3}He-^{10}Be data can be generated by erosion from a minimum depth and a maximum erosion time (see Figure 6.10). This model assumes that the xenoliths may have started their way to the surface at different depths accumulating cosmogenic signature for long periods of time at depth and coming to the current surface at different times. Complex exposure scenarios can produce the ^{3}He-^{10}Be data when the samples have been at depths that range from 0.82 to 2.62 m for maximum times of 3.82 to 7.13 Ma (Table 6.5).

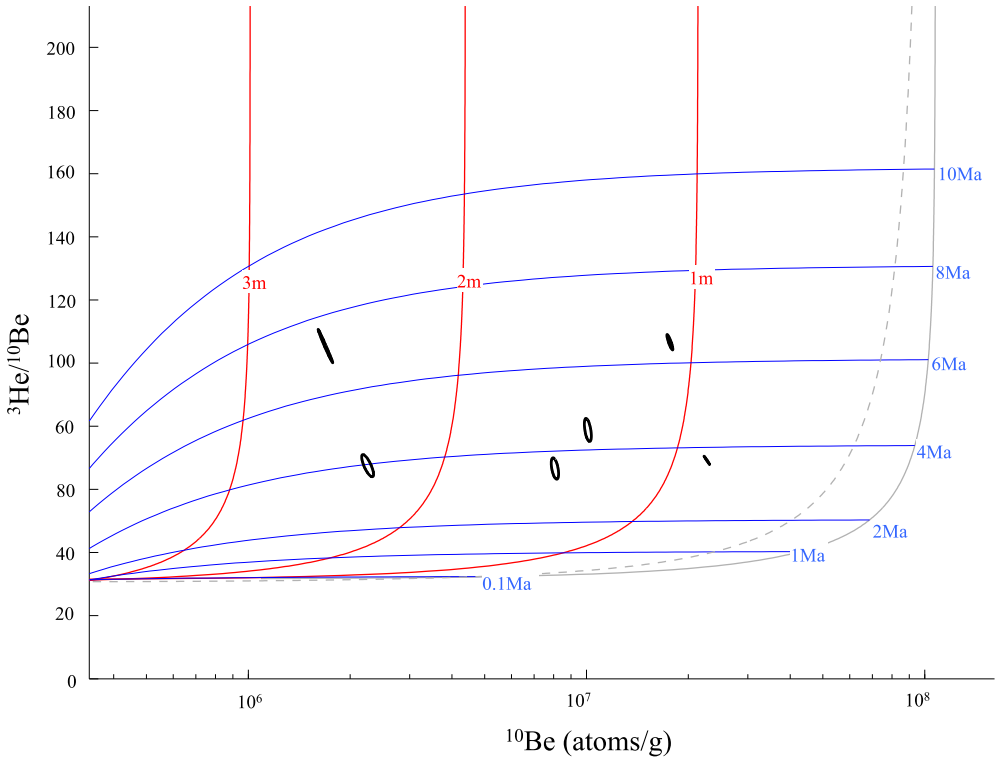

Figure 6.10. Plot of the sample ^{10}Be concentrations against $^{3}He/^{10}Be$. Ellipses represent the 68% confidence interval. The grey continuous and discontinuous lines represent the steady-state erosion area (Lal, 1991; Balco et al., 2008). The blue lines represent theoretical lines of different cosmogenic signal accumulation times and the red lines represent theoretical lines of continuous production at different depths. Theoretical lines have been determined following the equations of Lal (1991) modified by Balco et al. (2008) to account for muon production. Each ($^{3}He/^{10}Be$)-^{10}Be represents a maximum accumulation time at a minimum depth.

Table 6.5. Summary of the minimum depth and the maximum time at depth required for generating the $^{3}He_{cos}$-$^{10}Be_{cos}$ signatures. Uncertainties are reported as 1σ.

Sample name	*Depth (m)*	±	*Time (Ma)*	±
MH.1	0.82	0.07	3.85	0.31
MH.2	1.43	0.11	4.17	0.33
MB.71.7	2.62	0.21	7.13	0.57
MB.71.8	1.23	0.10	6.43	0.51
MB.71.9	1.45	0.12	3.82	0.31
MB.71.10	2.40	0.19	4.00	0.32

6.6.4.2 Episodic erosion

Episodic erosion seems the mechanism that could generate samples staying at depth for long periods of time and then being at the surface. This episodic erosion can occur in one or various steps at various rates. To generate this model we assume that the material removed in one event is always the same. The amount of material removed from one single event and the average erosion rate, over 11.4 Ma have been modelled (Figure 6.11) and the total amount of material partially shielding the samples and the number of events over 11.4 Ma can be calculated. The output results are summarized in Table 6.6.

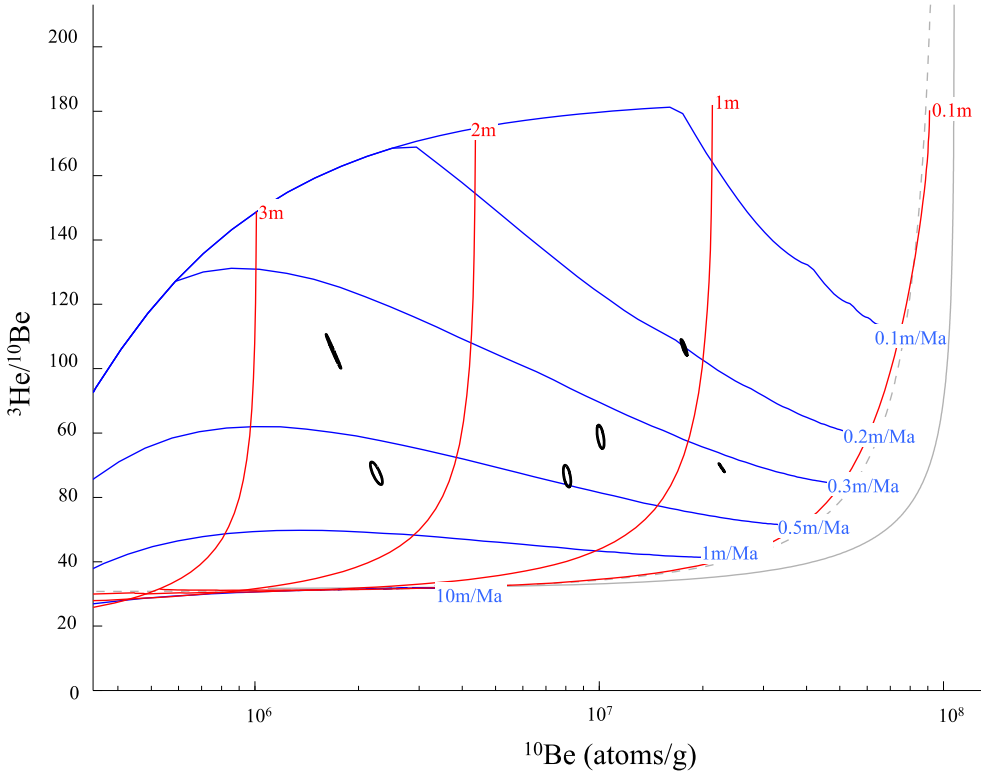

Figure 6.11. Plot of the sample ^{10}Be concentrations against $^{3}He/^{10}Be$. Ellipses represent the 68% confidence interval. The grey continuous and discontinuous lines represent the steady-state erosion area (Lal, 1991; Balco et al., 2008). The red lines represent theoretical amount of material removed in one single event and the blue lines represent theoretical lines of average erosion rate over 11.4 Ma of history. Theoretical lines have been determined following the equations of Lal (1991) modified by Balco et al. (2008) to account for muon production. Each ($^{3}He/^{10}Be$)-^{10}Be is a combination of minimum amount of material removed and maximum average erosion rate over 11.4 Ma.

Table 6.6. Summary of the minimum amount of material removed and maximum erosion rates (ε) over the total time of exposure history required for generating the $^{3}He_{cos}$-$^{10}Be_{cos}$ signatures. The total material material removed over 11.4 Ma and the minimum number of events necessary to remove this material has been calculated. Uncertainties are reported as 1σ.

Sample name	*Material removed in one event (m)*	±	*ε (m/Ma) over 11.4Ma*	±	*Total material removed (m)*	±	*n. events*	±
MH.1	0.82	0.07	0.32	0.03	3.65	0.34	4.4	0.6
MH.2	1.43	0.11	0.33	0.03	3.76	0.34	2.6	0.3
MB.71.7	2.62	0.21	0.32	0.03	3.65	0.34	1.4	0.2
MB.71.8	1.23	0.1	0.49	0.04	5.59	0.46	4.5	0.5
MB.71.9	1.45	0.12	0.20	0.02	2.28	0.23	1.6	0.2
MB.71.10	2.4	0.19	0.71	0.06	8.09	0.68	3.4	0.4

The low erosion rates calculated over the total exposure history (0.20 to 0.71 m/Ma) are not a consequence of steady-state erosion. These erosion rates are the result of periods of negligible erosion (assumed to be 0) combined with two or more (up to 5) periods where the erosion rates increase dramatically removing from 0.8 to 2.6 m of material at the time. This implies that the landscape has evolved episodically. Figure 6.12 shows the evolution of the xenoliths according to this model.

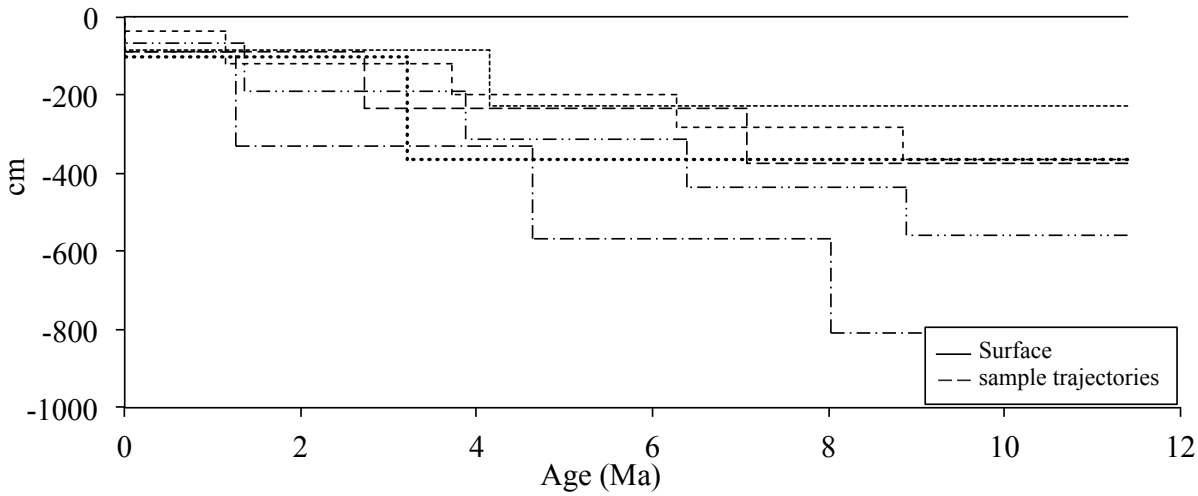

Figure 6.12. Schematic plot of the episodic erosion. The different episodes of erosion required to generate the cosmogenic signature over 11.4 Ma of exposure history of the Mount Hampton nunatak are represented as vertical drops as this is the most extreme scenario. The episodes of erosion are assumed to be homogeneously distributed in time for simplification of the figure. The path to the surface over time by each of the xenoliths is represented by the different dotted lines.

6.6.4.3 Erosion rate change

A dramatic increase in the erosion rate can cause the cosmogenic $^{3}He/^{10}Be$ ratios to move into the complex exposure area of the banana plot. To constrain the time when erosion rate changed, zero erosion has been assumed for the period of storage of

cosmogenic signature at depth. The minimum depths at which the samples have been stored, and the maximum time for the erosion rate to change, have been modelled (Figure 6.13). Consequently an apparent short-term erosion rate can be calculated. Table 6.7 summarises the output results.

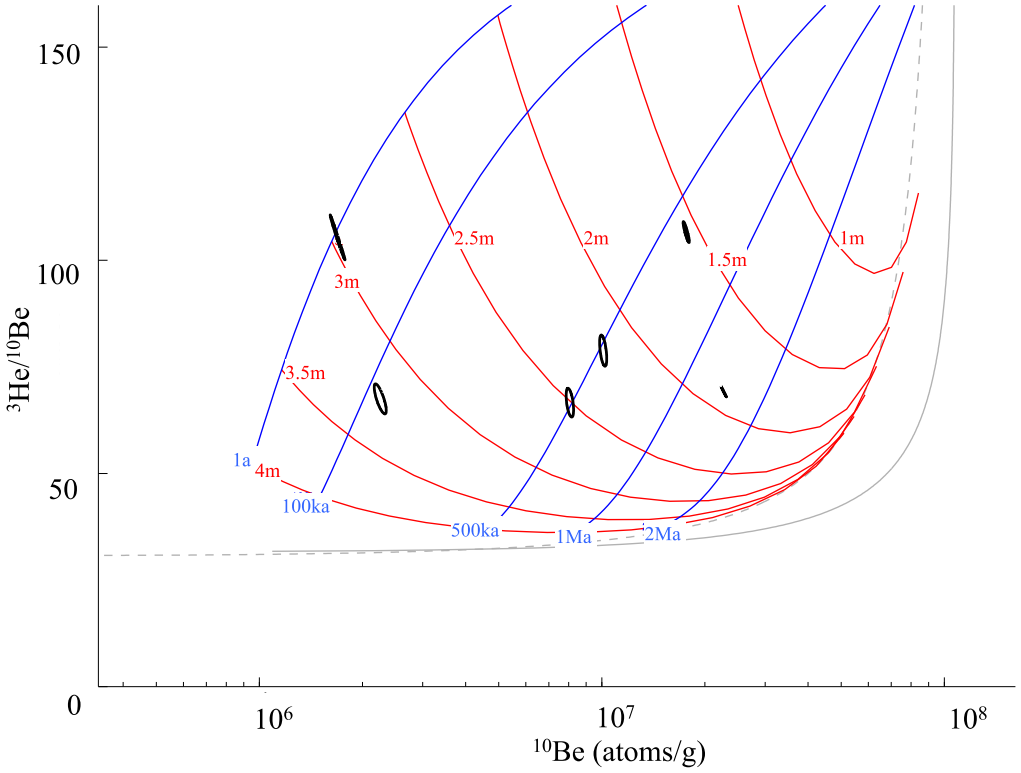

Figure 6.13. Plot of the sample ^{10}Be concentrations against ^{3}He/^{10}Be. Ellipses represent the 68% confidence interval. The grey continuous and discontinuous lines represent the steady-state erosion area (Lal, 1991; Balco et al., 2008). The red lines represent theoretical depth of accumulation and the blue lines represent theoretical lines of time of erosion change over 11.4 Ma of history. Theoretical lines have been determined following the equations of Lal (1991) modified by Balco et al. (2008) to account for muon production. Each (^{3}He/^{10}Be)-^{10}Be is a combination of minimum depth of accumulation and maximum time of erosion rate change.

Table 6.7. Summary of the minimum depth at which samples have been accumulating cosmogenic signal and apparent erosion rates (ε) over a maximum time (time of removal) required for generating the ^{3}He$_{cos}$-^{10}Be$_{cos}$ signatures. Uncertainties are reported as 1σ.

Sample name	*Depth (m)*	±	*Time of removal (Ma)*	±	*Apparent short-term ε (m/Ma)*	±
MH.1	1.80	0.14	1.50	0.12	1.20	0.14
MH.2	2.20	0.18	0.50	0.04	4.40	0.50
MB.71.7	3.06	0.24	0.01	0.00	306.00	34.6
MB.71.8	1.60	0.13	0.60	0.05	2.67	0.30
MB.71.9	2.50	0.20	0.50	0.04	5.00	0.57
MB.71.10	3.27	0.26	0.11	0.01	29.70	3.4

In this scenario the data require partial shielding for long period of time. To generate the cosmogenic signature observed the samples required storage at depths between 1.60 and 3.27 m for most of the time since eruption (9.90 to 11.39 Ma), and a dramatic increase in erosion rate over the last 1.5 Ma, from between 1.2 to 306 m/Ma.

These short-term erosion rates are not representative of the whole history of Mount Hampton as they record the maximum amount of material removed in a minimum period of time with erosion process able to remove up to 3.3 m in a short period of time. Over the total history of Mount Hampton nunatak the erosion rates observed are of < 1 m/Ma (Figure 6.14).

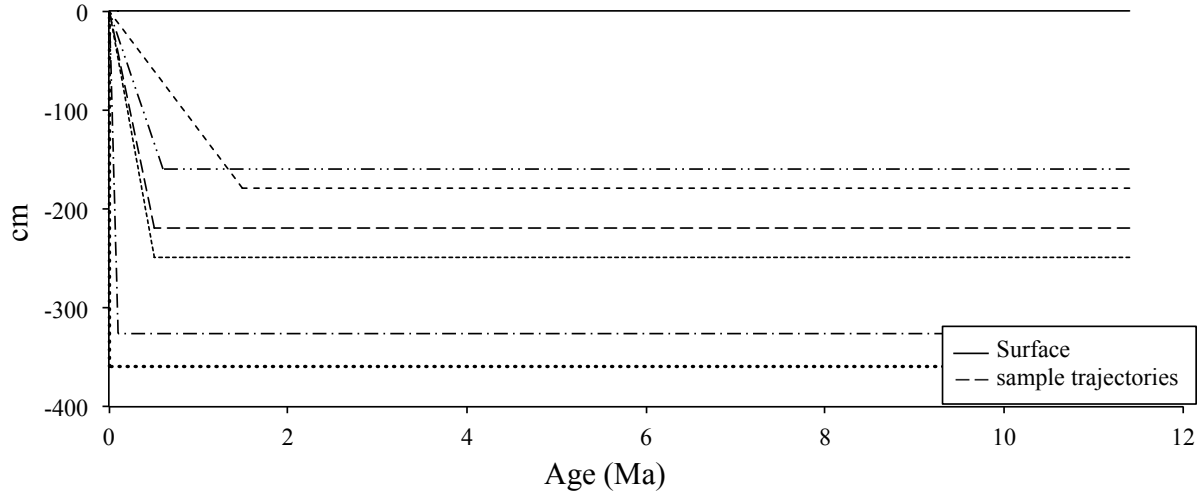

Figure 6.14. Schematic plot of the change in erosion rate over 11.4 Ma of exposure history of the Mount Hampton nunatak. The path to the surface over time by each of the xenoliths is represented by the different dotted lines.

The models presented in this section have led to two main extreme scenarios. These two hypotheses that can explain the complex exposure history of the xenoliths from the summit of Mount Hampton are: (1) shielding by intermittent cold-base ice during the cold glacial cycles of the Plio-Pleistocene, and (2) slow erosion since eruption time followed by a dramatic increase in the erosion rates since the Pleistocene if one erosion change is assumed or two several episodes of erosion combined with slow erosion over long periods of time. The two main scenarios are summarized in Figure 6.15.

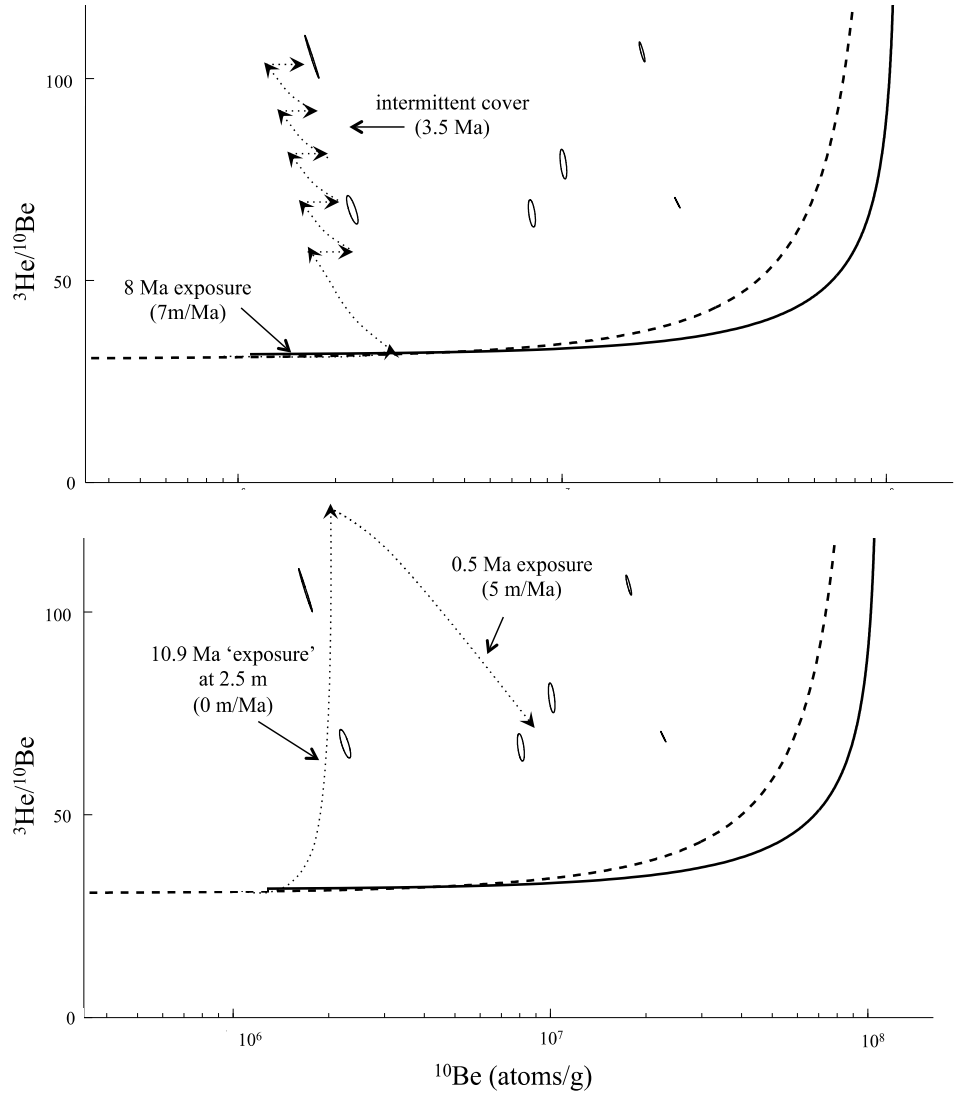

Figure 6.15. Examples of complex exposure histories that generate cosmogenic ^{3}He-^{10}Be concentrations within the range of our dataset. Ellipses represent the 68% confidence interval. Both of the figures include the steady-state erosion curves. Upper figure: dotted line represents the evolution of the cosmogenic signature as a model surface experiences 8 Ma of exposure at 7m/Ma erosion rate followed by 3.5 Ma of intermittent cold-based ice cap cover. Lower figure: the evolution of cosmogenic signature as a model surface experiences a change in the rate of erosion after 10.9 Ma of accumulation at a depth of 2.5m and zero erosion and changing to an erosion rate of 5m/Ma in the last 0.5 Ma of its exposure history. More episodes of erosion change can also generate the same isotopic signature.

6.7 Discussion

6.7.1 Cold-based ice cover during Plio-Pleistocene glacial cycles

Extensive shielding by multiple episodes of cover under ice could generate the complex exposure signature. Cold-based alpine glaciers in Antarctica often do not leave obvious geomorphic features (Naslund, 1997; Sugden et al., 2005). Close to the coast (i.e. Ford Ranges) it has been determined that the cold-based glaciers have over-ridden the

nunataks on several occasions in the past few million years producing insignificant sub-glacial erosion especially at higher elevations (Sugden et al., 2005).

Mount Hampton shows no glacial erosion features as the majority of the volcanoes of the WAIS interior where conditions are cold and dry suggesting that if any ice cover has happened must have been produced by local cold-based ice cap (Le Masurier, 1987; Le Masurier and Rocchi, 2005; Rocchi et al., 2006). Modelling the data has suggested that in Mount Hampton nunatak the formation of a cold-based ice cap could have happened during the glacial cycles of the past ~3.5 Ma in combination with erosion rates < 7m/Ma. This scenario although theoretically possible seems unlikely on the MBL as it is the only Antarctic region where the mean katabatic flow has a strong southward component causing a precipitation shadow effect over the ECR producing a strong foehn wind effect responsible for snowfall to sublimate/evaporate (Nicolas and Bromwich, 2010) which makes the possibility of an ice cap formation to be an unlikely scenario.

6.7.2 Late Pleistocene increase in erosion rate or episodic erosion during the total time of exposure

The data are consistent with the continuous exposure of the summit of Mount Hampton since eruption followed by a dramatic increase in the erosion rate during the Pleistocene. This erosion pulse would have to have been capable of removing the top layers of material and exposing the nuclide-poor material beneath. Assuming negligible erosion during the time at depth, our dataset suggest that an increase in the erosion rate capable of removing up to ~3 m of material occurred during the last 1.5 Ma. The dataset also agrees with erosion being negligible during most of the time with various episodes of erosion capable of removing up to ~2.6 m of material at the time distributed throughout the 11.4Ma of mountain top exposure. The environmental changes that would have generated such increase in the erosion rates are although unclear.

In Antarctica, at high altitude, rocks are exposed to weathering processes that are typical of extreme cold and dry desert (Campbel and Claridge, 1987). Winds in Antarctica play an important role in the snow accumulation and erosion patterns (Welch and Jacobel, 2005). Katabatic winds in the WAIS interior can reach speeds of up to 9 m/s (Parish and Browmwich, 1991); which could cause the removal of the loose material on the uppermost surface of the Mount Hampton nunatak generating the high apparent short-term erosion

rates observed. The loose nature of the surface in conjunction with topographic noise and the action of the katabatic winds could be responsible for the differences in the individual histories of the xenoliths. Despite the individual differences on apparent erosion rates all the xenoliths record a history of episodic erosion with episodes of rapid increase of the erosion rates capable of generating a maximum long-term erosion rate of ~0.4 m/Ma over the total 11.4 Ma. The common history of all the xenoliths suggests the dynamic nature of the surface of Mount Hampton nunatak above the WAIS.

6.9 Conclusions

This is the first attempt to combine $^{10}Be_{cos}$ and $^{3}He_{cos}$ in olivine to resolve complexity of long-term landscape development. With the production of $^{10}Be_{cos}$ being 33 times than that of $^{3}He_{cos}$ (Amidon et al., 2009; Blard et al., 2013) this technique is most useful in long-exposed surfaces at high latitudes were production rates are high enough to produce measurable $^{10}Be_{cos}$ signals avoiding the analysis of extremely large amounts of sample. For this study ~1 g of olivine has been enough to measure $^{10}Be_{cos}$ to a precision better than 5%.

The high precision $^{3}He_{cos}$ data in combination with $^{10}Be_{cos}$ has revealed the dynamic exposure history of the Mount Hampton nunatak and has widen the application of the combination of stable and radioactive cosmogenic nuclides to surfaces where quartz is not available. Using $^{3}He_{cos}$ as the stable isotope improves the reliability of the stable nuclide results as the use of $^{3}He_{cos}$ rules out the difficulty of isolating the Ne nucleogenic component when using $^{21}Ne_{cos}$.

The data are consistent with intermittent cold-based ice cover of the Mount Hampton nunatak during the Plio-Pleistocene glacial cycles in combination with a long-term erosion rate of < 7 m/Ma although the conditions required to generate such ice cover are unlikely to have occurred. An alternative and valid interpretation for the dataset is that the Mount Hampton nunatak has been ice-free since the time of formation 11.4 Ma, experiencing a dramatic increase on erosion rates, removing up to 3 m of material in the last 1.5 Ma. The results require an average erosion rate for the Mount Hampton nunatak of ~0.4 m/Ma for the 11.4 Ma of exposure (which is within Antarctic limits) generated as a result of episodes of higher erosion rate during short periods of time.

This work has demonstrated empirically that changes in the erosion rates over long periods of time can generate cosmogenic nuclide signatures that plot in the complex exposure area of the ($^{3}He/^{10}Be_{cos}$)-$^{10}Be_{cos}$ diagram with no need of surface burial. The data have revealed the dynamic nature of the landscape in the Mount Hampton nunatak. More detailed site examination and further investigation on other mountaintops above the WAIS is required in order to extrapolate this dynamic to other high elevation mountaintops of the ECR.

7. Conclusions

The main thrust of this study has been to report new data for cosmogenic ^{3}He and ^{21}Ne in a variety of mafic minerals (olivine, orthopyroxene, clinopyroxene and spinel) from high altitude and high latitude. To achieve high precision measurements for mineral inter-comparison of production rates, analytical procedures have been developed. The multicollector ThermoFisher Helix SFT mass spectrometer at SUERC has been fully characterized and is capable of routinely generating measurements of standard gas (HESJ, Matsuda et al., 2002) with reproducibility (0.2% and 1.1%, 1σ, for ^{4}He and ^{3}He respectively) approximately 3 times better than that obtain from peak jumping collection using the MAP 215-50 at SUERC (Dymock, 2014). In this work I have set up the helix SFT to be highly stable allowing for better reproducibility of the measurements and improving the quality of the data generated from the laboratory at SUERC. This has allowed performing high precision measurements of mineral standards to test the laser degassing technique.

Using an 808 nm diode laser precision of 0.4 % (2σ) for ^{3}He measurement of CRONUS pyroxene standard was achieved. This is comparable to other laboratories (Blard et al., 2015). In the case of olivine (MH.2) precision of ^{3}He measurement is 4.6 % (2σ). These analyses were performed on small samples (~15 mg) encapsulated in Pt tubes. The high precision achieved on the measurement of small samples is better that the uncertainty on the scaling factors (~10%) and allows for high precision inter-comparison within the same area when the scaling factors are not relevant. Complete degassing of larger samples (50-250 mg) has proved challenging. Olivine from Holocene lava flows from Kula Volcanic Province, Western Turkey proved difficult to degas, however reliable data were obtained when degassing pyroxene, which leaves hope for future development of the technique.

The first attempt to determine $^{3}He_{cos}$ in detrital gold grains has been reported in this work. Laser degassing has proved a reliable method for extraction of He and has the potential to be automated allowing for analysis of tens to hundreds of grains from the same deposit in relatively short time. Thirty-six detrital gold grains from eight alluvial deposits from across Scotland were analysed. Some grains record ^{3}He concentrations that correspond to minimum exposure ages of over 200 ka. However, the difficulty in

measuring low Li concentrations in gold leaves it possible that much of the He is generated by nucleogenic reactions. Automation of laser extraction and He isotope determination from detrital minerals holds great potential to quantifying transport and storage of sediments. Accurate estimation of the production rate of $^{3}He_{cos}$ in gold and other metals is now necessary in order to be able to use the data for exposure age interpretations.

Some of the highest $^{3}He_{cos}$ and $^{21}Ne_{cos}$ concentrations recorded in terrestrial samples have been obtained from the analysis of xenolith minerals from Mount Hampton in West Antarctica. The low uncertainties obtained from the analysis of mineral separates using the laser and the Helix SFT allow for comparison of $^{3}He_{cos}$ concentration in different mafic minerals from Mount Hampton xenoliths. The results have demonstrated that chemical composition controls the production rate of $^{3}He_{cos}$ and $^{21}Ne_{cos}$ and therefore scaling for composition using theoretical elemental production rates is necessary for accurate cosmogenic nuclide interpretation. A normalization factor (N) for scaling production rate for chemical composition has been recommended. Theoretical elemental production rates of Masarik (2002) and Kober et al. (2005) generate normalization factors that are indistinguishable with uncertainty. Therefore the choice of theoretical method remains to the discretion of the user. Applying a normalization factor improves the quality of the interpretation of the cosmogenic signatures for exposure dating. The relative production rate of $^{21}Ne_{cos}$ and $^{3}He_{cos}$ at Mount Hampton (high altitude, ~3 km, and high latitude, ~76˚S) seem to show no altitude dependence as the $^{21}Ne_{cos}/^{3}He_{cos}$ ratios that were consistent with previously reported ratios from other locations at lower altitudes.

This study also reports the first attempt to combine $^{10}Be_{cos}$ and $^{3}He_{cos}$ in olivine to resolve complexity of long-term landscape development demonstrating that changes in the erosion rates over long periods of time are capable to generate complex exposure cosmogenic nuclide signatures with no need of surface burial. The $^{10}Be_{cos}$ and $^{3}He_{cos}$ data from xenolith olivine from the summit of Mount Hampton can be explained with a dramatic increase on erosion rates, removing up to 3 m of material in the last 1.5 Ma. This requires an average erosion rate for the Mount Hampton nunatak of ~0.3 m/Ma for the 11.4 Ma of exposure generated as a result of episodes of higher erosion rate during short periods of time. The most important message from this work is that the landscape in the high elevation mountaintop of the Mount Hampton nunatak has a dynamic nature.

7.1 Perspective

Continuing development of the laser extraction technique introducing the use of a copper pan with larger and deeper wells and improving the encapsulation of olivine grains to allow for accurate and precise measurement of He isotopes from young exposed samples. This will widen the use of the laser to date limited to old exposed samples were 15 mg is enough to generate a measurable signal.

Automation of the laser extraction system to allow continuous measurements of individual grains will increase sample throughput and will make He blank levels more constant

This study is one of only two studies to measure $^{3}He_{cos}$ and $^{10}Be_{cos}$ in olivine. This has the potential to widen the application of stable and radioactive cosmogenic nuclides to landscapes that are composed of lithologies where quartz is not abundant (i.e. olivine-bearing basaltic volcanic surfaces).

Modelling the data obtained by combining the two cosmogenic isotopes has demonstrated that exposure-burial-exposure histories (i.e. complex exposure) is not the only way to generate $^{3}He_{cos}$-$^{10}Be_{cos}$ signatures that do no plot on the exposure-erosion island. The extent to which changing bedrock erosion rates can explain the abundant cosmogenic ^{21}Ne-^{10}Be data from Antarctica has not been explored. In future resolving this will prove important for addressing major uncertainties in long-term landscape history in Antarctica such as reconciling the extent of past ice cover.

The data from Mount Hampton has demonstrated the dynamic nature of the volcanic landscape in such extreme arid environment. The abundance of volcanic tops above the West Antarctic Ice Sheet suggests that understanding how these landscapes respond to climate change will be essential for unravelling ice sheet history.

References

Aciego, S.M., Cuffey, K.M., Kavanaugh, J.L., Morse, D.L. and Severinghaus, J.P., 2007. Pleistocene ice and paleo-strain rates at Taylor Glacier, Antarctica. *Quaternary Research*, *68*(3), pp.303-313.

Ackert, R.P., Barclay, D.J., Borns, H.W., Calkin, P.E., Kurz, M.D., Fastook, J.L. and Steig, E.J., 1999. Measurements of past ice sheet elevations in interior West Antarctica. *Science*, *286*(5438), pp.276-280.

Ackert, R.P., Singer, B.S., Guillou, H., Kaplan, M.R. and Kurz, M.D., 2003. Long-term cosmogenic 3 He production rates from 40 Ar/39 Ar and K–Ar dated Patagonian lava flows at 47 S. *Earth and Planetary Science Letters*, *210*(1), pp.119-136.

Ackert, R.P., Mukhopadhyay, S., Parizek, B.R. and Borns, H.W., 2007. Ice elevation near the West Antarctic Ice Sheet divide during the last glaciation. *Geophysical Research Letters*, *34*(21).

Ackert, R.P., Mukhopadhyay, S., Pollard, D., DeConto, R.M., Putnam, A.E. and Borns, H.W., 2011. West Antarctic Ice Sheet elevations in the Ohio Range: Geologic constraints and ice sheet modeling prior to the last highstand. *Earth and Planetary Science Letters*, *307*(1), pp.83-93.

Ackert, R.P., Putnam, A.E., Mukhopadhyay, S., Pollard, D., DeConto, R.M., Kurz, M.D. and Borns, H.W., 2013. Controls on interior West Antarctic Ice Sheet Elevations: inferences from geologic constraints and ice sheet modeling. *Quaternary Science Reviews*, *65*, pp.26-38.

Aldrich, L.T. and Nier, A.O., 1948. The occurrence of He 3 in natural sources of helium. *Physical Review*, *74*(11), p.1590.

Alıcı, P., Temel, A. and Gourgaud, A., 2002. Pb–Nd–Sr isotope and trace element geochemistry of Quaternary extension-related alkaline volcanism: a case study of Kula region (western Anatolia, Turkey). *Journal of Volcanology and Geothermal Research*, *115*(3), pp.487-510.

Alvarez, L.W. and Cornog, R., 1939. Helium and hydrogen of mass 3. *Physical Review*, *56*(6), p.613.

Amidon, W.H., Farley, K.A. and Rood, D.H., 2008, December. Considerations for successful cosmogenic 3He dating in accessory phases. In *AGU Fall Meeting Abstracts* (Vol. 1, p. 03).

Amidon, W.H., Rood, D.H. and Farley, K.A., 2009. Cosmogenic 3 He and 21 Ne production rates calibrated against 10 Be in minerals from the Coso volcanic field. *Earth and Planetary Science Letters*, *280*(1), pp.194-204.

Amidon, W.H. and Farley, K.A., 2011. Cosmogenic 3 He production rates in apatite, zircon and pyroxene inferred from Bonneville flood erosional surfaces. *Quaternary Geochronology*, *6*(1), pp.10-21.

Anderson, J.B. and Shipp, S.S., 2001. Evolution of the West Antarctic ice sheet. *The West Antarctic ice sheet: behavior and environment*, pp.45-57.

Anderson, J.B., Shipp, S.S., Lowe, A.L., Wellner, J.S. and Mosola, A.B., 2002. The Antarctic Ice Sheet during the Last Glacial Maximum and its subsequent retreat history: a review. *Quaternary Science Reviews*, *21*(1), pp.49-70.

Ando, K. and Oishi, Y., 1974. Self‐diffusion coefficients of oxygen ion in single crystals of MgO· n Al2O3 spinels. *The Journal of Chemical Physics*, *61*(2), pp.625-629.

Andrews, J.N. and Kay, R.L.F., 1982. Natural production of tritium in permeable rocks.

Alsmiller Jr, R.G. and Barish, J., 1982. Neutron-Photon Multigroup Cross Sections for Neutron Energies. *Nuclear Science and Engineering*, *80*(3), pp.448-452.

Badenhoop, J.K. and Weinhold, F., 1997. Natural bond orbital analysis of steric interactions. *The Journal of chemical physics*, *107*(14), pp.5406-5421.

Bamber, J.L., Riva, R.E., Vermeersen, B.L. and LeBrocq, A.M., 2009. Reassessment of the potential sea-level rise from a collapse of the West Antarctic Ice Sheet. Science, 324(5929), pp.901-903.

Balco, G. and Shuster, D.L., 2009a. Production rate of cosmogenic 21 Ne in quartz estimated from 10 Be, 26 Al, and 21 Ne concentrations in slowly eroding Antarctic bedrock surfaces. *Earth and Planetary Science Letters*, *281*(1), pp.48-58.

Balco, G. and Shuster, D.L., 2009b. 26 Al–10 Be–21 Ne burial dating. *Earth and Planetary Science Letters*, *286*(3), pp.570-575.

Balco, G., Stone, J.O., Lifton, N.A. and Dunai, T.J., 2008. A complete and easily accessible means of calculating surface exposure ages or erosion rates from 10 Be and 26 Al measurements. *Quaternary geochronology*, *3*(3), pp.174-195.

Balco, G., Soreghan, G.S., Sweet, D.E., Marra, K.R. and Bierman, P.R., 2013. Cosmogenic-nuclide burial ages for Pleistocene sedimentary fill in Unaweep Canyon, Colorado, USA. *Quaternary Geochronology*, *18*, pp.149-157.

Ballentine, C.J. and Burnard, P.G., 2002. Production, release and transport of noble gases in the continental crust. *Reviews in mineralogy and geochemistry*, *47*(1), pp.481-538.

Bao, H. and Thiemens, M.H., 2000. Generation of O2 from BaSO4 using a CO2-laser fluorination system for simultaneous analysis of δ18O and δ17O. *Analytical chemistry*, *72*(17), pp.4029-4032.

Barfod, D.N., Mark, D.F., Tait, A., Dymock, R.C. and Imlach, J., 2014. Argon extraction from geological samples by CO2 scanning laser step-heating. *Geological Society, London, Special Publications*, *378*(1), pp.79-90.

Bhandari, C.M. and Verma, G.S., 1965. Role of Longitudinal and Transverse Phonons in Lattice Thermal Conductivity of GaAs and InSb. *Physical Review*, *140*(6A), p.A2101.

Blard, P.H. and Farley, K.A., 2008. The influence of radiogenic 4 He on cosmogenic 3 He determinations in volcanic olivine and pyroxene. *Earth and Planetary Science Letters*, *276*(1), pp.20-29.

Blard, P.H., Lavé, J., Pik, R., Quidelleur, X., Bourles, D. and Kieffer, G., 2005. Fossil cosmogenic 3 He record from K–Ar dated basaltic flows of Mount Etna volcano (Sicily, 38 N): evaluation of a new paleoaltimeter. *Earth and Planetary Science Letters*, *236*(3), pp.613-631.

Blard, P.H., Pik, R., Lavé, J., Bourles, D., Burnard, P.G., Yokochi, R., Marty, B. and Trusdell, F., 2006. Cosmogenic 3 He production rates revisited from evidences of grain size dependent release of matrix-sited helium. *Earth and Planetary Science Letters*, *247*(3), pp.222-234.

Blard, P.H. and Farley, K.A., 2008. The influence of radiogenic 4 He on cosmogenic 3 He determinations in volcanic olivine and pyroxene. *Earth and Planetary Science Letters*, *276*(1), pp.20-29.

Blard, P.H., Braucher, R., Lavé, J. and Bourlès, D., 2013. Cosmogenic 10 Be production rate calibrated against 3 He in the high Tropical Andes (3800–4900 m, 20–22 S). *Earth and Planetary Science Letters*, *382*, pp.140-149.

Blard, P.H., Balco, G., Burnard, P.G., Farley, K.A., Fenton, C.R., Friedrich, R., Jull, A.T., Niedermann, S., Pik, R., Schaefer, J.M. and Scott, E.M., 2015. An inter-laboratory comparison of cosmogenic 3 He and radiogenic 4 He in the CRONUS-P pyroxene standard. *Quaternary Geochronology*, *26*, pp.11-19.

Bochsler, P., Stettler, A., Bird, J.M. and Weathers, M.S., 1978. Excess 3He and 21Ne in josephinite. *Earth and Planetary Science Letters*, *39*(1), pp.67-74.

Bogard, D.D. and Cressy, P.J., 1973. Spallation production of 3 He, 21 Ne, and 38 Ar from target elements in the Bruderheim chondrite. *Geochimica et Cosmochimica Acta*, *37*(3), pp.527-546.

Bourles, D., Raisbeck, G.M. and Yiou, F., 1989. 10Be and 9Be in marine sediments and their potential for dating. *Geochimica et Cosmochimica Acta*, *53*(2), pp.443-452.

Braucher, R., Bourlès, D., Merchel, S., Romani, J.V., Fernadez-Mosquera, D., Marti, K., Leanni, L., Chauvet, F., Arnold, M., Aumaître, G. and Keddadouche, K., 2013. Determination of muon attenuation lengths in depth profiles from in situ produced cosmogenic nuclides. *Nuclear Instruments and Methods in Physics Research Section B: Beam Interactions with Materials and Atoms*, *294*, pp.484-490.

Briesmeister, J.F., 2000. MCNPTM-A general Monte Carlo N-particle transport code. *Version 4C, LA-13709-M, Los Alamos National Laboratory*.

Brinkmann, W.A.R., 1971. What is a foehn?. *Weather*, *26*(6), pp.230-240.

Borchers, B., Marrero, S., Balco, G., Caffee, M., Goehring, B., Lifton, N., Nishiizumi, K., Phillips, F., Schaefer, J. and Stone, J., 2016. Geological calibration of spallation production rates in the CRONUS-Earth project. *Quaternary Geochronology*, *31*, pp.188-198.

Bowen, D.Q., Phillips, F.M., McCabe, A.M., Knutz, P.C. and Sykes, G.A., 2002. New data for the last glacial maximum in Great Britain and Ireland. *Quaternary Science Reviews*, *21*(1), pp.89-101.

Bromwich, D.H., 1988. Snowfall in high southern latitudes. *Reviews of Geophysics*, *26*(1), pp.149-168.

Brown, E.T., Edmond, J.M., Raisbeck, G.M., Yiou, F., Kurz, M.D. and Brook, E.J., 1991. Examination of surface exposure ages of Antarctic moraines using in situ produced 10 Be and 26 Al. *Geochimica et Cosmochimica Acta*, *55*(8), pp.2269-2283.

Brown, E.T., Brook, E.J., Raisbeckl, G.M., Yioul, F. and Kurz, M.D., 1992. 10Be and 26Al in quartz: implications for exposure age dating. *Geophysical Research Letters*, *19*(4), pp.369-372.

Bruno, L.A., Baur, H., Graf, T., Schlu, C., Signer, P. and Wieler, R., 1997. Dating of Sirius group tillites in the Antarctic Dry Valleys with cosmogenic 3 He and 21 Ne. *Earth and Planetary Science Letters*, *147*(1), pp.37-54.

Bryce, J.G. and Farley, K.A., 2002, August. He-3 exposure dating of magnetite. In Geochimica et Cosmochimica Acta,Vol. 66, No. 15 A, pp. A108-A108.

Bunbury, J.M., Hall, L., Anderson, G.J. and Stannard, A., 2001. The determination of fault movement history from the interaction of local drainage with volcanic episodes. *Geological Magazine*, *138*(02), pp.185-192.

Brun, R., Bruyant, F., Maire, M., McPherson, A.C. and Zanarini, P., 1987. *GEANT3 user's guide*. CERN DD/EE/84-1.

Burnard, P., 2013. *The Noble Gases as Geochemical Tracers* (p. 391). Springer.

Campbell, I.B. and Claridge, G.G.C., 1987. *Antarctica: soils, weathering processes and environment* (Vol. 16). Elsevier.

Canet, J. and Jaoul, P., 1946. Report on the Geology of the Manisa-Ayd› n-Kula-Gördes Area. *Mineral Research Exploration Institute of Turkey Project Report*, (2068).

Cerling, T.E. and Craig, H., 1994. Geomorphology and in-situ cosmogenic isotopes. *Annual Review of Earth and Planetary Sciences*, *22*, pp.273-317.

Chapman, R.J., Leake, R.C., Moles, N.R., Earls, G., Cooper, C., Harrington, K. and Berzins, R., 2000a. The application of microchemical analysis of alluvial gold grains to the understanding of complex local and regional gold mineralization: A case study in the Irish and Scottish Caledonides. *Economic Geology*, *95*(8), pp.1753-1773.

Chapman, R.J., Leake, R.C. and Floyd, J.D., 2000b. Regional variation in gold mineralization in the vicinity of the Glengaber Burn, Scottish Borders. *Scottish Journal of Geology*, *36*(2), pp.165-176.

Chapman, R.J., Shaw, M.H., Leake, R.C. and Jackson, B., 2005. Gold in the Central Ochil Hills, ScotlandTransactions-Institution of Mining and Metallurgy. Section B. Applied Earth Science, 114, pp. B53–B64.

Chapman, R.J. and Mortensen, J.K., 2006. Application of microchemical characterization of placer gold grains to exploration for epithermal gold mineralization in regions of poor exposure. *Journal of Geochemical Exploration*, *91*(1), pp.1-26.

Chapman, R.J., 2007. An overview of gold mineralization in the Caledonides of Great Britain and Ireland: insights from placer gold geochemistry. Proc. Ninth biennial SGA meeting, Dublin, C.J. Andrew ed., pp. 943-946.

Chmeleff, J., von Blanckenburg, F., Kossert, K. and Jakob, D., 2010. Determination of the 10 Be half-life by multicollector ICP-MS and liquid scintillation counting. *Nuclear Instruments and Methods in Physics Research Section B: Beam Interactions with Materials and Atoms*, *268*(2), pp.192-199.

Clark, P.U., Dyke, A.S., Shakun, J.D., Carlson, A.E., Clark, J., Wohlfarth, B., Mitrovica, J.X., Hostetler, S.W. and McCabe, A.M., 2009. The last glacial maximum. *science*, *325*(5941), pp.710-714.

Coble, M.A., Grove, M. and Calvert, A.T., 2011. Calibration of Nu-Instruments Noblesse multicollector mass spectrometers for argon isotopic measurements using a newly developed reference gas. *Chemical Geology*, *290*(1), pp.75-87.

Craig, H. and Poreda, R.J., 1986. Cosmogenic 3He in terrestrial rocks: The summit lavas of Maui. *Proceedings of the National Academy of Sciences*, *83*(7), pp.1970-1974.

Cressy, P.J. and Bogard, D.D., 1976. On the calculation of cosmic-ray exposure ages of stone meteorites. *Geochimica et Cosmochimica Acta*, *40*(7), pp.749-762.

Crummy, J., Hall, A.J., Haszeldine, R.S. and Anderson, I.K., 1997. Potential for epithermal gold mineralization in east and central Sutherland, Scotland: indications from River Brora headwaters. *Transactions of the Institution of Mining and Metallurgy. Section B. Applied Earth Science*, *106*.

Davidheiser-Kroll, B., Stuart, F.M. and Boyce, A.J., 2014. Mantle heat drives hydrothermal fluids responsible for carbonate-hosted base metal deposits: evidence from 3He/4He of ore fluids in the Irish Pb-Zn ore district. *Mineralium Deposita*, *49*(5), pp.547-553.

Davis, R. and Schaeffer, O.A., 1955. Chlorine‐36 in nature. *Annals of the New York Academy of Sciences*, *62*(5), pp.107-121.

Deer, W.A., Howie, R.A. and Zussman, J., 1992. *An introduction to the rock-forming minerals* (Vol. 696). London: Longman.

Delunel, R., Blard, P.H., Martin, L.C., Nomade, S. and Schlunegger, F., 2016. Long term low latitude and high elevation cosmogenic 3 He production rate inferred from a 107ka-old lava flow in northern Chile; 22° S-3400ma. sl. *Geochimica et Cosmochimica Acta*, *184*, pp.71-87.

Dempster, A.J., 1918. A new method of positive ray analysis. *Physical Review*, *11*(4), p.316.

Denton, G.H., Sugden, D.E., Marchant, D.R., Hall, B.L. and Wilch, T.I., 1993. East Antarctic Ice Sheet sensitivity to Pliocene climatic change from a Dry Valleys perspective. *Geografiska Annaler. Series A. Physical Geography*, pp.155-204.

Desilets, D. and Zreda, M., 2003. Spatial and temporal distribution of secondary cosmic-ray nucleon intensities and applications to in situ cosmogenic dating. *Earth and Planetary Science Letters*, *206*(1), pp.21-42.

Desilets, D., Zreda, M. and Prabu, T., 2006. Extended scaling factors for in situ cosmogenic nuclides: new measurements at low latitude. *Earth and Planetary Science Letters*, *246*(3), pp.265-276.

Di Nicola, L., Strasky, S., Schlüchter, C., Salvatore, M.C., Akçar, N., Kubik, P.W., Christl, M., Kasper, H.U., Wieler, R. and Baroni, C., 2009. Multiple cosmogenic nuclides document complex Pleistocene exposure history of glacial drifts in Terra Nova Bay (northern Victoria Land, Antarctica). *Quaternary Research*, *71*(1), pp.83-92.

Di Nicola, L., Baroni, C., Strasky, S., Salvatore, M.C., Schlüchter, C., Akçar, N., Kubik, P.W. and Wieler, R., 2012. Multiple cosmogenic nuclides document the stability of the East Antarctic Ice Sheet in northern Victoria Land since the Late Miocene (5–7 Ma). *Quaternary Science Reviews*, *57*, pp.85-94.

Doran, P.T., McKay, C.P., Fountain, A.G., Nylen, T., McKnight, D.M., Jaros, C. and Barrett, J.E., 2008. Hydrologic response to extreme warm and cold summers in the McMurdo Dry Valleys, East Antarctica. *Antarctic Science*, *20*(05), pp.499-509.

Dunai, T.J., 2000. Scaling factors for production rates of in situ produced cosmogenic nuclides: a critical reevaluation. *Earth and Planetary Science Letters*, *176*(1), pp.157-169.

Dunai, T.J., 2001. Influence of secular variation of the geomagnetic field on production rates of in situ produced cosmogenic nuclides. *Earth and Planetary Science Letters*, *193*(1), pp.197-212.

Dunai, T.J., 2010. *Cosmogenic nuclides: principles, concepts and applications in the earth surface sciences*. Cambridge University Press.

Dunai, T.J. and Wijbrans, J.R., 2000. Long-term cosmogenic 3 He production rates (152 ka–1.35 Ma) from 40 Ar/39 Ar dated basalt flows at 29 N latitude. *Earth and Planetary Science Letters*, *176*(1), pp.147-156.

Dunai, T.J., López, G.A.G. and Juez-Larré, J., 2005. Oligocene–Miocene age of aridity in the Atacama Desert revealed by exposure dating of erosion-sensitive landforms. *Geology*, *33*(4), pp.321-324.

Dunai, T.J., Stuart, F.M., Pik, R., Burnard, P. and Gayer, E., 2007. Production of 3 He in crustal rocks by cosmogenic thermal neutrons. *Earth and Planetary Science Letters*, *258*(1), pp.228-236.

Dunne, J., Elmore, D. and Muzikar, P., 1999. Scaling factors for the rates of production of cosmogenic nuclides for geometric shielding and attenuation at depth on sloped surfaces. *Geomorphology*, *27*(1), pp.3-11.

Dymock, R.C., 2014. *Developing the cosmogenic He chronometer* (Doctoral dissertation, University of Glasgow).

Eberhardt, P., Eugster, O. and Marti, K., 1965. Notizen: A Redetermination of the Isotopic Composition of Atmospheric Neon. *Zeitschrift für Naturforschung A*, *20*(4), pp.623-624.

Eidelman, S., Hayes, K.G., Olive, K.E., Aguilar-Benitez, M., Amsler, C., Asner, D., Babu, K.S., Barnett, R.M., Beringer, J., Burchat, P.R. and Carone, C.D., 2004. Review of particle physics. *Physics Letters B*, *592*(1), pp.1-5.

Elmore, D. and Phillips, F.M., 1987. Accelerator mass spectrometry for measurement of long-lived radioisotopes. *Science*, *236*(4801), pp.543-550.

Espanon, V.R., Honda, M. and Chivas, A.R., 2014. Cosmogenic 3 He and 21 Ne surface exposure dating of young basalts from Southern Mendoza, Argentina. *Quaternary Geochronology*, *19*, pp.76-86.

Eugster, O. and Michel, T., 1995. Common asteroid break-up events of eucrites, diogenites, and howardites and cosmic-ray production rates for noble gases in achondrites. *Geochimica et Cosmochimica Acta*, *59*(1), pp.177-199.

Evenstar, L.A., Hartley, A.J., Stuart, F.M., Mather, A.E., Rice, C.M. and Chong, G., 2009. Multiphase development of the Atacama Planation Surface recorded by cosmogenic 3He exposure ages: Implications for uplift and Cenozoic climate change in western South America. *Geology*, *37*(1), pp.27-30.

Fabel, D. and Harbor, J., 1999. The use of in-situ produced cosmogenic radionuclides in glaciology and glacial geomorphology. *Annals of Glaciology*, *28*(1), pp.103-110.

Farley, K.A., 2002. (U-Th)/He dating: Techniques, calibrations, and applications. *Reviews in Mineralogy and Geochemistry*, *47*(1), pp.819-844.

Farley, K.A., 2007. He diffusion systematics in minerals: Evidence from synthetic monazite and zircon structure phosphates. *Geochimica et Cosmochimica Acta*, *71*(16), pp.4015-4024.

Farley, K.A., Libarkin, J., Mukhopadhyay, S. and Amidon, W., 2006. Cosmogenic and nucleogenic 3 He in apatite, titanite, and zircon. *Earth and Planetary Science Letters*, *248*(1), pp.451-461.

Faure, G. and Mensing, T.M., 2005. *Isotopes: principles and applications*. John Wiley & Sons Inc.

Feige, Y., Oltman, B.G. and Kastner, J., 1968. Production rates of neutrons in soils due to natural radioactivity. *Journal of Geophysical Research*, *73*(10), pp.3135-3142.

Feldmann, J. and Levermann, A., 2015. Collapse of the West Antarctic Ice Sheet after local destabilization of the Amundsen Basin. *Proceedings of the National Academy of Sciences*, *112*(46), pp.14191-14196.

Fenton, C.R., Cerling, T.E., Nash, B.P., Webb, R.H. and Poreda, R.J., 2002. Cosmogenic 3He Ages and Geochemical Discrimination of Lava‐Dam Outburst‐Flood Deposits in Western Grand Canyon, Arizona. *Ancient Floods, Modern Hazards*, pp.191-215.

Fenton, C.R., Niedermann, S., Goethals, M.M., Schneider, B. and Wijbrans, J., 2009. Evaluation of cosmogenic 3 He and 21 Ne production rates in olivine and pyroxene from two Pleistocene basalt flows, western Grand Canyon, AZ, USA. *Quaternary Geochronology*, *4*(6), pp.475-492.

Fenton, C.R., Mark, D.F., Barfod, D.N., Niedermann, S., Goethals, M.M. and Stuart, F.M., 2013. 40 Ar/39 Ar dating of the SP and Bar Ten lava flows AZ, USA: Laying the foundation for the SPICE cosmogenic nuclide production-rate calibration project. *Quaternary Geochronology*, *18*, pp.158-172.

Fenton, C.R. and Niedermann, S., 2014. Surface exposure dating of young basalts (1–200 ka) in the San Francisco volcanic field (Arizona, USA) using cosmogenic 3 He and 21 Ne. *Quaternary Geochronology*, *19*, pp.87-105.

Fernandez‐Mosquera, D., Hahm, D. and Marti, K., 2010. Calculated rates of cosmic ray muon‐produced Ne in subsurface quartz. *Geophysical Research Letters*, *37*(15).

Foeken, J., Stuart, F.M., Dobson, K.J., Persano, C. and Vilbert, D., 2006. A diode laser system for heating minerals for (U‐Th)/He chronometry. *Geochemistry, Geophysics, Geosystems*, *7*(4).

Foeken, J.P., Day, S. and Stuart, F.M., 2009a. Cosmogenic 3 He exposure dating of the Quaternary basalts from Fogo, Cape Verdes: implications for rift zone and magmatic reorganisation. *Quaternary Geochronology*, *4*(1), pp.37-49.

Foeken, J.P., Stuart, F.M. and Francalanci, L., 2009b. Dating Holocene lavas on Stromboli, Italy using cosmogenic He. *Quaternary Geochronology*, *4*(6), pp.517-524.

Foeken, J.P., Stuart, F.M. and Mark, D.F., 2012. Long-term low latitude cosmogenic 3 He production rate determined from a 126ka basalt from Fogo, Cape Verdes. *Earth and Planetary Science Letters*, *359*, pp.14-25.

Fretwell, P., Pritchard, H.D., Vaughan, D.G., Bamber, J.L., Barrand, N.E., Bell, R., Bianchi, C., Bingham, R.G., Blankenship, D.D., Casassa, G. and Catania, G., 2013. Bedmap2: improved ice bed, surface and thickness datasets for Antarctica. *The Cryosphere*, *7*(1).

Füri, E., Hilton, D.R., Murton, B.J., Hémond, C., Dyment, J. and Day, J., 2011. Helium isotope variations between Réunion Island and the Central Indian Ridge (17–21 S): New evidence for ridge–hot spot interaction. *Journal of Geophysical Research: Solid Earth*, *116*(B2).

Gall, R., 1960. The secular variation and the geomagnetic theory of cosmic radiation. *Journal of Geophysical Research*, *65*(11), pp.3545-3558.

Garrison, D.H., Rao, M.N. and Bogard, D.D., 1995. Solar‐proton‐produced neon in shergottite meteorites and implications for their origin. *Meteoritics*, *30*(6), pp.738-747.

Gayer, E., Pik, R., Lavé, J., France-Lanord, C., Bourles, D. and Marty, B., 2004. Cosmogenic 3 He in Himalayan garnets indicating an altitude dependence of the 3 He/10 Be production ratio. *Earth and Planetary Science Letters*, *229*(1), pp.91-104.

Gillen, D., Honda, M., Chivas, A.R., Yatsevich, I., Patterson, D.B. and Carr, P.F., 2010. Cosmogenic 21 Ne exposure dating of young basaltic lava flows from the Newer

Volcanic Province, western Victoria, Australia. *Quaternary Geochronology*, *5*(1), pp.1-9.
Goehring, B.M., Kurz, M.D., Balco, G., Schaefer, J.M., Licciardi, J. and Lifton, N., 2010. A reevaluation of in situ cosmogenic 3 He production rates. *Quaternary Geochronology*, *5*(4), pp.410-418.
Goethals, M.M., Hetzel, R., Niedermann, S., Wittmann, H., Fenton, C.R., Kubik, P.W., Christl, M. and Von Blanckenburg, F., 2009. An improved experimental determination of cosmogenic 10 Be/21 Ne and 26 Al/21 Ne production ratios in quartz. *Earth and Planetary Science Letters*, *284*(1), pp.187-198.
Gordon, M.S., Goldhagen, P., Rodbell, K.P., Zabel, T.H., Tang, H.H.K., Clem, J.M. and Bailey, P., 2004. Measurement of the flux and energy spectrum of cosmic-ray induced neutrons on the ground. *IEEE Transactions on Nuclear Science*, *51*(6), pp.3427-3434.
Gosse, J.C. and Phillips, F.M., 2001. Terrestrial in situ cosmogenic nuclides: theory and application. *Quaternary Science Reviews*, *20*(14), pp.1475-1560.
Graham, D.W., 2002. Noble gas isotope geochemistry of mid-ocean ridge and ocean island basalts: Characterization of mantle source reservoirs. *Reviews in mineralogy and geochemistry*, *47*(1), pp.247-317.
Granger, D.E. and Muzikar, P.F., 2001. Dating sediment burial with in situ-produced cosmogenic nuclides: theory, techniques, and limitations. *Earth and Planetary Science Letters*, *188*(1), pp.269-281.
Granger, D.E., Kirchner, J.W. and Finkel, R.C., 1997. Quaternary downcutting rate of the New River, Virginia, measured from differential decay of cosmogenic 26Al and 10Be in cave-deposited alluvium. *Geology*, *25*(2), pp.107-110.
Hamilton, W.J. and Strickland, H.E., 1841. I.—On the Geology of the Western Part of Asia Minor. *Transactions of the Geological Society of London*, (1), pp.1-39.
Heineke, C., Niedermann, S., Hetzel, R. and Akal, C., 2016. Surface exposure dating of Holocene basalt flows and cinder cones in the Kula volcanic field (Western Turkey) using cosmogenic 3 He and 10 Be. *Quaternary Geochronology*, *34*, pp.81-91.
Heisinger, B., Lal, D., Jull, A.T., Kubik, P., Ivy-Ochs, S., Neumaier, S., Knie, K., Lazarev, V. and Nolte, E., 2002. Production of selected cosmogenic radionuclides by muons: 1. Fast muons. *Earth and Planetary Science Letters*, *200*(3), pp.345-355.
Heisinger, B., Lal, D., Jull, A.T., Kubik, P., Ivy-Ochs, S., Neumaier, S., Knie, K., Lazarev, V. and Nolte, E., 2002. Production of selected cosmogenic radionuclides by muons: 1. Fast muons. *Earth and Planetary Science Letters*, *200*(3), pp.345-355.
Herbert, C. G., and R. A. W. Johnstone. "Z-Spray combined inlet/ion source." *Mass Spectrometry Basics, CRC Press* (2003): 65-69.
Hetzel, R., Niedermann, S., Ivy-Ochs, S., Kubik, P.W., Tao, M. and Gao, B., 2002. 21 Ne versus 10 Be and 26 Al exposure ages of fluvial terraces: the influence of crustal Ne in quartz. *Earth and Planetary Science Letters*, *201*(3), pp.575-591.
Hilton, D.R., Hammerschmidt, K., Teufel, S. and Friedrichsen, H., 1993. Helium isotope characteristics of Andean geothermal fluids and lavas. *Earth and Planetary Science Letters*, *120*(3), pp.265-282.
Hohenberg, C.M., 1980. High sensitivity pulse‐counting mass spectrometer system for noble gas analysis. *Review of Scientific Instruments*, *51*(8), pp.1075-1082.
Hohenberg, C.M., Podosek, F.A., Shirck, J.R., Marti, K. and Reedy, R.C., 1978. Comparisons between observed and predicted cosmogenic noble gases in lunar samples. In *Lunar and Planetary Science Conference Proceedings* (Vol. 9, pp. 2311-2344).
Holden, N.E., 1990. Total half-lives for selected nuclides. *Pure and Applied Chemistry*, *62*(5), pp.941-958.
Holzer, T.L., 2000. Implications for earthquake risk reduction in the United States from the Kocaeli, Turkey, earthquake of August 17, 1999 (p. 64). US Geological Survey, Information Services.

Honda, M. and Imamura, M., 1971. Half-life of Mn 53. *Physical Review C*, *4*(4), p.1182.
Honda, M., McDougall, I. and Patterson, D., 1993. Solar noble gases in the Earth: The systematics of helium-neon isotopes in mantle derived samples. *Lithos*, *30*(3-4), pp.257-265.
House, M.A., Farley, K.A. and Stockli, D., 2000. Helium chronometry of apatite and titanite using Nd-YAG laser heating. *Earth and Planetary Science Letters*, *183*(3), pp.365-368.
House, M.A., Gurnis, M., Sutherland, R. and Kamp, P.J., 2005. Patterns of Late Cenozoic exhumation deduced from apatite and zircon U‐He ages from Fiordland, New Zealand. *Geochemistry, Geophysics, Geosystems*, *6*(9).
Innocenti, F., Agostini, S., Di Vincenzo, G., Doglioni, C., Manetti, P., Savaşçin, M.Y. and Tonarini, S., 2005. Neogene and Quaternary volcanism in Western Anatolia: magma sources and geodynamic evolution. *Marine Geology*, *221*(1), pp.397-421.
Ivy-Ochs, S., Kubik, P.W., Masarik, J., Wieler, R., Bruno, L. and Schluchter, C., 1998. Preliminary results on the use of pyroxene for Be-10 surface exposure dating. *Schweizerische mineralogische und petrographische Mitteilungen*, *78*(3), pp.375-382.
Joughin, I. and Alley, R.B., 2011. Stability of the West Antarctic ice sheet in a warming world. *Nature Geoscience*, *4*(8), pp.506-513.
Kennedy, B.M., Hiyagon, H. and Reynolds, J.H., 1990. Crustal neon: a striking uniformity. *Earth and Planetary Science Letters*, *98*(3), pp.277-286.
Klein, J., Giegengack, R., Middleton, R., Sharma, P.T., Underwood, J.R. and Weeks, R.A., 1986. Revealing histories of exposure using in situ produced 26Al and 10Be in Libyan desert glass. *Radiocarbon*, *28*(2A), pp.547-555.
Klein, J., Middleton, R. and Tang, H., 1982. Modifications of an FN tandem for quantitative 10Be measurement. *Nuclear Instruments and Methods in Physics Research*, *193*(3), pp.601-616.
Kober, F., Ivy-Ochs, S., Leya, I., Baur, H., Magna, T., Wieler, R. and Kubik, P.W., 2005. In situ cosmogenic 10 Be and 21 Ne in sanidine and in situ cosmogenic 3 He in Fe–Ti-oxide minerals. *Earth and Planetary Science Letters*, *236*(1), pp.404-418.
Kober, F., Ivy-Ochs, S., Schlunegger, F., Baur, H., Kubik, P.W. and Wieler, R., 2007. Denudation rates and a topography-driven rainfall threshold in northern Chile: multiple cosmogenic nuclide data and sediment yield budgets. *Geomorphology*, *83*(1), pp.97-120.
Kohl, C.P. and Nishiizumi, K., 1992. Chemical isolation of quartz for measurement of in-situ-produced cosmogenic nuclides. *Geochimica et Cosmochimica Acta*, *56*(9), pp.3583-3587.
Kounov, A., Niedermann, S., De Wit, M.J., Viola, G., Andreoli, M. and Erzinger, J., 2007. Present denudation rates at selected sections of the South African escarpment and the elevated continental interior based on cosmogenic 3He and 21Ne. *South African Journal of Geology*, *110*(2-3), pp.235-248.
Kurz, M.D., 1986. In situ production of terrestrial cosmogenic helium and some applications to geochronology. *Geochimica et Cosmochimica Acta*, *50*(12), pp.2855-2862.
Kurz, M.D., Jenkins, W.J., Schilling, J.G. and Hart, S.R., 1982. Helium isotopic variations in the mantle beneath the central North Atlantic Ocean. *Earth and Planetary Science Letters*, *58*(1), pp.1-14.
Kurz, M.D., Jenkins, W.J., Schilling, J.G. and Hart, S.R., 1982. Helium isotopic variations in the mantle beneath the central North Atlantic Ocean. *Earth and Planetary Science Letters*, *58*(1), pp.1-14.
Kurz, M.D., Colodner, D., Trull, T.W., Moore, R.B. and O'Brien, K., 1990. Cosmic ray exposure dating with in situ produced cosmogenic 3 He: results from young Hawaiian lava flows. *Earth and Planetary Science Letters*, *97*(1), pp.177-189.

Kutschera, W., Ahmad, I. and Paul, M., 1992. Half-life determination of 41Ca and some other radioisotopes. *Radiocarbon*, *34*(3), pp.436-446.
Lal, D., 1987. Production of 3 He in terrestrial rocks. *Chemical Geology: Isotope Geoscience section*, *66*(1), pp.89-98.
Lal, D., 1988. In situ-produced cosmogenic isotopes in terrestrial rocks. *Annual Review of Earth and Planetary Sciences*, *16*, pp.355-388.
Lal, D., 1991. Cosmic ray labeling of erosion surfaces: in situ nuclide production rates and erosion models. *Earth and Planetary Science Letters*, *104*(2-4), pp.424-439.
Lal, D. and Arnold, J.R., 1985. Tracing quartz through the environment. *Proceedings of the Indian Academy of Sciences-Earth and Planetary Sciences*, *94*(1), pp.1-5.
Lal, D. and Peters, B., 1962. Cosmic ray produced isotopes and their application to problems in geophysics. *Progr. Elem. Particle Cosmic Ray Phys.*, *6*.
Lal, D. and Peters, B., 1967. Cosmic ray produced radioactivity on the earth. In *Kosmische Strahlung II/Cosmic Rays II* (pp. 551-612). Springer Berlin Heidelberg.
Lavielle, B., Sauvageon, H. and Bertin, P., 1989. *Cross sections of neon and krypton isotopes produced by neutrons* (No. CENBG--8929). Bordeaux-1 Univ.
LeMasurier, W.E. and Kawachi, Y. 1987. Mount Hampton. *Volcanoes of the Antarctic Plate and southern oceans*, pp.189-194.
LeMasurier, W.E., 1990. B. Marie Byrd Land. *Volcanoes of the Antarctic Plate and southern oceans*, pp.146-255.
LeMasurier, W.E., 1990. *Late Cenozoic volcanism on the Antarctic plate: an overview* (pp. 1-17). American Geophysical Union.
LeMasurier, W.E. and Rex, D.C., 1989. Evolution of linear volcanic ranges in Marie Byrd Land, west Antarctica. *Journal of Geophysical Research: Solid Earth*, *94*(B6), pp.7223-7236.
LeMasurier, W.E. and Rocchi, S., 2005. Terrestrial record of post-Eocene climate history in Marie Byrd Land, West Antarctica. *Geografiska Annaler. Series A. Physical Geography*, pp.51-66.
Leake, R.C., Chapman, R.J., Bland, D.J., Stone, P., Cameron, D.G. and Styles, M.T., 1998. The origin of alluvial gold in the Leadhills area of Scotland: evidence from interpretation of internal chemical characteristics. *Journal of Geochemical Exploration*, *63*(1), pp.7-36.
Lederer, C.M. and Shirley, V.S., 1978. Table of Isotopes (; New York. *Soil Science Likar, A., Omahen, G., Lipoglavsek, M., Vidmar*, pp.191-201.
Leya, I., Lange, H.J., Neumann, S., Wieler, R. and Michel, R., 2000. The production of cosmogenic nuclides in stony meteoroids by galactic cosmic‐ray particles. *Meteoritics & Planetary Science*, *35*(2), pp.259-286.
Libby, W.F., 1946. Atmospheric helium three and radiocarbon from cosmic radiation. *Physical Review*, *69*(11-12), p.671.
Licciardi, J.M., Kurz, M.D., Clark, P.U. and Brook, E.J., 1999. Calibration of cosmogenic 3 He production rates from Holocene lava flows in Oregon, USA, and effects of the Earth's magnetic field. *Earth and Planetary Science Letters*, *172*(3), pp.261-271.
Licciardi, J.M., Kurz, M.D. and Curtice, J.M., 2006. Cosmogenic 3 He production rates from Holocene lava flows in Iceland. *Earth and Planetary Science Letters*, *246*(3), pp.251-264.
Lifton, N.A., Bieber, J.W., Clem, J.M., Duldig, M.L., Evenson, P., Humble, J.E. and Pyle, R., 2005. Addressing solar modulation and long-term uncertainties in scaling secondary cosmic rays for in situ cosmogenic nuclide applications. *Earth and Planetary Science Letters*, *239*(1), pp.140-161.
Lifton, N., Smart, D.F. and Shea, M.A., 2008. Scaling time-integrated in situ cosmogenic nuclide production rates using a continuous geomagnetic model. *Earth and Planetary Science Letters*, *268*(1), pp.190-201.

Lifton, N., Sato, T. and Dunai, T.J., 2014. Scaling in situ cosmogenic nuclide production rates using analytical approximations to atmospheric cosmic-ray fluxes. *Earth and Planetary Science Letters*, *386*, pp.149-160.

Lisiecki, L.E. and Raymo, M.E., 2005. A Pliocene‐Pleistocene stack of 57 globally distributed benthic δ18O records. *Paleoceanography*, *20*(1).

Mabry, J., Burnard, P., Blard, P.H. and Zimmermann, L., 2012. Mapping changes in helium sensitivity and peak shape for varying parameters of a Nier-type noble gas ion source. *Journal of Analytical Atomic Spectrometry*, *27*(6), pp.1012-1017.

McIntosh, W.C. and Heizler, M.T., 1994. Applications of CO2 laser heating in 40Ar/39Ar geochronology. *USGS Circular*, *1107*.

Mamyrin, B.A., Anufriev, G.S., Kamenskii, I.L. and Tolstikhin, I.N., 1970. *Determination of the isotopic composition of the atmospheric Helium.* All-Union Petroleum Geology Exploration Inst., Moscow. Inst. of Precambrian Geology and Geochronology, Leningrad.

Marchetti, D.W., Hynek, S.A. and Cerling, T.E., 2014. Cosmogenic 3 He exposure ages of basalt flows in the northwestern Payún Matru volcanic field, Mendoza Province, Argentina. *Quaternary Geochronology*, *19*, pp.67-75.

Margerison, H., Phillips, W., Stuart, F. and Sugden, D., 2004, December. Miocene Flood Deposits in the Dry Valleys, Antarctica Dated Using Cosmogenic 3He Isotopes. In *AGU Fall Meeting Abstracts*.

Margerison, H.R., 2005. *The application of cosmogenic 3He surface exposure dating within the dry valleys of East Antarctica* (Doctoral dissertation, University of Edinburgh).

Mark, D.F., Barfod, D., Stuart, F.M. and Imlach, J., 2009. The ARGUS multicollector noble gas mass spectrometer: Performance for 40Ar/39Ar geochronology. *Geochemistry, Geophysics, Geosystems*, *10*(10).

Mark, D.F., Rice, C.M., Fallick, A.E., Trewin, N.H., Lee, M.R., Boyce, A. and Lee, J.K.W., 2011. 40 Ar/39 Ar dating of hydrothermal activity, biota and gold mineralization in the Rhynie hot-spring system, Aberdeenshire, Scotland. *Geochimica et Cosmochimica Acta*, *75*(2), pp.555-569.

Marrero, S.M., Phillips, F.M., Borchers, B., Lifton, N., Aumer, R. and Balco, G., 2016. Cosmogenic nuclide systematics and the CRONUScalc program. *Quaternary Geochronology*, *31*, pp.160-187.

Martel, D.J., O'nions, R.K., Hilton, D.R. and Oxburgh, E.R., 1990. The role of element distribution in production and release of radiogenic helium: The Carnmenellis Granite, southwest England. *Chemical geology*, *88*(3-4), pp.207-221.

Marti, K. and Craig, H., 1987. Cosmic-ray-produced neon and helium in the summit lavas of Maui.

Martinerie, P., Raynaud, D., Etheridge, D.M., Barnola, J.M. and Mazaudier, D., 1992. Physical and climatic parameters which influence the air content in polar ice. *Earth and Planetary Science Letters*, *112*(1-4), pp.1-13.

Masarik, J., 2002. Numerical simulation of in situ production of cosmogenic nuclides.

Masarik, J. and Beer, J., 1999. Simulation of particle fluxes and cosmogenic nuclide production in the Earth's atmosphere. *Journal of Geophysical Research: Atmospheres*, *104*(D10), pp.12099-12111.

Masarik, J. and Reedy, R.C., 1995. Terrestrial cosmogenic-nuclide production systematics calculated from numerical simulations. *Earth and Planetary Science Letters*, *136*(3), pp.381-395.

Matsuda, J., Matsumoto, T., Sumino, H., Nagao, K., Yamamoto, J., Miura, Y., Kaneoka, I., Takahata, N. and Sano, Y., 2002. The 3He/4He ratio of the new internal He Standard of Japan (HESJ). *Geochemical Journal*, *36*(2), pp.191-195.

McGowan, H.A., Sturman, A.P. and Owens, I.F., 1996. Aeolian dust transport and deposition by foehn winds in an alpine environment, Lake Tekapo, New Zealand. *Geomorphology*, *15*(2), pp.135-146.

Megrue, G.H., 1967. Isotopic analysis of rare gases with a laser microprobe. *Science*, *157*(3796), pp.1555-1556.

Meijer, P.T. and Wortel, M.J.R., 1997. Present‐day dynamics of the Aegean region: A model analysis of the horizontal pattern of stress and deformation. *Tectonics*, *16*(6), pp.879-895.

Merrill, R. T., McElhinny, M. W. and McFadden, P. L., 1998. The Magnetic Field of the Earth, San Diego: Academic Press, 531 pp.

Michel, T. and Eugster, O., 1989. Cosmic-ray exposure ages of howardites, eucrites, and diogenites. *Meteoritics*, *24*, p.304.

Middleton, J.L., Ackert, R.P. and Mukhopadhyay, S., 2012. Pothole and channel system formation in the McMurdo Dry Valleys of Antarctica: new insights from cosmogenic nuclides. *Earth and Planetary Science Letters*, *355*, pp.341-350.

Miller, G.H., Briner, J.P., Lifton, N.A. and Finkel, R.C., 2006. Limited ice-sheet erosion and complex exposure histories derived from in situ cosmogenic 10 Be, 26 Al, and 14 C on Baffin Island, Arctic Canada. *Quaternary Geochronology*, *1*(1), pp.74-85.

Miura, Y., Nagao, K., Sugiura, N., Fujitani, T. and Warren, P., 1998. Noble gases, 81 Kr-Kr exposure ages and 244 Pu-Xe ages of six eucrites, Bereba, Binda, Camel Donga, Juvinas, Millbillillie, and Stannern. *Geochimica et cosmochimica acta*, *62*(13), pp.2369-2387.

Monaghan, M.C., Krishnaswami, S. and Turekian, K.K., 1986. The global-average production rate of 10 Be. *Earth and Planetary Science Letters*, *76*(3), pp.279-287.

Moreira, M. and Madureira, P., 2005. Cosmogenic helium and neon in 11 Myr old ultramafic xenoliths: consequences for mantle signatures in old samples. *Geochemistry, Geophysics, Geosystems*, *6*(8).

Mukhopadhyay, S., Ackert, R.P., Pope, A.E., Pollard, D. and DeConto, R.M., 2012. Miocene to recent ice elevation variations from the interior of the West Antarctic ice sheet: Constraints from geologic observations, cosmogenic nuclides and ice sheet modeling. *Earth and Planetary Science Letters*, *337*, pp.243-251.

Naish, T., Powell, R., Levy, R., Wilson, G., Scherer, R., Talarico, F., Krissek, L., Niessen, F., Pompilio, M., Wilson, T. and Carter, L., 2009. Obliquity-paced Pliocene West Antarctic ice sheet oscillations. *Nature*, *458*(7236), pp.322-328.

Näslund, J.O., 1997. Subglacial preservation of valley morphology at Amundsenisen, western Dronning Maud Land, Antarctica. *Earth Surface Processes and Landforms*, *22*(5), pp.441-455.

Niedermann, S., 2002. Cosmic-ray-produced noble gases in terrestrial rocks: dating tools for surface processes. *Reviews in Mineralogy and Geochemistry*, *47*(1), pp.731-784.

Niedermann, S., Graf, T. and Marti, K., 1993. Mass spectrometric identification of cosmic-ray-produced neon in terrestrial rocks with multiple neon components. *Earth and Planetary Science Letters*, *118*(1), pp.65-73.

Niedermann, S., Graf, T., Kim, J.S., Kohl, C.P., Marti, K. and Nishiizumi, K., 1994. Cosmic-ray-produced 21 Ne in terrestrial quartz: the neon inventory of Sierra Nevada quartz separates. *Earth and Planetary Science Letters*, *125*(1), pp.341-355.

Niedermann, S., Bach, W. and Erzinger, J., 1997. Noble gas evidence for a lower mantle component in MORBs from the southern East Pacific Rise: Decoupling of helium and neon isotope systematics. *Geochimica et Cosmochimica Acta*, *61*(13), pp.2697-2715.

Nier, A.O., 1947. A mass spectrometer for isotope and gas analysis. *Review of Scientific Instruments*, *18*(6), pp.398-411.

Nier, A.O. and Schlutter, D.J., 1988. Helium isotopic ratios in native and processed metals. *Meteoritics*, *23*, p.294.

Nishiizumi, K., Lal, D., Klein, J., Middleton, R. and Arnold, J.R., 1986. Production of 10Be and 26Al by cosmic rays in terrestrial quartz in situ and implications for erosion rates.

Nishiizumi, K., Klein, J., Middleton, R. and Craig, H., 1987. In situ produced 10Be and 26Al in olivine from Maui. *EOS*, *68*, p.1268.

Nishiizumi, K., Winterer, E.L., Kohl, C.P., Klein, J., Middleton, R., Lal, D. and Arnold, J.R., 1989. Cosmic ray production rates of 10Be and 26Al in quartz from glacially polished rocks. *Journal of Geophysical Research: Solid Earth*, *94*(B12), pp.17907-17915.

Nishiizumi, K., Klein, J., Middleton, R. and Craig, H., 1990. Cosmogenic10Be, 26Al, and3He in olivine from Maui lavas. *Earth and Planetary Science Letters*, *98*(3-4), pp.263-266.

Nishiizumi, K., Kohl, C.P., Arnold, J.R., Klein, J., Fink, D. and Middleton, R., 1991. Cosmic ray produced 10 Be and 26 Al in Antarctic rocks: exposure and erosion history. *Earth and Planetary Science Letters*, *104*(2), pp.440-454.

Nishiizumi, K., 2004. Preparation of 26 Al AMS standards. *Nuclear Instruments and Methods in Physics Research Section B: Beam Interactions with Materials and Atoms*, *223*, pp.388-392.

Nishiizumi, K., Imamura, M., Caffee, M.W., Southon, J.R., Finkel, R.C. and McAninch, J., 2007. Absolute calibration of 10 Be AMS standards. *Nuclear Instruments and Methods in Physics Research Section B: Beam Interactions with Materials and Atoms*, *258*(2), pp.403-413.

Oberholzer, P., Baroni, C., Schaefer, J.M., Orombelli, G., Ochs, S.I., Kubik, P.W., Baur, H. and Wieler, R., 2003. Limited Pliocene/Pleistocene glaciation in Deep Freeze Range, northern Victoria Land, Antarctica, derived from in situ cosmogenic nuclides. *Antarctic Science*, *15*(04), pp.493-502.

Oppenheimer, M., 1998. Global warming and the stability of the West Antarctic Ice Sheet. *Nature*, *393*(6683), pp.325-332.

Paneth, F.A., Reasbeck, P. and Mayne, K.I., 1952. Helium 3 content and age of meteorites. *Geochimica et Cosmochimica Acta*, *2*(5), pp.300-303.

Panter, K.S., McIntosh, W.C. and Smellie, J.L., 1994. Volcanic history of Mount Sidley, a major alkaline volcano in Marie Byrd Land, Antarctica. *Bulletin of Volcanology*, *56*(5), pp.361-376.

Panter, K.S., Hart, S.R., Kyle, P., Blusztanjn, J. and Wilch, T., 2000. Geochemistry of Late Cenozoic basalts from the Crary Mountains: characterization of mantle sources in Marie Byrd Land, Antarctica. *Chemical Geology*, *165*(3), pp.215-241.

Parai, R., Mukhopadhyay, S. and Lassiter, J.C., 2009. New constraints on the HIMU mantle from neon and helium isotopic compositions of basalts from the Cook–Austral Islands. *Earth and Planetary Science Letters*, *277*(1), pp.253-261.

Parish, T.R. and Bromwich, D.H., 1991. Continental-scale simulation of the Antarctic katabatic wind regime. *Journal of Climate*, *4*(2), pp.135-146.

Paulsen, T.S. and Wilson, T.J., 2010. Evolution of Neogene volcanism and stress patterns in the glaciated West Antarctic Rift, Marie Byrd Land, Antarctica. *Journal of the Geological Society*, *167*(2), pp.401-416.

Phillips, F.M., Leavy, B.D., Jannik, N.O., Elmore, D. and Kubik, P.W., 1986. The accumulation of cosmogenic chlorine-36 in rocks: A method for surface exposure dating. *Science*, *231*(4733), pp.41-43.

Phillips, F.M., Stone, W.D. and Fabryka-Martin, J.T., 2001. An improved approach to calculating low-energy cosmic-ray neutron fluxes near the land/atmosphere interface. *Chemical Geology*, *175*(3), pp.689-701.

Pollard, D. and DeConto, R.M., 2009. Modelling West Antarctic ice sheet growth and collapse through the past five million years. *Nature*, *458*(7236), pp.329-332.

Porcelli, D., Ballentine, C.J. and Wieler, R., 2002. An overview of noble gas geochemistry and cosmochemistry. *Reviews in mineralogy and geochemistry*, *47*(1), pp.1-19.
Poreda, R.J. and Cerling, T.E., 1992. Cosmogenic neon in recent lavas from the western United States. *Geophysical Research Letters*, *19*(18), pp.1863-1866.
Powell, C.F., Perkins, D.H. and Fowler, P.H., 1959. The study of elementary particles by the photographic method. London: Pergamon, 669 pp.
Ravelo, A.C., Andreasen, D.H., Lyle, M., Lyle, A.O. and Wara, M.W., 2004. Regional climate shifts caused by gradual global cooling in the Pliocene epoch. *Nature*, *429*(6989), pp.263-267.
Raymo, M.E. and Horowitz, M., 1996. Organic carbon paleo‐pCO2 and marine‐ice core correlations and chronology. *Geophysical research letters*, *23*(4), pp.367-370.
Reynolds, J.H., 1956. High sensitivity mass spectrometer for noble gas analysis. *Review of Scientific Instruments*, *27*(11), pp.928-934.
Richardson-Bunbury, J.M., 1996. The Kula volcanic field, western Turkey: the development of a Holocene alkali basalt province and the adjacent normal-faulting graben. *Geological Magazine*, *133*(03), pp.275-283.
Robert, U., Foden, J. and Varne, R., 1992. The Dodecanese Province, SE Aegean: a model for tectonic control on potassic magmatism. *Lithos*, *28*(3), pp.241-260.
Rocchi, S., LeMasurier, W.E. and Di Vincenzo, G., 2006. Oligocene to Holocene erosion and glacial history in Marie Byrd Land, West Antarctica, inferred from exhumation of the Dorrel Rock intrusive complex and from volcano morphologies. *Geological Society of America Bulletin*, *118*(7-8), pp.991-1005.
Rocchi, S., Di Vincenzo, G., Dini, A., Petrelli, M. and Vezzoni, S., 2015. Time–space focused intrusion of genetically unrelated arc magmas in the early Paleozoic Ross–Delamerian Orogen (Morozumi Range, Antarctica). *Lithos*, *232*, pp.84-99.
Rothwell, P., 1958. Cosmic rays in the earth's magnetic field. *Philosophical Magazine*, *3*(33), pp.961-970.
Ryan, J.G. and Kyle, P.R., 2004. Lithium abundance and lithium isotope variations in mantle sources: insights from intraplate volcanic rocks from Ross Island and Marie Byrd Land (Antarctica) and other oceanic islands. *Chemical Geology*, *212*(1), pp.125-142.
Sano, Y., Tominaga, T., Nakamura, Y. and Wakita, H., 1982. 3He/4He ratios of methane-rich natural gases in Japan. *Geochemical Journal*, *16*(5), pp.237-245.
Sano, Y. and Wakita, H., 1988. Precise measurement of helium isotopes in terrestrial gases. *Bulletin of the Chemical Society of Japan*, *61*(4), pp.1153-1157.
Sano, Y., Tokutake, T. and Takahata, N., 2008. Accurate measurement of atmospheric helium isotopes. *Analytical Sciences*, *24*(4), pp.521-525.
Sarda, P., Staudacher, T. and Allègre, C.J., 1988. Neon isotopes in submarine basalts. *Earth and Planetary Science Letters*, *91*(1), pp.73-88.
Sarda, P., Staudacher, T., Allègre, C.J. and Lecomte, A., 1993. Cosmogenic neon and helium at Réunion: measurement of erosion rate. *Earth and Planetary Science Letters*, *119*(3), pp.405-417.
Scarsi, P., 2000. Fractional extraction of helium by crushing of olivine and clinopyroxene phenocrysts: effects on the 3 He/4 He measured ratio. *Geochimica et Cosmochimica Acta*, *64*(21), pp.3751-3762.
Schäfer, J.M., Ivy-Ochs, S., Wieler, R., Leya, I., Baur, H., Denton, G.H. and Schlüchter, C., 1999. Cosmogenic noble gas studies in the oldest landscape on earth: surface exposure ages of the Dry Valleys, Antarctica. *Earth and Planetary Science Letters*, *167*(3), pp.215-226.
Schäfer, J.M., 2000. *Reconstruction of landscape evolution and continental paleoglaciations using in-situ cosmogenic nuclides*. Diss. Naturwissenschaften ETH Zürich, Nr. 13542, 2000.

Schaefer, J.M., Denton, G.H., Kaplan, M., Putnam, A., Finkel, R.C., Barrell, D.J., Andersen, B.G., Schwartz, R., Mackintosh, A., Chinn, T. and Schlüchter, C., 2009. High-frequency Holocene glacier fluctuations in New Zealand differ from the northern signature. *science*, *324*(5927), pp.622-625.

Schaefer, J.M., Winckler, G., Blard, P.H., Balco, G., Shuster, D.L., Friedrich, R., Jull, A.T., Wieler, R. and Schluechter, C., 2016. Performance of CRONUS-P–a pyroxene reference material for helium isotope analysis. *Quaternary Geochronology*, *31*, pp.237-239.

Scherer, R.P., Aldahan, A., Tulaczyk, S., Possnert, G., Engelhardt, H. and Kamb, B., 1998. Pleistocene collapse of the West Antarctic ice sheet. *Science*, *281*(5373), pp.82-85.

Schimmelpfennig, I., Williams, A., Pik, R., Burnard, P., Niedermann, S., Finkel, R., Schneider, B. and Benedetti, L., 2011. Inter-comparison of cosmogenic in-situ 3 He, 21 Ne and 36 Cl at low latitude along an altitude transect on the SE slope of Kilimanjaro volcano (3 S, Tanzania). *Quaternary Geochronology*, *6*(5), pp.425-436.

Schott, J. and Berner, R.A., 1985. Dissolution mechanisms of pyroxenes and olivines during weathering. In *The chemistry of weathering* (pp. 35-53). Springer Netherlands.

Schultz, L. and Kruse, H., 1989. Helium, neon, and argon in meteorites—A data compilation. *Meteoritics*, *24*(3), pp.155-172.

Seidl, M.A., 1993. *Form and process in channel incision of bedrock*. University of California, Berkeley.

Seidl, M.A., Finkel, R.C., Caffee, M.W., Hudson, G.B. and Dietrich, W.E., 1997. Cosmetic Isotope Analyses Applied to River Longitudinal Profile Evolution: Problems and Interpretations. *Earth Surface Processes and Landforms*, *22*(3), pp.195-209.

Sharp, Z.D., 1990. A laser-based microanalytical method for the in situ determination of oxygen isotope ratios of silicates and oxides. *Geochimica et Cosmochimica Acta*, *54*(5), pp.1353-1357.

Sharp, Z.D., 1992. In situ laser microprobe techniques for stable isotope analysis. *Chemical Geology: Isotope Geoscience section*, *101*(1-2), pp.3-19.

Shea, M.A. and Smart, D.F., 1983, August. A wold grid of calculated cosmic ray vertical cutoff rigidities for 1980. 0. In *International Cosmic Ray Conference* (Vol. 3, p. 415).

Shukolyukov, Y.A., Yakubovich, O.V., Yakovleva, S.Z., Sal'nikova, E.B., Kotov, A.B. and Rytsk, E.Y., 2012. Geothermochronology based on noble gases: III. Migration of radiogenic He in the crystal structure of native metals with applications to their isotopic dating. *Petrology*, *20*(1), pp.1-20.

Shuster, D.L., Farley, K.A., Vasconcelos, P.M., Balco, G., Monteiro, H.S., Waltenberg, K. and Stone, J.O., 2012. Cosmogenic 3 He in hematite and goethite from Brazilian "canga" duricrust demonstrates the extreme stability of these surfaces. *Earth and Planetary Science Letters*, *329*, pp.41-50.

Smith, M.E., Singer, B.S. and Simo, T., 2011. A time like our own? Radioisotopic calibration of the Ordovician greenhouse to icehouse transition. *Earth and Planetary Science Letters*, *311*(3), pp.364-374.

Speirs, J.C., Steinhoff, D.F., McGowan, H.A., Bromwich, D.H. and Monaghan, A.J., 2010. Foehn Winds in the McMurdo Dry Valleys, Antarctica: The Origin of Extreme Warming Events*. *Journal of Climate*, *23*(13), pp.3577-3598.

Spell, T.L., Smith, E.I., Sanford, A. and Zanetti, K.A., 2001. Systematics of xenocrystic contamination: preservation of discrete feldspar populations at McCullough Pass Caldera revealed by 40 Ar/39 Ar dating. *Earth and Planetary Science Letters*, *190*(3), pp.153-165.

Srinivasan, B., 1976. Barites: anomalous xenon from spallation and neutron-induced reactions. *Earth and Planetary Science Letters*, *31*(1), pp.129-141.

Staudacher, T. and Allègre, C.J., 1993. The cosmic ray produced He/21Ne ratio in ultramafic rocks. *Geophysical research letters*, *20*(11), pp.1075-1078.

Steig, E.J., Fastook, J.L., Zweck, C., Goodwin, I.D., Licht, K.J., White, J.W. and Ackert, R.P., 2001. West Antarctic ice sheet elevation changes. *The West Antarctic Ice Sheet: Behavior and Environment*, pp.75-90.

Stone, J.O., 2000. Air pressure and cosmogenic isotope production. *Journal of Geophysical Research: Solid Earth*, *105*(B10), pp.23753-23759.

Stone, J.O., Balco, G.A., Sugden, D.E., Caffee, M.W., Sass, L.C., Cowdery, S.G. and Siddoway, C., 2003. Holocene deglaciation of Marie Byrd land, west Antarctica. *Science*, *299*(5603), pp.99-102.

Størmer, C., 1935. *...Remarkable Aurora-forms from Southern Norway...* I kommisjon hos Cammermeyers boghandel.

Strasky, S., Graf, A.A., Zhao, Z., Kubik, P.W., Baur, H., Schlüchter, C. and Wieler, R., 2009. Late Glacial ice advances in southeast Tibet. *Journal of Asian Earth Sciences*, *34*(3), pp.458-465.

Strobl, M., Hetzel, R., Niedermann, S., Ding, L. and Zhang, L., 2012. Landscape evolution of a bedrock peneplain on the southern Tibetan Plateau revealed by in situ-produced cosmogenic 10 Be and 21 Ne. *Geomorphology*, *153*, pp.192-204.

Stuart, F.M. and Turner, G., 1992. The abundance and isotopic composition of the noble gases in ancient fluids. *Chemical Geology: Isotope Geoscience section*, *101*(1-2), pp.97-109.

Stuart, F., Turner, G. and Taylor, R., 1994. He–Ar isotope systematics of fluid inclusions: resolving mantle and crustal contributions to hydrothermal fluids. *Noble gas geochemistry and cosmochemistry*, pp.261-277.

Stuart, F.M., Lass-Evans, S., Fitton, J.G. and Ellam, R.M., 2003. High 3He/4He ratios in picritic basalts from Baffin Island and the role of a mixed reservoir in mantle plumes. *Nature*, *424*(6944), pp.57-59.

Sugden, D.E., Balco, G., Cowdery, S.G., Stone, J.O. and Sass, L.C., 2005. Selective glacial erosion and weathering zones in the coastal mountains of Marie Byrd Land, Antarctica. *Geomorphology*, *67*(3), pp.317-334.

Summerfield, M.A., Stuart, F.M., Cockburn, H.A.P., Sugden, D.E., Denton, G.H., Dunai, T. and Marchant, D.R., 1999. Long-term rates of denudation in the Dry Valleys, Transantarctic Mountains, southern Victoria Land, Antarctica based on in-situ-produced cosmogenic 21Ne. *Geomorphology*, *27*(1), pp.113-129.

Tabushi, M., 1958. Solvent Extraction of Beryllium as Acetylacetonate.

Templeton, D.H., 1953. Nuclear reactions induced by high energy particles. *Annual review of nuclear science*, *2*(1), pp.93-104.

Teng, F.Z., McDonough, W.F., Rudnick, R.L., Dalpé, C., Tomascak, P.B., Chappell, B.W. and Gao, S., 2004. Lithium isotopic composition and concentration of the upper continental crust. *Geochimica et Cosmochimica Acta*, *68*(20), pp.4167-4178.

Thomson, J.J., 1913. Bakerian lecture: Rays of positive electricity. *Proceedings of the Royal Society of London. Series A, Containing Papers of a Mathematical and Physical Character*, *89*(607), pp.1-20.

Trull, T.W., 1989. *Diffusion of helium isotopes in silicate glasses and minerals: Implications for petrogenesis and geochronology. Doctoral thesis* (No. PB-90-241738/XAB; WHOI--89-15). Woods Hole Oceanographic Institution, MA (USA).

Trull, T.W., Kurz, M.D. and Jenkins, W.J., 1991. Diffusion of cosmogenic3He in olivine and quartz: implications for surface exposure dating. *Earth and Planetary Science Letters*, *103*(1-4), pp.241-256.

Trull, T.W. and Kurz, M.D., 1993. Experimental measurements of 3He and 4He mobility in olivine and clinopyroxene at magmatic temperatures. *Geochimica et Cosmochimica Acta*, *57*(6), pp.1313-1324.

Turner, G. and Stuart, F., 1992. Helium/heat ratios and deposition temperatures of sulphides from the ocean floor. *Nature*, *357*(6379), pp.581-583.

Van der Wateren, F.M., Dunai, T.J., Van Balen, R.T., Klas, W., Verbers, A.L., Passchier, S. and Herpers, U., 1999. Contrasting Neogene denudation histories of different structural regions in the Transantarctic Mountains rift flank constrained by cosmogenic isotope measurements. *Global and Planetary Change*, *23*(1), pp.145-172.

van Gorp, W., Veldkamp, A., Temme, A.J.A.M., Maddy, D., Demir, T., van der Schriek, T., Reimann, T., Wallinga, J., Wijbrans, J. and Schoorl, J.M., 2013. Fluvial response to Holocene volcanic damming and breaching in the Gediz and Geren rivers, western Turkey. *Geomorphology*, *201*, pp.430-448.

Vermeesch, P., Balco, G., Blard, P.H., Dunai, T.J., Kober, F., Niedermann, S., Shuster, D.L., Strasky, S., Stuart, F.M., Wieler, R. and Zimmermann, L., 2015. Interlaboratory comparison of cosmogenic 21 Ne in quartz. *Quaternary Geochronology*, *26*, pp.20-28.

Von Blanckenburg, F., 2005. The control mechanisms of erosion and weathering at basin scale from cosmogenic nuclides in river sediment. *Earth and Planetary Science Letters*, *237*(3), pp.462-479.

Welch, K.A., Lyons, W.B., McKnight, D.M., Doran, P.T., Fountain, A.G., Wall, D., Jaros, C., Nylen, T. and Howard-Williams, C., 2003. *Climate and hydrological variations and implications for lake and stream ecological response in the McMurdo Dry Valleys, Antarctica* (pp. 174-195). Oxford University: New York.

Welch, B.C. and Jacobel, R.W., 2005. Bedrock topography and wind erosion sites in East Antarctica: observations from the 2002 US-ITASE traverse. *Annals of Glaciology*, *41*(1), pp.92-96.

Westaway, R., Pringle, M., Yurtmen, S., Demir, T., Bridgland, D., Rowbotham, G. and Maddy, D., 2004. Pliocene and Quaternary regional uplift in western Turkey: the Gediz river terrace staircase and the volcanism at Kula. *Tectonophysics*, *391*(1), pp.121-169.

Westaway, R., Guillou, H., Yurtmen, S., Beck, A., Bridgland, D., Demir, T., Scaillet, S. and Rowbotham, G., 2006. Late Cenozoic uplift of western Turkey: Improved dating of the Kula Quaternary volcanic field and numerical modelling of the Gediz river terrace staircase. *Global and Planetary Change*, *51*(3), pp.131-171.

Wieler, R., 2002. Cosmic-ray-produced noble gases in meteorites. *Reviews in Mineralogy and geochemistry*, *47*(1), pp.125-170.

Williams, A.J., Stuart, F.M., Day, S.J. and Phillips, W.M., 2005. Using pyroxene microphenocrysts to determine cosmogenic 3 He concentrations in old volcanic rocks: an example of landscape development in central Gran Canaria. *Quaternary Science Reviews*, *24*(1), pp.211-222.

Wilson, P., Bentley, M.J., Schnabel, C., Clark, R. and Xu, S., 2008. Stone run (block stream) formation in the Falkland Islands over several cold stages, deduced from cosmogenic isotope (10Be and 26Al) surface exposure dating. *Journal of Quaternary Science*, *23*(5), pp.461-473.

Wilson, J.W. and Costner, C.M., 1975. Nucleon and heavy-ion total and absorption cross section for selected nuclei.

Wolf, R.A., Farley, K.A. and Kass, D.M., 1998. Modeling of the temperature sensitivity of the apatite (U–Th)/He thermochronometer. *Chemical Geology*, *148*(1), pp.105-114.

Yanev, Y., Innocenti, F., Manetti, P. and Serri, G., 1998. Upper Eocene-Oligocene collision-related volcanism in Eastern Rhodopes (Bulgaria)-Western Thrace (Greece): petrogenetic affinity and geodynamic significance. *Acta Vulcanologica*, *10*, pp.279-292.

Yokoyama, Y., Reyss, J.L. and Guichard, F., 1977. Production of radionuclides by cosmic rays at mountain altitudes. *Earth and Planetary Science Letters*, *36*(1), pp.44-50.

York, D., Hall, C.M., Yanase, Y., Hanes, J.A. and Kenyon, W.J., 1981. 40Ar/39Ar dating of terrestrial minerals with a continuous laser. *Geophysical Research Letters*, *8*(11), pp.1136-1138.

Zachos, J.C., Dickens, G.R. and Zeebe, R.E., 2008. An early Cenozoic perspective on greenhouse warming and carbon-cycle dynamics. *Nature*, *451*(7176), pp.279-283.

Zheng, Y.F. and Fu, B., 1998. Estimation of oxygen diffusivity from anion porosity in minerals. *Geochemical Journal*, *32*(2), pp.71-89.

Ziegler, J.F., 2004. SRIM-2003. *Nuclear instruments and methods in physics research section B: Beam interactions with materials and atoms*, *219*, pp.1027-1036.

Ziegler, J.F., Biersack, J.P. and Ziegler, M.D., 2008. SRIM, the stopping and range of ions in matter.

Ziegler, James F. *Helium: stopping powers and ranges in all elemental matter*. Vol. 4. pergamon, 1977.

Zimmermann, L., Blard, P.H., Burnard, P., Medynski, S., Pik, R. and Puchol, N., 2012. A new single vacuum furnace design for cosmogenic 3He dating. *Geostandards and Geoanalytical Research*, *36*(2), pp.121-129.

Appendix A. MAP 215-50

The MAP 215-50 is an all-metal magnetic sector mass spectrometer with 90° extended geometry and a 15cm radius dispersion. It is equipped with a dual collector consisting on a Photonis Channeltron ion counter electron multiplier operated in pulse counting mode and a Faraday detector with an amplifier circuit equipped with a 10^{11} ohm resistor (Figure A.1). The system is designed to operate in peak jumping mode. It has a reported internal volume of ~1300 cc and it operates statically under ultra high vacuum achieved by a 30 L/s triode ion pump. It is equipped with a Nier-type electron bombardment ion source with Y steering. Two external source magnets are used to collimate the electron beam. All source parameters (HV, focus, electron volts, ion repeller, trap and Y steering) are computer controlled by GV Instruments Noble Ion Vantage software. The electromagnet is fabricated from high purity (minimum 99.9%) soft iron fitted with a temperature controlled Hall probe for read back control of the magnetic field strength.

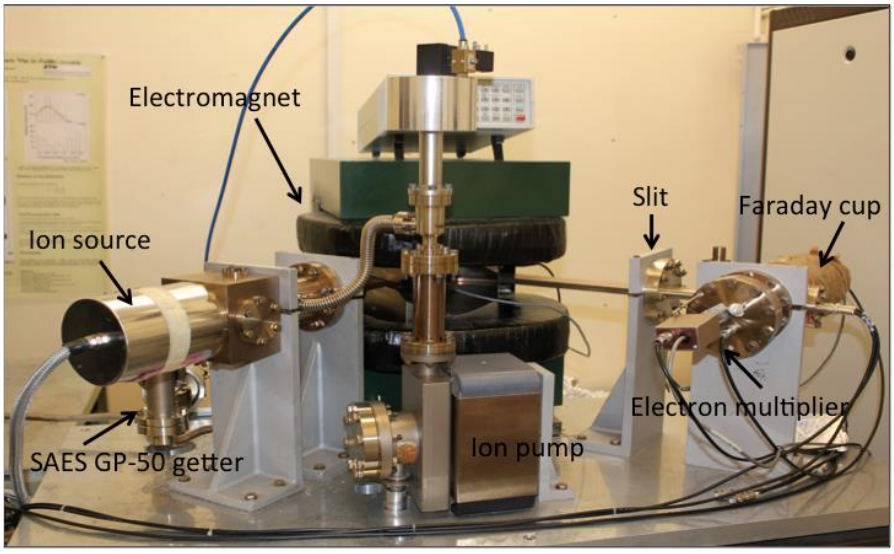

Figure A.1. MAP 215-50 mass spectrometer features. Photograph modified from Dymock (2014).

To remove any residual active and heavy gasses that may interfere in the measurements the mass spectrometer is equipped with a SAES GP50 getter operated at room temperature and an activated charcoal-filled stainless steel finger cooled to -196°C using liquid nitrogen positioned near the ion source. An adjustable slit in front of the electron multiplier is used to achieve a resolving power (m/ Δm) of 600 for He isotopes measurements allowing for separation of interferences of HD^+ and $^3H^+$ from $^3He^+$.

Variation on the shape of the slit permits to achieve a resolving power of approximately 400 required for Ne isotope measurements. In the case of Ne corrections are made to account for interferences at m/z = 20 (from $^{40}Ar^{+}/^{40}Ar^{++}$) and at m/z = 22 (from CO_2^{+}/CO_2^{++}) therefore no peak separation is needed. The source is tuned for He and Ne sensitivity prior to analytical periods. For He measurements typically electron voltage of 69 V, trap current of 300 μA and an acceleration voltage of 3 kV are used. In the case of Ne electron voltage of 88 V, trap current of 500 μA and an acceleration voltage of 3 kV are preferred. An embedded computer operating National Instruments Labview software controls all analyses parameters and data regression is performed using in-house-built *Regression* software.

A sample preparation line built on-site allows for purification of the noble gases from reactive gases extracted from mineral samples prior to mass spectrometer inlet (Figure A.2). The line is equipped with two manifold blocks (M1 and M2). Block M1 is equipped with two *SAES* GP50 getters both operated at 250ºC to remove the active gases (H_2, O_2, N_2, CO, H_2O, CH_4) and it is connected to an all-metal multi-sample hydraulic crusher and a resistance-heated double vacuum furnace (see Appendix B). Block M2 is equipped with one *SAES* GP50 getter operated at 250ºC and an activated charcoal-filled stainless steel cooled to -196°C using liquid nitrogen to remove the heavy noble gases (Ar, Kr and Xe). A cryostatic pump at -243˚C (30K) is used to trap Ne for Ne isotope analysis. M2 is connected to a vacuum laser cell for gas extraction. Ultra-high vacuum is achieved by 70 l/s turbo-molecular pump (*Pfeiffer* HiCube 80) with a baking two-stage diaphragm pump and a 30 l/s triode ion pump (*Varian*, Starcell). A 5-litre bottle containing helium standard gas HESJ (Matsuda et al., 2002) with $^{3}He/^{4}He$ ratio of 20.63 ± 0.10 R_A (R_A being the $^{3}He/^{4}He$ ratio of air 1.39 x 10^{-6}) and a 5-liter bottle containing air allow for the determination of He and Ne mass spectrometer sensitivity. All the valves in the system are manual *Varian* DN16CF valves with the exception of the inlet valve and the mass spectrometer valve to the ion pump, which are *VAT* pneumatic DN16CF valves.

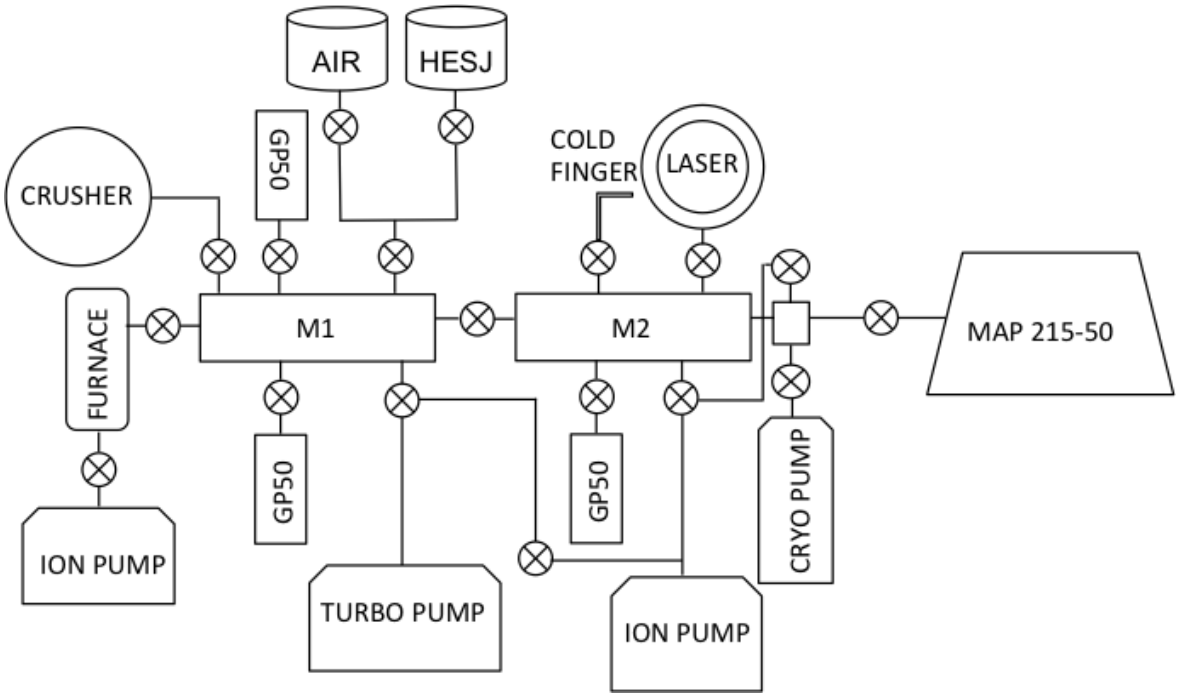

Figure A.2. Schematic of the gas purification line on the MAP 215-50 mass spectrometer. The system allows for isolation of all individual gas extraction methods**.**

References

Dymock, R.C., 2014. *Developing the cosmogenic He chronometer* (Doctoral dissertation, University of Glasgow).

Matsuda, J., Matsumoto, T., Sumino, H., Nagao, K., Yamamoto, J., Miura, Y., Kaneoka, I., Takahata, N. and Sano, Y., 2002. The 3He/4He ratio of the new internal He Standard of Japan (HESJ). *Geochemical Journal*, *36*(2), pp.191-195.

Appendix B. Supplementary details of gas extraction techniques

In addition to the use of a diode laser as a degassing method to release the cosmogenic helium (^{3}He) trapped in the mineral lattice, two other degassing techniques were used to produce the data presented in this thesis. To identify the cosmogenic helium component the determination of the magmatic component (^{3}He and ^{4}He) trapped in fluid and melt-inclusions is required. The trapped component is released from *in-vacuo* crushing (Stuart et al., 2003; Foeken et al., 2009a). A brief description of the crusher and analysis of a mineral standard are described in section B.1.

Degasing high amounts of material (> 20mg) can be challenging when a laser is used (see Chapter 4). In the case of the analysis of cosmogenic neon (^{21}Ne) with a production rate ~3 times lower than that of cosmogenic ^{3}He, the amount of material necessary to produce a measurable signal exceeds the amount limit by the laser requiring the use of a furnace to ensure complete degassing of the samples. Section B.2 describes the furnace used for the analysis of Ne isotopic composition of different mineral from Mount Hampton xenoliths.

B.1. In-vacuo crusher for extraction of magmatic ^{3}He/^{4}He ratios

A hydraulic crusher is used to release the magmatic component trapped in fluid and melt-inclusions. The crusher does not release a significant proportion of the cosmogenic ^{3}He (Foeken et al., 2009a) or radiogenic ^{4}He (Stuart et al., 2003) hosted in the mineral lattice. The gas released from the crushing of the minerals was cleaned for 15 minutes by two *SAES* GP50 getters operated at 250ºC to remove the active gases and by an activated charcoal-filled stainless steel finger cooled to -196°C using liquid nitrogen to remove the heavy noble gases. The gas is then let into the mass spectrometer for He isotope analysis. Any partial pressure of residual gases during the analysis is minimized by a *SAES* GP50 and a *SAES* NP10 getters operated at room temperature and a stainless steel charcoal cold finger at -196°C close to the ion source. Blanks from the crusher volume are typically ~3.2 x 10^{8} atoms for ^{4}He and 2.1 x 10^{4} atoms for ^{3}He, which represents less than 1 % of the helium released from crushing samples.

B.1.1. Reunion mineral standard

To test our ability to reproduce magmatic $^3He/^4He$ ratios four aliquots of Reunion olivine of different weights have been analysed. The aliquots yielded ^4He signals that vary from 2.0 x 10^{11} to 2.5 x 10^{12} atoms and ^3He signals from 3.8 x 10^6 to 4.2 x 10^7 atoms (Table B.1). The weighted mean of the $^3He/^4He$ ratio is 13.92 ± 0.2 (1.5 %, 2σ) with a mean square weighted deviation (MSWD) of 1.03 indicating stability of the crushing technique and appropriate determination of the uncertainty (Figure B.1). The value obtained from the crushing experiments fits within the range of values reported by previous studies varying from 11.8 to 14.5 R_A (Kaneoka et al., 1986; Staudacher et al., 1986; Graham et al., 1990; Staudacher et al., 1990; Hanyu et al., 2001; Trieloff et al., 2002; Hopp and Trieloff, 2005; Furi et al., 2011) demonstrating the robustness of the method.

Table B.1. Data from crushing aliquots of different weights of Reunion olivine standard. The uncertainties reported are the propagated 1σ uncertainty.

Weight (mg)	*^4He (10^{12}atoms)*	±	*^3He (10^7atoms)*	±	*$^3He/^4He$ (R_A)*	±
982	2.50	0.01	4.19	0.05	14.12	0.22
630	1.52	0.01	2.46	0.03	13.69	0.21
132	0.20	0.01	0.38	0.01	14.16	0.27
368	0.94	0.01	1.60	0.02	13.82	0.20

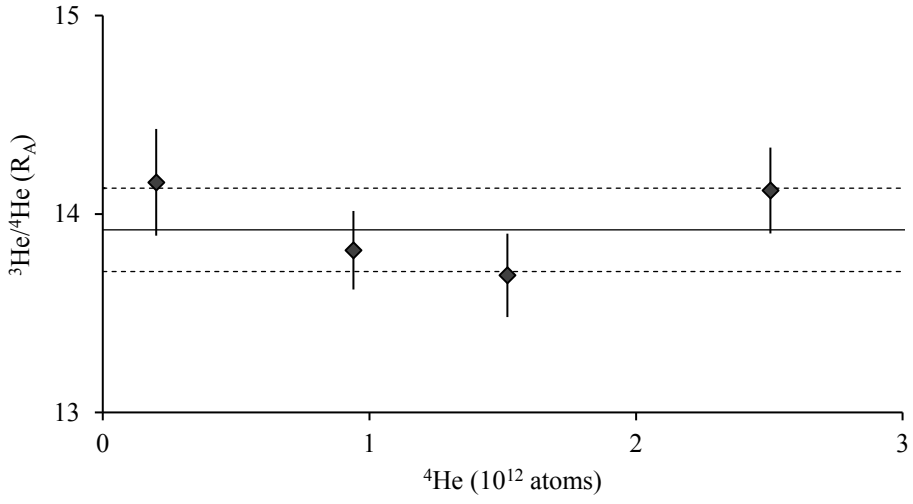

Figure B.1. Plot of the results of $^3He/^4He$ (R/R_A) for samples of different weights. Plotted individual analytical uncertainties are at 1σ. Continuous line represents the value of the weighted mean and dotted line delimits the uncertainty of the mean (2σ).

B.2. Furnace heating for cosmogenic Ne analysis

In order to fully degas samples of mass higher than the 15 mg allowance in a Pt packet, the use of a resistance-heated double vacuum furnace is required. In the case of Mount Hampton xenoliths, the amount of sample analysed ranges from 30 to 90 mg. The mineral separates were wrapped in Mo foil to allow for preservation of the Mo furnace liner. To extract the cosmogenic Ne each sample packet was heated for 20 minutes at a temperature ~1700˚C. During the heating, active gases were removed by two *SAES* GP50 getters operated at 250ºC and for further 20 minutes while the furnace cooled down. The heavy noble gases and residual active gases were absorbed by a *SAES* GP50 getter operated at room temperature and an activated charcoal-filled stainless steel finger cooled to -196°C for subsequent 10 minutes. Neon was then trapped on activated charcoal in a cryostatic cold head at 30K for another 10 minutes. At the end of this process He was removed by pumping for 1 minute and the Ne was released from the charcoal trap at 100K for 10 minutes. The Ne isotopes were then analysed statically in the MAP 215-50 described in appendix A. A *SAES* GP50 getter at room temperature and a liquid-nitrogen-cooled finger close to the ion source minimize any residual gases interference during analysis. The abundances of masses 18, 19, 20, 21, 22, 40 and 44 were determined by integrating counts recorded in 40-100 blocks of 5 second each. Peak height of mass 2 was measured on the Faraday detector. The instrument sensitivity is calculated from repeated analysis of 2.16×10^{10} atoms ^{20}Ne in air sampled from a 5-liter reservoir. Data obtained from analysis of several 0.1cc pipette samples are summarized in Table B.2 and Figure B.2. A correction factor is applied to all the calculated Ne isotope ratios to account for isotopic fractionation.

Table B.2. Data from the analysis of several 0.1cc pipette aliquots of air from the 5-liter reservoir. The sensitivity of the ion counter is calculated from 2.16 x 10^{10} atoms of ^{20}Ne in each pipette volume.

	^{20}Ne sensitivity*	±	$^{21}Ne/^{20}Ne$ (10^{-3})	±	$^{22}Ne/^{20}Ne$ (10^{-3})	±
	2.26	0.02	2.91	0.03	101.20	0.14
	2.29	0.01	2.94	0.03	101.47	0.16
	2.28	0.02	2.96	0.01	101.77	0.29
	2.24	0.03	2.96	0.02	101.32	0.36
	2.25	0.03	2.94	0.02	102.00	0.21
	2.26	0.02	2.91	0.02	101.18	0.17
	2.20	0.02	2.92	0.03	101.57	0.30
	2.27	0.01	2.93	0.03	101.63	0.29
Mean	***2.27***	***0.02***	***2.94***	***0.02***	***101.44***	***0.22***

*The ^{20}Ne sensitivity is reported in 10^4 atoms/count/5seconds. The uncertainties of the individual measurements are the propagated 1σ uncertainty. The mean values are the calculated weighted mean and the uncertainties on the mean are 2σ. The MSWDs are 2.0, 0.95 and 1.8 for the ^{20}Ne sensitivity, $^{21}Ne/^{20}Ne$ and $^{22}Ne/^{20}Ne$ showing high precision of the instrument and appropriate estimation of the uncertainty.

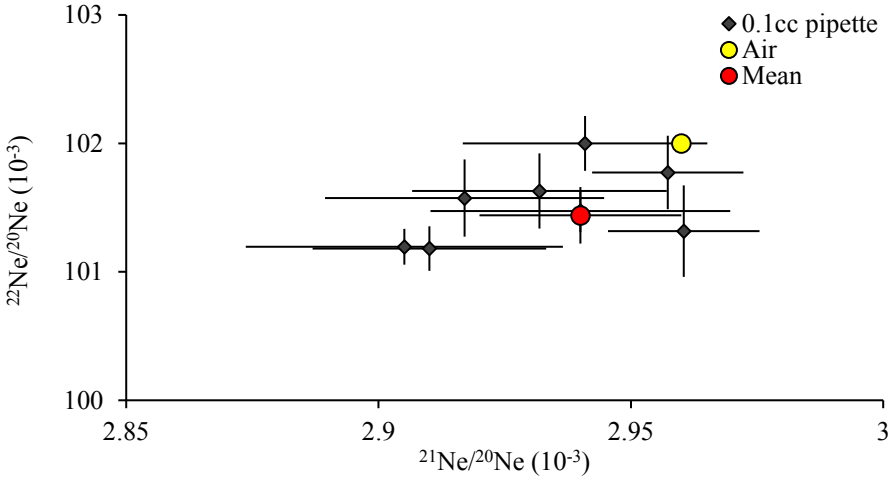

Figure B.2. Plot of the results of Ne isotopic composition of several 0.1cc pipette aliquots of air containing 2.16 x 10^{10} atoms of ^{20}Ne. The weighted mean (red dot) and air (yellow dot) isotopic composition are used to correct for isotopic fractionation.

The average high temperature (~1700˚C) ^{20}Ne blank is 4.09 ± 1.75 ×10^{8} atoms. There is no observed variation when empty Mo foil was heated. The Ne isotopic composition of the blank measurements after correction is indistinguishable from air ratios. Since it is likely that air-derived Ne is released from the Mount Hampton samples during heating, no blank correction has been made to the data.

Table B.3. Data from the analysis of several hot blanks, where the furnace is heated empty to 1700˚C for 20 minutes and one blank where empty Mo foil was placed in the furnace and heated to 1700˚C for 20 minutes. The uncertainties of the individual measurements are the propagated 1σ uncertainty.

Blank	*^{20}Ne (10^{8} atoms)*	±	*$^{21}Ne/^{20}Ne$ (10^{-3})*	±	*$^{22}Ne/^{20}Ne$ (10^{-3})*	±
Mo foil	5.20	0.16	3.00	0.17	96.91	1.60
Furnace	1.63	0.05	3.18	0.50	100.56	3.53
Furnace	5.42	0.16	2.44	0.16	97.61	1.96
Furnace	2.81	0.08	1.96	0.44	103.62	3.54
Furnace	5.37	0.16	2.67	0.27	106.31	1.26
Average	***4.09***	***1.75***	***2.65***	***0.48***	***101.00***	***3.98***

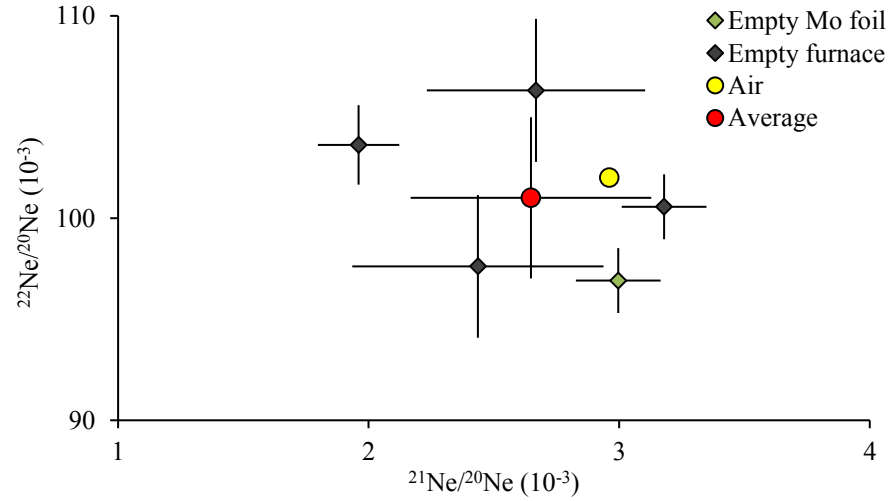

Figure B.3. Plot of the results of Ne isotopic composition of four high temperature empty furnace blanks (black diamonds) and one Mo foil blank (green diamond). The average (red dot) isotopic composition is indistinguishable from air (yellow dot) within 1σ uncertainty.

B.2.1. Calculating cosmogenic Ne concentration

To calculate the cosmogenic Ne concentration in the samples corrections for interferences at mass/charge (m/z) 20 and 22 and determination of excess ^{21}Ne ($^{21}Ne^*$) are undertaken. $^{21}Ne^*$ concentrations are calculated assuming an atmospheric origin of all the measured ^{20}Ne according to Equation B.1.

$$^{21}Ne^* = {}^{21}Ne_m \text{ x } (R_m - R_A)/R_m \quad \text{(B.1)}$$

where, $^{21}Ne_m$ is the measured ^{21}Ne, R_m is the measured $^{21}Ne/^{20}Ne$ ratio and R_A is the atmospheric $^{21}Ne/^{20}Ne$ ratio (0.00296). Interference at m/z = 20 from $H_2{}^{18}O^+$ was calculated from measurement of $H_2{}^{16}O^+$ at mass 18. The contribution never exceeded 0.03%. No $H^{19}F^+$ signal was observed in blanks and mass spectrometer backgrounds. The dominant interference at m/z = 20 comes from $^{40}Ar^{++}$. The charge state ratio $^{40}Ar^+/^{40}Ar^{++}$ is governed by the partial pressure of H in the mass spectrometer ionization region. At constant partial pressure of H the resulting $^{40}Ar^+/^{40}Ar^{++}$ is 3.05 ± 0.11. The contribution of $^{40}Ar^{++}$ to the measured ^{20}Ne signal in Mount Hampton samples was 5-50 %. Correction for $^{12}C^{16}O_2{}^{++}$ at m/z = 22 is calculated from measured mass 44 ($^{12}C^{16}O_2{}^+$) using a $CO_2{}^+/CO_2{}^{++}$ ratio of 53.23 ± 1.44. Correction for interfering $^{12}C^{16}O_2{}^{++}$ represents 5-30 % of the measured ^{22}Ne signal.

B.2.2. He isotopes in mineral standards

The results from degassing CRONUS pyroxene standard and MH.2 olivine using different laser heating techniques are shown in tables B.4 and B.5 respectively. Table B.6 compiles the He isotope data for CRONUS pyroxene standard reported in the inter-laboratory comparison of Blard et al. (2015) and includes the data from this work.

Table B.4. Results from the degasing of CRONUS pyroxene mineral standard using three different degasing techniques. The ^{4}He concentration is expressed in 10^{13} atoms/g and the ^{3}He concentration in 10^9 atoms/g.

Degasing	*Weight (mg)*	*^{4}He*	±	*^{3}He*	±	*^{3}He/^{4}He (R_A)*	±
Diode laser	10.6	3.20	0.01	5.17	0.07	117.17	0.89
Diode laser	10.1	3.27	0.01	4.96	0.07	109.75	0.81
Diode laser	7.6	3.41	0.01	4.91	0.07	104.41	0.91
Diode laser	10.5	3.41	0.01	5.04	0.07	107.08	0.73
Diode laser	7.5	3.43	0.01	4.92	0.07	103.66	0.90
Diode laser	7	3.55	0.01	5.08	0.07	98.94	0.62
Diode laser	33.5	3.57	0.01	5.02	0.06	101.91	0.59
Diode laser	23.8	3.61	0.01	4.90	0.06	98.33	0.68
Diode laser	12.4	3.63	0.01	4.71*	0.07	93.97	0.77
Diode laser	9.5	3.66	0.01	4.88	0.07	96.55	0.83
Diode laser	25.1	3.71	0.01	4.85	0.06	95.63	0.54
Diode laser	10.1	3.77	0.01	4.98	0.07	98.33	0.68
Diode laser	7.8	3.77	0.01	5.02	0.07	97.07	0.81
Diode laser	8.8	3.85	0.01	5.00	0.07	94.08	0.76
Diode laser	14.6	3.96	0.01	5.08	0.07	98.94	0.62
Mean[a]		***3.56***	***0.12***	***4.98***	***0.05***	***100.3***	***3.2***
Pt packet	12.80	3.47	0.02	4.75*	0.07	99.67	0.60
Pt packet	18.60	3.38	0.02	4.76*	0.05	79.21	0.48
Pt packet	14.00	3.53	0.02	4.86	0.07	100.51	0.60
Pt packet	12.30	3.62	0.02	4.92	0.07	99.13	0.59
Pt packet	9.95	3.33	0.01	4.95	0.04	108.41	0.65
Pt packet	14.70	4.21*	0.01	4.95	0.03	85.75	0.51
Pt packet	12.75	3.61	0.01	4.96	0.03	100.09	0.60
Pt packet	13.20	3.22	0.01	4.96	0.03	112.14	0.67
Pt packet	11.30	3.50	0.02	4.98	0.07	103.86	0.62
Pt packet	12.50	3.27	0.40	4.98	0.01	111.11	0.67
Pt packet	11.05	3.60	0.01	4.99	0.04	100.89	0.61
Pt packet	13.30	3.35	0.04	5.01	0.07	108.95	0.65
Pt packet	11.70	3.48	0.02	5.24	0.07	109.75	0.66
Pt packet	24.60	4.77*	0.04	5.26	0.05	80.42	0.48
Mean		***3.50***	***0.12***	***4.98***	***0.03***	***97.4***	***0.68***
CO_2 laser	22.97	3.34	0.01	4.76	0.06	103.26	0.58
CO_2 laser	6.37	3.40	0.01	4.96	0.07	105.71	0.74
CO_2 laser	24	3.41	0.01	4.61	0.06	98.02	0.56
CO_2 laser	13	3.44	0.01	4.95	0.07	102.86	0.78
CO_2 laser	18.2	3.46	0.01	4.59*	0.06	95.06	0.59
CO_2 laser	20.5	3.57	0.01	4.73	0.06	95.13	0.61
CO_2 laser	20.49	3.61	0.01	4.98	0.06	99.84	0.59
CO_2 laser	7.4	3.61	0.01	5.10	0.07	101.81	0.92
CO_2 laser	10.71	3.64	0.01	4.94	0.07	98.10	0.69
CO_2 laser	20.63	3.73	0.01	4.91	0.06	95.24	0.61
CO_2 laser	8.9	3.73	0.01	5.23	0.07	99.79	0.85
CO_2 laser	9.7	3.78	0.01	5.22	0.07	99.79	0.85
CO_2 laser	23.8	3.84	0.01	4.71	0.06	88.12	0.51
CO_2 laser*	93.70	3.03*	0.01	4.58*	0.06	109.82	0.59
CO_2 laser*	180.00	2.61*	0.01	4.22*	0.05	117.33	0.61
Mean		***3.57***	***0.10***	***4.90***	***0.12***	***100.1***	***4.2***

All the data have been used for comparing the efficiency of the three methods with the exception of * that have not been considered for this purpose as the samples were not completely degassed (see text). The uncertainties of the measurements are the propagated 1σ uncertainty. a. Means are the calculated weighted means and the 2σ standard deviation.

Table B.5. Results from the degasing of MH.2 olivine using three different degasing techniques. The ^{4}He concentration is expressed in 10^{11} atoms/g and the ^{3}He concentration in 10^8 atoms/g.

*Degasing **	*Weight (mg)*	*^{4}He*	±	*^{3}He*	±	*^{3}He/^{4}He (R_A)*	±
Diode laser	3.30	2.36	0.24	6.02	0.21	1850	198
Diode laser	5.23	1.59	0.18	6.22	0.22	2838	344
Diode laser	11.00	2.73	0.14	6.26	0.09	1663	90
Diode laser	6.00	4.63	0.16	6.33	0.27	993	54
Diode laser	11.90	4.65	0.08	6.34	0.18	989	33
Diode laser	5.30	15.55	0.20	6.41	0.12	299	7
Diode laser	12.77	6.06	0.08	6.41	0.25	768	32
Diode laser	2.80	7.05	0.03	6.42	0.27	660	28
Diode laser	5.62	1.86	0.11	6.56	0.16	2554	159
Diode laser	11.12	1.89	0.09	6.77	0.11	2600	135
Diode laser	9.94	1.57	0.07	6.84	0.10	3165	157
Diode laser	22.40	2.28	0.02	6.90	0.13	2194	45
Diode laser	7.98	1.79	0.11	6.92	0.09	2813	180
Diode laser	5.70	1.72	0.10	6.94	0.20	2930	197
Diode laser	21.00	1.71	0.03	7.01	0.09	2978	59
Diode laser	5.50	5.29	0.22	7.07	0.17	970	46
Diode laser	5.20	1.98	0.23	7.08	0.13	2591	302
Mean[a]				***6.71***	***0.38***		
Pt packet	14.90	0.51	0.01	7.64	0.12	10693	245
Pt packet	17.00	2.25	0.27	7.64	0.14	2032	40
Pt packet	15.00	0.47	0.01	7.67	0.12	11543	279
Pt packet	12.20	1.1	0.03	7.70	0.13	5001	157
Pt packet	10.50	2.74	0.33	7.73	0.15	2032	40
Pt packet	15.00	4.94	0.59	7.78	0.16	1131	23
Pt packet	11.10	4.57	0.54	7.78	0.17	1227	26
Pt packet	8.00	7.59	0.91	7.81	0.2	740	19
Pt packet	10.80	7.28	0.87	7.84	0.15	775	20
Pt packet	14.00	1.16	0.01	7.96	0.11	4902	101
Pt packet	12.00	4.4	0.53	8.03	0.15	1312	26
Pt packet	13.50	5.25	0.02	8.27	0.15	1469	33
Pt packet	12.00	28.52	0.1	8.43	0.14	211	4
Pt packet	12.00	30.3	0.06	8.45	0.15	202	3
Pt packet	11.30	1.21	0.02	8.54	0.15	5130	138
Mean				***7.91***	***0.36***		
CO_2 laser	15.24	4.22	0.01	6.48	0.10	1114	18
CO_2 laser	17.35	3.93	0.01	6.62	0.09	1222	18
CO_2 laser	13.10	4.99	0.03	6.73	0.13	980	20
CO_2 laser	12.80	4.73	0.05	6.94	0.13	1065	22
CO_2 laser	23.20	3.16	0.01	6.95	0.10	1595	25
CO_2 laser	26.70	3.87	0.01	7.07	0.11	1326	21
CO_2 laser	28.26	4.02	0.01	7.09	0.11	1282	21
CO_2 laser	23.00	2.30	0.03	7.24	0.07	2284	40
CO_2 laser	5.16	3.55	0.04	7.78	0.15	1592	34
Mean				***6.98***	***12.2***		

***** The measurements of the helium isotopes from the aliquots degassed using the diode laser have been performed using the MAP 215-50 at SUERC, in this case the olivine separates were mixed with degassed pyroxene flux to facilitate laser coupling (Foeken et al., 2009). The uncertainties on the individual measurements are reported as propagated 1σ uncertainty. a. Means are the calculated weighted means and inflated (x MSWD$^{1/2}$) 2σ uncertainty to account for data over dispersion.

Table B.6. Compilation of the results from the analysis of CRONUS pyroxene standard performed by six laboratories (data taken from Blard et al., 2015) and the results obtained from this work using the Helix SFT at SUERC. The ^{4}He concentrations are expressed in 10^{13} atoms/g and the ^{3}He concentrations in 10^{9}atoms/g. The on the individual measurements are reported as propagated 1σ uncertainty.

Laboratory	*Mass (mg)*	*Temperature (°C)*	*Heating time (min)*	*^{4}He*	±	*^{3}He*	±	*$^{3}He/^{4}He$ (R_A)*	±
Caltech Pasadena	33.1	1600	15	3.29	0.10	4.64	0.10	102	4
Caltech Pasadena	83.5	1600	15	10.86	0.33	5.09	0.14	34	1
Caltech Pasadena	36.2	1600	15	12.69	0.02	5.03	0.14	29	1
Caltech Pasadena	26.8	1600	15	3.41	0.01	4.83	0.13	102	3
Caltech Pasadena	29.5	1600	15	3.66	0.01	4.79	0.13	95	3
Caltech Pasadena	10.6	1600	15	3.40	0.01	4.89	0.13	104	3
Caltech Pasadena	8.8	1600	15	3.32	0.01	4.79	0.13	104	3
Caltech Pasadena	14.6	1600	15	3.70	0.08	4.98	0.17	97	4
Caltech Pasadena	17.7	1600	15	3.62	0.08	4.82	0.16	96	4
Mean[a,b]				***3.45***	***0.13***	***4.85***	***0.11***	***101***	***2***
GFZ Potsdam		900	20	3.51	0.09	4.92	0.13	101	1
GFZ Potsdam		1750	20	0.04	0.01	0.05	0.01	98	4
GFZ Potsdam	99.4	Total		3.55	0.09	4.97	0.13	101	1
GFZ Potsdam		900	20	2.90	0.07	3.25	0.09	81	1
GFZ Potsdam		1750	20	0.51	0.01	1.47	0.04	208	3
GFZ Potsdam	51.7	Total		3.41	0.07	4.72	0.10	100	1
GFZ Potsdam		900	20	3.51	0.09	4.86	0.13	100	1
GFZ Potsdam		1750	20	0.05	0.01	0.07	0.01	106	4
GFZ Potsdam	49.6	Total		3.56	0.09	4.93	0.13	100	1
GFZ Potsdam		900	20	3.53	0.09	4.93	0.14	101	1
GFZ Potsdam		1750	20	0.04	0.01	0.06	0.01	97	6
GFZ Potsdam	50.1	Total		3.57	0.09	4.99	0.14	101	1
GFZ Potsdam		900	20	3.40	0.09	5.04	0.14	107	2
GFZ Potsdam		1750	20	0.03	0.01	0.05	0.01	118	6
GFZ Potsdam	50.7	Total		3.43	0.09	5.09	0.14	107	2
GFZ Potsdam		900	20	3.43	0.09	4.81	0.13	101	1
GFZ Potsdam		1750	20	0.04	0.01	0.05	0.01	109	5
GFZ Potsdam	50.8	Total		3.46	0.09	4.86	0.13	102	1
GFZ Potsdam		900	20	3.47	0.09	4.89	0.13	102	1
GFZ Potsdam		1750	20	0.03	0.01	0.03	0.01	96	4
GFZ Potsdam	21	Total		3.50	0.09	4.92	0.13	102	1
Mean				***3.49***	***0.06***	***4.90***	***0.09***	***101***	***1***
CRPG Nancy	54.5	1400	15	3.68	0.04	4.93	0.09	97	2
CRPG Nancy	12.2	1400	15	4.19	0.04	4.87	0.09	84	2
CRPG Nancy	10.4	1400	15	3.43	0.03	4.94	0.09	104	2
CRPG Nancy	27.9	1400	15	3.69	0.04	4.91	0.09	96	2
CRPG Nancy	42	1400	15	3.63	0.04	4.93	0.09	98	2
CRPG Nancy	23	1400	15	3.56	0.04	5.05	0.10	103	2
CRPG Nancy	23.6	1400	15	3.64	0.04	4.97	0.09	99	2
CRPG Nancy	11	1400	15	4.01	0.04	4.97	0.10	89	2
CRPG Nancy	27.4	1400	15	3.32	0.06	4.86	0.10	106	3
CRPG Nancy	14.4	1400	15	3.33	0.06	4.87	0.10	106	3
Mean				***3.67***	***0.19***	***4.93***	***0.06***	***97***	***5***
SUERC Glasgow	26.8	>1400	5	3.46	0.11	5.11	0.16	107	5
SUERC Glasgow	4.1	>1400	5	2.97	0.10	4.95	0.16	120	6
SUERC Glasgow	3.9	>1400	5	3.12	0.11	4.91	0.16	114	5
SUERC Glasgow	2.4	>1400	5	3.27	0.12	5.36	0.18	118	6
SUERC Glasgow	7.5	>1400	5	3.25	0.11	4.97	0.16	110	5
SUERC Glasgow	14.2	>1400	5	3.71	0.12	5.23	0.17	102	5
SUERC Glasgow	10.6	>1400	5	3.26	0.11	5.10	0.16	113	5
SUERC Glasgow	12.5	>1400	5	3.20	0.10	5.22	0.17	118	5
SUERC Glasgow	10	>1400	5	3.12	0.10	5.09	0.16	118	5
SUERC Glasgow	23.4	>1400	5	3.19	0.10	5.02	0.16	114	5
SUERC Glasgow	7.3	>1400	5	2.85	0.09	4.75	0.15	120	6
SUERC Glasgow	4.5	>1400	5	3.22	0.11	4.61	0.15	103	5
SUERC Glasgow	16.9	>1400	5	3.41	0.11	5.12	0.16	108	5
SUERC Glasgow	10	>1400	5	3.27	0.10	4.81	0.15	106	5
SUERC Glasgow	1.9	>1400	5	2.88	0.10	4.90	0.17	123	6
SUERC Glasgow	3.6	>1400	5	3.06	0.11	4.75	0.16	112	6

Laboratory	*Mass (mg)*	*Temperature (°C)*	*Heating time (min)*	*^{4}He*	±	*^{3}He*	±	*^{3}He/^{4}He (R_A)*	±
SUERC Glasgow	5.4	>1400	5	3.17	0.11	4.80	0.16	109	5
SUERC Glasgow	10.5	>1400	5	3.14	0.10	4.73	0.15	109	5
SUERC Glasgow	15.5	>1400	5	3.40	0.11	4.96	0.16	105	5
SUERC Glasgow	12.9	>1400	5	3.26	0.10	4.85	0.15	108	5
SUERC Glasgow	21.8	>1400	5	3.43	0.11	5.15	0.16	109	5
Mean				***3.21***	***0.09***	***4.96***	***0.08***	***111***	***3***
BGC Berkeley	16.6	1200	15	3.78	0.10	5.20	0.16	99	4
BGC Berkeley	33.9	1200	15	4.15	0.11	5.24	0.16	91	4
BGC Berkeley	51.7	1200	15	3.77	0.09	5.08	0.15	97	4
BGC Berkeley	26.5	1200	15	3.97	0.10	5.31	0.17	97	4
BGC Berkeley	19.9	1200	15	3.90	0.09	5.16	0.15	96	3
Mean				***3.90***	***0.18***	***5.19***	***0.14***	***96***	***3***
Lamont NY	16.29	1350	15	3.78	0.08	5.30	0.13	101	3
Lamont NY	17.05	1350	15	3.66	0.07	5.27	0.13	104	3
Lamont NY	16.26	1350	15	3.87	0.02	5.44	0.11	102	2
Lamont NY	17.29	1350	15	3.78	0.02	5.39	0.09	103	2
Lamont NY	14.33	1350	15	3.92	0.02	5.34	0.09	98	2
Lamont NY	14.65	1350	15	3.88	0.02	5.26	0.08	98	2
Lamont NY	18.35	1350	15	3.67	0.02	5.25	0.09	103	2
Lamont NY	12.42	1350	15	3.87	0.05	5.21	0.11	97	2
Lamont NY	16.43	1350	15	3.82	0.03	5.32	0.08	101	2
Lamont NY	15.67	1350	15	3.55	0.04	5.04	0.09	102	2
Lamont NY	17.34	1350	15	3.86	0.01	5.20	0.06	97	1
Lamont NY	15.17	1350	15	3.77	0.01	5.20	0.07	100	1
Lamont NY	15.08	1350	15	3.69	0.01	5.19	0.05	102	1
Mean				***3.79***	***0.05***	***5.24***	***0.06***	***100***	***1***
Helix SFT	14.00	1300	20	3.54	0.02	4.86	0.07	100	1
Helix SFT	12.30	1300	20	3.63	0.02	4.92	0.07	99	1
Helix SFT	9.95	1300	20	3.33	0.01	4.95	0.04	108	1
Helix SFT	14.70	1300	20	3.71	0.01	4.95	0.03	97	1
Helix SFT	12.75	1300	20	3.61	0.01	4.96	0.03	100	1
Helix SFT	13.20	1300	20	3.22	0.01	4.96	0.03	112	1
Helix SFT	12.50	1300	20	3.21	0.04	4.98	0.07	113	2
Helix SFT	11.05	1300	20	3.60	0.01	4.98	0.01	101	0
Helix SFT	13.30	1300	20	3.29	0.03	4.99	0.04	111	1
Helix SFT	11.30	1300	20	3.50	0.02	5.01	0.07	104	1
Mean				***3.50***	***0.14***	***4.97***	***0.02***	***102***	***4***

a. Means are the calculated weighted means and the correspondent 2σ uncertainty.
b. Two outliers were removed from the Caltech dataset before calculating the weighted mean.

B.3. ICP-MS for Li concentration in gold

In order to measure the Li concentration in gold, the gold grains were dissolved using 5 cycles of freshly prepared aqua regia (8 ml, HNO_3 and HCl at 1:3) at 100 ˚C, each cycle lasting 5 hours. After this process the samples were completely dried and then dissolved in 20 ml of HNO_3 0.8M. Ten blanks were prepared simultaneously following the same procedures and 10 ml of HNO_3 were added at the end of the process prior to analysis in the ICP-MS (Agilent 7500ce) at SUERC. A clean solution of HNO_3 0.8M was analysed at the start of the day in order to set the baseline for the measurements. And after this, Li standards (Specpure® trace element certified) at 5, 10 and 20 ppb of Li were analysed to calculate the concentration factor (Figure B.4). A Li standard at 10 ppb was also analysed every 5 samples. Internal standard (In) was measured in order to correct for possible fluctuation of the sensitivity. The data obtained from the ICP-MS measurements and the calculated Li concentrations are presented in table B.4.

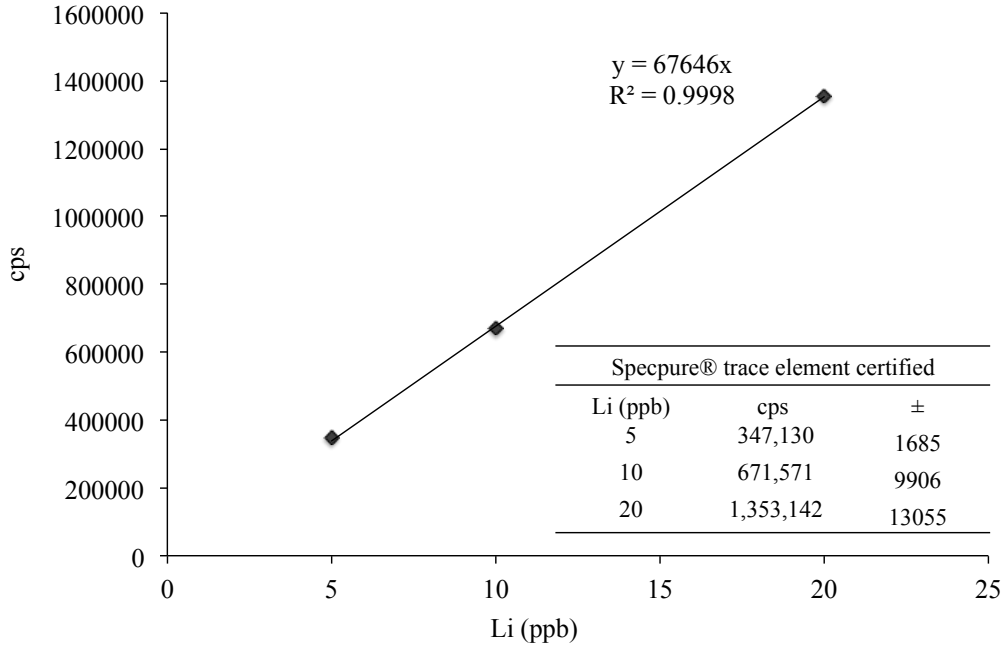

Figure B.4. Plot of the results of the Li standards (Specpure® trace element certified) at 5, 10 and 20 ppb of Li. The value of the slope (67,646) is the factor used to calculate the Li concentrations in the solutions.

Table B.4. Data from ICP-MS analysis of gold grains. The Li concentrations in the samples have been calculated on based on the measurements of the standards and blank corrected. All the uncertainties are reported as propagated 1σ.

Sample Name	Weight (mg)	Li (cps)	±	In (cps)	±	In factor	±	In corected	±	Baseline corrected	±	Li ppb sol	±	Li ng	±	Li blk corr (ng)	±	Li (ppm)	±
HNO_3 (Baseline)		6,202	167	179,842	1236	100	1												
Specpure (5)		347,130	1685	178,417	2086	99	1.3												
Specpure (10)		671,571	9906	174,644	1109	97	0.9												
Specpure (20)		1,353,142	13055	173,598	1143	97	0.9												
blank1		534,818	2501	179,480	921	100	0.9	535,896	5,237	529,693	5,070	7.83	0.07	78.3	0.75				
blank2		604,624	4539	179,722	1592	100	1.1	605,029	8,164	598,826	7,997	8.85	0.12	88.52	1.18				
blank3		625,649	2571	176,105	1647	98	1.1	638,927	7,868	632,724	7,702	9.35	0.11	93.53	1.14				
blank4		383,195	2126	181,685	1356	101	1	379,307	4,386	373,105	4,220	5.52	0.06	55.16	0.62				
blank5		570,247	2303	179,387	1034	100	0.9	571,692	5,624	565,490	5,458	8.36	0.08	83.6	0.81				
blank6		657,728	3569	177,224	1130	99	0.9	667,442	7,231	661,240	7,065	9.78	0.1	97.75	1.04				
blank7		61,769	659	181,375	936	101	0.9	61,247	839	55,045	673	0.81	0.01	8.14	0.1				
blank8		2,896,473	13458	131,975	808	73	0.7	3,947,013	40,708	3,940,810	40,542	58.26	0.6	582.56	5.99				
blank9		1,111,269	6762	179,767	1154	100	0.9	1,111,731	12,455	1,105,528	12,289	16.34	0.18	163.43	1.82				
blank10		348,556	1575	175,459	1598	98	1.1	357,263	4,385	351,060	4,219	5.19	0.06	51.9	0.62	80.04	42.01		
Specpure (10)		682,148	14356	176,961	1248	98	1												
L.6-1	25.6	1,432,371	9585	147,514	779	82	0.7	1,746,276	19,125	1,740,073	18,959	25.72	0.28	514.46	5.61	434.43	42.38	16.97	1.66
L.6-2	25.3	615,691	2882	150,900	738	84	0.7	733,778	7,080	727,576	6,913	10.76	0.1	215.11	2.04	135.08	42.06	5.34	1.66
L.6-3	23.6	651,519	3768	143,910	1188	80	0.9	814,193	9,934	807,991	9,767	11.94	0.14	238.89	2.89	158.85	42.11	6.73	1.78
L.6-4	11.6	277,487	1244	145,587	886	81	0.7	342,775	3,503	336,573	3,336	4.98	0.05	99.51	0.99	19.47	42.02	1.68	3.62
L.7-1	25.7	237,194	1154	141,967	916	79	0.7	300,474	3,188	294,272	3,022	4.35	0.04	87	0.89	6.97	42.02	0.27	1.63
Specpure (10)		560,552	3436	150,112	1636	83	1.1												
L.7-2	41.3	457,863	1800	126,055	910	70	0.7	653,229	7,001	647,026	6,835	9.56	0.1	191.3	2.02	111.26	42.06	2.69	1.02
L.7-3	34	226,600	1277	135,469	548	75	0.6	300,822	2,938	294,620	2,772	4.36	0.04	87.11	0.82	7.07	42.02	0.21	1.24
C.4-1	21.7	295,543	1632	139,726	670	78	0.7	380,395	3,818	374,193	3,652	5.53	0.05	110.63	1.08	30.6	42.02	1.41	1.94
C.4-2	23	801,262	2957	139,886	704	78	0.7	1,030,131	9,567	1,023,928	9,401	15.14	0.14	302.73	2.78	222.7	42.1	9.68	1.83
C.4-3	21.5	199,898	1024	140,572	1000	78	0.8	255,742	2,849	249,540	2,682	3.69	0.04	73.78	0.79	-	-	-	-
Specpure (10)		557,922	4415	149,136	1518	83	1												
KB.4	4	560,556	2242	150,487	752	84	0.7	669,901	6,294	663,699	6,127	9.81	0.09	196.23	1.81	116.19	42.05	29.05	10.51
GB.1	3.8	386,729	1547	149,589	748	83	0.7	464,940	4,368	458,738	4,202	6.78	0.06	135.63	1.24	55.59	42.03	14.63	11.06
WW.9	13.5	420,546	3364	147,440	1180	82	0.9	512,967	6,791	506,765	6,625	7.49	0.1	149.83	1.96	69.79	42.06	5.17	3.12
LF.3-1	32.4	815,150	5706	132,929	1063	74	0.8	1,102,834	13,962	1,096,632	13,795	16.21	0.2	324.23	4.08	244.19	42.21	7.54	1.3
LF.3-2	19.7	743,403	4460	140,344	702	78	0.7	952,624	9,912	946,421	9,746	13.99	0.14	279.82	2.88	199.78	42.11	10.14	2.14
Specpure (10)		557,718	3904	149,743	1198	83	0.9												
LF.3-3	23.6	214,573	1287	132,362	794	74	0.7	291,545	3,184	285,342	3,017	4.22	0.04	84.36	0.89	4.33	42.02	0.18	1.78
LF.3-4	11.6	326,763	1307	130,647	653	73	0.6	449,806	4,226	443,604	4,059	6.56	0.06	131.15	1.2	51.12	42.03	4.41	3.62
A.2-1	20.3	1,442,246	7211	137,838	551	77	0.6	1,881,744	17,680	1,875,542	17,513	27.73	0.26	554.52	5.18	474.48	42.33	23.37	2.09
A.2-2	27.5	564,800	1694	135,109	676	75	0.6	751,798	6,777	745,595	6,611	11.02	0.1	220.44	1.95	140.4	42.05	5.11	1.53
A.2-3	18.4	244,489	978	134,976	1215	75	0.9	325,757	3,913	319,555	3,746	4.72	0.06	94.48	1.11	14.44	42.02	0.78	2.28
Specpure (10)		541,434	3249	143,658	1437	80	1	677,808	9,176	671,605	9,009	9.93	0.13						

* Li ppb in solution has been calculated applying the slope factor (67,646). ** Average blank level in ppb.

References

Blard, P.H., Balco, G., Burnard, P.G., Farley, K.A., Fenton, C.R., Friedrich, R., Jull, A.T., Niedermann, S., Pik, R., Schaefer, J.M. and Scott, E.M., 2015. An inter-laboratory comparison of cosmogenic 3 He and radiogenic 4 He in the CRONUS-P pyroxene standard. *Quaternary Geochronology*, *26*, pp.11-19.

Foeken, J.P., Day, S. and Stuart, F.M., 2009a. Cosmogenic 3He exposure dating of the Quaternary basalts from Fogo, Cape Verdes: implications for rift zone and magmatic reorganisation. *Quaternary Geochronology*, *4*(1), pp.37-49.

Füri, E., Hilton, D.R., Murton, B.J., Hémond, C., Dyment, J. and Day, J., 2011. Helium isotope variations between Réunion Island and the Central Indian Ridge (17–21 S): New evidence for ridge–hot spot interaction. *Journal of Geophysical Research: Solid Earth*, *116*(B2).

Graham, D., Lupton, J., Albarede, F. and Condomines, M., 1990. Extreme temporal homogeneity of helium isotopes at Piton de la Fournaise, Réunion Island. *Nature*, *347*(6293), pp.545-548.

Hanyu, T., Dunai, T.J., Davies, G.R., Kaneoka, I., Nohda, S. and Uto, K., 2001. Noble gas study of the Reunion hotspot: evidence for distinct less-degassed mantle sources. *Earth and Planetary Science Letters*, *193*(1), pp.83-98.

Hopp, J. and Trieloff, M., 2005. Refining the noble gas record of the Réunion mantle plume source: Implications on mantle geochemistry. *Earth and Planetary Science Letters*, *240*(3), pp.573-588.

Kaneoka, I., Takaoka, N. and Upton, B.G.J., 1986. Noble gas systematics in basalts and a dunite nodule from Réunion and Grand Comore Islands, Indian Ocean. *Chemical Geology: Isotope Geoscience section*, *59*, pp.35-42.

Staudacher, T., Kurz, M.D. and Allègre, C.J., 1986. New noble-gas data on glass samples from Loihi Seamount and Hualalai and on dunite samples from Loihi and Reunion Island. *Chemical geology*, *56*(3), pp.193-205.

Staudacher, T., Sarda, P. and Allègre, C.J., 1990. Noble gas systematics of Réunion island, Indian Ocean. *Chemical geology*, *89*(1), pp.1-17.

Stuart, F.M., Lass-Evans, S., Fitton, J.G. and Ellam, R.M., 2003. High 3He/4He ratios in picritic basalts from Baffin Island and the role of a mixed reservoir in mantle plumes. *Nature*, *424*(6944), pp.57-59.

Trieloff, M., Kunz, J. and Allègre, C.J., 2002. Noble gas systematics of the Réunion mantle plume source and the origin of primordial noble gases in Earth's mantle. *Earth and Planetary Science Letters*, *200*(3), pp.297-313.

Appendix C. Supplementary details of Mount Hampton xenoliths

C.1. Description of thin sections

Thin sections of samples MH.1, MH.2, MB.71.7, MB.71.8 and MB.71.9 were prepared and observed under petrographic microscope. Samples MB.71.10 and MM were not available for thin section preparation due to their crumbled state. This section includes descriptions of hand-specimens and thin sections of all the samples analysed for Chemical composition control study (Chapter 5). The volume of the specimens range from 30 to 50cm^3. Crossed nicols images of the thin sections are presented in Figure C.1.

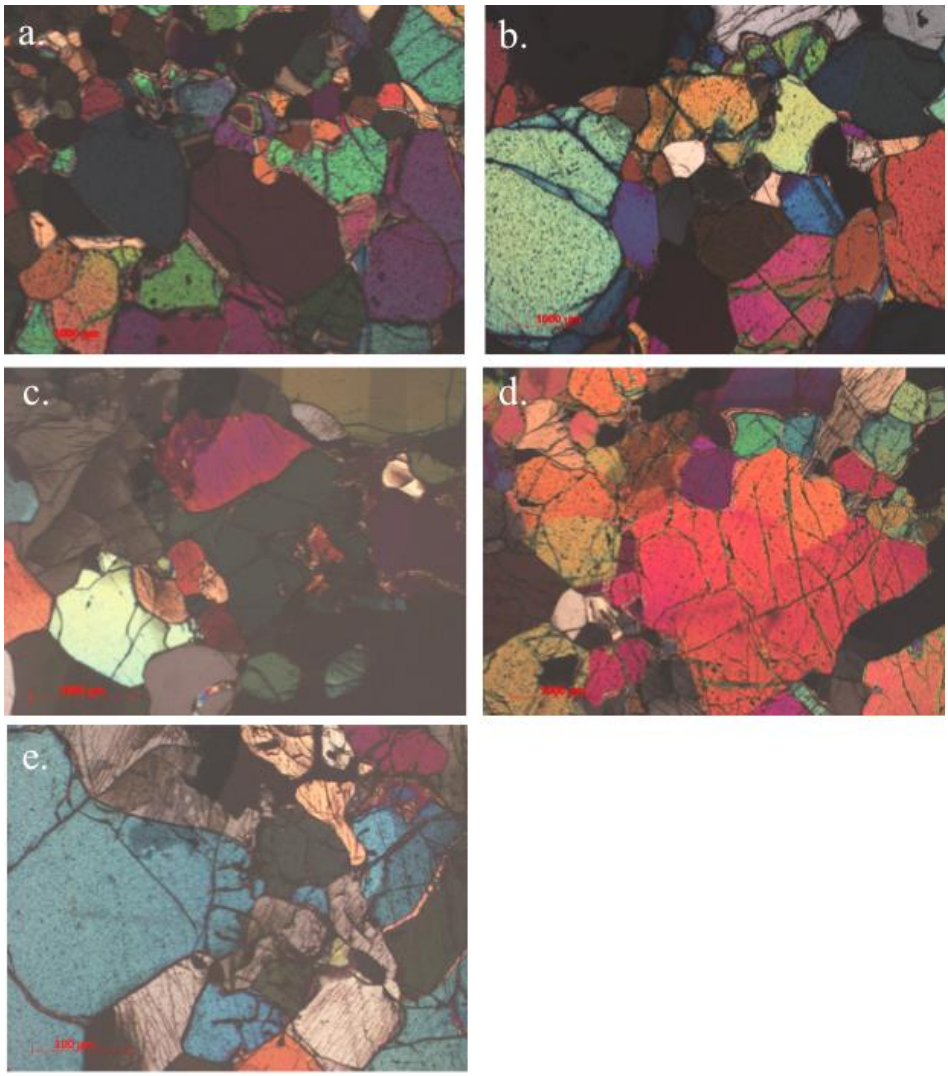

Figure C.1. Crossed nicols images of thin sections from sample MH.1 (a), MH.2 (b), MB.71.7 (c), MB.71.8 (d) and MB.71.9 (d).

Sample MH.1 in hand-specimen is pale green in colour, with average grain-size of ~1mm. The bulk majority of the grains are identified as olivine and orthopyroxene, clinopyroxene and spinel grains are observed. In thin-section the minerals seem to appear unaltered and ~2% of the olivine crystals present small (< 50 μm) spinel inclusions. The modal abundances are approximately 80% olivine of sizes that generally exceed 1 mm, 10% orthopyroxene of ~500 μm, 5% clinopyroxene of 200 to 500 μm and 5% spinel < 200 μm in size. Grains of spinel and clinopyroxene appear generally surrounded by bigger crystals of olivine and orthopyroxene.

Sample MH.2 in hand-specimen is darker green in colour with a hint of brown on some of the crystals indicative of superficial serpentine alteration. The average grain-size is ~500μm. Crystals of olivine, orthopyroxene, clinopyroxene and spinel are identified. In thin-section most of the minerals appear unaltered confirming that the serpentine alteration observed in hand-specimen was mostly superficial although small amount of orthopyroxene crystals (~1%) present fractures with mild serpentine alteration (grains that presented alteration were not analysed for He isotopic composition). The modal abundances are approximately 48% olivine of sizes that range from 500 μm to > 1 mm, 48 % orthopyroxene of the same size than olivine, 3% clinopyroxene of < 400 μm and 1% spinel < 200 μm. Grains of spinel and clinopyroxene appear generally surrounded by bigger crystals of olivine and orthopyroxene.

MB.71.7 in hand-specimen presents olivine grains that dominate the mineral suite conferring a pale green colour to the specimen. Crystals present sizes of up to 1mm with orthopyroxene, clinopyroxene and spinel also visible in the sample. In thin-section most of the minerals appear unaltered and free of inclusions. The modal abundances are approximately 64% olivine of sizes > 1 mm, 30 % orthopyroxene of the same size than olivine, 5% clinopyroxene of 300 to 400 μm and 1% spinel < 200 μm. Grains of spinel and clinopyroxene appear generally surrounded by bigger crystals of olivine and orthopyroxene.

MB.71.8 in hand-specimen presents pale green crystals of olivine and orthopyroxene with clinopyroxene and spinel in smaller quantities. In thin-section most of the minerals appear unaltered and free of inclusions. The modal abundances are approximately 60% olivine of sizes > 500 μm, 35 % orthopyroxene > 500 μm, 3% clinopyroxene of 200 to 400 μm and 2% spinel < 300 μm. Grains of spinel and

clinopyroxene appear generally surrounded by bigger crystals of olivine and orthopyroxene.

Sample MB.71.9 in hand-specimen appears darker green in colour with a hint of brown indicative of superficial serpentine alteration. The average grain-size is ~1 mm. Crystals of olivine and orthopyroxene are identified and clinopyroxene and spinel appear to be more abundant than in other specimens. In thin-section most of the minerals appear unaltered confirming that the serpentine alteration observed in hand-specimen was mostly superficial. The modal abundances are approximately 50% olivine > 1 mm, 35 % orthopyroxene of the same size than olivine, 12% clinopyroxene of 200 to 500 μm and 3% spinel of up to 400 μm. Grains of spinel and clinopyroxene appear generally surrounded by bigger crystals of olivine and orthopyroxene.

Sample MB.71.10 in hand-specimen is mostly pale green in colour, dominated by olivine and orthopyroxene crystals with small proportion (~5%) of clinopyroxene also visible in the specimen. The grain size for the olivine and orthopyroxene is ~500 μm and ~300 μm for clinopyroxene crystals.

Crystals of olivine, orthopyroxene, clinopyroxene and spinel were already separated from specimen MM when the sample arrived to SUERC. The olivine and orthopyroxene are of sizes ~500 μm with clinopyroxene and spinel crystals of ~200 μm.

C.2. Major element analysis

Major element compositional analyses of all the samples used for assessment of the chemical control on cosmogenic He and Ne production rates were performed using scanning electron microscope analysis (SEM) generating semi-quantitative analysis of all the samples and using a electron prove micro-analyser (EMPA) to provide precise quantitative analysis. Samples were carbon-coated by vacuum evaporation to 250 Angstroms to render them electrically conductive.

C.2.1 SEM

Scanning electron microscope analyses (SEM) of olivine, clinopyroxene, orthopyroxene and spinel from all the Mount Hampton samples were carried out using the Carl Zeiss Sigma field emission SEM at the Imaging Spectroscopy and Analysis Centre (ISAAC) at University of Glasgow. An accelerating voltage of 15 kV with a resolution of 1.5 nm and a current of 20 nA were used. Counting time was 30 seconds per element peak. Iron is reported as FeO and assumed to exist as Fe^{2+}. Data from the measurement of 3 points per grain (one in the centre of the mineral, two in the rim) over 5 to 10 grains per mineral separate are reported in Table C.1. Images of the grains are presented in Figure C.2.

C.2.2. EPMA

Electron prove micro-analysis (EPMA) of olivine, clinopyroxene, orthopyroxene and spinel from samples MH.1, MH.2, MB.71.7, MB.71.8 and MB.71.9 were carried out using the Cameca SX1000 Electron prove micro-analyser at University of Edinburgh. An accelerating voltage of 15 kV and a beam current of 35 nA were used. Counting time was 30 seconds per element peak and 10 seconds on two backgrounds on each side of the peak position. Detection limits are better than 0.05 elemental weight %. Iron is reported as FeO and assumed to exist as Fe^{2+}. Synthetic and natural mineral standards were used. Data from the measurement of 3 points per grain (one in the centre of the mineral, two in the rim) over 5 grains per mineral separate are reported in Table C.2.

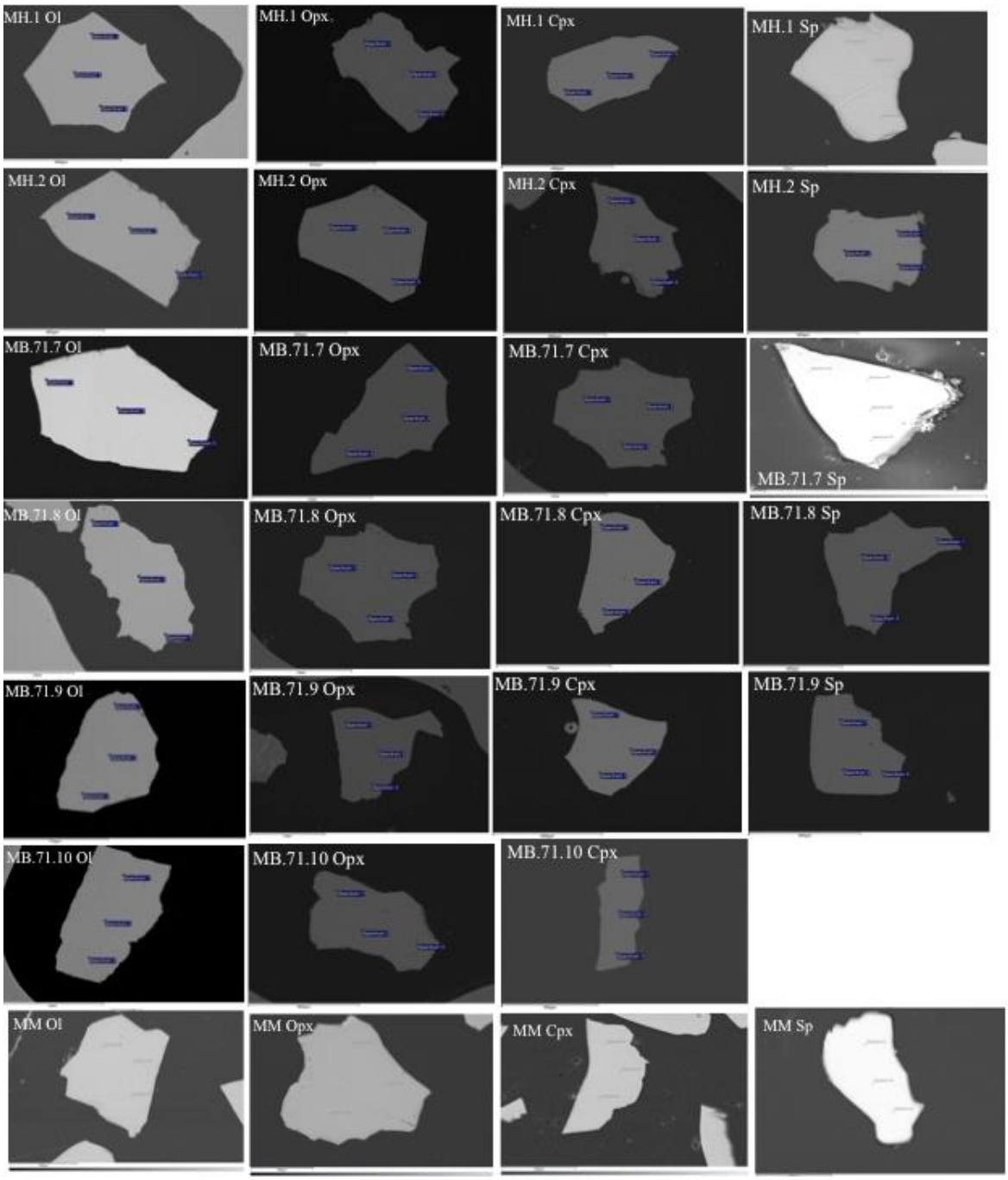

Figure C.2. Backscatter SEM images of one grain of each mineral analysed. Olivine (Ol), orthopyroxene (Opx), clinopyroxene (Cpx) and spinel (Sp) were present in all the samples with the exception of MB.71.10 that didn't present any spinel grains**.**

Table C.1. Semi-quantitative major element contents expressed in oxide wt % of olivine, clinopyroxene, orthopyroxene and spinel separates from SEM analysis of Mount Hampton xenoliths. The Mg content is expressed as Fo(100*Mg/Mg+Fe) in the case of olivine; En(100*Mg/Mg+Fe+Ca) for clinopyroxene and orthopyroxene and Sp(100*Mg/(Mg+Fe+Cr) for spinel

Sample	*Grain*	*MgO*	*FeO*	*SiO_2*	*CaO*	*Na_2O*	*Al_2O_3*	*NiO*	*Cr_2O_3*	*Sum*	*Mg (%)*
Olivine											***Fo***
MH.1	1.1	49.00	8.98	40.95						98.93	90.68
MH.1	1.2	48.75	8.90	41.18						98.84	90.71
MH.1	1.3	49.13	9.08	41.01						99.23	90.60
MH.1	2.1	48.97	8.81	40.97						98.75	90.83
MH.1	2.2	48.72	8.97	41.20						98.89	90.64
MH.1	2.3	32.57	5.76	55.00						93.34	90.97
MH.1	3.1	48.95	8.99	40.86						98.81	90.66
MH.1	3.2	48.97	9.10	40.97						99.03	90.56
MH.1	3.3	49.00	9.07	41.16						99.23	90.59
MH.1	4.1	48.97	8.93	40.82						98.72	90.72
MH.1	4.2	48.77	8.92	41.31						99.00	90.70
MH.1	4.3	48.75	8.99	41.38						99.12	90.62
MH.1	5.1	48.62	8.93	40.93						98.48	90.66
MH.1	5.2	48.79	9.11	41.03						98.93	90.52
MH.1	5.3	49.13	9.11	41.23						99.47	90.58
Average		*47.81*	*8.78*	*42.00*						*98.48*	*90.67*
1σ		*4.22*	*0.84*	*3.60*						*1.64*	*0.12*
MH.2	1.1	48.74	8.66	40.61						98.00	90.94
MH.2	1.2	48.50	8.59	40.43						97.53	90.96
MH.2	1.3	48.92	8.72	41.03						98.68	90.91
MH.2	2.1	48.80	8.57	40.99						98.36	91.03
MH.2	2.2	51.31	11.63	44.67						107.61	88.72
MH.2	2.3	48.72	9.03	41.72						99.47	90.58
MH.2	3.1	48.87	8.66	40.80						98.33	90.96
MH.2	3.2	48.80	8.83	40.91						98.53	90.79
MH.2	3.3	48.95	9.03	41.61						99.59	90.62
MH.2	4.1	32.00	5.54	54.17	1.01		4.59		0.50	97.81	91.14
MH.2	4.2	32.09	5.52	54.23	1.04		4.53		0.58	98.00	91.20
MH.2	4.3	32.09	5.61	54.60	0.97		4.69		0.58	98.53	91.07
MH.2	5.1	48.72	8.92	41.03						98.67	90.69
MH.2	5.2	48.72	8.90	41.16						98.78	90.70
MH.2	5.3	48.82	8.81	41.12						98.75	90.80
Average		*45.60*	*8.34*	*43.94*						*99.37*	*90.69*
1σ		*7.04*	*1.62*	*5.47*						*2.64*	*0.66*
MB.71.7	1.1	48.82	9.04	40.95				0.39		99.21	90.59
MB.71.7	1.2	48.60	8.93	40.97				0.39		98.90	90.66
MB.71.7	1.3	48.70	8.77	40.93				0.39		98.80	90.82
MB.71.7	2.1	48.50	8.97	40.65				0.53		98.65	90.60
MB.71.7	2.2	48.57	8.58	40.65				0.48		98.28	90.98
MB.71.7	2.3	48.70	8.80	41.14						98.64	90.80
MB.71.7	3.1	48.85	9.01	41.05				0.53		99.45	90.63
MB.71.7	3.2	49.08	8.84	41.14				0.48		99.55	90.83
MB.71.7	3.3	47.39	7.42	38.68				0.31		93.80	91.92
MB.71.7	4.1	47.97	7.91	39.99				0.48		96.36	91.53
MB.71.7	4.2	48.22	8.02	39.92				0.43		96.59	91.47
MB.71.7	4.3	48.70	8.97	40.84						98.51	90.64
MB.71.7	5.1	48.65	9.04	40.82				0.33		98.85	90.56
MB.71.7	5.2	50.81	11.00	44.03				0.52		106.36	89.17
MB.71.7	5.3	48.97	8.77	40.93				0.46		99.13	90.87
MB.71.7	6.1	48.79	9.01	40.99						98.78	90.62
MB.71.7	6.2	48.95	8.79	40.97				0.38		99.09	90.85
MB.71.7	6.3	48.69	8.85	41.38				0.37		99.28	90.75
MB.71.7	7.1	48.74	8.59	40.67				0.43		98.43	91.00
MB.71.7	7.2	48.67	9.01	41.01				0.56		99.25	90.60
MB.71.7	7.3	48.74	8.67	40.67				0.38		98.46	90.92
MB.71.7	8.1	48.57	8.67	40.84				0.48		98.57	90.90
MB.71.7	8.2	48.95	8.94	40.86				0.43		99.19	90.71
MB.71.7	8.3	48.80	9.03	41.03				0.38		99.25	90.59
MB.71.7	9.1	48.24	9.46	42.57				0.43		100.70	90.09
MB.71.7	9.2	48.80	8.94	41.10				0.43		99.27	90.68
MB.71.7	9.3	48.07	9.82	43.09				0.53		101.51	89.72
MB.71.7	10.1	48.54	9.04	40.97						98.55	90.54
MB.71.7	10.2	48.75	9.06	40.99						98.80	90.56
MB.71.7	10.3	48.90	9.21	41.03				0.45		99.59	90.44
Average		*48.69*	*8.91*	*41.03*				*0.44*		*98.99*	*90.70*
1σ		*0.53*	*0.59*	*0.92*				*0.07*		*1.92*	*0.49*

Sample	*Grain*	*MgO*	*FeO*	*SiO_2*	*CaO*	*Na_2O*	*Al_2O_3*	*NiO*	*Cr_2O_3*	*Sum*	*Mg (%)*
MB.71.8	1.1	48.75	8.90	40.82				0.57		99.05	90.71
MB.71.8	1.2	48.95	8.93	40.88				0.42		99.18	90.72
MB.71.8	1.3	48.99	9.04	41.31				0.38		99.72	90.61
MB.71.8	2.1	48.92	8.86	41.16				0.41		99.35	90.77
MB.71.8	2.2	48.01	7.77	39.73				0.41		95.91	91.68
MB.71.8	2.3	45.35	8.61	42.64			3.36			99.96	90.38
MB.71.8	3.1	49.15	8.75	40.97				0.45		99.31	90.92
MB.71.8	3.2	48.79	8.53	40.99				0.47		98.78	91.07
MB.71.8	3.3	50.46	11.50	44.09				0.50		106.55	88.66
MB.71.8	4.1	49.17	9.07	41.03				0.53		99.81	90.62
MB.71.8	4.2	49.17	9.15	41.78				0.43		100.53	90.55
MB.71.8	4.3	48.75	8.40	41.10				0.39		98.65	91.19
MB.71.8	5.1	48.82	8.62	41.29						98.73	90.99
MB.71.8	5.2	49.90	10.46	42.40				0.55		103.31	89.48
MB.71.8	5.3	49.02	9.29	41.76				0.42		100.49	90.39
Average		*48.81*	*9.06*	*41.46*				*0.46*		*100.12*	*90.56*
1σ		*1.10*	*0.88*	*1.00*				*0.06*		*2.64*	*0.80*
MB.71.9	1.1	47.31	10.76	40.56				0.43		99.06	88.69
MB.71.9	1.2	47.39	10.15	40.13				0.41		98.09	89.27
MB.71.9	1.3	47.63	10.73	40.63				0.34		99.33	88.78
MB.71.9	2.1	47.14	10.11	40.37				0.37		98.00	89.26
MB.71.9	2.2	47.19	10.38	40.07				0.37		98.02	89.01
MB.71.9	2.3	47.58	10.11	40.33				0.39		98.41	89.35
MB.71.9	3.1	47.38	10.50	40.58				0.45		98.90	88.94
MB.71.9	3.2	47.31	10.45	40.50				0.38		98.64	88.98
MB.71.9	3.3	47.44	10.56	40.39				0.50		98.89	88.90
MB.71.9	4.1	47.18	10.42	40.58				0.37		98.55	88.97
MB.71.9	4.2	47.16	10.41	40.41				0.38		98.36	88.98
MB.71.9	4.3	47.39	10.73	40.67						98.79	88.73
MB.71.9	5.1	47.28	10.23	40.69						98.20	89.18
MB.71.9	5.2	47.53	10.47	40.61				0.45		99.05	89.00
MB.71.9	5.3	47.18	10.09	40.13				0.42		97.82	89.29
Average		*47.34*	*10.41*	*40.44*				*0.40*		*98.47*	*89.05*
1σ		*0.16*	*0.23*	*0.20*				*0.04*		*0.40*	*0.18*
MB.71.10	1.1	48.22	9.62	40.26				0.45		98.55	89.93
MB.71.10	1.2	48.04	9.74	40.54				0.32		98.64	89.79
MB.71.10	1.3	48.19	9.78	40.76				0.34		99.07	89.78
MB.71.10	2.1	48.17	9.89	40.54						98.61	89.67
MB.71.10	2.2	47.74	9.43	40.76				0.55		98.47	90.02
MB.71.10	2.3	48.06	9.66	40.67						98.39	89.86
MB.71.10	3.1	46.96	9.73	39.99				0.32		96.99	89.59
MB.71.10	3.2	47.26	10.51	40.54						98.31	88.91
MB.71.10	3.3	47.38	10.33	40.37				0.56		98.64	89.10
MB.71.10	4.1	48.17	9.70	40.63				0.42		98.92	89.85
MB.71.10	4.2	48.24	9.64	40.73						98.61	89.92
MB.71.10	4.3	47.99	9.57	40.78						98.34	89.94
MB.71.10	5.1	48.12	9.89	40.67						98.69	89.66
MB.71.10	5.2	48.12	9.62	40.48				0.46		98.68	89.91
MB.71.10	5.3	48.02	9.88	41.10						99.00	89.65
Average		*47.91*	*9.80*	*40.59*				*0.43*		*98.47*	*89.67*
1σ		*0.40*	*0.28*	*0.26*				*0.10*		*0.51*	*0.34*
MM	1.1	52.05	9.38	42.96						104.39	90.82
MM	1.2	51.94	9.76	43.39						105.09	90.46
MM	1.3	51.85	9.92	43.94						105.72	90.31
MM	2.1	51.80	9.47	42.92						104.19	90.70
MM	2.2	51.92	9.35	42.98						104.25	90.82
MM	2.3	52.07	10.10	43.62						105.79	90.19
MM	3.1	51.75	9.49	43.09						104.34	90.67
MM	3.2	51.72	9.76	43.58						105.07	90.42
MM	3.3	52.02	10.06	43.39						105.47	90.21
MM	4.1	51.72	8.94	42.96						103.62	91.16
MM	4.2	51.85	9.91	43.32						105.08	90.32
MM	4.3	51.67	9.17	43.24						104.08	90.94
MM	5.1	51.61	9.20	42.79						103.59	90.91
MM	5.2	51.67	9.52	43.13						104.32	90.63
MM	5.3	51.80	9.66	43.66						105.13	90.53
Average		*51.83*	*9.58*	*43.26*						*104.58*	*90.63*
1σ		*0.15*	*0.34*	*0.33*						*0.71*	*0.30*
Clinopyroxene											***En***
MH.1	1.1	16.04	2.51	51.05	20.61	0.97	4.46		1.27	96.90	49.71
MH.1	1.2	16.12	2.59	51.02	20.71	0.97	4.52		1.20	97.12	49.67
MH.1	1.3	15.82	2.56	51.52	20.68	1.06	4.52		1.17	97.33	49.25

Sample	*Grain*	*MgO*	*FeO*	*SiO_2*	*CaO*	*Na_2O*	*Al_2O_3*	*NiO*	*Cr_2O_3*	*Sum*	*Mg (%)*
MH.1	2.1	16.02	2.56	51.24	20.85	1.08	4.57		1.08	97.40	49.38
MH.1	2.2	16.05	2.55	51.13	20.54	0.96	4.69		1.20	97.11	49.78
MH.1	2.3	15.97	2.52	51.13	20.64	0.98	4.61		1.17	97.02	49.57
MH.1	3.1	15.92	2.44	51.02	20.49	1.11	4.69		1.13	96.79	49.73
MH.1	3.2	16.15	2.50	51.11	20.54	1.12	4.50		1.10	97.01	49.98
MH.1	3.3	15.97	2.47	50.92	20.78	1.04	4.63		1.20	97.00	49.46
MH.1	4.1	16.09	2.57	51.37	20.63	0.92	4.69		1.20	97.45	49.72
MH.1	4.2	15.82	2.46	51.17	20.72	1.09	4.57		1.13	96.96	49.30
MH.1	4.3	16.12	2.53	51.05	20.35	1.08	4.57		1.13	96.82	50.12
MH.1	5.1	16.15	2.47	50.92	20.49	1.09	4.53		1.18	96.83	50.07
MH.1	5.2	16.02	2.56	50.94	20.67	1.13	4.63		1.17	97.12	49.58
MH.1	5.3	16.14	2.56	51.45	21.35	1.06	4.59		1.26	98.41	49.02
Average		*16.03*	*2.52*	*51.14*	*20.67*	*1.04*	*4.58*		*1.17*	*97.16*	*49.64*
1σ		*0.11*	*0.05*	*0.19*	*0.23*	*0.07*	*0.07*		*0.05*	*0.45*	*0.33*
MH.2	1.1	16.04	2.73	50.81	20.49	0.96	5.40		0.77	97.19	49.66
MH.2	1.2	15.75	2.74	50.72	20.60	1.16	5.40		0.94	97.31	49.09
MH.2	1.3	15.79	2.70	50.87	20.67	1.08	5.33		0.95	97.39	49.09
MH.2	2.1	15.90	2.62	51.00	20.11	1.09	5.61		1.01	97.35	49.97
MH.2	2.2	15.85	2.53	50.34	20.46	1.04	5.31		0.91	96.44	49.58
MH.2	2.3	15.77	2.61	50.60	20.44	1.11	5.56		1.04	97.12	49.39
MH.2	3.1	15.90	2.77	50.38	20.21	1.06	5.50		0.94	96.76	49.73
MH.2	3.2	15.90	2.62	50.25	20.14	1.02	5.56		1.04	96.53	49.94
MH.2	3.3	15.85	2.68	50.77	20.46	0.98	5.50		1.07	97.30	49.45
MH.2	4.1	15.94	2.71	50.38	20.12	1.02	5.61		1.05	96.84	49.92
MH.2	4.2	16.00	2.65	50.72	20.30	1.13	5.29		1.02	97.13	49.88
MH.2	4.3	15.85	2.77	50.79	20.61	1.11	5.52		0.89	97.53	49.21
MH.2	5.1	16.07	2.66	50.83	20.29	1.12	5.61		0.96	97.55	49.99
MH.2	5.2	15.74	2.57	51.05	20.43	1.09	5.46		1.02	97.36	49.39
MH.2	5.3	15.85	2.51	51.02	20.64	1.02	5.33		1.07	97.45	49.40
Average		*15.88*	*2.66*	*50.70*	*20.40*	*1.07*	*5.47*		*0.98*	*97.11*	*49.65*
1σ		*0.10*	*0.08*	*0.26*	*0.19*	*0.06*	*0.12*		*0.08*	*0.38*	*0.28*
MB.71.7	1.1	15.37	2.35	50.45	19.42	1.60	5.37		1.11	95.68	50.15
MB.71.7	1.2	15.17	2.50	50.64	20.02	1.47	5.54		1.24	96.58	49.00
MB.71.7	1.3	15.32	2.39	50.94	20.30	1.42	5.40		1.32	97.09	49.02
MB.71.7	2.1	15.14	2.15	50.32	19.83	1.56	5.25		1.23	95.48	49.48
MB.71.7	2.2	15.19	2.51	50.51	19.84	1.50	5.42		1.33	96.30	49.23
MB.71.7	2.3	15.36	2.60	50.79	19.95	1.47	5.57		1.20	96.94	49.29
MB.71.7	3.1	15.12	2.24	50.79	20.08	1.56	5.37		1.11	96.27	49.09
MB.71.7	3.2	15.31	2.53	50.66	20.00	1.52	5.44		1.34	96.81	49.22
MB.71.7	3.3	15.42	2.43	51.43	20.32	1.70	5.57		1.08	97.96	49.13
MB.71.7	4.1	15.42	2.32	51.05	19.88	1.52	5.37		1.20	96.75	49.73
MB.71.7	4.2	15.29	2.41	50.94	20.14	1.58	5.35		1.23	96.92	49.15
MB.71.7	4.3	15.22	2.70	50.68	20.14	1.42	5.42		1.21	96.79	48.78
MB.71.7	5.1	15.44	2.48	50.87	19.62	1.43	5.48		1.13	96.45	49.91
MB.71.7	5.2	15.32	2.47	50.79	20.09	1.52	5.48		1.24	96.92	49.19
MB.71.7	5.3	15.27	2.65	51.17	20.19	1.46	5.63		1.15	97.53	48.84
Average		*15.29*	*2.45*	*50.80*	*19.99*	*1.52*	*5.44*		*1.21*	*96.76*	*49.25*
1σ		*0.10*	*0.15*	*0.29*	*0.24*	*0.08*	*0.10*		*0.08*	*0.63*	*0.33*
MB.71.8	1.1	16.55	2.35	51.43	21.14	0.62	7.37		2.10	101.57	50.05
MB.71.8	1.2	16.62	2.38	51.28	21.18	0.58	7.26		1.81	101.11	50.08
MB.71.8	1.3	16.78	2.29	51.11	21.14	0.61	7.41		2.25	101.59	50.45
MB.71.8	2.1	16.57	2.33	51.17	21.07	0.63	7.41		2.10	101.29	50.17
MB.71.8	2.2	16.75	2.37	51.77	21.20	0.66	7.18		2.22	102.15	50.28
MB.71.8	2.3	16.73	2.38	51.24	21.37	0.54	7.44		2.05	101.75	50.06
MB.71.8	3.1	16.77	2.26	50.90	21.17	0.59	7.37		1.90	100.96	50.42
MB.71.8	3.2	16.58	2.39	51.43	21.28	0.55	7.33		2.25	101.82	49.92
MB.71.8	3.3	16.63	2.35	51.58	21.51	0.61	7.37		2.22	102.27	49.78
MB.71.8	4.1	16.81	2.23	50.75	20.96	0.57	7.41		1.84	100.56	50.76
MB.71.8	4.2	16.83	2.39	50.87	21.38	0.55	7.37		2.25	101.65	50.18
MB.71.8	4.3	16.75	2.52	51.20	21.21	0.58	7.71		2.46	102.42	50.13
Average		*16.70*	*2.35*	*51.23*	*21.22*	*0.59*	*7.38*		*2.12*	*101.60*	*50.19*
1σ		*0.10*	*0.08*	*0.30*	*0.15*	*0.04*	*0.13*		*0.19*	*0.55*	*0.26*
MB.71.9	1.1	14.59	2.63	50.00	19.80	1.78	6.56		0.61	95.97	48.16
MB.71.9	1.2	14.38	2.76	49.87	19.55	1.74	6.50		0.79	95.58	47.96
MB.71.9	1.3	14.46	2.79	49.74	19.35	1.81	6.75		0.67	95.56	48.31
MB.71.9	2.1	14.28	2.62	50.21	19.88	1.64	6.65		0.64	95.93	47.53
MB.71.9	2.2	14.69	2.86	49.98	19.63	1.69	6.63		0.88	96.36	48.32
MB.71.9	2.3	14.64	2.90	49.74	19.65	1.67	6.71		0.77	96.09	48.18
MB.71.9	3.1	14.48	2.84	49.93	19.49	1.70	6.61		0.72	95.77	48.13
MB.71.9	3.2	14.53	2.60	50.43	19.95	1.77	6.73		0.83	96.83	47.90
MB.71.9	3.3	14.34	2.79	50.36	20.04	1.71	6.58		0.73	96.55	47.33
MB.71.9	4.1	14.58	2.79	49.76	19.60	1.69	6.59		0.67	95.68	48.22

Sample	*Grain*	*MgO*	*FeO*	*SiO_2*	*CaO*	*Na_2O*	*Al_2O_3*	*NiO*	*Cr_2O_3*	*Sum*	*Mg (%)*
MB.71.9	4.2	14.49	3.21	50.25	20.32	1.56	6.46		0.75	97.04	46.91
MB.71.9	4.3	14.51	2.80	50.32	19.84	1.71	6.42		0.86	96.47	47.82
MB.71.9	5.1	14.48	2.81	49.74	19.70	1.75	6.50		0.79	95.77	47.91
MB.71.9	5.2	14.34	2.79	50.06	19.86	1.79	6.75		0.77	96.36	47.53
MB.71.9	5.3	14.39	2.66	50.08	19.67	1.67	6.46		0.76	95.70	47.94
Average		*14.48*	*2.79*	*50.03*	*19.76*	*1.71*	*6.59*		*0.75*	*96.21*	*47.81*
1σ		*0.12*	*0.15*	*0.24*	*0.24*	*0.06*	*0.11*		*0.08*	*0.46*	*0.42*
MB.71.10	1.1	14.87	2.71	49.72	19.56	1.77	5.69		1.23	95.55	48.84
MB.71.10	1.2	14.84	2.71	50.60	19.74	1.73	5.91		1.48	97.01	48.58
MB.71.10	1.3	14.74	2.89	49.93	19.44	1.67	5.80		1.58	96.05	48.60
MB.71.10	2.1	15.09	2.79	50.34	18.78	1.75	5.74		1.14	95.63	50.05
MB.71.10	2.2	15.01	2.66	50.15	19.58	1.67	5.84		1.29	96.19	49.09
MB.71.10	2.3	15.07	2.70	51.11	19.65	1.81	5.73		1.36	97.42	49.09
MB.71.10	3.1	15.26	2.55	50.23	18.85	1.71	5.63		1.45	95.67	50.47
MB.71.10	3.2	15.14	2.62	49.81	18.51	1.78	5.57		1.36	94.79	50.61
MB.71.10	3.3	15.07	2.72	49.42	18.95	1.79	5.65		1.26	94.86	49.88
MB.71.10	4.1	14.79	2.79	49.57	18.95	1.91	5.76		1.34	95.12	49.35
MB.71.10	4.2	14.66	2.69	49.74	19.02	1.78	5.74		1.45	95.07	49.14
MB.71.10	4.3	14.99	2.63	50.06	19.45	1.81	5.80		1.45	96.19	49.24
MB.71.10	5.1	14.89	2.66	49.91	19.24	1.82	5.76		1.30	95.59	49.29
MB.71.10	5.2	15.11	2.65	50.40	19.14	1.77	5.80		1.42	96.28	49.78
MB.71.10	5.3	14.87	2.76	50.36	19.23	1.73	5.69		1.33	95.97	49.19
Average		*14.96*	*2.70*	*50.09*	*19.20*	*1.77*	*5.74*		*1.36*	*95.73*	*49.60*
1σ		*0.17*	*0.08*	*0.44*	*0.36*	*0.06*	*0.09*		*0.11*	*0.75*	*0.55*
MM	1.1	17.81	2.62	55.58	22.39	0.00	3.97		1.21	103.58	50.35
MM	1.2	17.83	2.41	55.07	22.79	0.77	3.74		1.24	103.85	50.13
MM	1.3	17.73	2.65	54.94	23.03	0.77	4.01		1.42	104.54	49.56
MM	2.1	17.81	2.69	54.79	22.28	0.78	3.87		1.23	103.45	50.41
MM	2.2	17.79	2.73	55.05	22.08	0.84	4.08		1.23	103.79	50.56
MM	2.3	17.68	2.70	55.67	22.88	0.00	4.04		1.52	104.49	49.61
MM	3.1	18.17	2.69	55.00	22.18	0.00	4.02		1.23	103.30	51.02
MM	3.2	17.63	2.79	54.96	22.65	0.75	3.93		1.29	104.01	49.69
MM	3.3	17.86	2.77	55.52	23.02	0.00	3.93		1.30	104.39	49.67
MM	4.1	17.84	2.65	54.58	21.46	0.80	4.04		1.36	102.73	51.34
MM	4.2	17.81	2.62	55.24	22.30	0.00	3.99		1.36	103.32	50.44
MM	4.3	17.74	2.60	55.26	22.74	0.84	4.10		1.36	104.64	49.92
MM	5.1	17.84	2.77	55.05	22.01	0.84	4.02		1.34	103.87	50.67
MM	5.2	17.94	2.64	54.88	21.94	0.00	3.99		1.33	102.71	50.99
MM	5.3	17.63	2.74	55.05	23.00	0.81	4.02		1.43	104.68	49.38
MM	6.1	18.01	2.55	54.17	20.93	0.00	3.95		1.29	100.89	52.23
MM	6.2	17.88	2.52	54.75	21.62	0.81	3.84		1.30	102.71	51.33
MM	6.3	17.82	2.65	55.03	22.31	0.47	3.97		1.32	103.59	50.42
Average		*17.82*	*2.65*	*55.03*	*22.31*	*0.47*	*3.97*		*1.32*	*103.59*	*50.43*
1σ		*0.13*	*0.10*	*0.36*	*0.58*	*0.39*	*0.09*		*0.08*	*0.93*	*0.75*
Orthopyroxene											***En***
MH.1	1.1	32.55	5.57	55.17	0.98		3.78		0.56	98.61	89.48
MH.1	1.2	32.47	5.36	54.47	0.95		3.57		0.66	97.48	89.79
MH.1	1.3	32.50	5.57	54.94	0.91		3.70		0.64	98.27	89.58
MH.1	2.1	32.39	5.66	54.83	0.84		3.95		0.56	98.22	89.55
MH.1	2.2	32.70	5.75	54.94	0.99		3.82		0.67	98.87	89.25
MH.1	2.3	32.55	5.76	54.98	0.92		3.87		0.73	98.83	89.31
MH.1	3.1	32.40	5.27	54.79	0.95		3.78		0.67	97.87	89.89
MH.1	3.2	32.35	5.48	54.70	1.02		3.67		0.60	97.82	89.47
MH.1	3.3	32.44	5.79	54.62	1.04		3.84		0.60	98.31	89.04
MH.1	4.1	32.20	6.21	56.97	1.13		4.10		0.67	101.30	88.22
MH.1	4.2	32.65	5.61	54.90	0.90		3.80		0.61	98.46	89.60
MH.1	4.3	32.42	5.70	55.03	1.02		3.61		0.63	98.40	89.18
MH.1	5.1	32.54	5.53	55.07	0.92		3.74		0.77	98.57	89.62
MH.1	5.2	32.49	5.44	54.28	1.01		3.87		0.75	97.83	89.58
MH.1	5.3	32.60	5.60	54.92	0.92		3.72		0.75	98.51	89.55
Average		*32.48*	*5.62*	*54.97*	*0.97*		*3.79*		*0.66*	*98.58*	*89.36*
1σ		*0.13*	*0.22*	*0.60*	*0.07*		*0.13*		*0.07*	*0.92*	*0.43*
MB.71.7	1.1	32.55	5.60	54.85	0.81		3.97		0.51	98.29	89.74
MB.71.7	1.2	32.30	5.30	54.45	0.80		4.08		0.51	97.44	90.11
MB.71.7	1.3	32.25	5.53	54.92	0.81		3.70		0.63	97.85	89.74
MB.71.7	2.1	32.70	5.47	54.77	0.81		3.95		0.32	98.02	89.96
MB.71.7	2.2	32.44	5.47	54.88	0.84		4.06		0.00	97.68	89.83
MB.71.7	2.3	32.67	5.79	55.15	0.91		3.91		0.00	98.43	89.33
MB.71.7	3.1	32.75	5.43	54.60	0.80		3.95		0.56	98.08	90.05
MB.71.7	3.2	32.49	5.73	55.39	0.84		4.02		0.50	98.96	89.49
MB.71.7	3.3	32.63	5.54	54.98	0.87		3.78		0.51	98.32	89.73
MB.71.7	4.1	32.70	5.42	55.13	0.83		3.89		0.64	98.61	90.00

Sample	*Grain*	*MgO*	*FeO*	*SiO_2*	*CaO*	*Na_2O*	*Al_2O_3*	*NiO*	*Cr_2O_3*	*Sum*	*Mg (%)*
MB.71.7	4.2	32.49	6.01	55.82	0.84		3.93		0.69	99.77	89.10
MB.71.7	4.3	32.55	5.69	55.17	0.80		3.84		0.63	98.68	89.64
MB.71.7	5.1	32.29	5.60	54.77	0.81		3.84		0.64	97.94	89.66
MB.71.7	5.2	32.45	5.78	54.85	0.76		4.01		0.67	98.52	89.56
MB.71.7	5.3	32.24	5.57	55.28	0.78		4.23		0.54	98.65	89.73
Average		*32.50*	*5.59*	*55.00*	*0.82*		*3.94*		*0.49*	*98.47*	*89.67*
1σ		*0.17*	*0.18*	*0.34*	*0.04*		*0.13*		*0.22*	*0.55*	*0.28*
MB.71.8	1.1	32.50	5.47	55.28	1.01		3.46		0.61	98.33	89.55
MB.71.8	1.2	32.42	5.42	54.51	0.94		3.34		0.54	97.17	89.73
MB.71.8	1.3	32.65	5.39	55.05	0.87		3.48		0.61	98.05	89.95
MB.71.8	2.1	32.68	5.65	54.96	0.99		3.46		0.76	98.50	89.38
MB.71.8	2.2	32.60	5.58	55.07	0.95		3.42		0.73	98.36	89.52
MB.71.8	2.3	32.49	5.20	54.75	0.92		3.44		0.56	97.35	90.07
MB.71.8	3.1	32.57	5.42	54.85	0.95		3.42		0.66	97.87	89.74
MB.71.8	3.2	32.72	5.31	54.98	0.92		3.36		0.57	97.87	89.98
MB.71.8	3.3	33.08	5.29	55.30	0.95		3.21		0.70	98.54	90.06
MB.71.8	4.1	32.65	5.56	54.75	0.85		3.50		0.75	98.05	89.74
MB.71.8	4.2	32.78	5.38	55.17	0.95		3.50		0.58	98.37	89.86
MB.71.8	4.3	32.62	5.65	55.26	0.91		3.46		0.61	98.51	89.51
MB.71.8	5.1	32.85	5.53	55.56	0.94		3.29		0.64	98.81	89.69
MB.71.8	5.2	32.73	5.62	54.81	0.92		3.29		0.61	97.99	89.56
MB.71.8	5.3	32.39	5.48	55.43	1.02		3.48		0.53	98.32	89.48
Average		*32.65*	*5.46*	*55.05*	*0.94*		*3.41*		*0.63*	*98.21*	*89.72*
1σ		*0.18*	*0.14*	*0.29*	*0.05*		*0.09*		*0.07*	*0.40*	*0.24*
MB.71.9	1.1	31.52	6.83	55.17	0.91		4.91		0.51	99.86	87.54
MB.71.9	1.2	31.23	6.79	54.06	0.76		5.18		0.41	98.42	87.76
MB.71.9	1.3	31.72	6.54	53.89	0.76		4.78		0.37	98.05	88.29
MB.71.9	2.1	31.71	6.93	54.36	0.70		4.69		0.00	98.39	87.83
MB.71.9	2.2	31.11	6.88	54.15	1.04		4.74		0.34	98.25	87.11
MB.71.9	2.3	31.61	6.54	54.28	0.71		4.59		0.39	98.12	88.32
MB.71.9	3.1	31.34	6.82	53.70	0.81		4.61		0.31	97.59	87.67
MB.71.9	3.2	31.54	6.70	54.13	0.73		4.52		0.34	97.95	88.04
MB.71.9	3.3	31.74	6.74	54.30	0.74		4.55		0.00	98.07	88.03
MB.71.9	4.1	31.81	6.64	53.66	0.77		4.59		0.00	97.46	88.15
MB.71.9	4.2	31.59	6.66	53.85	0.73		4.69		0.00	97.52	88.11
MB.71.9	4.3	31.57	6.72	54.00	0.71		4.55		0.45	98.01	88.06
MB.71.9	5.1	32.42	10.72	63.01	1.05		4.87		0.00	112.07	82.73
MB.71.9	5.2	31.62	6.72	54.17	0.71		4.44		0.31	97.97	88.08
MB.71.9	5.3	31.57	6.72	54.83	0.66		4.59		0.41	98.78	88.16
Average		*31.61*	*7.00*	*54.77*	*0.79*		*4.69*		*0.26*	*99.18*	*87.52*
1σ		*0.29*	*1.04*	*2.31*	*0.12*		*0.19*		*0.19*	*4.07*	*1.54*
MB.71.10	1.1	32.10	6.18	54.98	0.77		3.82		0.54	98.39	88.88
MB.71.10	1.2	31.86	6.33	54.62	0.83		3.82		0.66	98.10	88.49
MB.71.10	1.3	32.29	6.09	55.03	0.78		3.70		0.64	98.53	89.03
MB.71.10	2.1	32.17	5.98	53.87	0.73		3.57		0.50	96.82	89.24
MB.71.10	2.2	31.92	6.24	54.47	0.77		3.55		0.53	97.48	88.73
MB.71.10	2.3	32.09	6.12	54.77	0.90		3.70		0.56	98.13	88.72
MB.71.10	3.1	32.29	6.12	54.30	0.81		3.72		0.57	97.81	88.93
MB.71.10	3.2	32.09	6.10	54.88	0.87		3.74		0.53	98.20	88.81
MB.71.10	3.3	31.94	6.05	54.66	0.84		3.74		0.64	97.87	88.88
MB.71.10	4.1	31.89	6.14	54.13	0.78		3.80		0.61	97.35	88.84
MB.71.10	4.2	31.91	6.12	54.38	0.81		3.78		0.64	97.65	88.81
MB.71.10	4.3	32.15	6.24	54.73	0.81		3.85		0.60	98.38	88.73
MB.71.10	5.1	32.15	5.92	54.79	0.87		3.65		0.64	98.02	89.08
MB.71.10	5.2	32.05	6.07	54.51	0.77		3.95		0.53	97.88	89.01
MB.71.10	5.3	32.00	6.11	55.09	0.81		3.72		0.60	98.34	88.86
Average		*32.06*	*6.12*	*54.61*	*0.81*		*3.74*		*0.59*	*97.83*	*88.89*
1σ		*0.14*	*0.10*	*0.34*	*0.04*		*0.10*		*0.05*	*0.45*	*0.16*
MM	1.1	34.76	5.83	58.17	1.05		3.44		0.77	104.02	89.62
MM	1.2	34.99	5.83	58.13	1.05		3.42		0.83	104.25	89.69
MM	1.3	35.11	5.92	59.18	1.13		3.57		0.86	105.77	89.46
MM	2.1	34.76	5.71	57.78	0.98		3.50		0.77	103.50	89.89
MM	2.2	34.71	5.76	58.58	1.04		3.38		0.80	104.27	89.72
MM	2.3	34.69	6.16	59.15	1.20		3.55		0.82	105.58	88.92
MM	3.1	34.79	5.75	58.08	1.15		3.53		0.80	104.11	89.57
MM	3.2	34.61	5.83	58.81	1.12		3.55		0.82	104.74	89.47
MM	3.3	34.86	5.98	59.03	1.15		3.38		0.77	105.17	89.29
MM	4.1	35.17	6.05	58.64	1.08		3.36		0.64	104.94	89.41
MM	4.2	34.96	6.01	59.39	1.12		3.40		0.79	105.66	89.33
MM	4.3	34.84	6.21	59.28	1.16		3.53		0.76	105.79	88.97
MM	5.1	34.51	5.84	58.79	1.06		3.55		0.91	104.66	89.52
MM	5.2	34.54	6.09	58.75	1.13		3.50		0.76	104.76	89.09

Sample	*Grain*	*MgO*	*FeO*	*SiO_2*	*CaO*	*Na_2O*	*Al_2O_3*	*NiO*	*Cr_2O_3*	*Sum*	*Mg (%)*
MM	5.3	34.79	5.98	58.58	1.12		3.53		0.79	104.79	89.32
MM	6.1	34.89	6.06	59.24	1.12		3.63		0.79	105.73	89.25
MM	6.2	35.14	5.92	58.73	1.12		3.55		0.75	105.20	89.50
MM	6.3	34.62	5.69	58.41	1.08		3.51		0.82	104.13	89.73
MM	6.4	34.82	5.92	58.71	1.10		3.49		0.79	104.84	89.43
Average		*34.82*	*5.92*	*58.71*	*1.10*		*3.49*		*0.79*	*104.84*	*89.43*
1σ		*0.19*	*0.15*	*0.45*	*0.05*		*0.08*		*0.05*	*0.68*	*0.26*
Spinel											***Sp***
MH.1	1.1	21.21	10.90				54.21		17.09	103.40	66.59
MH.1	1.2	21.16	11.36				54.64		17.93	105.10	65.53
MH.1	1.3	21.19	11.86				54.25		18.43	105.73	64.74
MH.1	2.1	21.16	10.94				54.68		17.48	104.26	66.27
MH.1	2.2	20.93	12.04				54.55		18.94	106.46	63.99
MH.1	2.3	20.98	11.33				54.46		18.36	105.12	65.14
MH.1	3.1	21.47	11.67				54.12		18.08	105.34	65.44
MH.1	3.2	21.54	11.08				54.29		17.44	104.34	66.53
MH.1	3.3	21.18	11.55				54.19		18.40	105.32	65.08
MH.1	4.1	21.28	10.87				54.38		16.92	103.45	66.77
MH.1	4.2	21.14	11.39				54.21		17.61	104.35	65.66
MH.1	4.3	20.41	11.68				54.47		18.66	105.23	63.96
MH.1	5.1	21.08	11.27				54.23		18.24	104.82	65.38
MH.1	5.2	21.26	11.44				54.59		17.90	105.19	65.57
MH.1	5.3	20.83	11.44				54.55		18.09	104.91	65.00
MH.1	6.1	20.33	10.99				55.21		18.08	104.61	64.98
MH.1	6.2	19.95	11.55				55.00		18.05	104.56	63.91
MH.1	6.3	20.56	11.27				54.66		17.90	104.40	65.00
MH.1	7.1	20.94	11.46				54.21		17.79	104.40	65.26
MH.1	7.2	21.16	11.91				54.38		18.53	105.99	64.60
MH.1	7.3	21.19	11.71				54.40		18.27	105.57	65.00
MH.1	8.1	21.52	11.21				54.08		17.41	104.21	66.38
MH.1	8.2	21.49	11.60				54.29		17.92	105.30	65.62
MH.1	8.3	21.49	11.90				54.04		18.27	105.70	65.10
MH.1	9.1	20.98	11.14				54.51		17.36	103.99	65.90
MH.1	9.2	20.96	11.62				54.30		18.39	105.27	64.79
MH.1	9.3	20.94	11.85				54.61		18.90	106.30	64.24
MH.1	9.4	21.05	11.45				54.43		18.02	104.94	65.27
Average		*21.05*	*11.45*				*54.43*		*18.02*	*104.94*	*65.28*
1σ		*0.37*	*0.32*				*0.27*		*0.50*	*0.76*	*0.78*
MB.71.7	1.1	21.57	6.66				51.05		13.59	92.89	74.61
MB.71.7	1.2	21.62	6.59				50.85		13.15	92.21	75.06
MB.71.7	2.1	21.57	7.00				51.75		14.25	94.58	73.68
MB.71.7	2.2	21.52	7.40				51.96		15.45	96.33	72.30
MB.71.7	2.3	21.57	6.91				51.40		14.11	94.00	73.90
Average		*19.93*	*9.25*				*49.76*		*15.57*	*94.47*	*63.86*
1σ		*5.42*	*3.33*				*13.77*		*4.62*	*26.49*	*17.95*
MM	1.1	18.97	12.89				37.75		33.22	102.83	54.18
MM	1.2	18.47	13.26				37.56		36.61	105.91	51.86
MM	1.3	18.52	12.78				37.71		35.56	104.57	52.74
MM	2.1	18.77	12.52				37.58		36.90	105.78	52.76
MM	2.2	18.27	13.33				37.87		36.67	106.14	51.51
MM	2.3	18.61	12.75				38.26		35.54	105.16	52.88
MM	3.1	18.44	12.79				38.07		34.05	103.36	53.23
MM	3.2	18.39	12.88				37.88		35.25	104.41	52.60
MM	3.3	18.46	13.15				37.81		35.97	105.38	52.18
MM	4.1	18.64	12.62				38.13		34.78	104.17	53.34
MM	4.2	18.61	13.02				37.85		34.83	104.30	52.94
MM	5.1	18.69	12.92				38.39		35.66	105.66	52.81
MM	5.2	18.19	13.23				37.36		36.96	105.73	51.37
MM	5.3	18.61	12.65				37.71		35.76	104.73	52.88
MM	6.1	17.91	13.82				36.83		38.18	106.73	50.05
MM	6.2	18.31	13.79				37.05		36.92	106.07	51.09
Average		*18.49*	*13.02*				*37.74*		*35.81*	*105.06*	*52.40*
1σ		*0.25*	*0.39*				*0.41*		*1.24*	*1.07*	*1.01*

Table C.2. Major element contents expressed in oxide wt % of olivine, clinopyroxene, orthopyroxene and spinel separates from EPMA of Mount Hampton xenoliths. The Mg content is expressed as Fo(100*Mg/Mg+Fe) in the case of olivine; En(100*Mg/Mg+Fe+Ca) for clinopyroxene and orthopyroxene and Sp(100*Mg/(Mg+Fe+Cr) for spinel.

Sample	*Grain*	*MgO*	*FeO*	*SiO_2*	*CaO*	*P_2O_5*	*TiO_2*	*MnO*	*Na_2O*	*Al_2O_3*	*NiO*	*Cr_2O_3*	*Sum*	*Mg(%)*
Olivine														***Fo***
MH.1	1.1	51.07	9.18	38.48	0.08	0.00	0.00	0.13	0.01	0.02	0.41		99.37	90.84
MH.1	1.2	50.49	9.22	40.50	0.08	0.00	0.01	0.11	0.00	0.02	0.41		100.84	90.70
MH.1	1.3	50.66	8.91	38.98	0.07	0.00	0.00	0.13	0.01	0.03	0.40		99.19	91.02
MH.1	2.1	50.55	8.72	40.12	0.08	0.01	0.00	0.13	0.01	0.02	0.39		100.02	91.17
MH.1	2.2	50.51	9.03	39.09	0.07	0.00	0.00	0.11	0.00	0.02	0.40		99.25	90.88
MH.1	2.3	50.15	9.15	39.37	0.08	0.01	0.01	0.12	0.01	0.02	0.41		99.33	90.72
MH.1	3.1	50.50	8.83	39.28	0.07	0.00	0.00	0.12	0.01	0.02	0.40		99.24	91.07
MH.1	3.2	50.33	8.47	38.89	0.08	0.01	0.00	0.12	0.01	0.02	0.41		98.35	91.38
MH.1	3.3	50.49	9.13	39.50	0.07	0.01	0.00	0.12	0.01	0.02	0.39		99.74	90.79
MH.1	4.1	50.93	8.95	38.80	0.08	0.00	0.00	0.12	0.00	0.02	0.40		99.32	91.02
MH.1	4.2	50.53	8.97	39.38	0.08	0.01	0.00	0.12	0.00	0.02	0.40		99.51	90.94
MH.1	4.3	50.43	8.73	38.73	0.08	0.01	0.00	0.13	0.00	0.02	0.41		98.53	91.15
Average		*50.55*	*8.94*	*39.26*	*0.08*	*0.01*	*0.00*	*0.12*	*0.00*	*0.02*	*0.40*		*99.39*	*90.97*
1σ		*0.25*	*0.22*	*0.58*	*0.00*	*0.00*	*0.00*	*0.01*	*0.00*	*0.00*	*0.01*		*0.64*	*0.20*
MH.2	1.1	50.52	8.62	40.25	0.08	0.01	0.01	0.12	0.00	0.03	0.41		100.05	91.27
MH.2	1.2	50.77	9.12	40.14	0.09	0.00	0.00	0.13	0.01	0.03	0.43		100.71	90.85
MH.2	1.3	50.20	9.07	40.68	0.09	0.01	0.01	0.11	0.01	0.02	0.44		100.64	90.79
MH.2	2.1	50.02	9.26	40.39	0.08	0.00	0.00	0.12	0.01	0.02	0.42		100.34	90.59
MH.2	2.2	50.35	8.71	39.95	0.08	0.01	0.01	0.13	0.00	0.03	0.43		99.70	91.16
MH.2	2.3	49.81	8.61	41.29	0.09	0.00	0.00	0.12	0.01	0.02	0.40		100.36	91.16
MH.2	3.1	50.22	8.77	40.53	0.08	0.00	0.01	0.11	0.01	0.03	0.43		100.20	91.08
MH.2	3.2	50.27	8.60	40.72	0.08	0.00	0.00	0.12	0.01	0.03	0.42		100.25	91.24
MH.2	3.3	49.77	9.17	40.68	0.08	0.01	0.00	0.13	0.00	0.03	0.41		100.28	90.63
MH.2	4.1	50.01	9.00	41.61	0.09	0.01	0.01	0.14	0.00	0.03	0.41		101.31	90.83
MH.2	4.2	50.48	9.09	41.03	0.08	0.01	0.01	0.12	0.01	0.02	0.42		101.26	90.82
MH.2	4.3	50.47	8.72	40.92	0.08	0.01	0.01	0.13	0.00	0.02	0.42		100.78	91.17
Average		*50.24*	*8.90*	*40.68*	*0.09*	*0.01*	*0.01*	*0.12*	*0.01*	*0.03*	*0.42*		*100.49*	*90.97*
1σ		*0.30*	*0.25*	*0.48*	*0.00*	*0.00*	*0.00*	*0.01*	*0.00*	*0.00*	*0.01*		*0.47*	*0.24*
MB.71.7	1.1	51.12	8.59	38.68	0.07	0.01	0.00	0.13	0.00	0.01	0.41		99.04	91.39
MB.71.7	1.2	50.74	9.20	38.46	0.07	0.01	0.00	0.12	0.00	0.02	0.40		99.03	90.77
MB.71.7	1.3	50.44	8.76	38.67	0.07	0.01	0.00	0.13	0.00	0.02	0.41		98.50	91.12
MB.71.7	2.1	50.75	8.99	38.30	0.07	0.01	0.01	0.12	0.01	0.02	0.40		98.68	90.96
MB.71.7	2.2	50.64	9.05	39.06	0.07	0.00	0.04	0.13	0.01	0.02	0.39		99.41	90.89
MB.71.7	2.3	50.44	8.97	38.93	0.07	0.01	0.00	0.14	0.00	0.02	0.41		98.99	90.93
MB.71.7	3.1	51.27	9.04	39.19	0.07	0.01	0.00	0.13	0.01	0.03	0.41		100.15	91.00
MB.71.7	3.2	50.47	9.45	40.19	0.07	0.00	0.01	0.12	0.01	0.02	0.40		100.74	90.49
MB.71.7	3.3	50.62	9.08	38.96	0.07	0.00	0.01	0.14	0.01	0.02	0.39		99.30	90.86
MB.71.7	4.1	50.59	9.05	40.41	0.07	0.00	0.01	0.11	0.00	0.03	0.41		100.68	90.88
MB.71.7	4.2	50.54	9.57	39.06	0.07	0.01	0.00	0.12	0.00	0.02	0.40		99.80	90.40
MB.71.7	4.3	50.87	9.08	39.17	0.07	0.01	0.00	0.11	0.00	0.02	0.42		99.76	90.90
MB.71.7	5.1	51.00	9.19	39.40	0.07	0.01	0.00	0.12	0.00	0.02	0.40		100.22	90.82
MB.71.7	5.2	50.59	8.77	39.23	0.07	0.01	0.00	0.15	0.00	0.02	0.42		99.27	91.14
MB.71.7	5.3	50.55	9.33	39.12	0.08	0.01	0.02	0.13	0.01	0.02	0.41		99.66	90.62
Average		*50.71*	*9.07*	*39.12*	*0.07*	*0.01*	*0.01*	*0.13*	*0.00*	*0.02*	*0.41*		*99.55*	*90.88*
1σ		*0.25*	*0.26*	*0.57*	*0.00*	*0.00*	*0.01*	*0.01*	*0.00*	*0.00*	*0.01*		*0.68*	*0.25*
MB.71.8	1.1	50.54	9.00	41.23	0.09	0.00	0.00	0.13	0.00	0.02	0.40		101.42	90.92
MB.71.8	1.2	50.65	8.80	40.55	0.08	0.01	0.00	0.12	0.00	0.01	0.42		100.65	91.12
MB.71.8	1.3	50.11	8.37	40.95	0.08	0.01	0.01	0.13	0.00	0.01	0.42		100.09	91.43
MB.71.8	2.1	50.38	8.89	40.39	0.08	0.01	0.00	0.13	0.00	0.02	0.43		100.33	90.99
MB.71.8	2.2	50.50	8.65	41.37	0.08	0.00	0.00	0.13	0.00	0.02	0.42		101.18	91.23
MB.71.8	2.3	50.36	8.97	41.41	0.08	0.00	0.00	0.13	0.00	0.02	0.39		101.37	90.92
MB.71.8	3.1	50.43	8.70	40.85	0.08	0.01	0.00	0.12	0.01	0.02	0.40		100.63	91.17
MB.71.8	3.2	50.71	8.78	40.89	0.08	0.00	0.00	0.11	0.00	0.02	0.40		100.99	91.15
MB.71.8	3.3	50.78	8.97	40.87	0.09	0.00	0.00	0.14	0.01	0.02	0.40		101.28	90.99
MB.71.8	4.1	50.39	8.66	41.45	0.08	0.01	0.00	0.11	0.00	0.02	0.41		101.13	91.21
MB.71.8	4.2	51.01	8.48	40.90	0.09	0.01	0.01	0.14	0.01	0.02	0.42		101.08	91.47
MB.71.8	4.3	50.51	9.08	41.60	0.08	0.00	0.00	0.13	0.00	0.02	0.40		101.83	90.84
MB.71.8	5.1	50.71	8.84	41.51	0.08	0.00	0.00	0.13	0.00	0.02	0.39		101.70	91.09
MB.71.8	5.2	50.20	8.85	41.62	0.08	0.01	0.00	0.14	0.01	0.02	0.41		101.34	91.00
MB.71.8	5.3	50.00	8.77	40.54	0.09	0.01	0.01	0.13	0.00	0.02	0.41		99.97	91.04
Average		*50.49*	*8.79*	*41.08*	*0.08*	*0.01*	*0.00*	*0.13*	*0.00*	*0.02*	*0.41*		*101.00*	*91.10*
1σ		*0.27*	*0.19*	*0.41*	*0.00*	*0.00*	*0.00*	*0.01*	*0.00*	*0.00*	*0.01*		*0.56*	*0.18*
MB.71.9	1.1	50.46	10.77	38.58	0.06	0.01	0.01	0.14	0.00	0.01	0.38		100.43	89.31
MB.71.9	1.2	49.24	11.33	38.87	0.06	0.02	0.01	0.15	0.00	0.02	0.38		100.07	88.57
MB.71.9	1.3	48.86	10.55	39.59	0.07	0.00	0.01	0.14	0.00	0.02	0.37		99.60	89.20
MB.71.9	2.1	49.61	10.44	38.99	0.06	0.02	0.01	0.14	0.01	0.02	0.39		99.68	89.44

Sample	*Grain*	*MgO*	*FeO*	*SiO_2*	*CaO*	*P_2O_5*	*TiO_2*	*MnO*	*Na_2O*	*Al_2O_3*	*NiO*	*Cr_2O_3*	*Sum*	*Mg(%)*
MB.71.9	2.2	48.21	10.95	40.22	0.06	0.02	0.01	0.14	0.01	0.01	0.38		100.02	88.69
MB.71.9	2.3	48.74	10.03	40.38	0.06	0.02	0.01	0.14	0.01	0.02	0.39		99.79	89.65
MB.71.9	3.1	49.40	10.47	39.65	0.06	0.02	0.00	0.14	0.01	0.02	0.38		100.15	89.37
MB.71.9	3.2	48.75	10.61	39.27	0.06	0.01	0.00	0.15	0.00	0.02	0.38		99.25	89.12
MB.71.9	3.3	49.10	10.47	39.85	0.06	0.01	0.00	0.15	0.00	0.02	0.37		100.03	89.31
MB.71.9	4.1	48.42	10.47	39.62	0.06	0.02	0.01	0.15	0.00	0.02	0.37		99.12	89.18
MB.71.9	4.2	49.13	10.11	37.98	0.06	0.01	0.01	0.14	0.00	0.02	0.38		97.84	89.65
MB.71.9	4.3	48.99	10.81	40.02	0.06	0.01	0.01	0.13	0.00	0.01	0.38		100.42	88.98
MB.71.9	5.1	49.32	10.83	39.31	0.06	0.01	0.00	0.13	0.00	0.02	0.37		100.06	89.03
MB.71.9	5.2	48.57	10.56	40.16	0.06	0.01	0.00	0.14	0.01	0.01	0.38		99.91	89.13
MB.71.9	5.3	49.39	10.75	39.54	0.06	0.02	0.00	0.14	0.00	0.01	0.39		100.31	89.12
Average		*49.08*	*10.61*	*39.47*	*0.06*	*0.01*	*0.01*	*0.14*	*0.00*	*0.02*	*0.38*		*99.78*	*89.18*
1σ		*0.55*	*0.32*	*0.66*	*0.00*	*0.00*	*0.00*	*0.01*	*0.00*	*0.00*	*0.01*		*0.66*	*0.30*
Clinopyroxene														***En***
MH.1	1.1	17.55	2.68	51.43	21.08	0.00	0.10	0.08	1.06	4.58	0.07		98.63	51.31
MH.1	1.2	17.13	2.37	51.83	21.18	0.00	0.10	0.10	1.02	4.64	0.06		98.43	50.85
MH.1	1.3	17.09	2.44	53.26	21.20	0.00	0.10	0.09	1.02	4.70	0.05		99.93	50.72
MH.1	2.1	16.88	2.83	51.88	21.34	0.00	0.10	0.09	1.00	4.63	0.05		98.80	49.94
MH.1	2.2	16.76	2.33	51.39	21.42	0.01	0.10	0.07	1.00	4.59	0.06		97.71	50.08
MH.1	2.3	17.14	2.57	52.47	21.36	0.00	0.10	0.09	1.03	4.63	0.06		99.44	50.51
MH.1	3.1	16.87	2.38	52.24	21.44	0.01	0.10	0.09	1.02	4.60	0.06		98.81	50.18
MH.1	3.2	16.81	2.58	52.43	21.19	0.00	0.10	0.08	1.01	4.57	0.06		98.83	50.20
MH.1	3.3	17.04	2.60	51.67	21.43	0.01	0.09	0.06	1.00	4.55	0.06		98.50	50.27
MH.1	4.1	16.91	2.62	52.40	21.36	0.00	0.10	0.08	1.01	4.62	0.06		99.15	50.13
MH.1	4.2	16.85	2.47	52.25	20.99	0.00	0.10	0.07	1.01	4.53	0.05		98.32	50.58
MH.1	4.3	17.30	2.70	51.86	21.57	0.01	0.10	0.09	1.02	4.52	0.05		99.23	50.41
MH.1	5.1	17.41	2.37	51.87	21.18	0.01	0.09	0.09	1.04	4.51	0.05		98.61	51.27
MH.1	5.2	16.51	2.25	52.13	21.33	0.00	0.09	0.08	1.00	4.58	0.05		98.03	49.88
MH.1	5.3	16.79	2.38	52.52	21.24	0.00	0.10	0.08	0.98	4.62	0.05		98.76	50.29
Average		*17.00*	*2.50*	*52.11*	*21.29*	*0.00*	*0.10*	*0.08*	*1.01*	*4.59*	*0.05*		*98.75*	*50.44*
1σ		*0.27*	*0.16*	*0.48*	*0.15*	*0.00*	*0.00*	*0.01*	*0.02*	*0.05*	*0.01*		*0.55*	*0.44*
MH.2	1.1	16.61	3.01	52.02	21.12	0.01	0.15	0.06	1.03	5.52	0.05		99.57	49.62
MH.2	1.2	16.74	2.68	52.28	21.06	0.00	0.16	0.08	1.05	5.54	0.05		99.64	50.16
MH.2	1.3	16.45	2.70	52.56	20.82	0.00	0.16	0.07	1.03	5.46	0.05		99.29	49.97
MH.2	2.1	16.94	2.64	51.86	20.93	0.00	0.16	0.08	1.04	5.55	0.05		99.25	50.62
MH.2	2.2	16.69	2.86	52.79	20.71	0.01	0.16	0.08	1.04	5.51	0.05		99.91	50.31
MH.2	2.3	16.50	2.76	52.14	21.19	0.01	0.16	0.09	1.02	5.51	0.03		99.39	49.58
MH.2	3.1	16.49	2.55	52.30	20.90	0.01	0.16	0.08	1.04	5.48	0.05		99.06	50.06
MH.2	3.2	16.46	2.67	51.89	21.12	0.00	0.17	0.08	1.04	5.52	0.05		99.00	49.67
MH.2	3.3	16.49	2.64	52.66	21.05	0.00	0.16	0.09	1.04	5.54	0.05		99.72	49.81
MH.2	4.1	16.56	2.74	51.86	20.87	0.00	0.16	0.09	1.04	5.50	0.06		98.88	50.04
MH.2	4.2	16.69	2.78	52.01	21.00	0.00	0.15	0.08	1.03	5.47	0.05		99.27	50.06
MH.2	4.3	16.58	2.62	52.30	21.06	0.01	0.15	0.07	1.04	5.52	0.05		99.40	49.96
MH.2	5.1	16.91	2.75	51.84	21.04	0.00	0.16	0.06	1.04	5.46	0.06		99.33	50.36
MH.2	5.2	16.75	2.71	52.02	20.93	0.01	0.15	0.08	1.04	5.45	0.05		99.18	50.27
MH.2	5.3	16.34	2.66	52.35	21.08	0.01	0.16	0.08	1.02	5.46	0.05		99.21	49.54
Average		*16.61*	*2.72*	*52.19*	*20.99*	*0.00*	*0.16*	*0.08*	*1.04*	*5.50*	*0.05*		*99.34*	*50.00*
1σ		*0.17*	*0.11*	*0.30*	*0.13*	*0.00*	*0.00*	*0.01*	*0.01*	*0.03*	*0.01*		*0.28*	*0.32*
MB.71.7	1.1	16.22	2.27	51.18	20.67	0.00	0.31	0.08	1.47	5.49	0.04		97.72	50.13
MB.71.7	1.2	16.19	2.52	51.47	21.10	0.00	0.31	0.09	1.45	5.41	0.06		98.60	49.41
MB.71.7	1.3	15.88	2.53	52.50	20.69	0.00	0.33	0.07	1.41	5.49	0.04		98.93	49.37
MB.71.7	2.1	16.14	2.46	51.52	20.55	0.00	0.33	0.08	1.45	5.54	0.05		98.13	49.99
MB.71.7	2.2	16.10	2.80	51.31	21.10	0.00	0.33	0.07	1.45	5.53	0.06		98.76	49.03
MB.71.7	2.3	15.82	2.49	51.77	20.98	0.00	0.33	0.07	1.42	5.54	0.05		98.46	48.99
MB.71.7	3.1	16.70	2.38	51.85	21.22	0.00	0.32	0.08	1.45	5.39	0.05		99.44	50.18
MB.71.7	3.2	16.13	2.46	51.78	20.29	0.00	0.31	0.08	1.43	5.50	0.05		98.02	50.27
MB.71.7	3.3	15.79	2.15	51.24	20.65	0.00	0.31	0.09	1.40	5.51	0.05		97.19	49.60
MB.71.7	4.1	16.21	2.31	50.85	20.53	0.01	0.31	0.08	1.47	5.48	0.06		97.30	50.25
MB.71.7	4.2	15.96	2.31	51.36	20.94	0.00	0.32	0.08	1.47	5.50	0.04		97.98	49.40
MB.71.7	4.3	16.06	2.43	51.56	20.72	0.00	0.32	0.07	1.43	5.47	0.03		98.10	49.70
MB.71.7	5.1	16.26	2.50	51.30	20.63	0.00	0.31	0.09	1.44	5.37	0.06		97.97	50.04
MB.71.7	5.2	16.13	2.59	51.48	20.54	0.00	0.32	0.07	1.43	5.46	0.05		98.08	49.86
MB.71.7	5.3	15.96	2.37	52.23	20.46	0.00	0.32	0.07	1.41	5.59	0.05		98.45	49.88
Average		*16.10*	*2.44*	*51.56*	*20.74*	*0.00*	*0.32*	*0.08*	*1.44*	*5.48*	*0.05*		*98.21*	*49.74*
1σ		*0.22*	*0.15*	*0.42*	*0.27*	*0.00*	*0.01*	*0.01*	*0.02*	*0.06*	*0.01*		*0.59*	*0.43*
MB.71.8	1.1	17.69	2.50	53.34	22.39	0.00	0.05	0.09	0.56	3.63	0.06		100.31	50.28
MB.71.8	1.2	17.32	2.15	52.96	22.25	0.00	0.06	0.09	0.56	3.64	0.05		99.08	50.18
MB.71.8	1.3	17.36	2.40	52.92	22.58	0.00	0.06	0.08	0.56	3.63	0.04		99.64	49.69
MB.71.8	2.1	17.36	2.32	52.56	22.24	0.00	0.05	0.06	0.57	3.67	0.06		98.88	50.11
MB.71.8	2.2	17.34	2.22	52.93	22.35	0.00	0.05	0.09	0.57	3.67	0.06		99.27	50.04
MB.71.8	2.3	17.39	2.38	54.00	22.42	0.00	0.06	0.08	0.58	3.78	0.06		100.76	49.92
MB.71.8	3.1	17.78	2.30	53.32	22.52	0.00	0.06	0.09	0.58	3.69	0.06		100.41	50.43

Sample	*Grain*	*MgO*	*FeO*	*SiO_2*	*CaO*	*P_2O_5*	*TiO_2*	*MnO*	*Na_2O*	*Al_2O_3*	*NiO*	*Cr_2O_3*	*Sum*	*Mg(%)*
MB.71.8	3.2	17.62	2.15	52.24	22.29	0.01	0.06	0.09	0.58	3.68	0.06		98.77	50.55
MB.71.8	3.3	17.50	2.38	52.98	22.28	0.00	0.05	0.09	0.57	3.69	0.05		99.59	50.22
MB.71.8	4.1	17.59	2.48	52.12	21.92	0.00	0.06	0.07	0.58	3.68	0.05		98.56	50.64
MB.71.8	4.2	17.39	2.35	52.46	22.08	0.00	0.05	0.08	0.58	3.69	0.05		98.73	50.30
MB.71.8	4.3	17.88	2.47	53.16	21.91	0.00	0.06	0.09	0.58	3.73	0.06		99.94	51.07
MB.71.8	5.1	18.09	2.46	52.86	22.09	0.00	0.05	0.07	0.60	3.63	0.05		99.90	51.17
MB.71.8	5.2	17.75	2.54	53.66	22.08	0.00	0.06	0.09	0.58	3.78	0.05		100.60	50.65
MB.71.8	5.3	17.39	2.51	52.44	21.82	0.00	0.06	0.08	0.56	3.63	0.05		98.52	50.44
Average		*17.56*	*2.37*	*52.93*	*22.21*	*0.00*	*0.06*	*0.08*	*0.57*	*3.68*	*0.05*		*99.53*	*50.38*
1σ		*0.23*	*0.13*	*0.52*	*0.23*	*0.00*	*0.00*	*0.01*	*0.01*	*0.05*	*0.01*		*0.77*	*0.40*
MB.71.9	1.1	15.34	2.96	50.21	20.04	0.00	0.57	0.09	1.68	6.37	0.04		97.31	48.84
MB.71.9	1.2	14.99	2.83	51.65	20.40	0.00	0.58	0.08	1.64	6.66	0.04		98.88	47.99
MB.71.9	1.3	15.39	2.96	51.55	20.65	0.00	0.56	0.10	1.64	6.64	0.04		99.54	48.24
MB.71.9	2.1	15.58	3.09	50.51	20.11	0.00	0.56	0.07	1.68	6.51	0.05		98.16	49.04
MB.71.9	2.2	14.85	3.15	52.36	20.56	0.00	0.57	0.09	1.62	6.66	0.04		99.90	47.30
MB.71.9	3.1	15.79	3.04	51.35	20.60	0.00	0.56	0.09	1.69	6.42	0.04		99.57	48.90
MB.71.9	3.2	15.00	2.99	52.16	20.51	0.00	0.58	0.08	1.66	6.72	0.05		99.74	47.75
MB.71.9	3.3	15.19	2.74	51.77	20.39	0.00	0.56	0.07	1.61	6.51	0.05		98.90	48.42
MB.71.9	4.1	15.52	2.93	50.77	20.74	0.00	0.58	0.09	1.68	6.40	0.05		98.74	48.40
MB.71.9	4.2	14.97	2.76	51.79	20.49	0.00	0.56	0.11	1.63	6.63	0.05		98.99	47.91
MB.71.9	4.3	15.60	2.74	51.09	20.75	0.00	0.57	0.09	1.66	6.63	0.06		99.20	48.67
MB.71.9	5.1	15.69	2.90	51.33	20.37	0.00	0.56	0.09	1.71	6.50	0.05		99.21	49.10
MB.71.9	5.2	15.38	3.15	50.65	20.72	0.00	0.55	0.10	1.65	6.63	0.04		98.87	48.00
MB.71.9	5.3	15.17	3.01	51.53	20.58	0.00	0.55	0.08	1.59	6.60	0.04		99.15	47.93
Average		*15.31*	*2.76*	*47.95*	*19.14*	*0.00*	*0.53*	*0.08*	*1.54*	*6.13*	*0.04*		*92.46*	48.33
1σ		*0.29*	*0.74*	*13.14*	*5.24*	*0.00*	*0.14*	*0.02*	*0.42*	*1.69*	*0.01*		*25.38*	*12.38*
Orthopyroxene														***En***
MH.1	1.1	33.57	5.34	52.91	0.94	0.01	0.03	0.13	0.08	3.78	0.11		96.89	90.15
MH.1	1.2	33.96	5.66	52.60	0.93	0.00	0.04	0.13	0.08	3.75	0.10		97.25	89.83
MH.1	1.3	33.27	5.67	54.06	0.93	0.00	0.03	0.13	0.08	3.78	0.13		98.07	89.64
MH.1	2.1	33.55	5.37	53.43	0.93	0.00	0.04	0.12	0.08	3.85	0.10		97.48	90.11
MH.1	2.2	33.47	5.90	53.08	0.92	0.01	0.04	0.11	0.08	3.79	0.11		97.52	89.39
MH.1	2.3	33.39	5.63	52.37	0.93	0.00	0.04	0.14	0.08	3.75	0.11		96.44	89.71
MH.1	3.1	33.59	5.26	53.15	0.94	0.01	0.04	0.13	0.08	3.75	0.10		97.04	90.25
MH.1	3.2	33.71	5.56	53.19	0.92	0.00	0.03	0.11	0.07	3.74	0.10		97.44	89.92
MH.1	3.3	34.17	5.29	52.66	0.93	0.00	0.04	0.13	0.08	3.73	0.10		97.14	90.37
MH.1	4.1	33.74	5.69	55.36	0.94	0.01	0.03	0.12	0.08	3.85	0.11		99.93	89.72
MH.1	4.2	33.76	5.26	54.25	0.95	0.01	0.03	0.12	0.08	3.75	0.10		98.31	90.28
MH.1	4.3	34.03	5.75	53.40	0.94	0.00	0.03	0.12	0.08	3.79	0.11		98.25	89.71
MH.1	5.1	34.28	5.97	53.31	0.94	0.00	0.03	0.13	0.08	3.79	0.11		98.65	89.49
MH.1	5.2	33.31	5.47	54.32	0.94	0.00	0.03	0.13	0.08	3.74	0.11		98.14	89.90
MH.1	5.3	33.97	5.82	52.96	0.94	0.00	0.04	0.10	0.08	3.70	0.11		97.72	89.61
Average		*33.72*	*5.58*	*53.40*	*0.94*	*0.00*	*0.03*	*0.12*	*0.08*	*3.77*	*0.11*		*97.75*	*89.87*
1σ		*0.31*	*0.23*	*0.79*	*0.01*	*0.00*	*0.00*	*0.01*	*0.00*	*0.04*	*0.01*		*0.85*	*0.30*
MH.2	1.1	50.28	8.79	40.81	0.08	0.00	0.01	0.11	0.01	0.02	0.43		100.54	90.97
MH.2	1.2	50.65	8.75	40.54	0.08	0.01	0.00	0.12	0.00	0.02	0.43		100.60	91.07
MH.2	1.3	50.15	8.82	40.45	0.08	0.00	0.01	0.11	0.01	0.03	0.44		100.10	90.93
MH.2	2.1	49.94	8.71	40.69	0.09	0.00	0.01	0.13	0.00	0.02	0.42		100.02	90.98
MH.2	2.2	50.47	8.74	40.28	0.08	0.01	0.00	0.12	0.00	0.03	0.44		100.18	91.05
MH.2	2.3	50.48	8.61	40.37	0.08	0.00	0.00	0.11	0.01	0.03	0.42		100.10	91.18
MH.2	3.1	51.17	8.23	40.26	0.08	0.01	0.00	0.11	0.00	0.03	0.42		100.32	91.63
MH.2	3.2	49.86	8.89	40.82	0.08	0.01	0.00	0.11	0.01	0.03	0.41		100.22	90.81
MH.2	3.3	50.36	8.74	40.83	0.09	0.00	0.00	0.12	0.00	0.03	0.42		100.59	91.02
MH.2	4.1	50.27	8.18	41.08	0.09	0.00	0.01	0.12	0.01	0.02	0.41		100.19	91.53
MH.2	4.2	50.39	8.78	40.67	0.09	0.00	0.01	0.12	0.01	0.02	0.43		100.52	90.99
MH.2	4.3	50.39	9.03	40.42	0.09	0.00	0.00	0.13	0.00	0.03	0.42		100.51	90.77
MH.2	5.1	50.53	8.75	40.37	0.09	0.00	0.00	0.12	0.01	0.03	0.43		100.33	91.04
MH.2	5.2	50.78	9.30	41.18	0.09	0.00	0.01	0.11	0.01	0.03	0.44		101.94	90.58
MH.2	5.3	50.04	8.83	40.71	0.09	0.01	0.00	0.11	0.01	0.03	0.43		100.25	90.89
Average		*50.38*	*8.74*	*40.63*	*0.09*	*0.00*	*0.00*	*0.12*	*0.01*	*0.03*	*0.43*		*100.43*	*91.03*
1σ		*0.33*	*0.27*	*0.28*	*0.00*	*0.00*	*0.00*	*0.01*	*0.00*	*0.00*	*0.01*		*0.46*	*0.27*
MB.71.7	1.1	33.74	5.80	53.60	0.79	0.00	0.08	0.14	0.10	3.98	0.09		98.33	89.83
MB.71.7	1.2	33.87	5.68	53.68	0.82	0.00	0.09	0.11	0.11	3.94	0.10		98.40	89.98
MB.71.7	1.3	33.77	5.71	53.33	0.81	0.00	0.09	0.13	0.10	3.94	0.11		97.99	89.93
MB.71.7	2.1	34.14	5.64	53.44	0.80	0.01	0.09	0.13	0.10	4.07	0.11		98.52	90.14
MB.71.7	2.2	33.93	6.12	53.35	0.79	0.00	0.09	0.11	0.10	3.91	0.10		98.50	89.46
MB.71.7	2.3	34.07	5.60	52.77	0.86	0.00	0.09	0.12	0.11	3.97	0.10		97.69	90.05
MB.71.7	3.1	33.10	5.61	53.29	0.79	0.00	0.08	0.11	0.10	3.97	0.11		97.15	89.91
MB.71.7	3.2	34.32	5.36	53.98	0.80	0.00	0.08	0.13	0.11	3.89	0.10		98.77	90.56
MB.71.7	3.3	33.97	5.88	53.86	0.79	0.01	0.08	0.13	0.11	3.93	0.11		98.87	89.78
MB.71.7	4.1	34.10	5.53	52.30	0.82	0.01	0.09	0.14	0.10	3.89	0.10		97.07	90.23

Sample	*Grain*	*MgO*	*FeO*	*SiO_2*	*CaO*	*P_2O_5*	*TiO_2*	*MnO*	*Na_2O*	*Al_2O_3*	*NiO*	*Cr_2O_3*	*Sum*	*Mg(%)*
MB.71.7	4.2	33.82	6.02	53.55	0.80	0.00	0.08	0.13	0.10	3.86	0.11		98.48	89.53
MB.71.7	4.3	33.48	5.63	52.67	0.84	0.00	0.09	0.11	0.11	3.89	0.12		96.94	89.90
MB.71.7	5.1	32.82	5.56	53.80	0.84	0.00	0.09	0.14	0.11	3.92	0.10		97.38	89.81
MB.71.7	5.2	33.86	5.78	53.03	0.81	0.01	0.09	0.13	0.11	3.85	0.10		97.76	89.85
MB.71.7	5.3	33.43	5.41	52.92	0.81	0.00	0.09	0.13	0.10	3.80	0.11		96.80	90.24
Average		*33.76*	*5.69*	*53.31*	*0.81*	*0.00*	*0.09*	*0.13*	*0.10*	*3.92*	*0.10*		*97.91*	*89.95*
1σ		*0.40*	*0.21*	*0.48*	*0.02*	*0.00*	*0.00*	*0.01*	*0.00*	*0.06*	*0.01*		*0.70*	*0.28*
MB.71.8	1.1	33.84	5.78	55.33	0.97	0.00	0.02	0.12	0.04	3.37	0.11		99.59	89.56
MB.71.8	1.2	34.19	5.73	55.59	0.95	0.00	0.02	0.13	0.05	3.34	0.11		100.09	89.78
MB.71.8	1.3	34.00	5.71	55.50	0.95	0.01	0.03	0.14	0.04	3.33	0.11		99.83	89.73
MB.71.8	2.1	33.71	5.66	55.90	0.94	0.01	0.03	0.13	0.04	3.34	0.09		99.84	89.76
MB.71.8	2.2	34.07	5.31	55.56	0.95	0.01	0.02	0.14	0.04	3.32	0.10		99.52	90.30
MB.71.8	2.3	33.71	5.26	55.77	0.95	0.00	0.02	0.13	0.05	3.31	0.11		99.32	90.26
MB.71.8	3.1	34.01	5.56	55.99	0.94	0.01	0.02	0.12	0.05	3.32	0.10		100.12	89.96
MB.71.8	3.2	33.81	5.67	56.04	0.95	0.00	0.02	0.12	0.04	3.36	0.11		100.12	89.74
MB.71.8	3.3	34.05	5.76	55.84	0.95	0.01	0.02	0.14	0.04	3.30	0.11		100.22	89.69
MB.71.8	4.1	33.70	5.29	56.71	0.97	0.00	0.03	0.14	0.04	3.40	0.13		100.41	90.20
MB.71.8	4.2	33.86	5.66	55.74	0.93	0.00	0.02	0.12	0.04	3.34	0.12		99.84	89.79
MB.71.8	4.3	33.75	5.31	56.89	0.96	0.00	0.03	0.11	0.04	3.33	0.11		100.54	90.19
MB.71.8	5.1	33.63	5.44	57.02	0.94	0.00	0.02	0.12	0.04	3.37	0.11		100.70	90.01
MB.71.8	5.2	33.72	5.62	56.26	0.95	0.00	0.02	0.13	0.04	3.35	0.11		100.20	89.79
MB.71.8	5.3	34.22	5.19	55.69	0.94	0.01	0.03	0.12	0.04	3.31	0.10		99.66	90.50
Average		*33.89*	*5.53*	*55.99*	*0.95*	*0.00*	*0.02*	*0.13*	*0.04*	*3.34*	*0.11*		*100.00*	*89.95*
1σ		*0.19*	*0.21*	*0.52*	*0.01*	*0.00*	*0.00*	*0.01*	*0.00*	*0.03*	*0.01*		*0.39*	*0.28*
MB.71.9	1.1	33.29	6.72	51.90	0.76	0.00	0.14	0.14	0.10	4.61	0.08		97.74	88.53
MB.71.9	1.2	32.72	7.02	52.99	0.78	0.00	0.13	0.15	0.11	4.64	0.10		98.64	87.91
MB.71.9	1.3	32.72	6.84	53.06	0.73	0.01	0.14	0.15	0.10	4.64	0.10		98.48	88.23
MB.71.9	2.1	32.82	6.61	52.27	0.77	0.00	0.13	0.14	0.11	4.72	0.10		97.67	88.50
MB.71.9	2.2	33.19	6.92	52.57	0.75	0.00	0.14	0.15	0.10	4.64	0.11		98.56	88.25
MB.71.9	2.3	32.89	6.57	51.62	0.77	0.00	0.14	0.15	0.10	4.65	0.09		96.99	88.59
MB.71.9	3.1	32.60	6.81	51.93	0.73	0.00	0.14	0.15	0.10	4.83	0.09		97.38	88.24
MB.71.9	3.2	32.57	6.26	51.72	0.75	0.00	0.14	0.16	0.10	4.86	0.09		96.66	88.93
MB.71.9	3.3	32.96	6.97	52.07	0.72	0.00	0.13	0.14	0.10	4.57	0.09		97.74	88.15
MB.71.9	4.1	33.29	6.55	51.74	0.73	0.00	0.13	0.15	0.10	4.56	0.10		97.34	88.81
MB.71.9	4.2	33.24	6.78	52.23	0.74	0.01	0.12	0.15	0.10	4.53	0.10		98.00	88.47
MB.71.9	4.3	33.09	6.53	51.98	0.74	0.00	0.13	0.14	0.10	4.54	0.11		97.36	88.74
MB.71.9	5.1	33.15	6.41	52.01	0.74	0.00	0.12	0.14	0.10	4.62	0.09		97.38	88.93
MB.71.9	5.2	33.14	6.75	52.37	0.71	0.00	0.13	0.15	0.10	4.52	0.11		97.98	88.52
MB.71.9	5.3	33.48	6.79	51.07	0.72	0.00	0.14	0.14	0.10	4.47	0.09		97.01	88.55
Average		*33.01*	*6.70*	*52.10*	*0.74*	*0.00*	*0.13*	*0.15*	*0.10*	*4.63*	*0.10*		*97.66*	*88.49*
1σ		*0.28*	*0.21*	*0.51*	*0.02*	*0.00*	*0.01*	*0.01*	*0.00*	*0.11*	*0.01*		*0.59*	*0.29*
Spinel														***Sp***
MH.2	1.1	20.77	10.39	0.13	0.00			0.10		52.30	0.38	16.05	100.12	67.31
MH.2	1.2	20.74	10.24	0.11	0.00			0.11		52.34	0.37	16.25	100.15	67.35
MH.2	1.3	20.79	10.23	0.11	0.00			0.11		52.83	0.37	16.29	100.73	67.40
MH.2	2.1	20.84	10.44	0.13	0.00			0.11		51.73	0.35	16.87	100.48	66.86
MH.2	2.2	20.64	10.38	0.12	0.00			0.12		53.33	0.37	15.90	100.85	67.28
MH.2	2.3	20.47	10.39	0.17	0.00			0.12		52.49	0.37	15.75	99.77	67.17
MH.2	3.1	20.74	9.28	0.11	0.00			0.10		53.22	0.38	16.51	100.33	68.41
MH.2	3.2	19.69	9.79	0.12	0.00			0.10		53.28	0.38	15.61	98.97	67.15
MH.2	3.3	21.41	8.49	0.12	0.00			0.11		53.85	0.38	16.49	100.87	70.09
MH.2	4.1	20.79	10.03	0.11	0.00			0.09		52.97	0.38	15.94	100.32	67.84
MH.2	4.2	20.77	10.96	0.12	0.00			0.10		52.72	0.37	15.84	100.88	66.75
MH.2	4.3	20.34	10.14	0.12	0.00			0.09		52.75	0.37	16.11	99.92	67.12
MH.2	5.1	20.62	10.07	0.12	0.00			0.11		52.32	0.38	15.46	99.08	67.90
MH.2	5.2	20.47	10.18	0.14	0.00			0.12		52.66	0.37	16.38	100.31	67.06
MH.2	5.3	20.72	10.59	0.12	0.00			0.11		52.50	0.40	15.82	100.26	67.16
Average		*20.65*	*10.11*	*0.12*	*0.00*			*0.11*		*52.75*	*0.37*	*16.08*	*100.20*	*67.52*
1σ		*0.36*	*0.58*	*0.02*	*0.00*			*0.01*		*0.52*	*0.01*	*0.38*	*0.58*	*0.83*
MB.71.8	1.1	18.18	11.28	0.17	0.01			0.13		41.36	0.26	28.43	99.81	56.73
MB.71.8	1.2	18.69	11.60	0.11	0.00			0.16		40.77	0.26	28.73	100.32	56.95
MB.71.8	1.3	18.91	10.93	0.11	0.00			0.15		40.71	0.26	28.68	99.75	57.93
MB.71.8	2.1	19.28	11.30	0.10	0.00			0.16		41.63	0.25	28.25	100.98	58.23
MB.71.8	2.2	18.59	11.92	0.11	0.00			0.15		40.66	0.24	28.34	100.01	56.70
MB.71.8	2.3	18.83	11.14	0.10	0.00			0.15		40.14	0.26	28.86	99.48	57.52
MB.71.8	3.1	19.01	11.52	0.11	0.00			0.14		41.10	0.25	27.81	99.93	57.88
MB.71.8	3.2	18.34	11.33	0.10	0.00			0.15		40.65	0.26	28.17	99.01	57.02
MB.71.8	3.3	18.44	11.64	0.11	0.00			0.15		41.21	0.26	28.92	100.73	56.49
MB.71.8	4.1	20.12	10.52	0.11	0.00			0.14		40.58	0.22	28.97	100.67	59.69
MB.71.8	4.2	18.68	11.08	0.10	0.00			0.16		40.39	0.24	29.02	99.68	57.31
MB.71.8	4.3	20.43	10.34	0.10	0.03			0.16		41.08	0.20	28.14	100.49	60.64

Sample	*Grain*	*MgO*	*FeO*	*SiO_2*	*CaO*	*P_2O_5*	*TiO_2*	*MnO*	*Na_2O*	*Al_2O_3*	*NiO*	*Cr_2O_3*	*Sum*	*Mg(%)*
MB.71.8	5.1	18.75	11.24	0.10	0.00			0.14		40.75	0.25	28.26	99.49	57.60
MB.71.8	5.2	18.85	11.26	0.09	0.00			0.15		40.63	0.26	28.82	100.07	57.46
MB.71.8	5.3	18.58	11.54	0.10	0.00			0.15		40.44	0.26	28.71	99.79	56.88
Average		*18.91*	*11.24*	*0.11*	*0.00*			*0.15*		*40.81*	*0.25*	*28.54*	*100.01*	*57.67*
1σ		*0.62*	*0.41*	*0.02*	*0.01*			*0.01*		*0.40*	*0.02*	*0.37*	*0.54*	*1.14*
MB.71.9	1.1	21.18	11.18	0.09	0.00			0.11		58.19	0.39	9.58	100.72	70.62
MB.71.9	1.2	20.60	11.28	0.09	0.00			0.10		57.79	0.40	9.51	99.77	69.95
MB.71.9	1.3	20.99	11.11	0.10	0.00			0.09		58.99	0.39	9.33	101.00	70.69
MB.71.9	2.1	21.41	11.09	0.09	0.00			0.10		57.63	0.39	10.18	100.89	70.59
MB.71.9	2.2	20.90	11.28	0.10	0.00			0.12		58.55	0.41	9.27	100.64	70.41
MB.71.9	2.3	20.64	11.37	0.11	0.00			0.10		58.64	0.41	9.55	100.82	69.85
MB.71.9	3.1	20.96	11.07	0.10	0.01			0.13		57.59	0.39	9.35	99.58	70.70
MB.71.9	3.2	20.55	11.46	0.09	0.01			0.10		58.35	0.39	10.29	101.25	69.17
MB.71.9	3.3	20.70	10.90	0.10	0.00			0.10		58.88	0.39	10.56	101.63	69.89
MB.71.9	4.1	20.99	11.75	0.11	0.00			0.09		58.51	0.40	9.56	101.41	69.70
MB.71.9	4.2	20.98	10.95	0.09	0.00			0.10		57.71	0.39	9.96	100.18	70.50
MB.71.9	4.3	21.06	11.14	0.10	0.00			0.11		58.59	0.40	9.91	101.31	70.35
MB.71.9	5.1	21.03	11.11	0.10	0.00			0.12		58.02	0.38	9.50	100.27	70.61
MB.71.9	5.2	20.91	11.62	0.11	0.00			0.11		57.94	0.38	10.29	101.36	69.33
MB.71.9	5.3	20.62	11.14	0.09	0.00			0.09		58.10	0.40	9.74	100.18	70.01
Average		*20.90*	*11.23*	*0.10*	*0.00*			*0.10*		*58.23*	*0.39*	*9.77*	*100.73*	*70.16*
1σ		*0.24*	*0.24*	*0.01*	*0.00*			*0.01*		*0.45*	*0.01*	*0.40*	*0.62*	*0.50*

C.3 $^{21}Ne_{cos}/^{3}He_{cos}$ in mafic minerals

Table C.3 compiles previously published $^{21}Ne_{cos}/^{3}He_{cos}$ ratios for different localities and the ratios from Mount Hampton xenoliths.

Table C.3. $^{21}Ne_{cos}/^{3}He_{cos}$ ratios for mafic minerals from different locations. Data are used in Figure 5.15 to compare where the ratios from Mount Hampton xenoliths are compared to previously published data. Pyroxene compositions are normalized to forsterite content following Poreda and Cerling (1992). Forsterite content of the olivines from Reunion and South East Mongolia are assumed to be the same as those measured for Reunion olivines by Furi et al. (2011).

Location	*Altitude (km)*	*Age (ka)*	*$^{21}Ne_{cos}/^{3}He_{cos}$*	*±*	*Fo (%)*	*Reference*
			0.48	0.05	84	Marti and Craig, 1987
East Antarctica	1.8 to 2	6,000	0.26	0.05	25	Bruno et al., 1997
			0.24	0.05	27	
			0.25	0.05	25	
			0.22	0.04	27	
			0.26	0.04	25	
			0.27	0.05	26	
			0.24	0.05	25	
			0.23	0.05	28	
			0.23	0.04	25	
			0.23	0.04	25	
West Grand Canyon	1.5 to 2.0	< 500	0.38	0.03	82	Fenton et al., 2009
			0.43	0.04	81	
			0.35	0.03	81	
			0.42	0.03	84	
			0.39	0.03	81	
			0.42	0.04	81	
			0.42	0.04	82	
			0.20	0.02	26	
			0.22	0.03	26	
			0.20	0.02	26	
			0.19	0.02	26	
West Grand Canyon	1.5 to 1.9	< 500	0.18	0.04	82	Fenton and Niedermann, 2014
			0.22	0.02	36	
			0.34	0.03	81	
			0.27	0.06	36	
			0.38	0.03	83	
			0.21	0.02	36	
			0.42	0.03	84	
			0.22	0.02	37	
			0.37	0.03	82	
			0.15	0.02	35	
			0.33	0.05	87	
			0.28	0.04	38	
			0.25	0.03	38	
			0.25	0.06	38	
			0.22	0.03	38	
			0.18	0.03	38	
			0.24	0.03	38	
			0.21	0.03	38	
West Grand Canyon	1.5 to 1.9	17.8	0.44	0.13	81	Poreda and Cerling, 1992
			0.40	0.07	81	
			0.33	0.05	81	
			0.43	0.03	81	
			0.44	0.03	81	
			0.34	0.04	74	
			0.38	0.03	83	
			0.43	0.04	82	
			0.39	0.02	82	
			0.49	0.03	79	
			0.40	0.15	79	
			0.40	0.02	82	
			0.43	0.02	84	
			0.22	0.02	25	
			0.34	0.02	77	
			0.47	0.05	87	
SE Mongolia	1.5	300	0.30	0.05	83	Staudacher et al.,1993
			0.23	0.02	83	
			0.32	0.03	83	
			0.27	0.03	83	
			0.32	0.02	83	

Location	*Altitude (km)*	*Age (ka)*	$^{21}Ne_{cos}/^{3}He_{cos}$	±	*Fo (%)*	*Reference*
			0.43	0.06	83	
			0.22	0.06	83	
			0.38	0.17	83	
			0.45	0.06	83	
			0.83	0.10	83	
Reunion	2.3	65	0.26	0.03	84	Staudacher et al.,1993
			0.28	0.05	84	
			0.29	0.06	84	
			0.27	0.07	84	
			0.23	0.02	84	
			0.27	0.04	84	
			0.30	0.10	84	
Tanzania	1 to 4	500	0.18	0.01	23	Schimmelpfenning et al., 2011
			0.20	0.00	23	
			0.18	0.01	24	
			0.19	0.01	23	
			0.20	0.02	23	
			0.18	0.01	24	
			0.40	0.02	68	
			0.37	0.02	70	
			0.38	0.02	69	
			0.36	0.06	70	
Australia	0.018	50	0.38	0.05	75	Gillen et al., 2010
			0.38	0.05	75	
			0.38	0.05	74	
			0.40	0.05	80	
			0.40	0.05	80	
			0.35	0.05	66	
			0.36	0.05	67	
			0.37	0.05	71	
West Antarctica	3	11,400	0.36	0.01	91	This study
			0.42	0.02	90	
			0.42	0.01	90	
			0.44	0.02	90	
			0.36	0.02	90	
			0.28	0.01	79	
			0.33	0.01	78	
			0.28	0.02	78	
			0.32	0.01	80	
			0.33	0.01	77	
			0.25	0.02	77	
			0.20	0.01	40	
			0.30	0.03	37	
			0.22	0.03	37	
			0.26	0.01	41	

References

Bruno, L.A., Baur, H., Graf, T., Schlu, C., Signer, P. and Wieler, R., 1997. Dating of Sirius group tillites in the Antarctic Dry Valleys with cosmogenic 3 He and 21 Ne. *Earth and Planetary Science Letters*, *147*(1), pp.37-54.

Fenton, C.R., Niedermann, S., Goethals, M.M., Schneider, B. and Wijbrans, J., 2009. Evaluation of cosmogenic 3 He and 21 Ne production rates in olivine and pyroxene from two Pleistocene basalt flows, western Grand Canyon, AZ, USA. *Quaternary Geochronology*, *4*(6), pp.475-492.

Fenton, C.R. and Niedermann, S., 2014. Surface exposure dating of young basalts (1–200 ka) in the San Francisco volcanic field (Arizona, USA) using cosmogenic 3 He and 21 Ne. *Quaternary Geochronology*, *19*, pp.87-105.

Füri, E., Hilton, D.R., Murton, B.J., Hémond, C., Dyment, J. and Day, J., 2011. Helium isotope variations between Réunion Island and the Central Indian Ridge (17–21 S): New evidence for ridge–hot spot interaction. *Journal of Geophysical Research: Solid Earth*, *116*(B2).

Gillen, D., Honda, M., Chivas, A.R., Yatsevich, I., Patterson, D.B. and Carr, P.F., 2010. Cosmogenic 21 Ne exposure dating of young basaltic lava flows from the Newer

Volcanic Province, western Victoria, Australia. *Quaternary Geochronology*, *5*(1), pp.1-9.

Marti, K. and Craig, H., 1987. Cosmic-ray-produced neon and helium in the summit lavas of Maui.

Poreda, R.J. and Cerling, T.E., 1992. Cosmogenic neon in recent lavas from the western United States. *Geophysical Research Letters*, *19*(18), pp.1863-1866.

Schimmelpfennig, I., Williams, A., Pik, R., Burnard, P., Niedermann, S., Finkel, R., Schneider, B. and Benedetti, L., 2011. Inter-comparison of cosmogenic in-situ 3 He, 21 Ne and 36 Cl at low latitude along an altitude transect on the SE slope of Kilimanjaro volcano (3 S, Tanzania). *Quaternary Geochronology*, *6*(5), pp.425-436.

Staudacher, T. and Allègre, C.J., 1993. The cosmic ray produced He/21Ne ratio in ultramafic rocks. *Geophysical research letters*, *20*(11), pp.1075-1078.

Appendix D. Ne isotope analysis of meteorites

For the analysis of Ne isotopes in extra-terrestrial samples, aliquots of 1.1 to 6.6 mg where encapsulated in Pt packets and degassed using the diode laser as described in Chapter 4. The samples were baked for ~12h at ~100˚C to remove atmospheric gases. Sample degassing was performed by heating the samples at ~1300˚C for 30 minutes. The gas released from the heating of the samples was purified by two *SAES* GP50 getters operated at 250ºC, a *SAES* GP50 getter operated at room temperature and an activated charcoal-filled stainless steel finger cooled to -196°C for 20 minutes. Neon was then trapped on activated charcoal in a cryostatic cold head at 30K for 10 minutes, He was removed by pumping for 1 minute and the Ne was released at 100K for 10 minutes. The Ne isotopes were then analysed statically in the MAP-215-50 as described in Appendix B (section B.2).

The system blanks were measured by heating an empty platinum tube to ~1300ºC for 30 minutes releasing ~3.4 x 10^7 atoms of ^{20}Ne, which represents <0.2% of the measured ^{20}Ne in the samples and has an isotopic composition indistinguishable with that of air. All the samples were reheated in order to ensure that all the gas was released from the sample. Ne from the reheat step was in all cases indistinguishable with the blank.

D.1. Millbillillie

Millbillillie is a brecciated eucrite composed of several distinct lithologies (Yamaguchi et al., 1994) and heterogeneous in composition (Miura et al., 1998). It fell in 1960 in Western Australia (Graham et al., 1985) and 26 kg were recovered from the impact (Fitzgerald, 1980). The Ne isotopic composition has been analysed by different laboratories and therefore it is the preferred one to be used as the standard for the measurement of extremely high cosmogenic Ne isotope signatures. Michel and Eugster (1989) and Miura et al. (1998) published Ne isotopic composition of two distinct Millbillillie fragments from the eucrite interior. For this work another fragment from the interior of the meteorite has been analysed. The same fragment was also analysed by two independent laboratories: IGGCAS (Institute of Geology and Geophysics Chinese Academy of Science, Beijing) and IGS (Institute of Geological Science, University of Bern). This allows for a laboratory comparison and the use of Millbillillie as standard. The

Ne isotopic data obtained from this work, IGGCAS and IGC from the inter-laboratory comparison and previously published data from Michel and Eugster (1989) and Miura et al. (1998) are reported in Table D.1.

Table D.1. Ne isotope data from the analysis of Millbillillie eucrite.

Reference	$^{21}Ne_{cos}$ (10^{11} atoms/g)	±	$^{21}Ne/^{22}Ne$	±	$^{20}Ne/^{22}Ne$	±
This work*	7.32	0.38	0.904	0.017	0.851	0.033
	8.62	0.44	0.899	0.017	0.878	0.032
	9.94	0.51	0.904	0.017	0.865	0.033
IGGCAS*	7.65	1.67	0.887	0.200	0.901	0.008
	7.84	3.02	0.887	0.371	0.906	0.008
	6.11	2.45	0.874	0.382	0.901	0.013
	8.94	4.97	0.891	0.575	0.916	0.010
	8.60	4.53	0.894	0.539	0.902	0.008
	6.91	5.33	0.902	0.889	0.925	0.012
IGS*	12.01	0.87	0.841	0.061	0.884	0.025
Miura et al,	10.83	0.13	0.838	0.010	0.790	0.001
1998	10.80	0.13	0.836	0.010	0.786	0.002
	8.63	0.10	0.839	0.010	0.782	0.002
	10.08	0.12	0.834	0.010	0.786	0.002
	12.36	0.15	0.848	0.007	0.785	0.001
	11.86	0.14	0.842	0.007	0.781	0.001
	12.75	0.15	0.851	0.006	0.788	0.001
	10.86	0.13	0.859	0.006	0.817	0.003
	10.63	0.13	0.853	0.006	0.802	0.002
Michel and	13.17	0.79	0.841	0.017	0.800	0.016
Eugster,1989	13.44	0.81	0.847	0.017	0.800	0.016

*Data from this work, IGGAS and IGS correspond to the analysis of several aliquots of the same fragment from the interior of the Millbillillie eucrite as part of an unpublished inter-laboratory calibration. Previously published data from different fragments of the interior of the eucrite are also included. Uncertainties reported are 1σ.

D.2. Strathmore and High Possil

Strathmore and High Possil are two of four meteorites found in Scotland that fell in 1804 and 1917 respectively. They are two stony meteorites classified as L-6 chondrites (Bevan et al., 1985); which are the most common and the largest group of chondrites analysed (Marti and Graf, 1992). These two chondrites have never been analysed before. Here I report the Ne isotope composition from the analysis of one fragment from the interior of Strathmore meteorite and one fragment from the interior of High Possil. Both specimens come from the collection of the Hunterian Museum and Art Gallery in Glasgow and were donated by Dr. John Faithfull. Data from the analysis of three aliquots of High Possil and two aliquots of Strathmore are presented in Table D.2.

Table D.2. Ne isotope data from the analysis of High Possil and Strathmore chondrites. Uncertainties reported are 1σ.

Meteorite	*weight (mg)*	*$^{21}Ne_{cos}$ (10^{12} atoms/g)*	±	*$^{21}Ne/^{22}Ne$*	±	*$^{21}Ne/^{22}Ne$*	±
High Possil	4.6	2.90	0.15	0.862	0.016	0.835	0.033
High Possil	2.9	3.21	0.16	0.866	0.016	0.836	0.033
High Possil	6.3	3.07	0.15	0.870	0.016	0.831	0.033
Strathmore	6.7	1.65	0.08	0.903	0.017	0.833	0.033
Strathmore	5.4	1.71	0.09	0.924	0.021	0.816	0.033

D.3. Tissint

Tissint is a picritic shergottite, consisting of olivine macrocrysts set in a matrix of fine pyroxene and feldspar fine-grained glass. This Martian meteorite fell to Earth on July 2011 in Morocco (Irving et al., 2012; Aoudjehane et al., 2012). The fragment that was analysed for his work comes from the shergottite interior. Olivine macrocrysts were separated from the matrix by hand picking under a binocular microscope and aliquots of olivine, matrix and whole rock were analysed for Ne isotopic composition. The results are reported in Table D.3.

Table D.3. Ne isotope data from the analysis of several aliquots of Tissint shergottite. Olivine macrocrysts, matrix and the whole rock were analysed separately. Uncertainties reported are 1σ.

Mineral	*weight (mg)*	*$^{21}Necos$ (10^{10} atoms/g)*	±	*$^{21}Ne/^{22}Ne$*	±	*$^{20}Ne/^{22}Ne$*	±
olivine	5.5	5.69	0.33	0.83	0.02	0.86	0.05
olivine	6.4	6.81	0.4	0.83	0.02	0.74	0.05
matrix	8	4.63	0.31	0.83	0.02	1.14	0.07
matrix	5.6	5.1	0.22	0.79	0.02	0.85	0.1
whole rock	7.8	5.21	0.21	0.83	0.02	0.88	0.07
whole rock	6.6	5.12	0.22	0.83	0.02	0.85	0.05

The results from the analysis of olivine, matrix and whole rock reflect the chemical composition control on the production rate with the average $^{21}Ne_{cos}$ measured being 6.25 ± 0.79, 4.87 ± 0.33 and 5.17 ± 0.06 x 10^{10} atoms/g for each separate respectively. This suggests a production rate of $^{21}Ne_{cos}$ in olivine 22% higher than that in the pyroxene and feldspar matrix and 17% higher with respect to the whole rock. Applying the theoretical elemental production rates of ^{21}Ne for L-chondrites proposed by Masarik and Reedy (1994) and Leya and Masarik (2009) to an average major element composition for Tissint olivine (Fo_{80}) and pyroxene (En_{76}) and feldspar (An_{63}) matrix (Irving et al., 2012) the production of ^{21}Ne in olivine is ~30% higher than in the matrix. Theoretical production rates are calculated assuming average chemical composition and the elemental production rates are those of L-chondrites considering only contribution from galactic cosmic rays

(GCR). These factors introduce a source of uncertainty in the results that could potentially make the theoretical and experimental values to be indistinguishable within uncertainty. An uncertainty of 15 % would cause the data to agree. Detailed analysis of major elemental composition and contribution of solar cosmic rays as well as shielding of the sample is required to make any reliable conclusions.

References

Aoudjehane, H.C., Avice, G., Barrat, J.A., Boudouma, O., Chen, G., Duke, M.J.M., Franchi, I.A., Gattacceca, J., Grady, M.M., Greenwood, R.C. and Herd, C.D.K., 2012. Tissint martian meteorite: A fresh look at the interior, surface, and atmosphere of Mars. *Science*, *338*(6108), pp.785-788.

Bevan, A.W.R., Hutchison, R., Easton, A.J., Durant, G.P. and Farrow, C.M., 1985. High Possil and Strathmore—A study of two L6 chondrites. *Meteoritics*, *20*(3), pp.491-501.

Fitzgerald, M.J., 1980. Muckera and Millbillillie-Australian achondritic meteorites. *Trans. R. Soc. South Australia*, *104*, p.201.

Graham A. L., Bevan A. W. R. and Htrrcmsox R. (1985) Catalogue of Meteorites, 4th edition. British Museum (Natural History), London, 460 pp.

Irving, A.J., Kuehner, S.M., Tanaka, R., Herd, C.D.K., Chen, G. and Lapen, T.J., 2012. The Tissint depleted permafic olivine-phyric shergottite: petrologic, elemental and isotopic characterization of a recent Martian fall in Morocco. In *Lunar Planet. Sci. Conf* (Vol. 43, p. 2510).

Leya, I. and Masarik, J., 2009. Cosmogenic nuclides in stony meteorites revisited. *Meteoritics & Planetary Science*, *44*(7), p.1061.

Marti, K. and Graf, T., 1992. Cosmic-ray exposure history of ordinary chondrites. *Annual Review of Earth and Planetary Sciences*, *20*, pp.221-243.

Masarik, J. and Reedy, R.C., 1994. Effects of bulk composition on nuclide production processes in meteorites. *Geochimica et Cosmochimica Acta*, *58*(23), pp.5307-5317.

Michel, T. and Eugster, O., 1989. Cosmic-ray exposure ages of howardites, eucrites, and diogenites. *Meteoritics*, *24*, p.304.

Miura, Y., Nagao, K., Sugiura, N., Fujitani, T. and Warren, P., 1998. Noble gases, 81 Kr-Kr exposure ages and 244 Pu-Xe ages of six eucrites, Bereba, Binda, Camel Donga, Juvinas, Millbillillie, and Stannern. *Geochimica et cosmochimica acta*, *62*(13), pp.2369-2387.

Yamaguchi, A., Takeda, H., Bogard, D.D. and Garrison, D., 1994. Textural variations and impact history of the Millbillillie eucrite. *Meteoritics*, *29*(2), pp.237-245.

Appendix E. Supplementary details of $^{10}Be_{cos}$ measurements

E.1. Separation of $^{10}Be_{cos}$

Eliminating the meteoric ^{10}Be from the surface of the olivine crystals requires three sequential HF and HCl dissolutions. Data from these dissolutions are shown in table E.1.

Table E.1. Data from HF+HCl etching to eliminate the meteoric ^{10}Be from the surface of the olivine crystals. Initial mass ($mass_{int}$) is reduced by three subsequent etching dissolutions. $Mass_1$, $mass_2$ and $mass_3$ are the masses after each of the etchings. The etching process was also performed in one blank containing no olivine.

		Etching 1				*Etching 2*				*Etching 3*			
Sample	*$Mass_{int}$ (g)*	*HF*	*HCl*	*$Mass_1$ (g)*	*% Loss*	*HF*	*HCl*	*$Mass_2$ (g)*	*% Loss*	*HF*	*HCl*	*$Mass_3$ (g)*	*% Loss*
MH.1	1.00	0.20	0.11	0.85	15.48	0.10	0.04	0.79	21.30	0.11	0.05	0.73	26.87
MH.2	0.99	0.18	0.10	0.71	28.92	0.09	1.04	0.69	30.44	0.11	0.06	0.67	32.17
MB.71.7	1.00	0.20	0.11	0.84	15.98	0.07	0.05	0.79	21.71	0.12	0.06	0.73	27.21
MB.71.8	1.01	0.18	0.11	0.83	18.48	0.11	0.05	0.79	22.52	0.12	0.06	0.75	26.20
MB.71.9	1.03	0.20	0.10	0.83	19.25	0.09	0.05	0.80	22.47	0.11	0.05	0.76	26.42
MB.71.10	1.01	0.21	0.09	0.82	18.35	0.10	0.05	0.78	22.19	0.08	0.04	0.77	23.68
Blank	0.00	0.21	0.11			0.10	0.05			0.11	0.05		

The remaining olivine cores were completely dissolved in HF and analysed by ICP-OES at SUERC for composition (Table E.2).

Table E.2. Data from ICP-OES of one aliquot of each sample. Elemental compositions are blank corrected and reported as concentration (ppm) in olivine**.**

Sample	*Al*	±	*Fe*	±	*Mg*	±	*Ca*	±	*Be*	*Cr*	±	*Ti*	±
MH.1	48	4	27,63	482	86,64	753	220	38	-	57	2	3	0
MH.2	74	4	26,93	504	82,48	957	229	39	-	48	1	5	0
MB.71.7	34	3	23,36	224	73,22	612	159	32	-	40	1	6	0
MB.71.8	57	4	29,06	760	92,06	1,486	228	42	-	63	2	1	0
MB.71.9	36	3	25,39	321	69,56	576	161	32	-	16	0	8	0
MB.71.10	49	5	28,31	359	85,43	1,029	181	41	-	50	1	14	0

Samples were spiked with ~500 µg of ^{9}Be (Bourlès, 1988; Brown et al., 1992) (Table E.3).

Table E.3. Data from addition of ^{9}Be carrier to six HF dissolved olivine cores and one blank.

Sample	*Olivine mass (g)*	*UHANN mass (g)*	*UHANN concentration (ppm)*	*^{9}Be (µg)*	*^{9}Be (10^{19} atoms)*
MH.1	0.73	1.27	406	516	3.45
MH.2	0.67	1.28	406	520	3.48
MB.71.7	0.73	1.29	406	523	3.49
MB.71.8	0.75	1.28	406	520	3.47
MB.71.9	0.76	1.29	406	522	3.49
MB.71.10	0.77	1.28	406	518	3.46
Blank	0.00	1.24	406	505	3.37

In order to eliminate the high concentration of Fe and Mg present in the olivine samples bulk separation was performed using a solvent extraction of beryllium by acetyl acetone at neutral pH in the presence of ethylenediaminetetraacetic acid (EDTA) (Tabushi, 1958; Seidl, 1993; Seidl et al., 1997). Following this process two aliquots of each of the samples and the blank were analysed in ICP-OES to test the effect of the process in the removal of the metals without removing the Be present in the sample (Table E4). The results show an effective elimination of the metals, 70 to 99% of the Fe and 95 to 100% of the Mg were removed with > 95% of the ^{9}Be recovered. After this process the remaining Fe and the rest of anions and cations were eliminated by column chromatography following the same procedures as for quartz (e.g. Wilson et al., 2008).

Table E.4. Data from ICP-OES of two aliquots per sample. Elemental compositions are blank corrected and reported as concentration (ppm) in olivine.

Sample	*Al*	±	*Fe*	±	*Mg*	±	*Ca*	±	*Be*	±	*Cr*	±	*Mn*	±	*Na*	±
MH.1	25	1	4,769	26	2,400	0	15	0	645	4	4	14	11	0	11,588	0
MH.1	21	1	5,120	43	2,552	0	17	0	692	6	5	25	12	0	12,462	0
MH.2	27	1	551	6	1,161	0	17	0	707	9	4	14	6	0	19,506	0
MH.2	28	1	592	11	1,228	0	18	1	756	9	4	17	6	0	20,575	0
MB.71.7	14	0	210	3	98	0	4	1	658	5	2	1	0	0	3,170	0
MB.71.7	15	0	220	4	102	0	5	1	702	4	2	2	0	0	3,270	0
MB.71.8	48	1	835	10	1,417	0	21	0	637	5	9	11	7	0	26,134	0
MB.71.8	50	1	882	6	1,527	0	23	0	677	4	9	7	8	0	Saturated	
MB.71.9	22	1	5,014	55	337	0	3	0	645	9	1	2	2	0	878	0
MB.71.9	27	1	5,233	67	351	0	4	0	675	9	1	2	2	0	903	0
MB.71.10	25	2	1,307	20	658	0	10	1	632	3	2	12	4	0	14,130	0
MB.71.10	27	1	1,355	13	676	0	11	1	649	13	2	11	4	0	14,505	0

E.2. AMS $^{10}Be_{cos}$ measurements

^{10}Be concentrations are based on 2.79 x 10^{-11} ^{10}Be/^{9}Be ratio for NIST SRM4325 standard. The BeO^- current is reported relative to that of KN51 standard (Nishiizumi et al., 2007). ^{9}Be AMS currents of the samples were similar to the KN51 primary standard AMS current. Standards KN54, KN61 and KN62 were used as secondary standards (Nishiizumi et al., 2007). Average uncertainties in the secondary standards KN54, KN61 and KN62 were 0.9%, 1.1% and 1.1% respectively. The processes blank ratio ^{10}Be/^{9}Be was between 0.4 to 6 % of the sample ratios. The uncertainty of blank correction is included in the stated standard uncertainties. Data from the AMS analysis are reported in Table E.5.

Table E.5. Results from AMS analysis of standards, olivine samples and one blank. The $^{10}Be/^{9}Be$ data are based on ^{10}Be half-live of 1.36 Ma (Nishiizumi et al., 2007).

Sample ID	*Material type*	*$^{10}Be/^{9}Be$ x10^{-12}*	±	*% of KN51 BeO^- current*
b9326-kn51	KN51	27.09	0.02	100
b9327-kn54	KN54	2.81	0.02	93
b9340-kn54	KN54	2.87	0.03	98
b9423-kn54	KN54	2.84	0.02	101
b9333-kn61	KN61	0.99	0.01	102
b9429-kn62	KN62	0.52	0.01	94
b9346-kn62	KN62	0.54	0.01	103
b9437-nist	NIST	27.73	0.06	86
b9343	MH.1	0.48	0.01	116
b9344	MH.2	0.20	0.00	115
b9345	MB.71.7	0.04	0.00	101
b9347	MB.71.8	0.38	0.01	118
b9348	MB.71.9	0.18	0.00	113
b9349	MB.71.10	0.05	0.00	95
b9350	Blank	0.002	0.00	100

References

Bourles, D., Raisbeck, G.M. and Yiou, F., 1989. 10Be and 9Be in marine sediments and their potential for dating. *Geochimica et Cosmochimica Acta*, *53*(2), pp.443-452.

Brown, E.T., Brook, E.J., Raisbeckl, G.M., Yioul, F. and Kurz, M.D., 1992. 10Be and 26Al in quartz: implications for exposure age dating. *Geophysical Research Letters*, *19*(4), pp.369-372.

Nishiizumi, K., Imamura, M., Caffee, M.W., Southon, J.R., Finkel, R.C. and McAninch, J., 2007. Absolute calibration of 10 Be AMS standards. *Nuclear Instruments and Methods in Physics Research Section B: Beam Interactions with Materials and Atoms*, *258*(2), pp.403-413.

Seidl, M.A., 1993. *Form and process in channel incision of bedrock*. University of California, Berkeley.

Seidl, M.A., Finkel, R.C., Caffee, M.W., Hudson, G.B. and Dietrich, W.E., 1997. Cosmetic Isotope Analyses Applied to River Longitudinal Profile Evolution: Problems and Interpretations. *Earth Surface Processes and Landforms*, *22*(3), pp.195-209.

Tabushi, M., 1958. Solvent Extraction of Beryllium as Acetylacetonate.

Wilson, P., Bentley, M.J., Schnabel, C., Clark, R. and Xu, S., 2008. Stone run (block stream) formation in the Falkland Islands over several cold stages, deduced from cosmogenic isotope (10Be and 26Al) surface exposure dating. *Journal of Quaternary Science*, *23*(5), pp.461-473.